Linköping studies in science and technology. Dissertations.
No. 1516

Modeling for control of centrifugal compressors

Oskar Leufvén

Linköpings universitet
INSTITUTE OF TECHNOLOGY

Department of Electrical Engineering
Linköpings universitet, SE–581 83 Linköping, Sweden

Linköping 2013

Linköping studies in science and technology. Dissertations. No. 1516

Modeling for control of centrifugal compressors
Oskar Leufvén
ISBN 978-91-7519-626-8
ISSN 0345-7524

Oskar Leufvén
oleufven@isy.liu.se
www.vehicular.isy.liu.se
Division of Vehicular Systems
Department of Electrical Engineering
Linköpings universitet
SE–581 83 Linköping
Sweden

The **front cover** illustration shows turbos of different sizes, ranging from a small unit for a high pressure stage application of a two stage series sequentially turbo system and up to a large unit for a heavy duty truck application.
The **rear cover** could symbolize humanities strive toward new goals, where occasionally some guidance is appreciated. Since the "fjäll" in the photo, Helags, contains the southern most glacier of Sweden, the rear cover could also illustrate the need to minimize the environmental footprint of the automotive sector. The rear cover might also simply show the author's family during a ski trip toward the highest peak in Sweden south of the polar circle (1796m), four weeks prior to the thesis print deadline. In either way, picture courtesy of Johan Leufvén.

Typeset with LaTeX 2_ε
Printed by LiU-Tryck, Linköping, Sweden 2013

Abstract

Downsizing and turbocharging of engines provide a way to meet increasing demands for efficiency and performance in the automotive industry. An engine design is a result of compromises, e.g. the selection of charging system, and the trend is to reduce these compromises by increasing system complexity. Models have come to play a central role to handle this rise in complexity, and are used for simulation, system optimization and control synthesis. The models should describe the entire operating range, be capable of extrapolation, be easily parameterizable, and wide cover a range of applications.

A novel compressor model is developed which, in addition to the nominal operation, also covers surge, choke and operation at pressure ratios less than one. The model is based on data from more than 300 compressor maps, measurements from engine test stands, and a surge test stand. The general knowledge gained from the in-depth analysis is condensed in the model equations. The model can be automatically parametrized using a compressor map, is based on static functions for low computational cost, and is shown to extrapolate low speed compressor operation well. Furthermore, it is shown to be applicable to compressors of different size, ranging from small car applications to large heavy duty vehicles. Compressor restriction operation is modeled down to a standstill compressor, and shown to agree well with gas stand measurements. Further, the analysis contributes with new knowledge and models for choking pressure ratio and flow.

A method to automatically determine a turbo map, when the turbo is installed on an engine in an engine test stand is developed. The method can be used to validate manufacturer maps or expand the region covered in a map. An analysis of the limits that an engine installation imposes on the reachable points in the compressor map is performed. The addition of a throttle before the compressor is suggested to increase the reachable map region, and an engine and test cell control structure that can be used to automate the measurements is proposed. Two methods that compensate for the deviation between measured and desired speeds, are proposed and investigated. A gas stand map is compared to the map generated in the engine test stand, and a generally good agreement results.

An experimental analysis of the applicability of the commonly used correction factors, used for estimating compressor performance when the inlet conditions deviate from nominal, is performed. Correction factors are vital, to e.g. estimate turbocharger performance for driving at high altitude or to characterize second stage compressor performance, where the variations in inlet conditions are large. Measurements from an engine test stand and a gas stand show a small but clearly measurable trend, with decreasing compressor pressure ratio for decreasing compressor inlet pressure, for points with equal corrected shaft speed and corrected mass flow. A method that enables measurements to be analyzed with modified corrections is developed. As a result, an adjusted shaft speed correction quantity is proposed, incorporating also the inlet pressure in the shaft speed correction.

Populärvetenskaplig sammanfattning

Nedskalning och turboöverladdning av motorer är ett sätt att möta ökande krav på effektivitet och prestanda. Ett antal kompromisser görs vid motorutvecklingen, där exempelvis motorns maximala effekt avgör turbokompressorns maximala flöde. Kompressorns flödesbredd är begränsad och därför blir tryckuppbyggnadsförmågan på låga motorvarvtal reducerad. Turbon måste vidare rotera med hög hastighet för att öka luftdensiteten, och att accelerera turbon till hög hastighet tar tid, vilket brukar kallas för turbofördröjning. Dessa begränsningar kan hanteras exempelvis genom att sekvensstyrda seriellt kopplade tvåstegsturboaggregat används. Ett mindre aggregat utnyttjas då för lägre motorvarvtal. På högre varvtal övertas överladdningsarbetet av ett större aggregat, och den mindre turbon kopplas förbi. För att hantera den ökade komplexitetsnivån hos överladdningssystem tillämpas modellbaserad reglering, där matematiska modeller för olika delkomponenter av motorn är fundamentala verktyg i konceptutveckling och implementering av regler- och övervakningssystem som hanterar kundernas prestandakrav, samtidigt som låga emissioner och lagkrav säkerställs. Kraven på modellerna är att komponentprestanda beskrivs i alla arbetsområden, parametersättning möjliggörs utifrån tillgänglig data, och god extrapolationsförmåga uppvisas. Vidare bör modellen hantera olika applikationer, exempelvis för turboaggregat från små bil- till stora lastbilsmotorer.

I denna avhandling utvecklas en reglerorienterad modell för turbokompressorn. Modellen hanterar samtliga relevanta arbetsregioner: surge, normalt arbetsområde, samt choke och restriktion. Modellen baseras på kunskap från en djuplodande undersökning av stora mängder mätdata, där slutsatser dragna i undersökningen kondenserats ned i modellekvationerna. Mätdatat innefattar bland annat mer än 300 kompressormappar, data från motortestbänkar och data från en speciellt framtagen surgetestutrustning. Modellens förmåga att beskriva turboaggregat av olika storlek visas vara god, och en bra extrapolationsförmåga till låga turbovarvtal visas. Modellens beskrivning av kompressorarbete vid tryckkvoter under ett, för användning i chokat tillstånd, och för turbovarvtal ned till stillastående modelleras och explicita modeller för detta utvecklas. Modellen implementeras i ett existerande motormedelvärdesmodelleringsramverk, och utökar ramverket med beskrivning av kompressorsurge. Modellen av surge visas vara god, och en ny reglerstrategi för att undvika surge föreslås. Prestandaförbättringen med den nya strategin kvantifieras. Vidare föreslås metoder för att mäta turbomappar för motortestcellsinstallationer, varvid två nya metoder för att justera mätta kompressormappunkter för mindre skillnader mellan önskat korrigerat kompressorvarvtal och uppmätt presenteras. En experimentell undersökning av de fundamentala korrektionsekvationerna som används i kompressormappen presenteras likaså, tillsammans med en förslagen utveckling av korrektionsekvationerna. Påverkan från den föreslagna utvecklingen på fordonsmotorers höghöjdsprestanda kvantifieras. Vikten av korrektionsekvationerna speciellt för tvåstegsturbosystem och höghöjdsbruk visas. En ny metod för att öka marginalen till surgelinjen i en kompressormapp föreslås, och metoder för att undersöka applicerbarheten av metoden visas.

Acknowledgment

Compared to common practice I first and foremost want to express my love for Maya and Isabelle, and thank you for being in my life. I love you both!

I then want to take the opportunity to thank a number of persons, without whom there probably would not have been any thesis. I want to express my gratitude to my friends and family for always making sure that I realize that it is not the entire world that spins and whirls (spoon intended) around turbos. Atheer "Turken" Sam, Robert "Slobb" Kihlberg and Erik Höckerdal are especially acknowledged for just being there.

Karl "Längden" Granström (all chargers on the front cover were hurt in the making of this thesis) is acknowledged for providing impressive length to any discussion, Poolpartys and trips to the small(?) cottage on the west coast. Per "TT" (and, while on it, Berit "denna underbara kvinna") Thyr, Martin "Rävhjielhm" Skoglund, Jonas "Callmertzzsch" Callmer, and Hanna Fager are acknowledged for numerous Torsdagslunchen. Patrik "Pata" Martinsson and Jonas "Eken" Ekerli are acknowledged for our nice MC trips.

My office room mate Christofer Sundström (with correct spelling) is acknowledged for endless discussions on all sorts of topics. Lars Nielsen is greatly acknowledged for letting me join Vehicular Systems, and for providing an environment where research topics can be freely pursued. The rest of the Vehicular Systems group is acknowledged for providing coffee break discussions on topics not necessarily related to turbos.

Andreas Thomasson is acknowledged for proofreading parts of this manuscript, and for being an appreciated research partner. Per Öberg and Erik Frisk are acknowledged for their valuable support with the computer systems. Erik and Gabriella Hellström are acknowledged for making it possible to benefit from the cheap dollar exchange rate, and in the continuation making the rear cover photo possible.

The financial support from the Vinnova industry excellence center LINK-SIC, and the industrial partners are also acknowledged. Johannes Andersen provided me with data during my year in Austria as a masters student, and he later, together with Fredrik Lindström, introduced me to the surge test stand. Fredrik Westin and Ragnar Burenius kindly answered my questions on the two stage data from the gas stand. Anders Lundgren and Anders Andreasson helped me during my weeks in the gas stand. Richard Backman and Jonas Cornelsen were invaluable during the installation of the LNF engine, and the two-stage system. Per-Inge Larsson, Anders Larsson and Henrik Flemmer have given valuable input in various topics. Per Andersson (and I do expect at least one question from you during the public defense of this thesis) has been providing helpful input throughout this entire thesis work, and also during the masters thesis work leading up to the PhD studies.

And last, but, (which is certainly true in this case) as the saying goes, not at all the least, I want to express my deepest gratitude for Lars "Lasse" Eriksson. Without your endless guidance this work would not have been accomplished (and probably never started). Thanks!

Contents

Introduction

1

Introduction

The internal combustion engine has for a long time been the most important prime mover for transportation globally. Even though the internal combustion engine basic design has been around since the late 19th century, it still represents an unbeaten compromise.

> "If a new and in truth better technology emerges, the ones who do not adopt the new technology will die overnight."[†]

A combustion engine is simple in its nature; a mix of fuel and air is combusted, and work is produced by the piston in an operating cycle. The amount of combusted air and fuel controls the amount of work that the piston produces. The piston work has to overcome friction and pumping losses, and by making the engine smaller the losses decrease and engine efficiency thereby increases. To increase engine efficiency in this way is commonly referred to as downsizing. However, downsizing has one important disadvantage; a smaller engine can not induct as much air as a larger one, and is therefore less powerful. The less powerful engine can lead to less customer acceptance. One way to increase the torque of the small engine and thereby regain customer acceptance, is by increasing the air charge density. A higher density increases the air mass that can be aspirated by an engine. The increased mass of air allows an increased fuel mass to be burned, increasing the engine torque. It is outside the scope of this thesis to give a comprehensive summary of basic engine operation and the interested reader is referred to e.g. [170], [78] and [153].

For automotive application, a number of charging systems can be used, e.g. supercharging, pressure wave charging or turbocharging. Turbocharging has become the most commonly used charging system, since it is a reliable and robust system. A turbo utilizes some of the energy in the exhaust gas, otherwise lost to the surroundings.

[†]Free translation from a seminar in Swedish by Per Gillbrand.

There are however some compromises in an engine with a single turbo. One compromise is connected to that the mass flow range of a compressor is limited. The compressor of a single turbo system is sized after the maximum engine power, which is tightly coupled to the maximum mass flow. The limited range then imposes restrictions on the pressure build up for small mass flows, and thereby engine torque at low engine speed. Further, a turbo needs to spin with high rotational speed to increase air density, and due to the turbo inertia it takes time to spin up the turbo. This means that the torque response of a turbocharged engine is slower than an equally powerful naturally aspirated engine, which could also lead to less customer acceptance.

Customer acceptance can then again be regained if the complexity of the charging system is allowed to increase, using e.g. a two stage system. A two stage turbo system combines two differently sized turbo units, where the smaller mass flow range of the smaller turbo, means that pressure can be increased for smaller mass flows. Further, due to the smaller inertia of the smaller turbo, it can be spun up faster and thereby improve the torque response of the engine. The smaller unit can then be bypassed for larger mass flows, where instead the larger turbo is used to supply the charge density needed, see e.g. [93] and [56]. Other studied and used charging systems include e.g. parallel sequential systems, combinations of a mechanical compressor and a turbo, or a system that enables both series and parallel configurations depending on operating point. A brief summary of the most important turbo characteristics, is found in Chapter 2, and the interested reader is referred to e.g. [170], [183], [38] and [9].

The increasingly advanced air charging systems add actuators and components to the engine system. This illustrates that in the process of designing more efficient engines, they are made more flexible to reduce design trade-offs and enable optimization, which adds complexity to the system. Systematic methods are needed to handle the increased complexity, and the model based approach has gained increasing interest in the automotive industry. Model based methods can be used as the foundation for concept development and implementation of control systems, that meet the increased demand for engine performance combined with increasingly stringent emission legislations. The model based approach relies upon models, and to be useful it is vital that the models have good descriptive capabilities over the relevant operating range. The models should be easily parameterizable using available data, and it is desirable that they are also able to describe the operation outside of the range of data that were used in the parametrization process, i.e. to extrapolate. It is also beneficial if a given model handles a wide range of applications, e.g. from a small car sized turbo up to a large heavy duty truck turbo. Turbo data is often measured in gas stands and supplied by the turbo manufacturer. These maps are commonly limited to operation in regions with good component performance. The availability of gas stands in the automotive industry and for researchers can be restricted, while engine test stands are more common. Further, measured turbo characteristic can be affected by installation details, and on engine installations can differ from gas stand installations. Hence, methods to characterize turbo performance on engine installations are beneficial, and can aid in validating and extending manufacturer maps.

1.1 Brief summaries and main contributions of appended papers

This section gives brief summaries and presents the main contributions of the papers included in this thesis.

A mean value engine modeling framework is in Paper 1 [95] extended with surge description capability. The Ellipse compressor model, based on a generalization of an ellipse, is proposed as well as a novel surge controller. The paper contributes with a sensitivity analysis, showing the important characteristics that influence surge properties in an engine. This knowledge is further used in the design of the surge controller, that avoids surge and improves vehicle acceleration performance. The gains for a full throttle acceleration scenario resulting from the improved surge control are quantified.

A method for characterizing turbo performance on engine test stand installations is developed in Paper 2 [96]. The paper contributes with a method for determining turbo performance on engine test bench installations. An engine installation imposes limits on the reachable points in the compressor map, and these limits are highlighted, as well as what they depend on. The novel use of a throttle before the compressor is proposed, enabling the engine and turbo system to span a larger region in the compressor map. The paper contributes with an engine and test cell control structure, that can be used to automate and monitor the measurements by controlling the system to the desired operating points. When measuring a speed line, deviations between measured and desired speed can occur, and two new methods for adjusting the measured points to the correct speed are proposed.

An analysis of the corrections used to scale compressor performance for varying inlet conditions is performed in Paper 3 [98]. A surge avoidance strategy is proposed, showing that a reduction in compressor inlet pressure can increase the surge margin. A method to investigate the applicability of the strategy, that is straight forward and general, is also proposed. An experimental analysis of the correction factors, commonly used to determine compressor performance when inlet conditions deviate from nominal conditions, is performed. As a result, extensions to the commonly used correction equations are proposed. Experimental data from an engine test cell and a gas stand show a small, but clearly measurable trend, with decreasing compressor pressure ratio for decreasing compressor inlet pressure. A novel method is developed, enabling measurements to be analyzed with modified corrections. An adjusted shaft speed correction equation is proposed, incorporating also the compressor inlet pressure in the shaft speed correction.

Paper 4 [100] extends the Ellipse compressor model, capable of normal, surge and choke/restriction description, that was proposed for car applications in Paper 1 and [97], to also cover heavy duty applications. The paper analyzes map properties for a database of 236 maps, discussing and highlighting the data distribution and what a practicing engineer can encounter when working with compressor modeling and parameter estimation. The analysis results in the development of a novel automated model parametrization process. The paper further contributes with an investigation that shows good low speed extrapola-

tion capability of the automatically parametrized extended model.

An experimental analysis and modeling of compressor flow for low pressure ratios, resulting from extensive measurements in a gas stand is presented in Paper 5 [99]. The paper contributes with methods to measure restriction map points in a gas stand, and proposes a systematic method to categorize maps into three types: normal, full, or extended. The paper further contributes with analysis and modeling of compressor operation at high flows and low pressure ratios, and also standstill operation. The Ellipse compressor model is validated as a tool to extrapolate unity pressure ratio flow. The model is exploited to deepen the understanding of compressor flow at unity pressure ratio, resulting in the development of models for this flow. An extension to the Ellipse model is presented, and it is exemplified how the experimental findings can be incorporated into a model that describes the high flow and low pressure ratio operation of centrifugal compressors. The extended model accurately describes the extended maps, also for operation at pressure ratios below unity and under choked conditions.

These five papers form the core of this thesis, and the author has been the principal investigator and main author of all five.

1.2 Other publications by the author

This section summarizes research publications the author have been involved in, that were not included in this thesis.

A Andreas Thomasson, Oskar Leufvén, Ivan Criscuolo and Lars Eriksson, *Modeling and validation of a boost pressure actuation system for a series sequentially turbocharged SI engine*, Accepted for publication in Control Engineering Practice [165]

B Lars Eriksson, Tobias Lindell, Oskar Leufvén, and Andreas Thomasson, *Scalable Component-Based Modeling for Optimizing Engines with Supercharging, E-Boost and Turbocompound Concepts*, 2012, SAE International Journal of Engines [45]

C Lars Eriksson, Tobias Lindell, Oskar Leufvén, and Andreas Thomasson, *Scalable Component-Based Modeling for Optimizing Engines with Supercharging, E-Boost and Turbocompound Concepts*, Technical paper 2012-01-0713, 2012, SAE World Congress, Detroit, USA [46]

D Oskar Leufvén and Lars Eriksson, *Surge and choke capable compressor model*, 2011, IFAC World Congress, Milan, Italy [97]

E Ivan Criscuolo, Oskar Leufvén, Andreas Thomasson, and Lars Eriksson, *Model-based boost pressure control with system voltage disturbance rejection*, 2011, IFAC World Congress, Milan, Italy [33]

F Andreas Thomasson, Lars Eriksson, Oskar Leufvén, and Per Andersson, *Wastegate Actuator Modeling and Model-Based Boost Pressure Control*,

2009, IFAC Workshop on Engine and Powertrain Control, Simulation and Modeling, Paris, France [164]

G Oskar Leufvén, *Compressor Modeling for Control of Automotive Two Stage Turbochargers*, 2010, Licentiate thesis, LiU-TEK-LIC-2010:32, Thesis No. 1463, Linköping University [94]

H Johan Bergström, and Oskar Leufvén, *Surge Modeling and Control of Automotive Turbochargers*, 2007 Masters thesis, LiTH-ISY-EX-07/3999–SE, 1463, Linköping University [14]

The authors contributions to these journal and conference publications are indicated by the author list, where the first author is the main contributor to a publication. In the analysis of the charging system actuator system presented in publications **A** and **E**, the author initialized the project, built the experimental setup and performed the majority of measurements and initial modeling. For publications **B** and **C** the author was contributing with the turbo modeling, and a literature survey of charging concepts. For publication **F** the author was involved in the turbo modeling. The licentiate compilation thesis **G** is based on Paper 1, Paper 2, and earlier versions of publication **D** and Paper 3. During the masters thesis **H**, the author was contributing with the turbo modeling, and the analysis of measurement data.

1.3 Future work

This section briefly presents continuations of this thesis, or research topics that have been found along the way, but that did not gain the deserved attention due to the time constraints.

A turbo consists of two main parts, a compressor and a turbine, and a natural continuation of this thesis is therefore found in its title. To evaluate and validate control oriented turbine models, can be motivated by the development and increased use of twin scroll turbines, mixed flow turbines, and variable geometry turbines.

To investigate and evaluate observer designs based on the developed compressor models is also an interesting continuation. To accurately know the two stage system states, e.g. pressures, temperatures and turbo speeds, is important for a controller. Especially to estimate the shaft speed of the bypassed high pressure stage is an interesting scope. This is important for transients involving a stage switch, where the charging effort is transferred from one of the stages to the other. Further investigation of shaft friction can be motivated by experimental experience from the engine test stand, where the bypassed second stage sometimes stops in friction. For transient two stage control, it is important for the controller to know the shaft speed of the turbos; if the high pressure turbo has stopped or is rotating along in 30 krpm is then vital information.

More measurements of turbo performance for larger variations in inlet conditions, and for more units, compared to the reference conditions, is also a research scope. Such an investigation is also closely related to further investigations of how engine system geometries and properties affect both compressor

and turbine performance, compared to the gas stand measured maps. Also to investigate the applicability of the here proposed centrifugal compressor models to even larger centrifugal compressors for industrial processes, is an interesting continuation.

1.4 Outline

The purpose of the introductory chapters is to introduce the topic, and place the research efforts of this thesis into the research field. An overview of experimental setups used during the thesis work, and a short summary of the appended papers are also given.

The main components making up a turbo: compressor, turbine and center housing with bearings, are introduced in Chapter 2. The goal with the first part of Chapter 2 is to introduce and give an overview of experimental and theoretical studies that not necessarily provide any modeling efforts, but are related to control. Inertia, heat transfer, friction and gas properties are discussed. The turbo performance maps and how they are measured are then presented, with further discussions on characteristic features of a map and phenomena that affect turbo performance. An introduction to model based control, and the mean value engine model framework are then given. This is followed by a short introduction to models of higher dimension than those investigated in this thesis, both for completeness and since higher order modeling has provided inspiration for the models developed in this thesis. Apart from a compressor model, turbine and friction models are needed for full turbo simulations. An overview of available models is presented, and the chapter ends with a presentation of how the turbine and friction models used in this thesis relates to other models.

The entire Chapter 3 then discusses compressor modeling, where compressor operation is divided into three separate regions that are discussed in individual subsections. Surge modeling efforts are presented first, followed by discussions of restriction and choke operation. The normal operation is then exemplified by following an air particle through the compressor stage, using the ideas belonging to the physical modeling family, since this provides an convenient introduction to the underlaying phenomena. The compressor model developed in this thesis belongs to the gray or black box family, which is introduced in the last section. A number of model examples available in the literature are presented, to show the vast flora available to the engineer. The last sub sections then discusses the Ellipse compressor model developed in this thesis, and how it relates to other available models.

Chapter 4 presents two of the experimental setups used for the measurements in this thesis: the engine laboratory at Vehicular Systems and the Saab Trollhättan gas stand. Details on the sensors and measurements systems used are given, along with general information of the test stands.

The five appended papers then make up the rest of the thesis.

2

Turbo

The most common automotive air charging system utilizes a turbo. A turbo consists of a compressor and a turbine on a common shaft, supported by bearings in a center housing. An example of a turbo is shown in Fig. 2.1, where some of the important parts are marked. The housing and bearings are cooled by oil, and commonly also water for the higher exhaust gas temperatures encountered in spark ignition engine applications. The turbine extracts some of the available energy in the exhaust gas stream, and provides a driving torque to the compressor through the common shaft. The compressor is used to increase the intake air density, and thereby the engine power, and the torque needed for the compression process loads the common shaft. The friction also contributes with a loading torque on the shaft. The change in turbo speed ω_{tc} is commonly described using Newton's second law for rotating systems as

$$\frac{d\omega_{tc}}{dt} = \frac{1}{J_{tc}} \left(Tq_t - Tq_c - Tq_{fric} \right) \tag{2.1}$$

where $\omega_{tc}[^{\text{rad}}/_{\text{s}}]$ is the turbo rotational speed, $J_{tc}[\text{kg m}^2]$ the inertia of the rotating components, $Tq_t[\text{Nm}]$ the turbine torque, $Tq_c[\text{Nm}]$ the compressor torque, and $Tq_{fric}[\text{Nm}]$ the torque acting on the shaft due to friction.

This chapter first gives and overview of the compressor, the turbine, and the center housing with bearings and the shaft connecting the compressor and turbine wheel. For each of these turbo components, a summary of theoretical and experimental work available in the literature is presented. Hence the result and conclusions from measurements and high order models will be presented and discussed. Discussions on inertia, unsteady flow, heat transfer, and friction are presented under the center housing section. Some brief comments on gas properties, and commonly used assumptions are also presented. The turbo performance maps are then presented, along with some compressor and

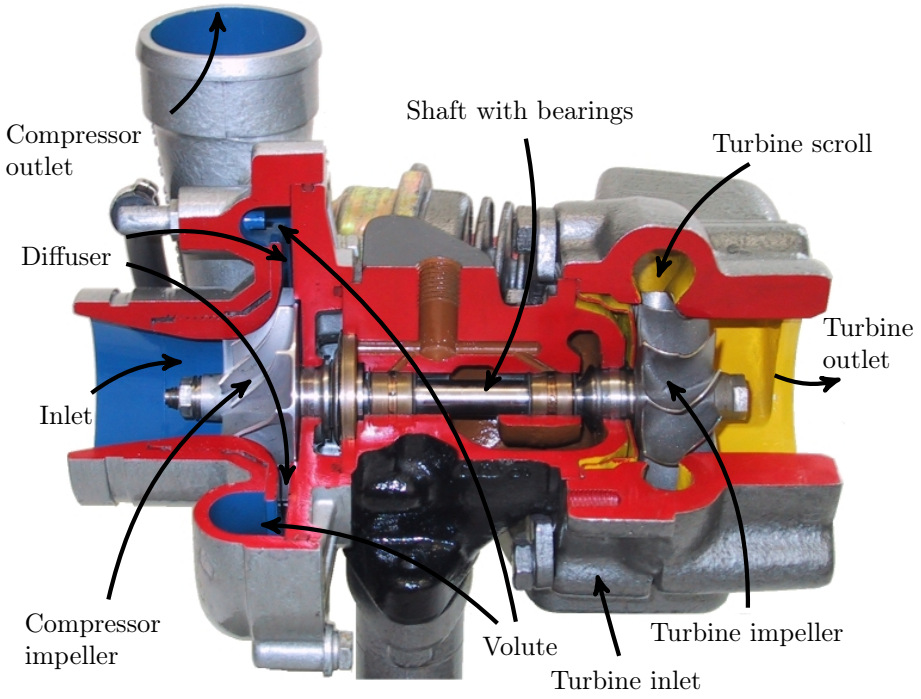

Figure 2.1: Picture of a turbo. The air enters the compressor through the inlet (left) and through the impeller. The heated and pressurized air is then collected in the volute and delivered to the outlet connection (up). The exhaust gas enters the turbine through the turbine inlet (hidden behind the turbo), is lead through the volute into the impeller, where energy is transferred to the impeller vanes and then exits through the outlet (right).

turbine operation characteristics. The next section then presents model based control and mean value engine modeling, followed by a section briefly discussing different model families of various complexity levels.

Modeling efforts related to turbo control are then presented and exemplified for the turbine, and the shaft friction. The presentation focuses on models of a complexity level close to the turbine and friction models used in Papers 1 and 4. The models for Tq_t and Tq_{fric} of (2.1), among others, used in these papers are presented in the last section. The main topic in this thesis, compressor modeling, is given the entire Chapter 3.

For further details and discussions on the turbo, turbo operation or characteristics, the interested reader is referred to the good turbo books that are available in the literature, e.g. [170], [183], [38], [101], [9], and [79].

2.1 Compressor

Centrifugal compressors are used almost exclusively for automotive applications. They are referred to as centrifugal, or radial compressors since the air enters axially, but leaves the compressor impeller in the radial direction. Axial compressors also exist, but are used mainly in e.g. aircraft or power generation applications. Centrifugal will commonly be omitted here for compactness of the following presentation, i.e. the centrifugal compressor will be referred to as only the compressor.

The main components of a compressor are the intake section, the inducer, the impeller, the shroud, the diffuser and the volute, see e.g. [170, 183]. The air flow is first collected in the compressor inlet, which guides the air to the impeller. The inlet casing is essentially a nozzle, used to make the boundary layer blockage thinner and thereby improve impeller performance, see [42, p.781]. The first part of the impeller is commonly referred to as the inducer section. The impeller then consists of many impeller vanes, that rotate at a high velocity. The small turbos making up the second stage of a two stage system can have maximum rotational speeds of 300krpm, and the maximum speed of a larger truck application turbo can be 100krpm. The impeller rotating with high velocity transfers energy to the air flow, and thereby increases the kinetic energy of the air. The air then leaves the compressor impeller in the radial and tangential direction.

Since centrifugal compressors are reaction machines, part of the compression occurs already in the impeller passages, but the main part occurs in the diffuser, see e.g [175, p.3] and [57, p.1466]. Both temperature and pressure increases during compression, even for an ideal compression process. The real pressure increase is however associated with different losses, e.g. flow friction, which increase the rise in temperature even further, and the process is hence not isentropic but polytropic, see e.g. [183, p.60] and [67, p.1344]. While the majority of the diffusion occurs in the diffuser, available kinetic energy can continue to diffuse in the volute, see e.g. [170, p.76], [183, p.55], and[20, p.153].

The diffuser section used for automotive applications is commonly vaneless, since vaned diffusers reduce the compressor flow width, see e.g. [170] and [130, p.131]. The volute works as a diffuser for low mass flow, or as a nozzle at high mass flow, and as neither at the volute design flow rate, see [145, p.118].

A valve can be mounted in close connection to the compressor. This valve is referred to as a surge or recirculation valve, and is used to decrease the pressure after the compressor. The valve opens a connection from the pipe after the compressor to the pipe before, to avoid compressor surge. An example of a closely coupled surge valve built into the compressor scroll is shown in Fig. 2.2. Control of the surge valve is connected to engine performance, and this is studied in Paper 1. For a series sequential two stage system the high pressure stage is commonly equipped with a by-pass valve, which leads compressed air from the first stage around the second stage.

During modeling efforts, different compressor diameters are commonly used. Commonly used diameters are presented in Fig. 2.3. The shaft diameter d_{cs}, the hub diameter d_{ch}, the outer impeller diameter d_{c1} at the inducer section, the exducer diameter d_{c2}, and the compressor diameter d_c are seen. d_c is calculated

Figure 2.2: Compressor scroll with built in recirculation valve or surge valve. For surge control, air is recirculated from the outlet duct through the banana shaped hole at the upper right, through the circular hole close to the banana, and then through internal channels to the compressor inlet which is at the center of the scroll. Control of the surge valve is discussed in Paper 1, and this particular scroll belongs to one of the turbos ran in surge for the measurements of Papers 1 and 4.

as the mean diameter that divides the inlet in two annuli of equal area as

$$d_c = \frac{1}{4}\sqrt{d_{c1}^2 + d_{ch}^2} \tag{2.2}$$

d_c will be commonly used in the compressor modeling in Chapter 3. The hub diameter is mainly given by the nut screwed onto the shaft, which sticks up in the center of the wheel.

The particular wheel design presented in Fig. 2.3 consists of six full impeller vanes, and six splitter blades that starts roughly half the way through the impeller. Splitter blades are commonly used in modern designs, see e.g. [20, p.147]. All twelve blades (both full and splitter) are back-swept at the exducer section of the wheel. The back-sweep angle is usually at least 30^o on modern designs to balance stage stability and impeller stress levels, see e.g. [20, p.142-143] and [170, p.74].

The commercially available single stage turbo designs peripheral rotor speeds, tip speeds, are increasing. A maximum tip speed of $460^{\text{m}}/_{\text{s}}$ is presented as material stress induced limit in [82, p.193], and for aluminum alloys a tip speed limit of $470^{\text{m}}/_{\text{s}}$ is indicated in [170, p.70], and stated to give a maximum pressure ratio limit of roughly 4. In [79, p105], the maximum tip speeds is indicated to be roughly $520^{\text{m}}/_{\text{s}}$, giving a maximum pressure ratio of 4.5. Even higher speeds

Figure 2.3: Example of compressor wheel with six full blades and six splitter blades. The gas enters from above, and leaves in radial direction, and the wheel rotates clockwise. Mitsubishi Heavy Industry (MHI) TD04L-14T compressor wheel used for surge measurement in Papers 1 and 4.

and pressure ratios can be achieved using titanium impellers [79, p105].

In e.g. [20, p.147] and [170, p.57], the vane thickness is said to be typically 0.3% of the d_{c2}, with a lower limit of approximately 0.35mm due to manufacturing processes. The vane thickness limits the vane number, to avoid reducing the compressor eye inlet area, see [170, p.58], while the slip factor indicating the fluid guidance of the wheel, increases with an increased number of blades. The hub thickness is chosen to ensure sufficiently high vibration frequencies, see [20, p.147], and the hub diameter is naturally determined by the shaft diameter, see [170, p.58]. The compressor hub to impeller tip ratio is ≈ 0.2, and the ratio of inducer tip diameter to exducer tip diameter is around 0.5, see [170, p.107]. The peak efficiency generally decreases with a decreased size, since the clearances, and losses are proportionally larger for a smaller design than on a larger, see e.g. [170, p.61] and [80].

Variable geometry compressors exist, see e.g. [170, p.137] and [23], but are not common for automotive applications due to additional cost and packaging constraints. Examples of different variable devices are pre-whirl-generators and variable compressor diffusers, see e.g. [9, p.70-72], [79, p.90], [37, p.184], and [23]. Also modifications to the compressor shroud can be used to widen the stable flow range, see e.g. [52], [9, p.67-70] and [151]. Changing the compressor geometry can give both a reduced surge mass flow, while at the same time not compromise high flow performance apart from the fluid frictional losses associated with the devices, see [37, p.184]. Measurements of compressor performance for different co-swirl are presented in e.g. [173] and [79, p.91].

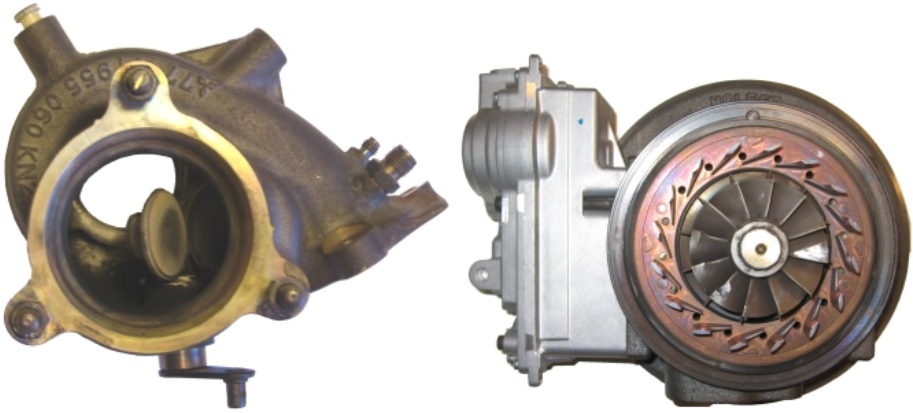

Figure 2.4: Photo into the exhaust side of a turbine housing with WG (left) and a VGT system (right).

2.2 Turbine

While research is being conducted on mixed flow turbines, current automotive applications almost exclusively utilize radial turbines. The radial turbine will therefore here commonly be referred to only as the turbine. The main components making up a turbine, and the occuring losses are presented e.g. in [170] and [79]. The turbine extracts some of the otherwise lost energy from the hot exhaust gas of the combustion engine. The exhaust gas flows through a turbine impeller, where energy is extracted and transferred to the compressor side. Turbines are reaction machines, and a part of the expansion occurs in the stator and the rotor respectively, see e.g. [170] and [57, p.1466]. The degree of reaction of a turbine states how much expansion that occurs in the rotor relative to the total expansion, see e.g. [170, p.151]. As for the compressor, peak turbine efficiency generally decreases with a decrease in size, see [154, p.1].

A waste-gate WG valve is commonly used to control the amount of exhaust gas that flows through the turbine, and thereby the turbine power in automotive petrol engines. The turbines of automotive diesel engines commonly use a variable geometry VGT to control the turbine power, instead of a WG. The VGT actuators effectively change the flow geometry within the turbine using e.g. variable guide vanes, or a variable turbine inlet area, see e.g. [170, p.188-] and [9, p.184-]. The use of VGT as also been studied for petrol engines, see e.g. [4]. A turbine scroll equipped with a built in WG is shown in Fig. 2.4, where also a turbine wheel with VGT guide vanes is shown.

2.3 Center housing

The turbo inertia and friction both have a direct influence on the acceleration of the turbo, see [137, p.187]. But also the heat transfer occurring in turbos have a strong influence on performance and measurements, see e.g. [107, p.227]

and [2].

The bearings of the turbo shaft are mounted in the center housing of the turbo, and are critical components, needed to support the shaft at high speeds. Fluid bearings and ball bearings are commonly used, and are supplied with oil to reduce friction. For small automotive-type turbos, plain bearings in the form or rotating floating bushes are used almost exclusively, see e.g. [170, p.49]. The plain or sleeve bearing is said to give an almost indefinite life, provided clean lubrication fluid, and accepts large out-of-balance loads, vibrations and shocks. However, high oil feeding pressure and flow rates are said to be needed, see [170, p.47]. Ball bearing turbos are also used. The oil supplied, or additional water cooling, is used to cool the turbo.

The different operation of sequential turbocharging systems, compared to a single turbo system, is in [124] said to increase the oil consumption by the turbos. This oil leaks from the center housing through the compressor or turbine. The main parameters affecting the oil consumption are from the experimental study said to be: the bearing house outlet duct oil pressure, the compressor discharge pressure, and the turbine outlet pressure.

In [123, p.377], a 'moment of inertia factor' is introduced. The moment of inertia factor is estimated from known data, and then used to scale inertia for variation in component sizes through a simple multiplication with the relevant radius squared. The effective turbo inertia is in [6, p.122], [19, p.28] and [147] adjusted so that a simulated transient response reflects a measured. Due to the turbo rotor inertia, cyclic torque caused by unsteady operation, only results in small changes in turbo speed (typically $2-5\%$ is stated), see [170, p.182]. However, the angular acceleration can still be large, see [104].

2.3.1 Heat transfer

Good summaries of relevant work surrounding heat transfer modeling of engine exhausts are found in e.g. [89], [43], and [132]. The effect of heat transfer in an automotive turbo system is analyzed in e.g. [3], [26], [10] and [114], and summarized in e.g. [11, p.3]. In [144] the effect on engine volumetric efficiency and turbo lag resulting from turbocharger heat transfer is investigated.

For the turbine, the most of the heat transfer occurs upstream of the rotor, and thus affects the work transfer process, see [11, p.2]. Compared to the turbine, the variation in compressor heat flux with turbine inlet temperature is much less strong, due to the lubricating oil acting as a heat sink, see [10, p.3,9] and [11, p.2]. The compressor external heat transfer is consistently low, but not a negligible fraction of the overall heat transfer. The main effects from the compressor heat transfer is in [26, p.786] said to be the apparent decrease in efficiency due to the additional temperature rise, and also due to the increase in work needed for the compression when the fluid temperature increases. The latter effect is referred to as the reheat effect, see e.g. [38, p.40]. According to predictions of heat flux to the inner surface of the compressor housing, as a function of distance from inlet, negligible heat flux occurs until the leading edge of the impeller, see e.g. [10, p.4] and [11]. An increasing heat flux thereafter results from the compression process, and the largest heat flux occurs for lowest

mass flow, see [10, p.4].

The measured η_c is in [26, p.793] found to only drop slightly with the turbine inlet temperature at higher speeds. For lower speeds, the turbine inlet temperature increasingly affects the measured compressor efficiency. Since the turbine efficiency is commonly estimated from the compressor temperature rise, also unphysical turbine efficiency values can be found for lower speeds, see e.g. [86], [3, p.121] and [145]. The not adiabatic operation of a turbo is further discussed in [26, p.785], where the effect for higher speeds decreases since the work transfer increases. In [31], the heat transfer is said to represent up to 20% of the compressor adiabatic power. The efficiency measured for an electrically driven compressor is, in [5, p.223], reported to be approximately 5% *lower* than comparable data from gas stand tests.

The flow maps are not significantly affected by the heat transfer from turbine to compressor, but the efficiency maps can be, see [86] and [145, p.74]. The measurements in [26, p.793] shows that the compressor pressure rise is unaffected by changing turbine inlet temperature, and it is concluded that the apparent compressor efficiency deficit at low speeds is entirely due to the heat transfer effect. Also the measurements in [150, p.4] show no effect on pressure ratio from heat transfer, and that the largest affect from heat transfer is expected close to surge on low speeds. The heat transfer is also proposed to be modeled and included in the efficiency models, especially for lower speeds, see [3, p.121]. In [150, p.5], a constant heat transfer rate is said to be a reasonable approximation.

The compressor backplate and housing are described as relatively efficient heat exchangers in [112, p.2], due to relatively large area, high temperature drops and low flow rates. A strong correlation between compressor outlet temperature and the compressor casing temperature is shown in [142]. In [10, p.3,11] it is said that while conduction and radiation can be modeled using material thermal properties and data, the convective heat transfer modeling can be challenging. Main heat transfer is said to occur in the diffuser and volute where large surface areas are exposed to the air flow, while heat transfer between the turbine and compressor wheel is said to be neglectable due to the lubricating oil.

Measurements of compressor performance for cases with and without insulation shows that the amount of heat transfer from the compressor through free convection and radiation has almost no effect on the measured compressor efficiency, see [145, p.73,162]. It is further concluded that the compressor can transfer heat to the oil at high turbo speeds. Further, the heat transfer by free convection and radiation from the turbine to the compressor has negligible effect on compressor efficiency. This is said to be due to the relatively small surface area available for convection and radiation compared to the conduction heat paths, and is also supported in [2]. It is stated in [145, p.11, 73] that the low absorptivity, given an emissivity of ≈ 0.63, of the bright compressor casing, reduces the effect of radiation heat transfer. In [142] emissivity levels of 0.1 and 0.9 are assumed for the compressor and turbine casings respectively, and radiation is concluded to be important at small compressor powers.

2.3.2 Friction

An experimental analysis shows the main bearing power losses to be: radial bearing, thrust bearing, wet-oil-cavity (slender shaft area) and seals, see [91, p.3]. In [91], a large oil pressure is said to increase the friction power losses. Further, the thrust bearing losses are the largest contributors to the total friction loss. The turbine power to overcome friction is said to be reduced by half for ball bearings in [172, p.24], and a reduction of 40-80% is presented in [137, p.187]. In [25, p.126], the bearing loss power is assumed to be unchanged in pulsating flow operation. More general pictures of measurements of friction can be found e.g. in [91, p.5] and [77]. Measurements of bearing friction torque vs. oil temperature, and a comparison to manufacturer data is presented in [137, p.194]. Both oil temperature and pressure are linked to friction in [36], using a dedicated torque meter. Friction increases with oil pressure due to that the increased oil flow decreases oil temperature, and thus increases viscosity.

Normally the axial thrust from the compressor and turbine balances each other, see e.g. [170, p.49], however for off-design operation an axial force can be created. Due to the hydrodynamic mode of friction of the thrust bearings, only a weak dependence on the friction forces should result from the loading forces, see e.g. [103] and [77]. The thrust bearing load for a case where no force is created by the compressor wheel is presented in [91]. The turbine side gas velocity is said to create an axial load acting on the thrust bearing, that depends on the gas temperature, due to its effect on the gas density [91, p.6]. Measurements of thrust bearing load can be found in [91, p.6], and models for thrust bearing force and bearing power resulting from variation in compressor inlet guide vane position is presented in [77]. Measurements of friction torque changes due to variations in axial load is compared to manufacturer data in [137, p.196], and it is concluded that a reasonable model for the axial thrust friction should add a friction torque component that is proportional to the magnitude of the axial force.

2.4 Gas properties

A number of fluid properties are commonly assumed to be constant when studying turbo operation. R is treated as constant for temperatures below 1500K in [114], and in [147] both R and c_p are assumed constant. The dynamic viscosity, the thermal conductivity, and the specific heat capacity c_p are assumed to be independent of pressure in [131, p.8], and modeled e.g. in [110]. The variations of c_p with temperature is in [141] said to be important, and the influence of temperature on the specific heat ratio γ_c should be considered when calculating isentropic temperatures. The variation in γ is further said to give rise to $\approx 2.5\%$ of η_c overestimation, and $\approx 5\%$ of η_c underestimation, for the studied temperature range. Variations in humidity are in [141] said to be important in efficiency calculations, only when a very high precision is required. The effect from assuming the humidity to be constant, is quantified to give rise to a underestimation in effective power of $\approx -0.5\%$, with almost negligible effect on the efficiency calculations.

2.5 Turbo performance maps

Turbo performance is usually presented in maps using corrected performance variables. The corrections are important, since the performance maps are otherwise only valid for the conditions under which they were measured. The inlet conditions for the turbine naturally varies with operating points, both in pressure and temperature. But also the compressor inlet conditions vary e.g. with changing ambient conditions (high altitude driving, or desert conditions). Also the engine compartment temperature, greatly affect the compressor inlet temperature [138, Sec. 4.2]. Still, ambient gas temperature is sometimes used in modeling, even though large differences exist [86].

The basis for the map corrections is dimensional analysis [160], and the correction equations relevant for turbos are presented e.g. in [101], [38] and [174]. The correction equations scale the turbine and compressor performance variables, based on the current inlet temperature and pressure. An experimental investigation of the correction quantities for the compressor is presented in Paper 3, and an investigation on compressor inlet gas properties is presented in [18]. The inlet conditions for the compressor for an engine installation, for example, is affected by both a pressure drop due to the air filter and heat transfer in the pipes increasing the air temperature from ambient, see e.g. [85, p.38] and [147].

There are standards describing the procedures involved in measuring a turbo map, see e.g. [133], [134], [8] and [28]. The definition of when surge occurs, which gives the smallest mass flow point for a corrected compressor speed, have been discussed in a number of works, see e.g. [59] and [5]. In [109], detection of surge precursors is experimentally evaluated using pressure and temperature sensors at the compressor inlet and outlet. A summary of different turbo test facilities is presented in [59]. Methodology to measure turbo performance on an engine in a test stand is the topic of Paper 2.

2.5.1 Compressor map

There are four performance variables for the compressor map: corrected mass flow, pressure ratio, corrected shaft speed and adiabatic efficiency. The *corrected compressor mass flow* is given by

$$\bar{W} = W_c \frac{\sqrt{\frac{T_{01}}{T_{c,ref}}}}{\frac{p_{01}}{p_{c,ref}}} [\mathrm{kg/s}] \tag{2.3}$$

where $W_c[\mathrm{kg/s}]$ is the compressor mass flow, $T_{01}[\mathrm{K}]$ is the compressor inlet temperature, and $p_{01}[\mathrm{Pa}]$ is the compressor inlet pressure. The temperature $T_{c,ref}[\mathrm{K}]$ and the pressure $p_{c,ref}[\mathrm{Pa}]$ are the reference states. The reference states must be supplied with the compressor map, since these states are used to correct the performance variables. The *compressor pressure ratio* is given by

$$\Pi_c = \frac{p_{02}}{p_{01}} [-] \tag{2.4}$$

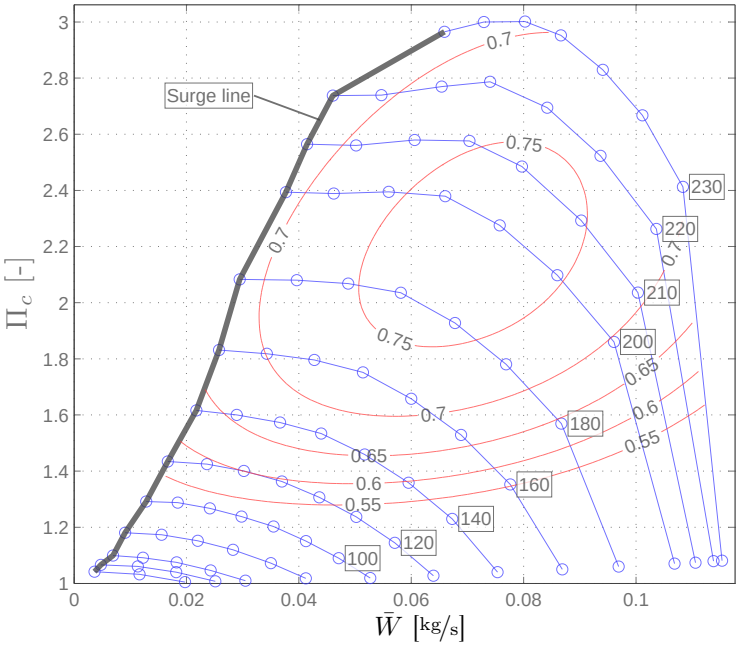

Figure 2.5: Example of a compressor map. The numbers in boxes indicate corrected shaft speeds $\bar{N}$ in krpm, i.e 180 means 180000rpm. Circles indicate measured points, and the contours represent the adiabatic efficiency. The surge line is also marked.

where p_{02}[Pa] is the compressor outlet pressure. The *corrected shaft speed* is defined as

$$\bar{N} = N_{\text{tc}} \frac{1}{\sqrt{\frac{T_{01}}{T_{c,ref}}}} [\text{rpm}] \tag{2.5}$$

where N_{tc} is the turbo shaft speed. The *adiabatic efficiency* of the compressor

$$\eta_c = \frac{\Pi_c^{\frac{\gamma_c - 1}{\gamma_c}} - 1}{\frac{T_{02}}{T_{01}} - 1} [-] \tag{2.6}$$

where γ_c [-] is the ratio of specific heats for air. The adiabatic efficiency describes how efficient the compression of the gas is, compared to an ideal adiabatic process. Or in other words, how much the pressure increases, compared to how much the temperature increases.

Points measured with equal $\bar{N}$ are connected in the compressor map, and are referred to as speed lines. A speed line consists of a number of measurements of Π_c and $\bar{W}$, and gives the characteristics of the compressor. Compressor efficiency η_c is also measured for each point, and contours of constant η_c are normally superimposed over the speed lines. The mass flows measured on each

speed line range from the surge line into the choke region. An example of a compressor map is shown in Fig. 2.5. The compressor models developed in Papers 1, 4 and 5 are given in corrected quantities.

2.5.2 Turbine map

As for the compressor map, there are four performance variables used in the turbine performance map: corrected mass flow, expansion ratio, corrected speed and adiabatic efficiency. It is further common to define two more variables for the turbine: turbine flow parameter and turbine speed parameter. The *corrected turbine mass flow* is given by

$$\bar{W}_t = W_t \frac{\sqrt{\frac{T_{03}}{T_{t,ref}}}}{\frac{p_{03}}{p_{t,ref}}} [\mathrm{kg/s}] \tag{2.7}$$

where $T_{t,ref}$[K] and $p_{t,ref}$[Pa] can be other standard states, than are used in the compressor map. The turbine mass flow W_t[kg/s], is the combustion products and thus normally the sum of fuel and air. The pressures p_{03}[Pa] and p_{04}[Pa] are the turbine inlet and outlet pressure, respectively, and T_{03}[K] and T_{04}[K] are the turbine inlet and outlet temperature, respectively. It is common to neglect the standard states in (2.7), and present turbine data using the *turbine flow parameter*, or TFP

$$\mathrm{TFP} = W_t \frac{\sqrt{T_{03}}}{p_{03}} [\mathrm{kg}\sqrt{\mathrm{K}}/\mathrm{s\,kPa}] \tag{2.8}$$

where p_{03} is usually given in [kPa], as indicated by the unit of (2.8). The *turbine pressure ratio* is here given by

$$\Pi_t = \frac{p_{03}}{p_{04}} [-] \tag{2.9}$$

Some authors prefer to have the pressure after the component divided by the pressure before as turbine pressure ratio as is the case for the compressor pressure ratio (2.4), this is however not chosen here to avoid having numbers of less than one. The *corrected turbine shaft speed* is given by

$$\bar{N}_t = N_{\mathrm{tc}} \frac{1}{\sqrt{\frac{T_{03}}{T_{t,ref}}}} [\mathrm{rpm}] \tag{2.10}$$

It is common to neglect $T_{t,ref}$ in (2.10) and define the *turbine speed parameter*, or TSP as

$$\mathrm{TSP} = N_{\mathrm{tc}} \frac{1}{\sqrt{T_{03}}} [\mathrm{rpm}/\mathrm{K}^{0.5}] \tag{2.11}$$

Since $p_{t,ref}$ and $T_{t,ref}$ are constants, neglecting them in equations (2.7) and (2.10) to give equations (2.8) and (2.11) respectively, gives only a scaling. The *adia-*

batic efficiency of the turbine is given by

$$\eta_t = \frac{1 - \frac{T_{03}}{T_{04}}}{1 - \left(\frac{p_{04}}{p_{03}}\right)^{\frac{\gamma_t - 1}{\gamma_t}}} [-] \tag{2.12}$$

where $\gamma_t[-]$ is the ratio of specific heats for the exhaust gas.

The high temperatures on the turbine side cause large heat fluxes. Measurement of T_{04} can have substantial systematic errors, due to the heat fluxes. An alternative efficiency definition for the turbine side is therefore commonly used, where no measurement of T_{04} is needed. The heat transfer effects are less pronounced on the compressor side, and the compressor power can be used to define an alternative turbine efficiency. The compressor power is given by

$$P_c = W_c \cdot c_{p,c} \left(T_{02} - T_{01}\right) [\mathrm{W}] \tag{2.13}$$

where $c_p[\mathrm{J/kg\,K}]$ is the specific heats at constant pressure. The alternative turbine efficiency definition includes the shaft friction, and is given by

$$\tilde{\eta}_t = \eta_t \cdot \eta_m = \frac{W_c c_{p,c} \left(T_{02} - T_{01}\right)}{W_t c_{p,t} T_{03} \left(1 - \left(\frac{1}{\Pi_t}\right)^{\frac{\gamma_t - 1}{\gamma_t}}\right)} \tag{2.14}$$

where the shaft friction is included in the mechanical efficiency η_m.

2.5.3 Measure maps

A turbo map is commonly measured in a gas stand. The gas stand has individual gas feeds to the compressor and turbine. The turbine feed gas is normally heated using e.g. a diesel burner. Different turbo operating points are measured after a thermal equilibrium is reached. Based on theory from dimensional analysis, corrected quantities are calculated from the mean values of the measured variables. These corrected quantities are then stored in a map. If care is taken to minimize external and internal heat transfer, a map referred to as adiabatic can be measured in a gas stand, this is however not common practice in industrial gas stand testing, see e.g. [145, p.11] and [11, p.1].

The compressor operating points are usually measured between what is referred to as the surge line, and up to what is referred to as the choke line or the stone wall. The turbine operating points are given by the compressor operation. Surge and choke are discussed below.

Normal gas stand turbine maps have a limited turbine flow range due to the restrictive flow ranges presented by the loading compressor. There exists different ways to wider the turbine flow range measured. The gas stand can be ran in closed-loop configuration, where the loading compressor inlet air density is increased using a feed back loop from the compressor discharge side. Another possibility is to replace the loading compressor with a dynamometer, or use a number of loading compressors. In [25] air injection nozzles are used on

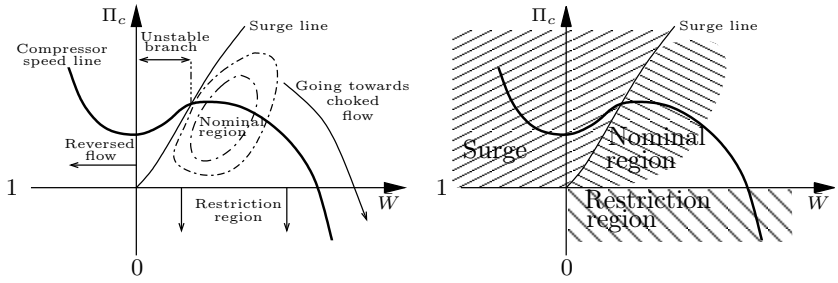

Figure 2.6: Schematic picture of the different compressor operating regions discussed in the text. The nominal region can be approximated with the efficiency contours shown. A decrease in mass flow to the left of the surge line can put the compressor in surge. The compressor is a restriction for $\Pi_c < 1$.

the compressor to increase the possible measured range in turbine flow. Measurements of permanent magnet eddy current dynamometer turbine maps are available in the literature, see e.g. [32] and [157, p.236].

A gas stand measured turbo map is a representation of the turbo performance on in the gas stand. The setup of the measurement equipment affects the performance, see e.g. [70, p.35], [88, p.323] and [13, p.123]. Further, the installation geometry and turbo operating conditions affects the performance, see e.g. [13, p.123], [138], or [107, p.227].

There also exist a spread in measured characteristics between turbo individuals of the same model, see [143] where a study focused on compressor characteristics resulting from introducing foreign objects into the impeller is presented. Measured characteristics of 40 turbos of the same model showed a relative difference between the measured pressure ratios of different chargers of approximately 1% at small flow, and approximately 2.5% for high flow. The corresponding relative difference for the measured efficiencies were approximately 1% at small flow and up to more than 5% at high flow. Further, the WG flow can affect turbine measured speed lines due to flow interaction in the outlet mixing chamber integrated in the turbine casing, see [25, p.100].

2.5.4 Compressor operation characteristics

In essence, the compressor map can be divided in three regions [170, p.33-34], exemplified in Fig. 2.6. The first is the normal operating region, which is stable. Left of this region, i.e. for smaller flows, is the unstable surge region going from the surge line and into negative flows. The surge line is commonly taken as the line connecting points with zero slope in the compressor characteristics,see e.g. [65, p.574]. For centrifugal compressors however, also positively sloped speed lines can be found, see e.g. [176, p.11]. The third region is associated with very high gas velocity, resulting in chocking in the limiting flow area of the machine. The compressor maps commonly supplied from the turbo manufacturers are usually focused on component operation at high efficiency, while the majority of engine operation is spent in regions that are not covered in

the standard maps, see [41]. Neither surge nor choke operation is covered in a standard map. The compressor models developed in Papers 1, 4 and 5 cover all three regions of compressor operation.

Surge and surge line

At least four different categories of surge, with respect to flow and pressure fluctuations can be distinguished, see e.g [34, p.1857] and [176, p.11]. The range goes from; mild surge, classic surge, modified surge, to deep surge. For mild surge, the annulus average mass flow oscillates, but remains in the forward direction at all times, see e.g. [51, p.322] and [35]. For deep surge, the order of magnitude of the negative flow rates is comparable to that of the positive flow rates, see e.g. [73, p.391]. Deep surge is said to occur for high speeds and pressure ratios, see [175, p.9].

Surge is said to occur for zero slope or slightly positive slope for vaneless diffusers and for slightly negative slopes with a vaned diffuser [129]. The positive slope itself is said to be related to the first stages of the instabilities associated with surge, see e.g. [149, p.66] and [57, p.1466]. In [177, p.258], it is stated that surge can also be induced for operating points on the linearly stable operating region of the characteristic, given an energetically large external trigger. There is also stated to be a line, referred to as the "Absolute stability boundary", from where and on surge will not occur independent on external triggers.

The simplest compressor system, made up by a control volume, a connecting pipe, a compressor and a throttling device, leads to a second-order differential equation for the system dynamics, see e.g. [69], [149, p.60] and [90]. The dynamic stability criterion resulting is due to inertia effects in the system and is referred to as the B-parameter, see e.g. [69, p.205]. The B-parameter is said to often be the governing criterion for compression systems, see [90]. Positively sloped points can be operated if the Greitzer B-parameter, see e.g. [69], is small enough (automotive sized compressors have $B \approx [0.5, 2]$, see [149, p.64]). Positively sloped speed lines are measured using active stabilization techniques in [177], where a loudspeaker is used as an actuator. Positively sloped points can further be measured if the discharge piping after the compressor is changed, see e.g. [51] and [58] where measurements of flow characteristics left of the surge line are presented. Stable positively sloped speed lines are measured down to close to zero flow, where the flow is said to exhibit some unsteadiness. Measurements of compressors driven with reversed flow using compressed air fed to the normal compressor outlet flange, are presented in e.g. [73] and [58]. A closely coupled valve is also used in [58] and [54], to measure compressor characteristics down to zero flow. Surge control using different actuators is investigated in [149, p.66], and it is found that the maximum slope that can be stabilized decreases as B increases, independent of actuator used.

The interaction between the compressor system components (impeller, diffuser, volute), leading up to instability is experimental analyzed and discussed in [179], where it is stated that surge is generally due to the interaction of the stalled and unstalled system components, and the tongue region is highlighted as important for system stability. The surge margin is said to improve with

a reduction of the number of diffuser vanes in [20, p.153]. The fluid dynamic circumstance leading to surge is, in [51, p.326], stated to be an inducer tip stall. The inducer tip flow reversal is most severe at the circumferential position corresponding to the volute tongue, for the particular compressor studied.

Given a system setup, surge can be seen down to very low speeds, see e.g. [73, p.392]. The surge line is further well defined and repeatable within 1% of maximum mass flow, see e.g. [51, p.324]. The position of the surge limit does not change in the compressor map with variation in the downstream volume, see [59, p.460].

In [88, p.325], an experimental study of how different compressor inlet geometries affects performance is conducted. Another investigation of surge lines for different system geometries are found in [54], where the surge occurrence dependency on installation conditions is measured and modeled. A comparison of surge line versus installation geometries is presented in [70, p.35]. The changing surge line positions for a two-stage system, compared to the individual units is highlighted in [173], where an increase in surge margin was found. The effect on the surge line from the test setup is also discussed in [106, p.598]. In [106, p.600], an increase in stable operation for unsteady flow conditions was presented. On-engine measurement of turbo surge limits are presented in [61, p.52], highlighting the importance of the compressor inlet piping. It is further shown that the surge line, in corrected variables, does not change with changing compressor inlet states (temperature and pressure), see [61, p.53]. It should be noted, though, that pulsations in the compressor inlet pressure also affect the surge margin, see [54].

Not only the surge behavior changes with size of downstream volumes, but also the power released during surge. Small control volume surge is assumed to be less harmful for the equipment in [68, p.850], and large volume surge makes extended surge measurements impossible, see [67, p.1342]. Surge further contributes to overall noise levels, see e.g. [35] and [166]. The operation on a compressor map point with a positive slope, is in [50] said to result in unstable running and generation of turbulence. This running is referred to as "marginal" or "soft" surge.

Surge operation and recirculation

When the compressor surges, some features of a surge cycle can be detected: flow reversal near constant pressure, an increasing mass flow at lower pressure, a rapid increasing mass flow back to a steady speed line point, and finally a an increase in pressure up to the point where the surge cycle starts again, see e.g. the surge measurements in [5, p.223]. The compressor operating points hence show a path dependent behavior during the stall and recovery processes, see [69, p.201]. Most of the surge cycle time is taken up by either emptying or filling the control volume downstream of the compressor, see [69, p.206-207]. The compressor moves quite rapidly between filling or emptying, and in addition, the filling period is generally longer due to the mass flow through the downstream throttle. At the end of the blowdown phase, the compressor reingests the residual hot gas present in the inlet, and this varying inlet gas

temperature and thus density contributes to a lag in the reverse to forward transition, see [51, p.325-326].

The surge frequencies are set by the overall systems dynamics and are, compared to rotating stall, not proportional to compressor speed. Changes in surge frequency with speed can be attributed to variations in e.g. the shape of the compressor characteristics, see [69, p.206-207] and [59, p.460].

Another phenomenon, closely related to surge, is rotating stall, which is a flow regime where stall cells propagate around the compressor circumference at speeds usually between twenty and seventy percent of the compressor speed [69, p.198]. In these stalled cells, negligible mass flow is at hand, and locally reversed flow can also be found. Rotating stall is though believed to have little effect on compressor performance, see e.g. [34, p.1857] and [175, p.10]. It is also stated in [175, p.10] that surge goes into rotating stall for a progressively reduced plenum size. In [120, p.106] it is stated that rotating stall occurs prior to surge initiation during turbo acceleration, and rotating stall is said to be observed prior to and following both mild and deep surge.

A connection between surge and recirculation, is presented in e.g. [5] and [106, p.598-600], where measurement of the gas temperature close to the compressor inlet is proposed as an indication of surge. Recirculation of air through the compressor system causes a drop in compressor efficiency for operation near the surge line [7]. The recirculation is due to the large pressure gradients existing in the compressor, and the clearances needed between compressor impeller wheel and volute. The recirculation mass flow thus follows the compressor shroud. In [70, p.26-27] both the temperature of and the amount of mass flow that recirculates are considered to be a functions of Π_c, independent on compressor speed. An increase in compressor inlet temperature with a decrease in W_c is there explained by the relative increase in recirculated mass flow, when the fresh air mass flow is reduced. Further, since the recirculation mass flow follows the shroud, a radial temperature gradient exists, which is said to be validated using measurements in [70, p.26-27]. The temperature increase due to backflow is measured in [5, p.226], and stated to be higher at the outer diameter of the inducer. Measurement of axial temperature distributions show larger temperature increases closer to the inducer. Measurement of the temperature increase when compressor operation approaches the surge line is presented in [61, p.51], where a high measured compressor inlet temperature is explained by the close proximity of the measurement probe, to the inducer. When surge is encountered, the temperature is said to suddenly increase up to the compressor outlet value. The recirculation is partly used to explain heat transfer modeling in [26, p.794], and in [27, p.245] it is stated that at low flows, some of the flow absorbs work but simply recirculates in the compressor inlet. A more consistent reverse flow is experimentally detected for smaller flows, causing an increase in inlet temperature in [106, p.598-600].

In e.g. [74, p.75], diffuser back-flow is said to occur in diffuser regions with high pressure and low velocity. Both fully and partly reversed flow is found at different instances and locations in the diffuser. Large radial pressure gradients are found at regions with fully reversed flow. The back flow is found to be able to go from the diffuser back to the compressor inlet region. It is in [74, p.79]

further stated that reversed flow on the suction side of the impeller vanes, due to the pressure gradients within the impeller, can exist even for increasing mass flow. In [180], the recirculation loss is said to dominate the disc friction loss under off-design operation. Thus the predicted efficiency curves are strongly influenced by the recirculation loss. Further, this loss is said to result from flow distortions at the impeller discharge section. When the flow is distorted enough, the flow separates close to the shroud and locally moves radially inwards and is again injected into the impeller flow.

Choke and restriction operation

The choke and restriction operating region is discussed in some papers, see e.g. [145], [79] and [49, p.40]. In [27] the operating characteristics for this region are estimated from normal compressor maps. The importance of this region for automotive applications are highlighted and exemplified, e.g. during tip-in or take-off or for unmatched operation of a two stage system. The operation in choke is further stated to be multi-valued in pressure ratio for a given flow. The restriction operation potential of the compressor was used in [116], where the compressor was used as a cold air turbine.

2.5.5 Turbine map characteristics

Compared to the axial flow turbine, the turbine map is noticeable wider due to the centrifugal field created by the rotor, see e.g. [170, p.34-35]. Compared to the compressor, the turbine map is still narrow in mass flow versus pressure ratio diagrams, and the efficiency map of a turbine is then plotted against the blade speed ratio. The blade speed ratio BSR relates the wheel tip speed of the turbine to the velocity equivalent of an isentropic enthalpy drop across the turbine stage, see e.g. [170, p.34-35, 152], as

$$\mathrm{BSR} = \frac{d_{t1}}{2} \frac{\omega_{tc}}{\sqrt{2c_{p,t}T_{03}\left(1 - \left(\frac{1}{\Pi_t}\right)^{\frac{\gamma_t - 1}{\gamma_t}}\right)}} \tag{2.15}$$

where d_{t1} is the outer diameter of the turbine wheel, $c_{p,t}$ and γ_t are gas constants.

Windmilling and turbine centrifugal pressure field

Windmilling refers to when the turbine acts as a bad centrifugal compressor and pumps in the "wrong" direction, due to the centrifugal pressure field created by the rotation of the turbine wheel, see e.g. [170, p.165-166, 185] and [172, p.150]. A certain turbine inlet pressure is required for the turbine flow to be in the correct direction already at low speeds, and this pressure increases with increased speeds since the centrifugal pressure field will oppose normal gas motion, see [170, p.185].

The centrifugal pressure field affects the full turbine flow range, and a greater turbine inlet pressure is required for a higher speed, given a mass flow [170,

p.185], however reversed turbine flow is usually not encountered, see [12, p.2], and is commonly neglected, see e.g [12, p.4] and [57, p.1467]. However the effect from the centrifugal force can be seen in data and used in models, see e.g. [145, p.78] and [112, p.13]. In [140, p.3739] the effect from the centrifugal forces are modeled using a changing effective equivalent nozzle area for the flow.

Unsteady turbine flow

The variation in turbine mass flow during an engine cycle is great, and the turbine can move from choked flow conditions to zero flow and back again, see [170, p.180] and [123, p.373]. Also negative flow parts can be found, see [178, p.198]. The complex pulse shapes resulting from engine operation, are primarily determined by the engine load, and the engine speed gives the frequency, see [108]. Instantaneous turbine torque is a function of the fluid state within the rotor passages and not at the turbine inlet, see [87, p.133], and to correctly estimate instantaneous turbine torque, care should be taken to account for possible mass/momentum accumulation inside the impeller channel, see [104].

The turbine efficiency η_t is generally lower if the turbine is operating under unsteady flow conditions, compared to the efficiency obtained in steady flow, see [170, p.165]. However some authors present the contrary, see e.g. [25, p.104]. A 10% loss in η_t for unsteady operation is presented in [81], and a 30% loss is stated in [85, p.43], and the losses are said to decrease with increasing pulse frequency, see [81].

Commonly a constant turbine outlet pressure p_{04} is assumed, though measurements show the contrary, see [12, p.9], and for a more thorough analysis also the p_{04} variations should be accounted for, see e.g. [24, p.557], [178, p.196,201] and [87, p.136]. However, in e.g [25, p.103] no appreciable p_{04} fluctuations are observed. Also the turbine inlet temperature T_{03} is sometime assumed to be constant, see e.g. [1, p.178], while other model T_{03} from the measured temperature signal and pressure, see e.g [12] and [53], as ${}^{T_3}/_{T} = \left({}^{p_3}/_{p}\right)^{({}^{\gamma_t - 1}/_{\gamma_t})}$, where T and p are the measured values for T_{03} and p_{03} respectively.

Pulsating flow through a twin entry turbine is studied in [32], where a quasi-steady behavior of the turbine stage in presence of pulsations typical of internal combustion engines is said to be insufficient. An extra volume is placed upstream of the turbine to model the effect of pulsations, but the rotor passages themselves are treated quasi-stationary with good results, see [32, p.2]. Measurements of unequal flow, as well as pulsating flows with different frequencies and phasing from a double entry turbine mounted in an eddy current dynamometer is presented in [30]. It is stated, that it is not immediately clear that a pulse event time an order of magnitude larger than the rotation of the wheel, will validate a quasi-steady assumption, see [30, p.5]. A significant overprediction of turbine efficiency is said to result, if the average velocity ratio and speed is compared to the steady-state equivalent, see [30, p.8], but a qualitatively sense of the expected performance will at least result. A further departure from quasi-steady operation was noted with an increase in pulse frequency in [30, p.10], while the contrary is presented in [87, p.136].

Measurement of circumferential pressure in the turbine volute is said to show

that the wave propagation speed is closer to the speed of sound, than to the bulk flow velocity, see [87, p.136]. It is further stated that at low frequency pressure wave propagation, the resulting wave shape is dominated by the effect of bulk mass transport, due to the very fast wave propagation compared to the pulse cycle time, see [32, p.3].

The static pressure development from the turbine inlet measuring plane to the rotor inlet is measured in [87, p.133], where it is shown that the pulse propagation is given by the appropriate sonic travel time. Exhaust pressure pulsations are estimated using N_{tc} measurements in [105], where it is also stated that the phasing of the exhaust pressure signal was clearly advanced compared to the turbo speed signal. The assumption of constant Tq_c is also questioned, and when using a high pressure EGR connection, the pulsating part of Tq_c is expected to increase, see [105, p.1190].

2.6 Model based control and mean value engine modeling

The use of mathematical models in an automotive control system is gaining increased interest from the industry. This increased interest comes from the complex engine concepts used, where additional actuators and degrees of freedom are added to the systems.

Complex boosting systems in series and parallel configurations are discussed in the literature. Series sequential control strategies are found in e.g [182], [29], [55], [118], and [63]. A parallel sequential turbo system for a heavy duty engine is presented in [16], where a larger turbo is used for the low speed operation and transient response. This larger unit is however smaller than the comparable single stage turbo unit, and is therefore improving performance. Also a smaller unit is engaged at higher engine speeds. An experimental study on a parallel system with unequal sized turbos is presented in [182]. A system with three turbos capable of both series and parallel operation is presented in [39]. Also turbo compounding, where the turbine torque is transfered directly to the crankshaft of the engine, or e-boost concepts, where an electric machine is connected to the turbo shaft are studied, see e.g. [45].

Model based control is proposed as a way of handling the increased complexity. The models are used for a number of things. Simulation environments can be constructed around the models to aid for example in controller design, in concept evaluations, or in the parametrization process of other controller structures, see e.g. [167], [164] and Paper 1. Observers can be built around the models to estimate non measured states of the system, see e.g. [15] and [6]. A direct use of an inverse model can be made, to handle a nonlinearity of a system, see e.g. [162], and [165]. Model based diagnosis is another example of an important field for control oriented models, see e.g. [119]. The model based control approach have been studied for different automotive control applications, for example in [67], [3], and [121].

Mean Value Engine Modeling (MVEM), see e.g. [75], [83], [76], [48], [43], [85] and [21], is a modeling framework used in the automotive society. MVEM

usually means that the model is based on average values of the engine cycle, i.e. in-cylinder processes such as valve opening and closing are averaged out. This simplification means that vehicle test cycles, consisting of many minutes of driving, can be simulated on a normal PC, with short calculation times.

In the full system modeling presented in Papers 1 and 4, the turbo model is implemented as part of an MVEM framework.

2.7 Model families

A model is here classified dependent on the complexity and computational burden of the model.

Gas motion can be modeled in 3D, e.g. solving the Navier-Stokes equations of gas motion numerically. Such modeling needs accurate geometric information of the system, see e.g. the complex impeller geometries of Fig. 3.1. The boundary conditions of the model are further important, i.e. how the gas enters and leaves the modeled component. Due to the complexity and the computational effort [11, p.1], these models are most often only used to model components of the engine, see e.g. [181], [71], and [74]. In [103], the 3D models are said to be worthwhile for detailed optimization of turbine aerodynamics, but else too demanding both in computational power and calibration effort. The solutions obtained, give valuable information of for example the gas motion, that can be used also for less complex model families. Also the reverse is true, see [27]; good models from less complex model structures can be used on a component level for a 3D simulation.

Another level of detail that is frequently used, is the 1D model family. They model the gas flow along pipes and account for properties in this dimension. 1D models of compressors are however rarely found. The computational cost is reduced, compared to 3D models, and large parts of an engine system can be simulated with reasonably short simulation times.

The last model class is given by the 0D models. The 0D models can be further divided in physical models and black or gray box models. The physical turbo models typically starts with an ideal component, and then subtracts different losses to give the component performance. The modeling effort is then concentrated to models for different losses. The black and gray box turbo models utilizes that turbo performance is conveniently given by the performance maps, and use curve fitting to the map variables. The modeling effort is then concentrated to developing mathematical functions that can be curve fitted to the data, and that gives good description of the component performance.

The following sections will present 0D models for the turbine and friction, while physical and black or gray box modeling of the compressor is presented in Chapter 3.

2.8 0D turbine modeling

This section presents a brief summary of turbine models available in the literature. To agree with the model complexity of the compressor models developed

in this thesis, only 0D models will be presented here. However physical models in 1D or 3D also exist, see e.g. [154]. A further division of the modeling effort is commonly chosen, where turbine mass flow and turbine efficiency are separately modeled. This division is also chosen here, and the modeling of the mass flow dimension of the turbine map is presented first, followed by turbine efficiency models.

2.8.1 Turbine mass flow modeling

A simple and well used model for turbine mass flow is based on the so-called single line characteristics, where a mean curve is drawn through the complete turbine map flow data, ignoring any variation with speed, see e.g. [9, p.162]. Compared to an axial turbine, neglecting speed can introduce substantial errors since the radial flow turbine shows a significantly wider flow map due to the centrifugal fields, see e.g. [79, p.72]. Many turbine mass flow models rely on the use of a nozzle equation, see e.g. [169, p.127], [170, p.541] and [78, App.C2], as

$$\dot{m}_t = \begin{cases} \frac{C_d A p_{03}}{\sqrt{RT_{03}}} \cdot \Pi_t^{-\frac{1}{\gamma_t}} \sqrt{\frac{2\gamma_t}{\gamma_t - 1}\left(1 - \Pi_t^{\frac{1-\gamma_t}{\gamma_t}}\right)} & \Pi_t < \Pi_{t,crit} \\ \frac{C_d A p_{03}}{\sqrt{RT_{03}}} \cdot \sqrt{\frac{2\gamma_t}{\gamma_t + 1}\frac{\gamma_t + 1}{\gamma_t - 1}} & \text{else} \end{cases} \tag{2.16}$$

for the turbine case using $\Pi_t = {}^{p_{03}}/_{p_{04}}$. The critical pressure ratio $\Pi_{t,crit}$, determining whether the flow is choked (sonic) or not (subsonic), is given by $\Pi_{t,crit} = \left({}^{2}/_{(\gamma_t+1)}\right)^{\gamma_t/(1-\gamma_t)}$. For $\gamma_t = 1.3$ and $\gamma_t = 1.4$ this gives a $\Pi_{t,crit} = 1.832$ and 1.893, respectively. However, the turbine does not choke completely even for this pressure ratio, and a better model is said to be obtained using two orifices in series, see e.g. [170, p.546] and [140, p.3730]. The same line of thought is followed in [79, p.70], where also the pressure losses due to fluid friction is accounted for resulting in a maximum pressure ratio capability of roughly 4 being expected for a single-stage turbine. It is further noted in e.g. [152, p.3], that the nozzle model is valid for steady flow states and boundary geometry being sufficiently smooth functions in a spatial variable. It is also important to note the the effective throat area is not made up by the only the geometrical layout but also the gas angles, in order to represent accurately the fluid-dynamic behavior of the turbine see [170, p.187] and [140, p.3730].

A model of different actuated turbines are found in [140]. The model is based on estimation of reaction degree of the turbine, and one nozzle model is parametrized for the stator and one for the rotor, see [140, p.3732]. A degree of reaction of 0.5, meaning that the same pressure drop occurs across the rotor as across the stator, is said to be the case for turbines without guide vanes, and radially vaned rotors, see [140, p.3731]. The degree of reaction assumption of 0.5 is, however, said to not necessarily be true for variable geometry turbines, see [140, p.3732].

Unsteady turbine flow performance is commonly accounted for using different scaling factors, adjusting the steady performance curves, see e.g. [12, p.1], [170, p.152 or p.520-521], and [25, p.97]. The scaling factors can be constant [19,

p.26], or vary with other parameters. The pressure pulse shape at the turbine inlet is commonly characterized by its frequency and amplitude [1, p.178]. The turbine mass flow scaling factor is stated to not be affected by heat transfer, see [2]. In [24, p.559] for a VGT, the only decisive trend with the pulse characteristics (amplitude and frequency) is said to be found for the mass flow factor, which shows a generally reducing trend with increased pulse amplitude. To handle VGT turbines, a turbine flow model is commonly adapted to each discrete VGT position measured, and interpolation between these models is then used. The variation between different VGT positions is however not linear, see e.g. [158, p.147].

In [145], a comparison of turbine performance for different turbine inlet temperatures can be found. The investigation shows that the turbine flow lines, measured for different turbine inlet temperatures differ rather much. The lower turbine inlet temperature, the lower reduced turbine flow given a turbine pressure ratio, see e.g. [145, p.78].

Examples of 0D turbine flow models In [83, p.4], the turbine flow characteristic was described using the concept of an equivalent turbine area $A_{t,eq}$, defined as that area which gives the correct turbine flow, when the turbine inlet temperature and overall pressure ratio are used in the isentropic flow equation. The equivalent turbine area is modeled as using an affine function in Π_t, where the affine coefficients in turn given by affine function in TSP. A slight variation to this model structure is proposed for a VGT in [112, p.11-13], where second order polynomials are used for the coefficients of the affine equivalent turbine area model, and the zero pressure ratio is taken into account using a quadratic function in VGT position. In [155, p.124] a two flow region turbine pressure ratio model is proposed, that uses a second order polynomial in $^{\mathrm{TFP}}/_{A_{t,eq}}$ for the lower flows, and an affine model for higher flows. A model where Π_t is given only as a second order polynomial in actual flow W_t is presented in [48, p.135]. A model in corrected turbine flow $\bar{W}_t$ is also presented in [48, p.136] as

$$\bar{W}_t = c_1 \sqrt{\max\left[0, 1 - \Pi_t^{-c_2}\right]} \tag{2.17}$$

This model is also used in [6, p.116], [44, p.534]. A closely related model is presented for a VGT in [168, p.972]. A model giving actual turbine flow W_t as a function of Π_t, is presented in [135], as $W_t = C_1 \left(1 - e^{-C_2 \Pi_t^{C_3}}\right)$ where C_1, C_2, C_3 are second order polynomials in VGT position. The model structure is also used in [62, p.1412]. In [22] a variation to (2.16), stated to be valid assuming the flow to be adiabatic and irreversible, is introduced as a model for actual flow of a VGT. Another VGT flow model is presented in [122, p.385], where the turbine outlet pressure and temperature are used as input to the model. A variation to the effective area turbine flow model is presented in [41], where again an exponential function is utilized

2.8.2 Turbine efficiency modeling

General thoughts on turbine efficiency models are found in [170] and [9], where it is stated that if turbine efficiency is plotted against blade speed ratio BSR, the effiency lines collapse into a narrow band at least for the lower speeds and pressure ratios. At higher speeds, a decreasing efficiency is expected, for a nozzleless turbine, due to the high gas velocities that these speeds imply. Further, it is stated that for turbines tested on dynamometers, the efficiency curves extend to both higher and lower values of BSR in a regular manner [9, p.163-164]. The turbine isentropic efficiency is not easy to measure and results can vary greatly dependent on test conditions, where e.g. turbine efficiency measured for varying turbine inlet temperature will be different due to the change in heat transfer [170, p.165].

Studying the connection between BSR and η_t, the following can be seen as a rough guideline, see e.g. [170, p.165-166], [9, p.165], and [47, p.160]. The efficiency must, from physical consideration, be zero at two points given a speed; for BSR $= 0$, and for a BSR $\in [1.1, 1.2(1.3)]$. The latter point is given by the, with speed, varying centrifugal pressure field, giving rise to a varying pressure ratio at zero flow, see Section 2.5.5. Beyond this point, the turbine will act as a compressor. A speed dependent maximum efficiency point occurs between these two outer points, at a BSR $\in [0.6, 0.7]$. For turbines where the maximum efficiency varies significantly with speed, separate curves for different speed ranges can be defined. These three points can then be connected using a cubic curve, so that the a rather steep drop in efficiency occurs for BSR > 0.8.

Examples of 0D turbine efficiency models In [83, p.3] the turbine efficiency is described as essentially a function of BSR, and the efficiency is modeled using a third order polynomial in BSR, where the coefficients C_i of the polynomial are in turn parametrized $C_i = {}^{(c_{i,1}+c_{i,2}N_t)}/_{(c_{i,3}-N_t)}$ with $i \in \{0, 1, 2, 3\}$, and N_t is described as turbine rotational speed. End points for low and high BSR were added, in [83], in the fitting procedure to ensure a sound extrapolation. The same η_t-model structure is presented in [112, p.13], where $C_0 = 0$ is used. In [155] a model for η_t is proposed as $\eta_t = c_1 C_2 \left(1 - (1 - {}^{\text{BSR}}/_{0.61})^2\right)$ where c_1 is the peak efficiency for any operating point, and $C_2 = \left(c_2 \Pi_t^2 + c_3 \Pi_t + c_4\right)$. In [72] the following model is given

$$\eta_t = C_1 \left(2\frac{\text{BSR}}{C_2} - \left[\frac{\text{BSR}}{C_2}\right]^2 \right) \tag{2.18}$$

For a turbine with variable nozzle area, C_2 is said to be a function of the VGT position, with only a minor effect on C_1. The same model is used in e.g. [6, p.118] and [44, p.533]. In [126, p.5] the same model structure is used for a fixed geometry turbine, and for a VGT also C_1 is a proposed to be a function of the VGT position. In [112, p.13] a model is proposed where η_t is given as a second order polynomial in BSR, with the coefficients of the polynomial in turn given as first order polynomials in N_{tc}. In [48, p.136] the following η_t-model is proposed as $\eta_t = c_1\sqrt{\Pi_t - 1} + c_2\sqrt[4]{\Pi_t - 1} + c_3$. A third order polynomial in BSR is

proposed as a η_c-model for a VGT in [122, p.386], where the polynomial coefficients are parametrized as second order polynomials in N_{tc} and VGT control signal u_{VGT} as $C_i = c_{i1} + c_{i2}N_{\text{tc}} + c_{i3}N_{\text{tc}}^2 + c_{i4}u_{\text{VGT}} + c_{i5}u_{\text{VGT}}^2 + c_{i6}u_{\text{VGT}}N_{\text{tc}}$ for $i \in \{0, 1, 2, 3\}$.

2.9 0D friction modeling

In [9, p.117] Petroff's equation is used to estimate journal bearing frictional torque as

$$Tq_{fric} = \frac{\pi}{4}\frac{\mu L D^3}{\epsilon_r}\omega_{tc} \tag{2.19}$$

where μ is the oil viscosity, ω is the rotational speed, L and D are the bearing length and diameter, and ϵ_r is the fluid film thickness. The friction power loss in a plain, double-sided thrust bearing is in [9, p.124], modeled using Petroff's equation. Since $P = Tq \cdot \omega$, the corresponding friction torque is given by

$$P_{fric}/\omega_{tc} = Tq_{fric} = \frac{\pi\mu\left(r_o^4 - r_i^4\right)}{\epsilon_z}\omega_{tc} \tag{2.20}$$

where r_i and r_o are the inner and outer radii of the thrust bearing, and ϵ_z is the axial clearance. The journal bearing friction power is in [114] modeled, assuming viscous friction, as $P_f = (2\pi n_{tc})^2 k_f = k_f \omega_{tc}^2$ and hence $Tq_{fric} = k_f \omega_{tc}$, where $k_f = 3.23 \cdot 10^{-6}\,\text{kg}\,\text{m}^2/\text{s}$ for a GT1749MV turbo.

In [172, p.78] it is stated that a detailed friction model should divide the friction loss at least into thrust bearing friction and radial bearing friction. In [137, p.194] it is concluded that a friction model that only depends on charger speed is insufficient, and that a more detailed modeled should include axial force, oil temperature and oil pressure. It is further concluded that the friction power polynomials delivered by the turbo manufacturer of the form $Tq_{fric} = a \cdot N_{\text{tc}} + b$ with constant a and b does not fit the measured friction, and shows up to 70% error compared to the experiments. Therefore, an improved model is proposed as $Tq_{fric} = a \cdot N_{\text{tc}}^b + c$, in [137, p.195]. A constant friction or an affine model in N_{tc} is said to be adequate in [36]. A linear Tq_{fric}-model in ω_{tc} is used in [6, p.122], where the constant is tuned manually. The friction losses are however often neglected, see e.g. [72, p.63] and [41], but the addition of a friction torque can be beneficial in some situations, see [72, p.64].

2.10 Turbine and friction models used in Papers 1 and 4

Both a turbine and a friction model are needed for the full engine simulations presented in Papers 1 and 4. While the compressor modeling is devoted the entire Chapter 3, the turbine and friction models used in these papers are briefly presented here.

The gas properties are first assumed to be constant. The turbine model is divided in a flow and an efficiency submodel. During the full system simulations, the turbo model was implemented as part of an MVEM. This means that unsteady flow due to cylinder pulsations are neglected. Further, the full system simulations presented in Papers 1 and 4 are mainly studies of surge, where usually a fully opened WG is commanded once surge is encountered. Hence, oscillations in turbine inlet states will decrease substantially. However, just prior to surge initialization the system is commonly operated with large oscillations in turbine inlet states. Turbine unsteady performance was then accounted for using scaling factors. The modeling further assumed that any heat transfer affecting the performance was already accounted for in the efficiency of the measured maps, e.g. using adiabatic map measurement procedures.

The turbine flow model is formulated in the corrected variables of the turbine map. Hence, the model utilizes dimensional analysis derived corrections to calculate turbine performance for variations in turbine inlet conditions. The model from [48] given by (2.17) is used, i.e.

$$\bar{W}_{t,mod} = c_1 \sqrt{\max\left[0, 1 - \Pi_t^{-c_2}\right]} \tag{2.21}$$

where the parameters c_1 and c_2 are estimated using nonlinear least squares. The model provides good fit to the available data for the turbines tested. The model hence neglects windmilling. Given a turbine pressure ratio Π_t this model is used to calculate $\bar{W}_{t,mod}$. Using the reference states $T_{t,ref}$ and $p_{t,ref}$, a turbine inlet temperature T_{03} and turbine inlet pressure p_{03}, a modeled actual turbine mass flow $W_{t,mod}$ is then calculated using (2.7).

The efficiency model makes use of the model from [72] given by (2.18) with a lower saturation on efficiency as

$$\eta_{t,mod} = \max\left[\eta_{t,\text{lower sat.}},\ C_1\left(2\frac{\text{BSR}}{C_2} - \left[\frac{\text{BSR}}{C_2}\right]^2\right)\right] \tag{2.22}$$

The model is parametrized to the manufacturer maps using nonlinear least squares. It should be noted that the manufacturer maps commonly calculates η_t using (2.14), and friction is hence included in this efficiency. Still, a separate friction model will be added, see below. Given model parameters, and BSR (from (2.15)), a modeled efficiency can be calculated. Using the modeled efficiency, Π_t and T_{03}, the turbine outlet temperature $T_{04,mod}$ is modeled using (2.12). The modeled turbine power is then calculated using (2.13) with changed subscripts as

$$P_{t,mod} = W_{t,mod} \cdot c_{p,t}\left(T_{03} - T_{04,mod}\right) \tag{2.23}$$

and the modeled turbine torque, Tq_t of (2.1), is given by

$$Tq_{t,mod} = \frac{P_{t,mod}}{\omega_{tc}} \tag{2.24}$$

The friction torque model $Tq_{fric,mod}$ is linear in ω_{tc}, and given by

$$Tq_{fric,mod} = c \cdot \omega_{tc} \tag{2.25}$$

where c is a constant. This model hence corresponds to the model in e.g. [114]. The constant c collects the geometric and oil properties of either (2.19) or (2.20). Friction is already accounted for in the η_t-model, but a separate friction model is still used since this increased the stability of the simulations.

3

Compressor modeling

This chapter presents an overview of compressor modeling efforts found in the literature, that have been the inspiration and motivation for the compressor model that is developed in this thesis.

Compressor operation can naturally be divided into three different regions: nominal operation, choke or a restriction like operation, and surge. A sketch of the different regions is presented in Fig. 2.6, and the modeling overview presented here is divided into these three parts. Surge, restriction and choke are discussed first. This is followed by modeling for mainly the normal operating region. The physical modeling approach is presented first. Even though the models developed in this thesis are not of the physical model family, a good overview of the modeling challenge and the phenomena that affects compressor performance, is gained from briefly presenting this model family. An overview of black and gray box compressor modeling is then given, and a number of models are exemplified, demonstrating the wide range of available models. An overview to the compressor models developed in this thesis are presented in the final section.

3.1 Compressor surge modeling

To model surge many authors follow the Moore-Greitzer approach, see e.g. [69] and [111]. A compressor mass flow state is introduced where, due to the gas inertia, the compressor mass flow deviates from stationary performance curves for a transient, see e.g. [58]. The version of the Moore-Greitzer state used in this thesis is

$$\frac{dW_c}{dt} = \frac{\pi d_c^2}{4L_c}\left(\hat{p} - p_{02}\right) \tag{3.1}$$

where $\hat{p} = \hat{\Pi} \cdot p_{01}$ is the compressor pressure build up during stationary operation, d_c is the compressor diameter, and L_c is the duct length. p_{01} and p_{02} are set by the system, while $\hat{p}$ (and $\hat{\Pi}$) is a measure of the pressure the compressor builds given an operating point. Using the model (3.1), it is hence only for stationary operation that $p_{02} = \hat{p}$.

Good summaries of surge modeling efforts are found in [34] and [176]. Compressor operation with negative flow is modeled as a parabola in [73, p.392] and [129]. A model like $\Psi_c = c_n W_c^2 + \Psi_{c,0}(\omega_{tc})$ was proposed for negative flows in [65, p.572], [67, p.1344] and [68, p.853], regarding the compressor as a throttling device with a positive pressure bias. The model is parametrized to give a negative slope of the compressor characteristic for negative flow. A second order polynomial was used as a negative flow model in [161]. In [175, p.9] it is stated that the compressor works on the steady-state back flow characteristic during the emptying phase of a surge cycle, where the steady-state back flow characteristic is defined as the resistance which the rotating blades offer to flow in the reversed direction. This characteristic is further thought to be of roughly parabolic shape. The negative flow region is modeled as $\Pi_c = \Pi_{c0} + cW_c^2$ in [70, p.67]. The reverse flow region is considered to be modeled as an isothermal flow process in [58, p.822] and in [54]. In [127, p.235], a methodology to measure ceramic rotor components is presented, where the compressor wheel is supplied with compressed air from the normal compressor outlet, and the compressor is hence used as a turbine in the measurements.

The region between the surge line and zero flow is modeled as a cubic polynomial in [73, p.394], where it is further stated that the exact modeling of the unstable branch could not be verified experimentally, but that sample calculations show the influence from the speed line shape to not greatly affect the simulations, due to the comparatively small time spent in that flow region. The same conclusion is drawn in [129]. A third order polynomial was also used as flow model for this flow region in [161]. In [70, p.66] the following was proposed as a model for the flow region between zero and the surge line $\Pi_c = \Pi_{c0} + \Pi_{c,\beta}\left(3\left({}^{W_c}/_{W_{c,\alpha}}\right)^2 - 2\left({}^{W_c}/_{W_{c,\alpha}}\right)^3\right)$.

The compressor pressure ratio at zero flow Π_{c0} can be modeled using radial equilibrium theory for the compressor impeller blades as

$$\Pi_{c0} = \left(1 + \frac{\gamma_c - 1}{2\gamma_c R T_1}\omega_{tc}^2 \frac{d_{c2}^2 - d_c^2}{4}\right)^{\frac{\gamma_c}{\gamma_c - 1}} \tag{3.2}$$

assuming no losses in the compressor impeller, see e.g. [161], [129], [70, p.66], [67, p.1344] and [66]. In [22], the same model is referred to as the "vortex equation", and in [17, p.136] another closely related formulation is given. It can be recognized that zero pressure build up is closely related to the discussions in Section 2.5.5, where an increasing Π_t with speed is found for zero turbine flow.

In [58], measurements of Π_{c0} shows good agreement with (3.2), especially for low to medium speeds. In [35], a gain is added to the model (3.2). The extended model is said to give good agreement with experimental data for low to medium speeds, with a gain close to one. The discrepancies are however increasing for higher speeds. In [54], Π_{c0} is closely related to the surge trajectories in the

compressor map at nearly constant compressor speed, going from the maximum compressor pressure ratio, found close to the surge line, to the minimum pressure ratio found at zero flow.

Modeling of surge for a parallel sequential turbo system is presented e.g. in [159] and [163]. Extensions of 1D models to also incorporate surge is presented in e.g. [58] and [35]. However, the underlying surge model is commonly taken as a lumped parameter 0D model.

3.2 Restriction and choke modeling

Two modes of compressor operation with $\Pi_c < 1$ are proposed in [145, p.16]. If a driving compressor torque results, the compressor operation is said to be as an abnormal turbine. Otherwise, the compressor is said to work as a throttle. A cold air turbine efficiency for the compressor of 20% is assumed for the compressor restriction operation in [116, p.4-7], where further a typical nozzle discharge characteristic is said to be apparent. Compressor speed line extensions below a compressor pressure ratio of unity is presented in [79, p.73]. The restriction operation for a mismatched operation of a single turbo system, or in a two-stage compression system is recognized in [27, p.240]. The model proposed in [27, p.247] is extrapolated down in Π_c to where the impeller outlet temperature equals the inlet. From this point downwards the compressor is said to work as a rather poor turbine, with excessive kinetic energy at the outlet.

Choking is discussed and modeled in [170, p.133], where reference is made to an earlier version of [38]. Assuming all flow processes to be adiabatic and the fluid as a perfect gas, the inducer choke flow is modeled as

$$W_c = A_{eff}\rho_{01}a_{01}\left(\frac{2}{\gamma_c+1}\right)^{(\gamma_c+1)/2(\gamma_c-1)} \tag{3.3}$$

where A_{eff} is an effective flow area, ρ is density, a local speed of sound, and γ_c is a gas constant, see e.g. [170, p.133], [38, p.230], [65, p.574] and [156, p.655]. Further it is noted that A_{eff} is the flow area, made up of both the geometric area and the blockage, see e.g. [156, p.655] and [27]. Assuming an isentropic flow, choking in the impeller is modeled as

$$W_c = A_{eff}\rho_{01}a_{01}\left[\frac{2+(\gamma_c-1){U_c}^2/a_{01}^2}{\gamma_c+1}\right]^{(\gamma_c+1)/2(\gamma_c-1)} \tag{3.4}$$

where $U_c = {}^{d_c}/_2 \cdot \omega_{tc}$, see e.g [64, p.346] and [38, p.231]. The choking mass flow dependency on blade speed is explicitly shown, with a greater limiting mass flow found at higher speeds. A small variation to this model, where $({}^{d_c}/_{d_{c2}})^2$ is added before U_c, is presented in [27]. The steep fall off in work input at very high flow on the high-speed characteristics, due to the choking of the flow in the impeller inlet, is discussed in [27, p.243], and used to determine the value of A_{eff}. It is stated that the calculated A_{eff} for each high-speed curve show a reasonable constant value, hence that A_{eff} is not strongly affected by the speed. The compressor density ratio associated with the choking was further

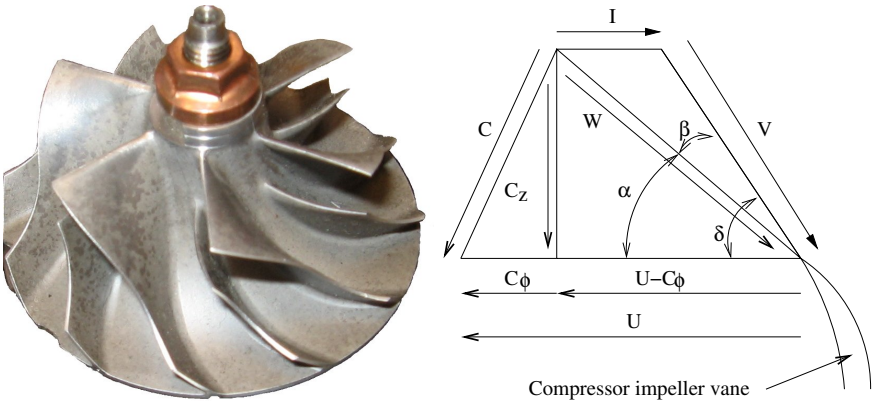

Figure 3.1: Picture of an impeller and the inducer velocity triangle. The Z-axis goes through the turbo shaft, W is the relative flow vector between the gas velocity vector C and the vane velocity vector U. The incidence loss in the inducer is connected to the velocity I. δ denotes the vane angle.

used to calculate the losses associated with choke [27, p.246]. The diffuser inlet conditions depend on the impeller properties. In e.g. [170, p.133] and [38, p.232] the following is proposed as a model for diffuser choking flow

$$W_c = A_{eff}\rho_{01}a_{01}\frac{1+(\gamma_c-1)\eta_{imp}\sigma\,{}^{U_2^2}/_{a_{01}^2}}{\left[1+(\gamma_c-1)\sigma\,{}^{U_2^2}/_{a_{01}^2}\right]^{1/2}}\left(\frac{2}{\gamma_c+1}\right)^{{}^{(\gamma_c+1)}/_{2(\gamma_c-1)}} \tag{3.5}$$

where σ is the slip, η_{imp} is the impeller efficiency, and $U_2 = {}^{d_{c2}}/_2 \cdot \omega_{tc}$ is the impeller exducer tip speed.

3.3 Physical modeling

The physical compressor model family is based on modeling the different losses that affect the fluid flow through the compressor. These models often make use of the velocity triangles, which are exemplified for the impeller entry in Fig. 3.1. An ideal compression process is commonly assumed, and losses are modeled and subtracted from the ideal component performance. This section presents modeling thoughts from the physical compressor modeling family, and a summary of the major compressor stage losses and velocity triangles are given in any of the basic turbocharging references, see e.g. [170, p.128], [38, p.202] and [9, p.56]. Some examples of physical model implementations can be found in e.g. [64] and [117]. Its common in the analysis to assume that both the inlet and outlet angles of the flow are considered given by geometric characteristic of the blade shape, but this is not rigorously true, since the angles depend on the flow physics, see e.g. [60], [64] and [65]. The angles also vary with radius and axial location, see [60] and Fig. 3.1.

A gas element is followed through the compressor stage components, and the first losses occur since the gas has to comply with the vane geometry at

the impeller inlet. These losses are referred to as incidence losses, and are due to that the inducer relative velocity vector W does not agree with the vector parallel to the vane surface V, see Fig. 3.1. The incidence loss connected to the velocity I can be modeled in different ways. In [65] two methods are given. (I): the "NASA shock loss theory", which is based upon the destruction of the kinetic energy associated with the velocity I. (II): a constant pressure incidence model, where it is assumed that the flow just inside the blades has adapted to the blades via a constant pressure process.

The concept of slip σ is commonly used to model the guidance the fluid attracts from the impeller vanes, and is discussed and modeled in e.g. [101], [38] and [128]. Generally, the less guidance the gas attracts from the vanes the more slip. The more guidance, the more friction. Slip is commonly modeled using the Stanitz formula as $\sigma = {}^{S}/_{U} = 1 - {}^{2}/_{n_b}$, where S and U are fluid velocities, and n_b is the number of blades. Another model of slip is found in [82, p.190]. In [113, p.6], it is stated that the entire number of blades (both splitter and normal blades) should be considered, since there is no difference between these two vane types at the impeller outlet. In [27, p.242,245] it is stated that the slip factor might not be constant along a speed line, but that the slip factor is generally constant for a given flow coefficient. For high flows though, the slip factor may change.

The fluid friction losses due to the gas viscosity and motion through the compressor are modeled e.g. in [64], [67], and [174]. The losses due to fluid friction against the impeller and stationary components are described in e.g. [47, p.144]. More details of impeller friction losses can be found in [170, p.99-100]. It is further stated in [170, p.100] that at pressure ratios commonly found in automotive turbos, the diffusion and the blade loading losses are usually not the dominant losses, and that these losses can therefore conveniently be included in the surface friction loss coefficient.

Models of recirculation losses are presented e.g in [84] and [65]. The back flow losses, both along the shroud and across the blade tip from the pressure to the suction side of the vanes, is suggested to be modeled as a decrease in stage efficiency of $\Delta\eta_{bf} = 0.03$ in [47]. The back flow loss due to that the compressor reprocesses fluid, that is reinjected into the impeller due to the pressure gradients existing in the impeller tip region, is modeled using a constant flow loss $\Delta\eta_{bf}$ in [65]. From [84] the loss in efficiency due to clearance can be expressed as $\Delta\eta_{cl} \approx 0.3{}^{L_{\mathrm{cl}}}/_{\mathrm{b}_2}$, where L_{cl} is the tip axial clearance and b_2 is the impeller tip width. In [90], the impeller/diffusion interaction is captured by a recirculation loss bucket, and the leakage flow is modeled. In [74], losses due to the "tongue" are presented. The "tongue" is here part of the geometrical shape of the volute located where the downstream piping connects.

Incidence losses using a vaned diffuser are discussed in [60]. Experimental investigations of the gas motion in the diffuser is found e.g in [136]. The main cause of the diffusion process losses are said to be separation of boundary layers and fluid friction, see [38].

Models of the volute losses are described e.g. in [170]. In [65], the volute loss is said to be approximately $\Delta\eta_{vl} \in [0.02, 0.05]$, and likely higher for vaned diffusers. In [42, p.779] it is stated that the inlet ducts and volute loss typically

account for roughly $4-6$ points in efficiency decrement. In [84, p.1336], it is noted that the relative magnitude of clearance, backflow and volute losses decreases gradually as mass flow rate goes up, due the increase in incidence losses and friction losses at higher mass flow rates. Disc friction losses are modeled in [180]. Losses due to choking are modeled in [27].

3.4 Black and gray box compressor modeling

Black and gray box compressor models are curve fitting based approaches, that recognize that all performance variables are conveniently given by the speed lines and the efficiency contours of the map. The modeling effort is then to fit different curves to the map, or to a transformed map. The semi-physical gray box models usually transform the compressor map variables into the dimensionless head parameter Ψ_c, the dimensionless mass flow coefficient Φ_c, and the inlet Mach number M_c as

$$\Psi_c = \frac{c_{p,c} T_{01} \left[\Pi_c^{(\gamma-1)/\gamma} - 1 \right]}{0.5 U_c^2} \tag{3.6}$$

$$\Phi_c = \frac{W_c}{\rho_{01} \cdot \pi/4 \cdot d_c^2 \cdot U_c} \tag{3.7}$$

$$M_c = \frac{U_c}{\sqrt{\gamma_c R T_{01}}} \tag{3.8}$$

Connections between Ψ_c, Φ_c and M_c are then parametrized and used as a models. The black box models apply curve fitting directly to the map variables (Π_c, $\bar{W}$, $\bar{N}$ and η_c) to produce a model. The modeling effort is then to create functions describing the speed lines and iso-contours of efficiency of the map.

The following two subsections present examples of black and gray box models, that serves and an indication of from where inspiration to the models developed in this thesis have come from. It should not be seen as an exhaustive summary of all available models. Compressor flow and efficiency are commonly modeled separately. This separation is also chosen here, and examples of compressor flow models are presented first, followed by examples of compressor efficiency models. The models should show the vast range of modeling approaches and complexity levels, where some models are especially designed for a certain purpose, while others are meant to be more general. The last section presents the Ellipse compressor model developed in this thesis, and overviews the small differences of the models used in the different appended papers.

3.4.1 Examples of compressor mass flow models

In [111, p.73] an S-shaped characteristics is proposed as

$$\Psi_c = \Psi_{c,0} + c_H \left(1 + \frac{3}{2} \left(\frac{\Phi_c - c_W}{c_W} \right) - \frac{1}{2} \left(\frac{\Phi_c - c_W}{c_W} \right)^3 \right) \tag{3.9}$$

where the model parameters c_W and c_H are referred to as "semi-width" and "semi-height", respectively. The same model is used also in e.g. [17, p.136], [139, p.1644] and [146, p.816]. In [139] the following two model modifications are proposed, to better describe the "skewness" of the characteristics

$$\Psi_c = \Psi_{c,0} + H \sin\left(\frac{\pi}{2}\frac{\Phi_c - c_W}{c_W}\right) \tag{3.10}$$

$$\Psi_c = \Psi_{c,0} + c_H\left(\sin\left(c_2\frac{\Phi_c - c_W}{c_W}\right) + c_3 \sin\left(\frac{c_2}{c_4}\frac{\Phi_c - c_W}{c_W}\right)\right) \tag{3.11}$$

where the second equation is referred to as the "two-sine"-model. A three region flow model is proposed in [73, p.392]. The model is formulated in dimensionless pressure rise ($\tilde{C} = {}^{\Delta p_c}/_{1/2\rho U^2}$), and dimensionless flow ($\dot{\tilde{m}} = {}^{C_x}/_{U} = {}^{W_c}/_{\rho A U_c}$) as

$$\tilde{C}_{mod} = \begin{cases} b_2\dot{\tilde{m}}^2 + b_0 & W_c < 0 \\ c_3\dot{\tilde{m}}^3 + c_2\dot{\tilde{m}}^2 + c_0 & 0 \le W_c \le W_{c,\mathrm{ZS}} \\ d_3\dot{\tilde{m}}^3 + d_2\dot{\tilde{m}}^2 + d_1\dot{\tilde{m}} + d_0 & \text{else} \end{cases} \tag{3.12}$$

The same model was used slightly modified in [129], where $b_0 = c_0$ are given by (3.2), and 2D interpolation in map data was instead proposed for $W_c > W_{c,\mathrm{ZS}}$. In [177, p.247] a model with two flow regions is proposed as

$$\Delta p_c = \begin{cases} \frac{\rho U^2}{2}\left[c_1 \arctan[c_2(\Phi_c - c_3)] + f(\Phi_c)\right] & \text{if } \Phi_c > \Phi_{c,lim} \\ c_4 + c_5\Phi_c^2 & \text{else} \end{cases} \tag{3.13}$$

where $f(\Phi_c)$ is a third order polynomial in Φ_c. The low flow part is referred to [73].

The following model based on affine functions in the Mach number is proposed in [83]

$$\Psi_c = \frac{k_1 + k_2 M_c + k_3\Phi_c + k_4\Phi_c M_c}{k_5 + k_6 M_c - \Phi_c} \tag{3.14}$$

The model is also used in e.g. [22, p.392] and [122, p.385]. Quadratic functions in M_c, instead of affine functions, are proposed in [126, p.5] to improve the model accuracy. Another extension to (3.14) is presented in [107] where again affine functions were used, but now for each compressor speed line SpL. Linear interpolation is then performed between the two SpL models that delimits a zone in the map to ensure continuity. In [40] and [41], the model from [107] is extended with thoughts from [44], utilizing quadratic functions in M_c for each SpL instead of affine. Interpolation between SpL models are used, which is said to give good performance for more than ten maps tested, see [40, p.366]. A physical model is presented in [117, p.2-3], and it is simplified to a black box model as

$$\Pi_c = \left(\frac{U_2^2\left[B\left({}^{W_c}/_{U_2}\right)^2 + C\left({}^{W_c}/_{U_2}\right) + D\right]}{c_{p,c}T} + 1\right)^{{}^{\gamma_c}/_{(\gamma_c - 1)}} \tag{3.15}$$

where $B = b_0 + b_1 U_2 + b_2 U_2^2$, $C = \frac{2 \cdot B \cdot W_{c,\mathrm{ZSL}}}{U_2}$, $D = d_0 + d_1 U_2 + d_2 U_2^2$. Mass flow at the zero slope line is explicitly modeled as $W_{c,\mathrm{ZSL}} = e_0 + e_1 U_2 + e_2 U_2^2$. The model is said to be validated on three automotive sized compressors with good accuracy. The following model is proposed in [72, p.64]

$$\Pi_c = C_3 - C_2 \left[\bar{W} - C_1\right]^2 \tag{3.16}$$

where C_i, $i \in \{1, 2, 3\}$ are polynomials in ω_{tc}. Citing an internal Ford document, the so called Zero Slope Line Method (ZSLM) is presented in [112, p.6], and compared to two other models (of which the model (3.14) is one). Two model regions are defined, one for flows left of the zero slope line ZSL, and one for flows right of the ZSL

$$\frac{\Phi_c}{\Phi_{c,top}} = \begin{cases} 1 + c_6 e^{-(c_7 N_{\mathrm{tc}})} \left(1 - e^{c_5 \left(\Pi_c / \Pi_{c,\mathrm{ZSL}} - 1\right)}\right) & \Phi_c > \Phi_{c,top} \\ 1 - c_6 e^{-(c_7 N_{\mathrm{tc}})} c_5 \left(\Pi_c / \Pi_{c,\mathrm{ZSL}} - 1\right) & \text{otherwise} \end{cases} \tag{3.17}$$

where $\Phi_{c,top}$ and $\Pi_{c,\mathrm{ZSL}}$ are given by

$$\Phi_{c,top} = c_1 N_{\mathrm{tc}} + c_2 N_{\mathrm{tc}}^2 \tag{3.18}$$

$$\Pi_{c,\mathrm{ZSL}} = c_3 + c_4 \Phi_{c,top}^2 \tag{3.19}$$

and are said to make up a line through the maximum mass flow points of each SpL. Though from the name of the model, and from the further presentation of the model, this seems to refer to the line through the maximum pressure ratio point of each SpL. A surge focused model is proposed in [66, p.1289-1290] as

$$\Pi_c = c_0 + c_1 W_c + c_2 W_c^2 + c_3 W_c^3 \tag{3.20}$$

where c_i, $i \in \{0, 1, 2, 3\}$ are third order polynomials in N_{tc}, which were said to be needed for the compressor studied. For the small region in the compressor map, usually encountered in normal engine operation, following model is proposed in [48, p.134]

$$W_c = c_5 \tilde{\Pi} + c_6 \tilde{\Pi}^2 + c_7 \tilde{\Pi}^3 \tag{3.21}$$

where $\tilde{\Pi} = \Pi_c - c_3 \tilde{N} - c_4 \tilde{N}^2$, and $\tilde{N} = \frac{N_{\mathrm{tc}} - c_1}{c_2}$. In [6, p.110] the following elliptic model structure is proposed

$$\Phi_c = \sqrt{\frac{1 - c_1 \Psi_c^2}{c_2}} \tag{3.22}$$

where c_i are fitted minimizing the total least squares of $\Psi_c^2 c_1 + \Phi_c^2 c_2 = 1$. In [163] the following model structure is proposed

$$\Psi_c = c_0 + c_1 \Phi_c + c_2 \Phi_c^2 + c_3 \Phi_c^3 \tag{3.23}$$

to model surge in a bi-turbo engine. An ellipse like model is proposed in [168, p.975] as

$$\Phi_c = \sqrt{\max\left(0, \frac{1 - C_2 \left(\Psi_c - c_3\right)^2}{C_2}\right)} + c_4 \tag{3.24}$$

where C_1 and C_2 are second order polynomials in ω_{tc}.

3.4.2 Examples of compressor efficiency models

An efficiency model parametrized as a function of Φ_c and M_c is presented in [83] as

$$\eta_c = \frac{c_{1,0} + c_{2,0}M_c}{c_{3,0} - M_c} + \frac{c_{1,1} + c_{2,1}M_c}{c_{3,1} - M_c}\Phi_c + \frac{c_{1,2} + c_{2,2}M_c}{c_{3,2} - M_c}\Phi_c^2 \tag{3.25}$$

The same approach is used in e.g. [22, p.393] and [126, p.5]. In [72], an efficiency model with six parameters are proposed as

$$\eta_c = c_1 - \chi^T Q \chi \tag{3.26}$$

where $Q = [c_2 \ c_3; \ c_3 \ c_4]$, and $\chi = \left[\bar{W} - c_5; \ \Pi_c - c_6\right]$. The parameter c_6 is interpreted as the maximum efficiency, and c_5 and c_6 then give the location in $\bar{W}$ and Π_c of the maximum efficiency point. The parameters c_{2-4} give elliptic shaped contours of constant efficiency. A small modification is proposed in [6, p.113] where the definition of χ is changed in $\chi = \left[\bar{W} - c_5; \sqrt{\Pi_c - 1} - (c_6 - 1)\right]$. The definition of χ was modified also in the efficiency model presented in [168, p.974-975], where $\chi = \left[\bar{W} - c_5; (\Pi_c - 1)^{c_7} - \left(c_6 - 1\right)^{c_7}\right]$, and c_7 is introduced as an extra tuning parameter. In [152, p.3] and [47, p.152] a six parameter efficiency model is proposed as

$$\eta_c = c_1 + c_2 N_{\text{tc}} + c_3 N_{\text{tc}}^2 + c_4 W_c + c_5 W_c^2 + c_6 W_c N_{\text{tc}} \tag{3.27}$$

By utilizing models for isentropic work, and models for actual work, the following eight parameter efficiency model is proposed in [48]

$$\eta_c = \frac{U_2^2 \left(c_1 + c_2 \left({}^{W_c}/_{U_2}\right) + c_3 \left({}^{W_c}/_{U_2}\right)^2\right)}{c_4 + c_5 W_c + c_6 U_2 + c_7 W_c U_2 + c_8 U_2^2} \tag{3.28}$$

Many MVEM mainly uses an η_c-model to calculate the compressor torque Tq_c, and a model for Tq_c is proposed in [129]

$$Tq_{c,mod} = N_{\text{tc}} \frac{p}{\sqrt{T}} \left(c_1 W_c \frac{\sqrt{T}}{p} + c_2\right) \tag{3.29}$$

which is said to be valid from choke flow down to zero flow. For negative flow it is further proposed to simply continue extrapolating the above model. An efficiency model was presented in [107] (and also used in [41] and [40]). The model relies on a compressor flow model that extends the model (3.14). Given a specific flow, the flow model is then used to calculate a modeled Π_c, and this is used to calculate a specific enthalpy gain through the compressor. A specific isentropic enthalpy gain $\Delta h_{is,m}$ is then modeled as affine function in W_c for each speed. The efficiency model is given by

$$\eta_c = \frac{c_{p,c} T \left(\Pi_c^{(\gamma_c - 1)/\gamma_c} - 1\right)}{C_1(N_{\text{tc}}) - C_2(N_{\text{tc}}) W_c} \tag{3.30}$$

where the nominator is Δh_m and the denominator is $\Delta h_{is,m}$, and C_1 and C_2 are second order polynomials in N_{tc}. In [122] the following nine parameter efficiency model is proposed

$$\eta_c = C_0 + C_1\Phi_c + C_2\Phi_c^2 \tag{3.31}$$

where C_{0-2} are three second order polynomials in M_c.

3.5 The Ellipse compressor model used in Papers 1, 4 and 5

Following the brief examples of related compressor models available in the literature, this section presents and discusses the Ellipse compressor model. The resulting model gives an S-shaped characteristic, where an approximate elliptic shape describes most of the normal operating range. The modeling effort is divided in three main regions in flow for a given speed.

The model is formulated in the corrected quantities of the compressor map, and the correction equations, see equations (2.3) and (2.5), are used to handle variations in compressor inlet conditions. The model describes the pressure ratio the compressor can maintain given an operating point in corrected flow $\bar{W}$ and corrected compressor speed $\bar{N}$ as

$$\hat{\Pi} = f_{\hat{\Pi}}(\bar{W}, \bar{N})$$

The model follows the Moore-Greitzer approach and introduces a compressor mass flow state as (3.1), i.e.

$$\frac{dW_c}{dt} = \frac{\pi d_c^2}{4L_c}\left(\hat{p}(\bar{W}, \bar{N}) - p_{02}\right)$$

where d_c and L_c are constants and $\hat{p} = \hat{\Pi}{\cdot}p_{01}$ is the modeled compressor pressure build up. The compressor inlet pressure p_{01} and outlet pressure p_{02} are given by the surrounding components. The mass flow state enables surge simulation, and is further used to change the causality of the model calculations. Instead of having a pressure ratio and speed defining a flow, the model calculates a pressure build up $\hat{p}$ given an operating point in $\bar{W}$ and $\bar{N}$. This is beneficial since most maps have a uniquely defined Π_c for given $\bar{W}$ and $\bar{N}$. This uniqueness is not necessarily found for all measured maps, and slightly backward bending speed lines were found in the analysis of compressor maps in Paper 5, where a reduction in $\bar{W}$ was seen for Π_c below the choking point pressure ratio $\Pi_{c,\mathrm{Ch}}$. The reduction in $\bar{W}$, i.e. the amount of backward bending, was though very limited. Further, the extra mass flow state means that a measured Π_c and $\bar{W}$ must deviate from $\hat{\Pi}$ and $\bar{W}$ during transients.

Given a $\bar{N}$, a number of characteristic points define a modeled speed line SpL, and an overview of these characteristic points of a SpL is shown in Fig. 3.5. Following the SpL from left to right, three main regions can be defined. Negative flow and up to zero flow is modeled using a polynomial in Paper 1, while a

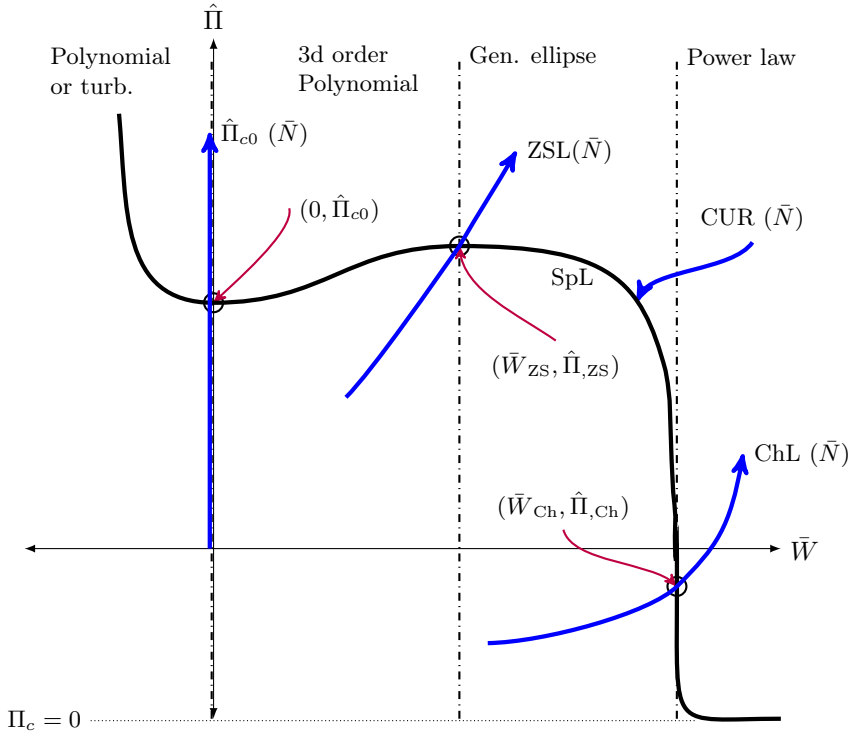

Figure 3.2: Overview of the Ellipse compressor model.

turbine flow like parabola model is used in Paper 4. In both papers the modeled SpL passes through the zero flow pressure build up point $(0, \hat{\Pi}_{c0})$. For Paper 5 no description for negative flow is implemented. From zero flow to the Zero Slope Line ZSL, found close to the surge line, a third order polynomial is used as a model. The polynomial is parametrized to give zero slope at zero flow and at the ZSL, and this part of a SpL is commonly referred to as the unstable branch. For flows from the ZSL to the choke line ChL, where the SpL has infinite slope, a generalization of an ellipse is used as a model. It should be noted though, that the curvature of the modeled ellipse is not necessarily equal to two, and a true mathematical ellipse does hence not result. For model implementations where the choking pressure ratio is larger than zero, also a fourth region is used for simulation purposes. A power law model is then used that converges asymptotically to $\hat{\Pi} = 0$ for infinite $\bar{W}$.

Descriptions of $\hat{\Pi}_{c0}(\bar{N})$, $\mathrm{ZSL}(\bar{N})$ and $\mathrm{ChL}(\bar{N})$ are key components of the model. These descriptions differed some between the papers, and the differences are described in the following. The compressor modeling of Paper 1 was based on data from four compressor maps, and polynomials were used to model $\hat{\Pi}_{\mathrm{ZSL}}$ (through 1 for $\bar{N} = 0$), $\bar{W}_{\mathrm{ZSL}}$ (through 0 for $\bar{N} = 0$), CUR, $\bar{W}_{\mathrm{ChL}}$ and $\hat{\Pi}_{c0}$, while a zero choking pressure ratio was modeled i.e. $\hat{\Pi}_{\mathrm{ChL}} = 0$.

Data from 236 compressor maps were used in Paper 4. $\hat{\Pi}_{\mathrm{ZSL}}$ and $\bar{W}_{\mathrm{ZSL}}$ were

modeled using power laws through 1 and 0 for $\bar{N} = 0$, respectively. $\hat{\Pi}_{c0}$ was further modeled using $\Gamma_{\Pi_{cs}}$, an affine model described $\bar{W}_{\text{ChL}}$, and a constant $\hat{\Pi}_{\text{ChL}} = 0$ was assumed. The curvature was divided into two models, utilizing an affine model and a power law model respectively.

For Paper 5, a total of 305 compressor maps were used in the modeling. The models for $\hat{\Pi}_{\text{ZSL}}$ and $\bar{W}_{\text{ZSL}}$ from Paper 4 were used. Power law models were then used for $\bar{W}_{\text{ChL}}$, $\hat{\Pi}_{\text{ChL}}$ and $\hat{\Pi}_{c0}$. A second order polynomial function in $\bar{N}$ was used to describe CUR.

To exemplify, the ellipse part of the final model from Paper 5 is presented here

$$\hat{\Pi}_{mod} = \left(1 - \left(\frac{\bar{W} - \bar{W}_{\text{ZSL}}}{\bar{W}_{\text{ChL}} - \bar{W}_{\text{ZSL}}}\right)^{\text{CUR}}\right)^{\frac{1}{\text{CUR}}} \cdot \left(\hat{\Pi}_{\text{ZSL}} - \hat{\Pi}_{\text{ChL}}\right) + \hat{\Pi}_{\text{ChL}} \quad (3.32)$$

where $\bar{W}_{\text{ZSL}}$, $\bar{W}_{\text{ChL}}$, $\hat{\Pi}_{\text{ZSL}}$, $\hat{\Pi}_{\text{ChL}}$ and CUR are all functions of $\bar{N}$. With the gas state at the compressor inlet given, i.e. T_{01} and p_{01} and the corresponding reference states, the corrected mass flow $\bar{W}$ is calculated from (2.3) using the model state W_c given by (3.1). The corrected compressor speed $\bar{N}$ is calculated using (2.5). The Ellipse model then gives $\hat{\Pi}_{mod}$, and $\hat{p}$ of (3.1) is then calculated as $\hat{p} = \hat{\Pi}_{mod} \cdot p_{01}$.

The efficiency model in Papers 1, 4 and 5, is based on the model from [72], with the extension from [6]. However, the efficiency model uses a lower saturation threshold as

$$\eta_{c,mod} = \max\left[\eta_{c,\text{lower sat.}},\ c_1 - \chi^T Q \chi\right] \quad (3.33)$$

where $Q = [c_2\ c_3;\ c_3\ c_4]$, and $\chi = \left[\bar{W} - c_5; \sqrt{\Pi_c - 1} - (c_6 - 1)\right]$. By selecting the same threshold for both surging and choking flows, a continuous efficiency model results. The threshold was commonly set to $\eta_{c,\text{lower sat}} = 30\%$.

Given an operating point in $\bar{W}$ and Π_c, the modeled $\eta_{c,mod}$ can be calculated, and a modeled compressor discharge temperature $T_{02,mod}$ can be calculated using $\eta_{c,mod}$ in (2.6) given T_{01} and Π_c. The modeled compressor power $P_{c,mod}$ is then given by

$$P_{c,mod} = W_c c_{p,c}(T_{02,mod} - T_{01}) \quad (3.34)$$

and the loading compressor torque of (2.1) is given by

$$Tq_{c,mod} = \frac{P_{c,mod}}{\omega_{tc}} \quad (3.35)$$

Some further comments to the model can be given. Since the surge line is a system property, no surge line is defined in the model. A temperature rise in the control volume before the compressor during surge, is described by the model for negative flow. However, no temperature rise at the compressor inlet will result for operation with flows close to the surge line, i.e. recirculation. The compressor model acts as a turbine during the reverse flow periods of surge, and for operation at pressure ratios of less than unity with positive flow.

4

Experimental setups

This chapter presents the sensory equipment and measurement systems of two of the experimental setups that have been used, and details some of their characteristics: the engine test stand at Vehicular systems (measurements for Papers 1, 2, 3 and 4), and the Saab Trollhättan gas stand (Papers 3 and 5). Sensor installation details, and details of the sensors used will be presented. The surge test stand, used for some of the surge measurements (Papers 1 and 4) is not presented here, and the interested reader is instead referred to [5] for details.

For general information on common automotive sensors, the reader is referred to e.g. [102] and [171]. A good overview of measuring pressure and temperature in a turbo is found in [148].

4.1 The engine laboratory at Vehicular Systems

The engine laboratory consists of one engine test cell, equipped with two engine test stands. The engines of each test stand are connected to individual Schenck Dynas3-LI250 electric dynamometers from 2002 (rated speed of 10krpm, rated power of 250kW, and rated torque of 480Nm). The electric dynamometers load the engines, and also act as the start motors. The electricity the dynamometer generates, is fed back to the electric grid, and the heat expelled by the engine to the coolant system, supports the heating of the university buildings.

The laboratory equipment and setup are subject to continuous development, and data from four different engine installations have been used for this thesis. Some main characteristics of the engines are presented in Table 4.1. An installation photo of the series sequentially turbocharged LNF engine is shown in Fig. 4.1, where the low pressure stage and the high pressure stage are marked. The two white rolled up cables are connected to the two turbo speed sensors.

Engine	Description
B235R	Saab, 2.3L, 230hp, 350Nm, fixed cams, single stage turbocharger, MHI TD04HL-15T
L850	Saab/GM (B207R), 2.0L, 210hp, 300Nm, extended with dual variable cam phasing, single stage turbocharger, MHI TD04L-14T
LNF	GM, 2.0L, 265hp, 350Nm, dual variable cam phasing, twin-scroll single stage turbo, BW K04-2277
LNF-TS	GM, 2.0L, dual variable cam phasing, series sequential two-stage turbo system extended with actively controlled high pressure stage compressor by-pass, BW K04-2270 + BW KP35-1574

Table 4.1: Main characteristics of the four different engine installations. All engines are water cooled four cylinder inline spark ignition engines with a single air-to-air intercooler, and 16 valves. Fuel used is petrol.

The packaging constrains the sensor installation, which can affect the measurements.

The engine control system is based on a dSPACE MicroAutoBox (MABx) and RapidPro (RP) architecture. The engine control system is a large Simulink model, that is compiled using Real Time Workshop. The generated code is then executed in real time on the MABx. The can directly control any of the actuator signals.

The test cell measurement system consists of an HP VXi system, with an HPE1415A module and an HPE1433A module. The HPE1415A module is used to measure analog and digital signals, with a sample frequency of up to 2000Hz, and has built in support for thermocouples. The HPE1433A module is a fast 8 channel converter with separate A/D-converters for each channel. The HPE1433A is used with a sampling frequency of up to 192kHz, and can also be used to sample in the crank angle domain.

The signals are measured by the HP VXi system. Commonly, a sampling frequency of 1000Hz is used for the HPE1415A and 128kHz is used on the HPE1433A. The dSPACE control system is also used to measure, where all engine production sensors and actuator signals can be sampled, along with a large number of extra digital and analog signals. On the dSPACE system, commonly a sampling frequency of 80Hz is used, which is equivalent to one of the main control loops of the engine control system. A summary of the measurement systems is presented in Table 4.2.

Most measurements conducted in the engine test stand for this thesis were for stationary engine operating points. For each operating point measured, the system was allowed time to stabilize all components thermally, and a mean value of 10s of each signal was then calculated and stored. The surge oscillations presented in Paper 1 and Paper 4 are typically phenomena with a corresponding frequency of approximately 10Hz, and a sampling frequency of at least 1000Hz was used for these measurements .

The next subsections will discuss the sensors and their installation, and for further information on the engine test stand the reader is referred to [6, p.217-].

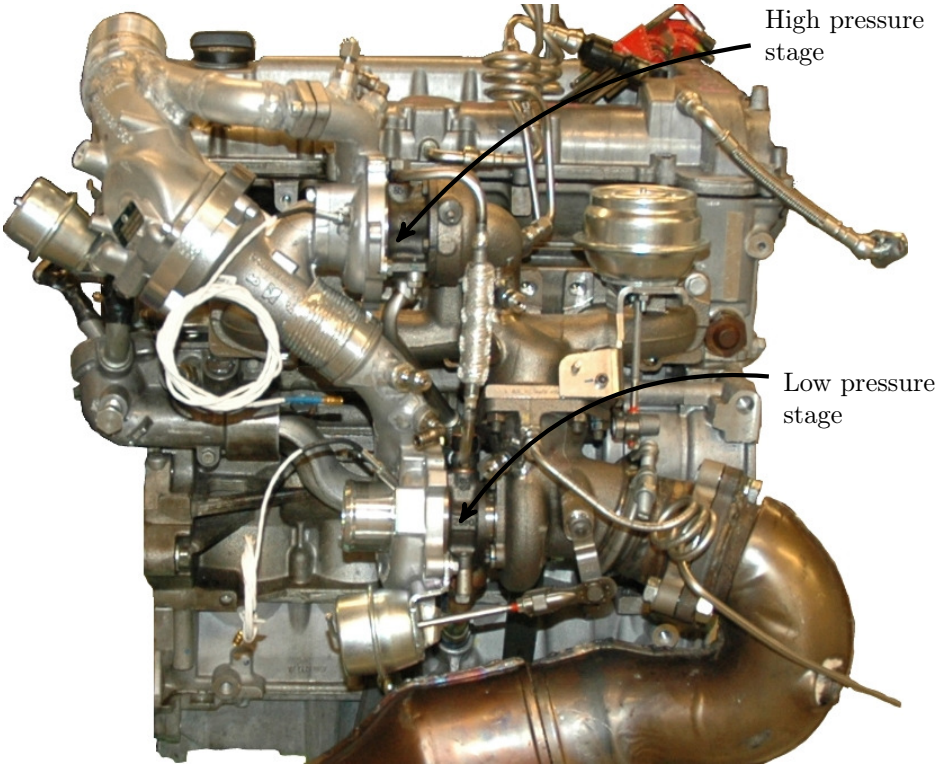

Figure 4.1: Photo of the LNF engine with the two stage series sequential turbo system.

4.1.1 Sensors

This section presents the typical sensors used during the experiments in the engine test stand: temperature T, pressure p, mass flow W, and turbo speed N_{tc}. The final subsection summarizes some of the other sensors mainly used for diagnostic purposes. An example of the locations of different sensors used in Paper 3 is shown in Fig. 4.2, and an actual photo of the same experimental setup is shown in Fig. 4.3.

Temperature

All temperature sensors are IEC class 1 K-type thermocouples from Pentronic, and the same thermocouple extends from the measurement location to the measurement system i.e. no connection cables of other materials are involved in the thermocouple circuit. Class 1 K-type thermocouples have an accuracy of $\pm 1.5^o\mathrm{C}@T \in [-40, 375]^o\mathrm{C}$ and $\pm 0.004 \cdot |T|@T \in [375, 1000]^o\mathrm{C}$, see e.g. [115, p.574] and [125, Ch.3:4]. The sensors are all shielded, and the width of the sensor bodies are mostly 3mm. The compressor outlet temperature sensors (e.g. T_{02} of Fig. 4.2) for the series sequential installation used a sensor width

Model	Description
HP VXI, HPE1415	64-channel algorithmic closed loop controller. 16-bit A/D-resolution, up to 56kSa/s maximum reading rate dependent upon configuration. 64kSa measurement FIFO memory built in. Installed modules of the VXI system are: HPE8400A, HPE8491A, 3xHPE1503A, HPE1505A, HPE1537A, and HPE1538A.
HP VXI, HPE1433	8-channel 196kSa/s digitizer (+DSP) with integrated sensor signal conditioning, anti-aliasing protection, digitization and high-speed measurement computation. 32Mb of RAM. Separate A/D converters.
MABx/RP	dSPACE Microautobox (MABx) and RapidPro-system (RP). The RP consists of four layers; two powerstage layers for output handling, one control unit layer capable of both input and output, and one signal conditioning layer for sensor input.

Table 4.2: Summary of the measurement systems in the engine laboratory of vehicular systems. The control system of the engine is a compiled Matlab Simulink model, that is run in real time on the dSPACE equipment (MABx/RP). All actuator control signals can also be sampled using the MABx/RP.

of 1.5mm. Most sensors are from 2008, but some 3mm sensors were from 2003. The temperature sensor T_{LFE3} is used by the LFE3 mass flow sensor, and is also 3mm in width.

During the measurements for this thesis, the sensor tips were adjusted to be close to the pipe center for each measurement location. Due to packaging constraints, mostly only single temperature sensors were fitted for each locations. Three sensors were used for the compressor inlet temperature measurement in Paper 2 and Paper 3. Ice water and boiling water were used to calibrate the temperature sensors, before the measurement series. The recovery factor used to calculate the total temperature from a measured temperature [8, p.44], is assumed to be 1. This means that the measured temperature is assumed to be the total temperature. The pulsations caused by the cylinder pumping of the engine, was not considered to cause significant oscillations in the control volumes surrounding the compressor. Most measurements are also stationary engine operating points. The temperature signals during compressor surge were not explicitly used in the modeling. For the turbine side measurements in Paper 2, only small Π_t was measured, and the oscillations in pressure were hence comparable small.

Pressure

The pressure sensors are all but one from Kistler, and of either the 4260-series (4260A50 340kPa and 4260A75 500kPa piezoresistive absolute pressure sensors, 0.05% Full Scale (FS) accuracy, 0.1% FS stability per year, 3xFS proof pressure, $f_{max} = 2$kHz) or the 4295-series (4295A2 and 4295A2V, 200kPa absolute pressure sensors). The absolute pressure sensor p_{LFE3} measured internally by the LFE3 mass flow sensor system, is manufactured by Micro Switch Honeywell.

The sensors for the compressor inlet pressure measurement in Paper 2 and Paper 3 ($p_{01,1}$, $p_{01,2}$ and $p_{01,3}$ in Fig. 4.2), are placed on a straight pipe, following an air filter to reduce flow disturbances. Four pressure taps are connected together, and the sensors $p_{01,1}$ and $p_{01,2}$ are connected to the four taps. The $p_{01,3}$-sensor in Fig. 4.2 uses a single pressure tap, due to packaging constraints.

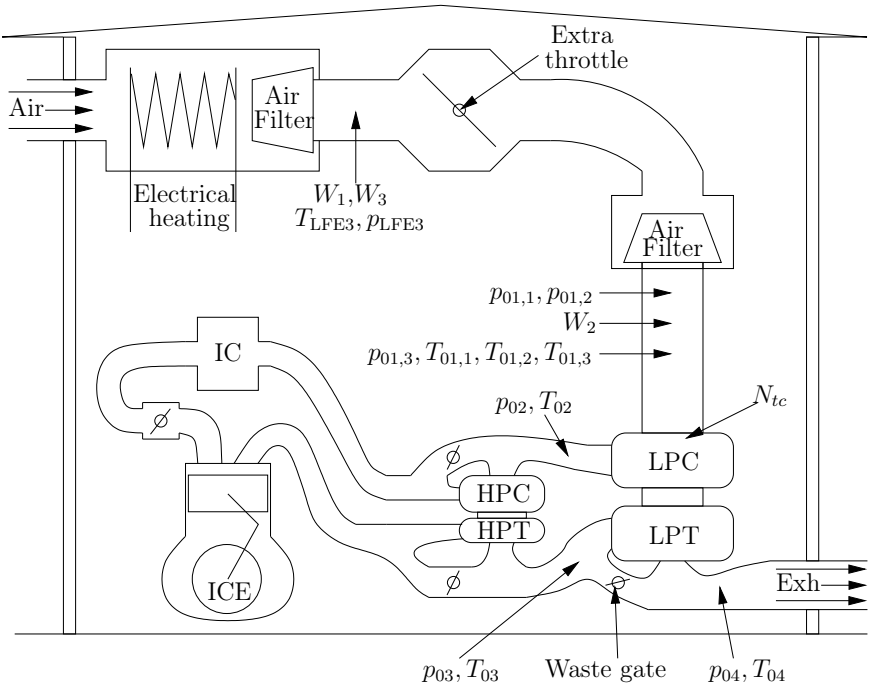

Figure 4.2: Schematic picture of the experimental setup used in Paper 3. The electrical heating section is removed when not required. The extra throttle is used to decrease compressor inlet pressure, and the throttle is controlled using the engine control system (MABx/RP). The air filters are used to straighten the air flow for the mass flow and pressure measurement locations. Air comes in from the left, runs through the compressor inlet variation rig, goes through the compressor stages, the engine, the turbine stages, catalyst, muffler and are expelled to the right.

The positioning of the pressure taps for p_{02}, p_{03} and p_{04} are also restricted due to the packaging, but placed at the most straight sections of the respective pipes. The exhaust side pressure sensors, p_{03} and p_{04}, are mounted on spiral shaped pipes approximately 0.50m in length, due to restricted temperature limits of the sensors. Also the cold side temperature sensors are typically mounted with connecting hoses, and only the intake manifold pressure is flush mounted. Measured pressures were assumed to be the static pressures. Total pressures are then calculated from each pressure measurement using the measured mass flow, measured temperature and the pipe area as

$$p_0 = p + \frac{\rho \cdot v^2}{2} = p + \frac{W^2}{2 \cdot \rho \cdot A^2}$$

where p_0 is the total pressure, p the measured pressure, v the flow velocity, ρ gas density, W measured mass flow, and A the cross sectional area at the measurement location. The difference between p_0 and p is the dynamic pressure,

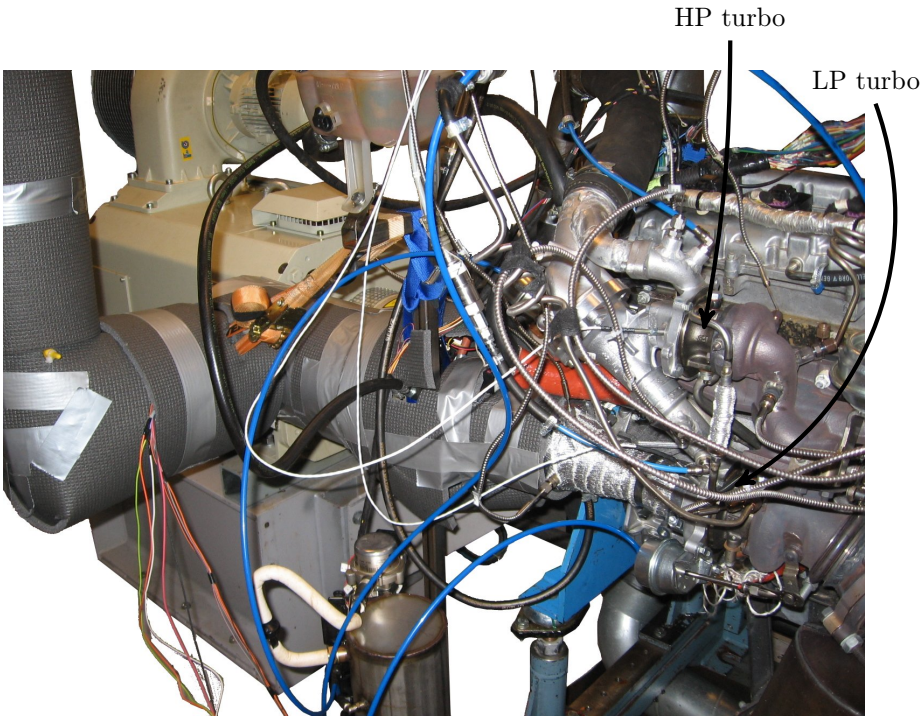

Figure 4.3: The compressor inlet condition variation rig, the Schenk dynamometer and the engine test stand with the two stage system mounted on the LNF engine. The high pressure turbo (HP) and the low pressure turbo (LP) are marked.

describing the increase in pressure that the gas experiences when it is brought to stand still. A reference sensor is used to calibrate the pressure sensors before a measurement series, to minimize any offset errors between the sensors. Further, all pressure sensors are measured at engine off conditions, both before and after each measurement sequence, to indicate any sensor drift during the measurements. Most investigations are conducted on the compressor side, where the oscillations in pressure due to the engine pumping are far less severe, and the engine is typically operated in stationary conditions (except for the surge measurements). Turbine inlet and outlet pressures are measured in Paper 2. However, the range in measured Π_t was limited due to the indirect measurement of turbine flow (compressor flow and fuel flow calculated using λ) and the limited spring pre-tension of the waste-gate valve (where the WG opens for large differential pressure across the turbine). The potential measurement errors due to pulsating flow was therefore considered neglectable.

Mass flow

For Paper 2 and Paper 3, three different mass flows are measured. W_1 in Fig. 4.2 is measured using the LFE3 system. The LFE3 sensor system is purpose built for automotive research by the Technical University of Denmark (DTU), and uses the differential pressure principle. The differential pressure is measured over a laminar flow element, that gives the volumetric flow. T_{LFE3} and p_{LFE3} are then used to calculate the density, and the mass flow is determined according to $W_1 = \dot{V} \cdot \rho_{\mathrm{LFE3}}$, where $\dot{V}$ is the volumetric flow and ρ_{LFE3} is the density at the measurement location. The LFE3 differential pressure sensor is a 164PC0137 from Micro Switch Honeywell. The mass flow sensor W_2 in Fig. 4.2 is a Bosch production sensor, based on the hot-wire principle producing a digital signal. An extra differential pressure sensor is for diagnosis purposes mounted in parallel with the LFE3 differential pressure. The mass flow W_3 in Fig. 4.2 is calculated from also this differential pressure sensor, using the T_{LFE3} and p_{LFE3} to calculate the air density. This extra differential pressure sensor is a Kistler 4264AB03-sensor (bi-directional differential pressure sensor, $\pm$17kPa, 0.2(0.05)% FS accuracy, 0.1% FS stability per year, 3xFS proof pressure, f_{max} = 2kHz). The differential pressure based sensor was installed approximately 1.5m of piping upstream of the compressor, and the hot wire sensor was approximately 0.5m upstream.

Here, mass flow was measured at two different locations and calculated from three sources. The mass flow measurement stations were located on approximately 0.5m straight pipe sections immediately downstream of an air filter, to make the air flow as uniform as possible within the packaging constraints of the test stand. For stationary measurements, the distance from the sensor to the location were the measurement is desired causes no problem, since in stationarity these flows will be equal. The mass flow signal measured during surge was not considered reliable.

Misc sensors

The turbo speed N_{tc} of Fig. 4.2 is measured using an Acam PicoTurn BM-V6 (range $0.2 - 400$krpm) system, using a ferrite core coil to sense a passing blade through change in inductance by eddy currents. The actual sensor installation can be seen in Fig. 4.1, where the rolled up white cables lead up the sensors mounted on each compressor housing. The BM-V6 system is capable of both analog and digital output signal, where the latter is used to reduce noise sensitivity. The speed sensor position is adjusted using the built in sensor positioning functions of the BM-V6, to ensure a good quality of the turbo speed measurement. The LNF engine is equipped with AVL GU21D cylinder pressure sensors, which were delivered newly calibrated with the engine in 2007. Waste-gate positions on the LNF two-stage turbo system was measured using Gill Blade 25 sensors ($0 - 25$mm, f_{max} = 1kHz, 125^{o}C max temperature). The installation required extra purpose built cooling systems. The Schenk dynamometers are equipped with GIF F1 (rated torque 650Nm, max speed 12krpm) torque sensors. LeineLinde crank angle sensors were used, with a resolution of 720 points per engine revolution.

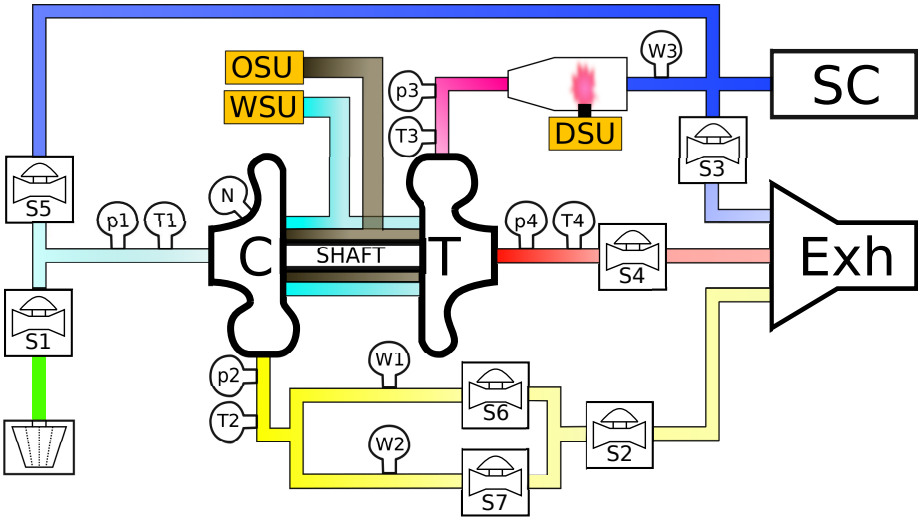

Figure 4.4: Schematic overview of the Saab gas stand. The abbreviations are: C compressor, T turbine, SC screw compressors, Exh exhaust chimney, DSU/OSU/WSU diesel/oil/water supply unit respectively, and S are valves to control flow. p, T, W, and N indicate measurement locations.

4.2 Saab Trollhättan gas stand

The extended maps presented in Paper 5 were measured at Saab Powertrain in Trollhättan, Sweden. As an unfortunate side note, the measurements conducted for Paper 5 were probably among the last ever to be made in the gas stand in Saab's name, as Saab was soon afterward declared bankrupt. The gas stand equipment is delivered by AVL. Two Atlas Copco ZR90VSD screw compressors (water cooled variable speed drives) deliver pressurized oil free air, that is being conditioned using an air-to-water intercooler. The air can be delivered to both compressor and turbine. A diesel burner is used to increase turbine gas flow temperature. Turbo oil and water supply can be controlled, both feeding pressure and temperature. The p_{oil}/T_{oil} and p_{water}/T_{water} circuits are individually controllable. The climate of the gas stand room is controlled. An overview of the gas stand is shown in Fig. 1, and actual gas stand installation photos (for the Paper 5 measurements) are shown in Fig. 4.5.

For further details on the gas stand setup, the interested reader is referred to e.g. [92] and [173].

4.2.1 Measurement equipment

The most important parts of the AVL data acquisition system were four F-FEM-AIN modules for analog, and two F-FEM-CNT modules for digital signals. The measurement stations for $T_{0i},\ i = \{1, 2, 3\}$ were equipped with 8 sensors each. The sensors were divided into two groups of four sensors, spread

out evenly circumferential around the measurement planes for redundancy and diagnostic purposes. PT100 sensors were used for the cold temperatures, and the documentation of the sensors stated $T_{max} = 300^o$C and an accuracy of $\pm(0.15 \pm 0.002T)^o$C. Eight sensors were used to measure T_{01}, and eight sensors were used for T_{02}. Pentronic K-type thermocouples were used in the hot flows, with $T_{max} = 1333^o$C and a stated relative accuracy is $< 0.75\%$. The compressor side pressures, p_1 and p_2, were relative pressure sensors, with a range of $\Delta p \in [-5, 600]$ kPa. Two individual sensors were connected to two individual measuring rings on each measurement location. At least 10 pipe diameters of straight pipes lead up the measurement locations. Sensor Total Error Band (TEB) accuracy was stated as $\pm 0.35\%$FS. The two turbine side pressures p_4 sensors had a range of $\Delta p \in [-100, 250]$ kPa, and a stated accuracy of 0.35% FS TEB. The two p_3 sensors had a stated accuracy of 0.35% FS TEB, and the range is thought to be $\Delta p \in [-5, 600]$ kPa. Two McCrometer Vcone differential pressure based measurement systems were used to measure different ranges of compressor mass flow ($W1$ and $W2$ in Fig. 1). For the small flow range, sensors with a range of $\pm$7kPa and a "Combined non-linearity & Hysteresis" accuracy of $\pm 0.08\%$ FS Best Straight Line (BSL) and "Temperature effect" of $\pm 1\%$ FS TEB are used. The range of the differential pressure sensors for the larger flow regime were $\pm$50kPa), but here the accuracy and temperature effect were stated as $\pm 0.08\%$ and $\pm 1\%$, respectively. The sensors were GE Druck sensors of series PMP4110. JAQUET T411-S5 tachometers were used to measure turbo shaft speed. The accuracy was stated to be $< 0.5\%$ FS, and a lower blade pass frequency of $f_{blade,min} = 3$kHz was stated.

(a) Gas stand room.

(b) Screw compressor room.

(c) Control room

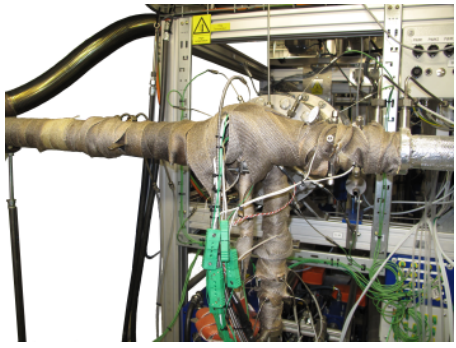

(d) Installation photo.

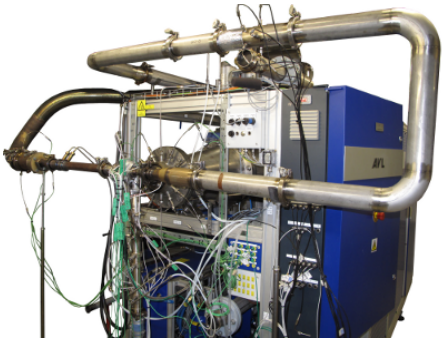

(e) Installation for pressurizing compressor inlet before insulation.

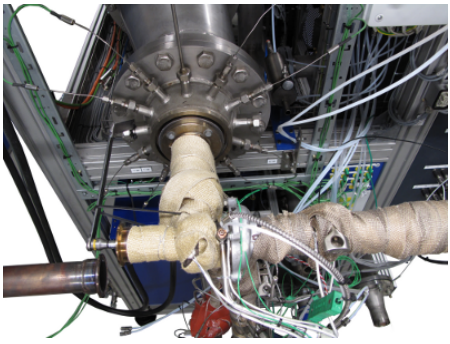

(f) Setup for zero turbo speed with typical insulation installed.

Figure 4.5: Photos from the measurements conducted in the Saab gas stand for Paper 5.

References

The *"(Cited on p. **7,8,12**)"* of the reference list indicates the pages within the introductory chapters of this compilation thesis, where the reference is used.

[1] M. Abidat, M. Hachemi, M.K. Hamidou, and N.C. Baines. Prediction of the steady and non-steady flow performance of a highly loaded mixed flow turbine. *Proc. of the IMechE, Part A: J. of Power and Energy*, 212:173–184, 1998. *(Cited on p. **27, 31**)*

[2] Habib Aghaali and Hans-Erik Ångström. Improving turbocharged engine simulation by including heat transfer in the turbocharger. In *SAE World Congr.*, Techn. Paper 2012-01-0703, 2012. *(Cited on p. **15, 16, 31**)*

[3] Markus Ammann. *Modellbasierte Regelung des Ladedrucks und der Abgasrückführung beim aufgeladenen PKW-Common-Rail-Dieselmotor*. PhD thesis 15166, ETH, Zürich, 2003. *(Cited on p. **15, 16, 28**)*

[4] Johannes Andersen, Erik Karlsson, and Anders Gawell. Variable turbine geometry on SI engines. In *SAE World Congr.*, Techn. Paper 2006-01-0020, Detroit, USA, March 2006. *(Cited on p. **14**)*

[5] Johannes Andersen, Fredrik Lindström, and Fredrik Westin. Surge definitions for radial compressors in automotive turbochargers. *SAE I.J. of Engines*, 1(1):218–231, 2009. *(Cited on p. **16, 18, 24, 25, 49**)*

[6] Per Andersson. *Air Charge Estimation in Turbocharged Spark Ignition Engines*. PhD thesis 989, Linköping University, 2005. *(Cited on p. **15, 28, 31, 32, 33, 44, 45, 48, 50**)*

[7] Steve Arnold. Turbocharging technologies to meet critital performance demands of ultra-low emissions diesel engines. In *SAE World Congr.*, Techn. Paper 2004-01-1359, 2004. *(Cited on p. **25**)*

[8] ASME. PTC 10-1997, Performance test code on compressors and exhausters. American Society of Mechanical Engineers, New York, 1997. *(Cited on p. **18, 52**)*

[9] Nicholas C. Baines. *Fundamentals of Turbocharging*. Concepts NREC, 1st edition, 2005. *(Cited on p. **4, 10, 13, 14, 30, 32, 33, 40**)*

[10] Nick Baines, Karl D. Wygant, and Antonis Dris. The analysis of heat transfer in automotive turbochargers. In *Proc. of ASME Turbo Expo*, GT2009-59353, June 2009. *(Cited on p. **15, 16**)*

[11] Nick Baines, Karl D. Wygant, and Antonis Dris. The analysis of heat transfer in automotive turbochargers. *Trans. of ASME, J. of Engineering for Gas Turbines and Power*, 132(4):1–8, 2010. *(Cited on p. **15, 21, 29**)*

[12] Rowland S. Benson. Nonsteady flow in a turbocharger nozzleless radial gas turbine. In *SAE*, Techn. Paper 740739, 1974. *(Cited on p. **27, 30**)*

[13] G. Benvenuto and U. Campora. Dynamic simulation of a high-performance sequentially turbocharged marine diesel engine. *I.J. of Engine Research*, 3(3):115–125, 2002. *(Cited on p. **22**)*

[14] Johan Bergström and Oskar Leufvén. Surge modeling and control of automotive turbochargers. Master's thesis LiTH-ISY-EX-3999, Linköping University, 2007. *(Cited on p. **7**)*

[15] Bjørnar Bøhagen and Jan Tommy Gravdahl. On active surge control of compressors using a mass flow observer. In *Proc. IEEE Conf. on Decision and Control*, volume 4, pages 3684–3689, Dec 2002. *(Cited on p. **28**)*

[16] Yurij G. Borila. A sequential turbocharging method for highly-rated truck diesel engines. In *SAE*, Techn. Paper 860074, 1988. *(Cited on p. **28**)*

[17] K.K. Botros. Transient phenomena in compressor stations during surge. *Trans. of ASME, J. of Engineering for Gas Turbines and Power*, (116):133–142, 1994. *(Cited on p. **38, 43**)*

[18] F. Bozza, V. De Bellis, S. Marelli, and M. Capobianco. 1D simulation and experimental analysis of a turbocharger compresor for automotive engines under unsteady flow conditions. In *SAE World Congr.*, Techn. Paper 2011-01-1147, 2011. *(Cited on p. **18**)*

[19] Julia H. Buckland. *Estimation Methods for Turbocharged Spark Ignition Engines*. PhD thesis, University of Michigan, 2009. *(Cited on p. **15, 30**)*

[20] P. M. Came and C. J. Robinson. Centrifugal compressor design. *Proc. of the IMechE, Part C: J. of Mechanical Engineering, Science*, 213(2), 1999. *(Cited on p. **11, 12, 13, 24**)*

[21] Marcello Canova. Development and validation of a control-oriented library for the simulation of automotive engines. *I.J. of Engine Research*, 5(3):219–228, 2004. *(Cited on p. **28**)*

[22] Marcello Canova, Fabio Chiara, Giorgio Rizzoni, and Yue-Yun Wang. Design and validation of a control-oriented model of a diesel engine with two-stage turbocharger. *SAE I.J. of Fuels and Lubricants*, 2(2):387–397, 2009. *(Cited on p. **31, 38, 43, 45**)*

[23] Marcello Canova, Junqiang Zhou, Lisa Fiorentini, Fabio Chiara, and Yue-Yun Wang. Model-based analysis and optimization of turbocharged diesel engines with a variable geometry compressor and turbine system. In *SAE World Congr.*, Techn. Paper 2012-01-0716, 2012. *(Cited on p. **13**)*

[24] Massimo Capobianco and Agostino Gambarotta. Variable geometry and waste-gated automotive turbochargers: Measurements and comparison of turbine performance. *Trans. of ASME, J. of Engineering for Gas Turbines and Power*, 114:553–560, 1992. *(Cited on p. **27, 31**)*

[25] Massimo Capobianco, Agostino Gambarotta, and Giovanni Cipolla. Effect of inlet pulsating pressure characteristics on turbine performance of an automotive wastegated turbocharger. In *SAE World Congr.*, Techn. Paper 900359, 1990. *(Cited on p. **17, 21, 22, 27, 30**)*

[26] Michael V. Casey and Thomas M. Fesich. On the efficiency of compressors with diabatic flows. In *Proc. of ASME Turbo Expo*, GT2009-59015, June 2009. *(Cited on p. **15, 16, 25**)*

[27] M.V. Casey and M. Schlegel. Estimation of the performance of turbocharger compressors at extremely low pressure ratios. *Proc. of the IMechE, Part A: J. of Power and Energy*, 224(2), 2010. *(Cited on p. **25, 26, 29, 39, 40, 41, 42**)*

[28] Kirby S. Chapman and Jacque Shultz. Guidelines for: Testing large-bore engine turbochargers. Technical report, The National Gas Machinery Laboratory, Kansas State University, 245 Levee Drive, 2003. *(Cited on p. **18**)*

[29] A. Chasse, P. Moulin, A. Albrecht, L. Fontvielle, A. Guinois, and L. Doléac. Double stage turbocharger control strategies development. In *SAE World Congr.*, Techn. Paper 2008-01-0988, 2008. *(Cited on p. **28**)*

[30] Colin D. Copeland, Ricardo Martinez-Botas, and Martin Seiler. Unsteady performance of a double entry turbocharger turbine with a comparison to steady flow conditions. In *Proc. of ASME Turbo Expo*, GT2008-50827, June 2008. *(Cited on p. **27**)*

[31] M. Cormerais, J.F. Hetet, P. Chesse, and A. Maiboom. Heat transfer analysis in a turbocharger compressor: modeling and experiments. In *SAE World Congr.*, Techn. Paper 2006-01-0023, Detroit, USA, March 2006. *(Cited on p. **16**)*

[32] Costall, McDavid, Martinez-Botaz, and Baines. Pulse performance modeling of a twin entry turbocharger turbine under full and and unequal admission. In *Proc. of ASME Turbo Expo*, GT2009-59406, June 2009. *(Cited on p. **22, 27, 28**)*

[33] Ivan Criscuolo, Oskar Leufvén, Andreas Thomasson, and Lars Eriksson. Model-based boost

pressure control with system voltage disturbance rejection. In *Proc. of IFAC World Congr.*, pages 5058–5063, 2011. *(Cited on p. **6**)*

[34] Bram de Jager. Rotating stall and surge control: A survey. In *Proc. IEEE Conf. on Decision and Control*, pages 1857–1862, Dec 1995. *(Cited on p. **23, 25, 38**)*

[35] R. Dehner, A. Selamet, P. Keller, and M Becker. Simulation of mild surge in a turbocharger compression system. In *SAE World Congr.*, Techn. Paper 2010-01-2142, 2010. *(Cited on p. **23, 24, 38, 39**)*

[36] Michael Deligant, Pierre Podevin, Georges Descombes, Lamquin Thierry, Vidal Fabrice, and Alexandre Marchal. Experimental study of turbocharger's performances at low speeds. In *Proc. ASME Int. Combustion Engine Division Fall Tech. Conf.*, ICEF2010-35071, pages 911–918, 2010. *(Cited on p. **17, 33**)*

[37] J.M. Desantes, B. Plá J.M. Luján, and J.A. Soler. Potential of using a nozzle at the compressor inlet of a high-speed direct-injection diesel engine. *J. of Applied Thermal Engineering*, 225:178–189, 2011. *(Cited on p. **13**)*

[38] S.L. Dixon. *Fluid Mechanics and Thermodynamics of Turbomachinery*. Butterworth-Heinemann, 4th edition, 1998. *(Cited on p. **4, 10, 15, 18, 39, 40, 41**)*

[39] Thomas Eidenböck, Karl Mayr, Werner Neuhauser, and Peter Staub. The new BMW six-cylinder diesel engine with three turbochargers part 1: Drive unit and turbocharger system. *MTZ*, 73(1):18–24, 2012. *(Cited on p. **28**)*

[40] Jamil El Hadef, Guillaume Colin, Yann Chamaillard, and Vincent Talon. Physical-based algorithms for interpolation and extrapolation of turbocharger data maps. *SAE I.J. of Engines*, 5(2), May 2012. *(Cited on p. **43, 45**)*

[41] Jamil El Hadef, Guillaume Colin, Vincent Talon, and Yann Chamaillard. New physics-based turbocharger data-maps extrapolation algorithms: Validation on a spark-ignited engine. In *IFAC ECOSM*, pages 213–220, 2012. *(Cited on p. **23, 31, 33, 43, 45**)*

[42] Abraham Engeda, Yanbae Kim, Ronald Aungier, and Gregory Direnzi. The inlet flow structure of a centrifugal compressor stage and its influence on the compressor performance. *J. of Fluids Engineering*, 125:779–785, 2003. *(Cited on p. **11, 41**)*

[43] Lars Eriksson. Mean value models for exhaust system temperatures. *SAE I.J. of Engines*, 111(3), Sept 2002. *(Cited on p. **15, 28**)*

[44] Lars Eriksson. Modeling and control of turbocharged SI and DI engines. *Oil & Gas Science and Technology - Rev. IFP*, 62(4):523–538, 2007. *(Cited on p. **31, 32, 43**)*

[45] Lars Eriksson, Tobias Lindell, Oskar Leufvén, and Andreas Thomasson. Scalable component-based modeling for optimizing engines with supercharging, E-boost and turbocompound concepts. *SAE I.J. of Engines*, 5(2):579–595, May 2012. *(Cited on p. **6, 28**)*

[46] Lars Eriksson, Tobias Lindell, Oskar Leufvén, and Andreas Thomasson. Scalable component-based modeling for optimizing engines with supercharging, e-boost and turbocompound concepts. In *SAE World Congr.*, Techn. Paper 2012-01-0713, 2012. *(Cited on p. **6**)*

[47] Lars Eriksson and Lars Nielsen. *Modeling and control of engines and drivelines*. Vehicular systems, ISY, Linköping Institute of Technology, 2009. *(Cited on p. **32, 41, 45**)*

[48] Lars Eriksson, Lars Nielsen, Jan Brugård, Johan Bergström, Fredrik Pettersson, and Per Andersson. Modeling of a turbocharged SI engine. *Annual Reviews in Control*, 26(1):129–137, 2002. *(Cited on p. **28, 31, 32, 34, 44, 45**)*

[49] Olof Erlandsson. *Thermodynamic Simulation of HCCI Engine Systems*. PhD thesis 989, Department of Heat and Power Engineering, Lund Institute of Technology, 2002. *(Cited on p. **26**)*

[50] Dominic Evans and Andrew Ward. Minimising turbocharger whoosh noise for diesel powertrains. In *SAE World Congr.*, Techn. Paper 2005-01-2485, 2005. *(Cited on p. **24**)*

[51] D.A. Fink, N.A. Cumpsty, and Edward M. Greitzer. Surge dynamics in a free-spool centrifugal compressor system. *J. of Turbomachinery*, 114:321–332, Apr 1992. *(Cited on p. **23, 24, 25**)*

[52] F.B. Fisher. Application of map width enhancement devices to turbocharger compressor stages. In *SAE*, Techn. Paper 880794, 1988. *(Cited on p. **13**)*

[53] Oscar Flärdh and Jonas Mårtensson. Analysis of a quasi-steady extension to the turbine model in mean value engine models. In *SAE World Congr.*, Techn. Paper 2010-01-1191, 2010. *(Cited on p. **27**)*

[54] J. Galindo, F. Arnau, A. Tiseira, R. Lang, H. Lahjaily, and T. Gimenes. Measurement and modeling of compressor surge on engine test bench for different intake line configurations. In

SAE World Congr., Techn. Paper 2011-01-0370, 2011. *(Cited on p. **23, 24, 38**)*

[55] J. Galindo, H. Climent, C. Guardiola, and J. Domenech. Strategies for improving the mode transition in a sequential parallel turbocharged automotive diesel engine. *I.J. of Automotive Technology*, 10(2):141–149, 2009. *(Cited on p. **28**)*

[56] J. Galindo, H. Climent, C. Guardiola, and A. Tiseira. Assessment of a sequantially turbocharged diesel engine on real-life driving cycles. *I.J. of Vehicle Design*, 49(1/2/3):214–234, 2009. *(Cited on p. **4**)*

[57] J. Galindo, J.M. Luján, C. Guardiola, and G.S. Lapuente. A method for data inconsistency checking in compressor and variable-geometry turbine maps. *Proc. of the IMechE, Part D: J. of Automobile Engineering*, 220(3):1465–1473, 2006. *(Cited on p. **11, 14, 23, 27**)*

[58] J. Galindo, J.R. Serrano, H. Climent, and A. Tiseira. Experiments and modelling of surge in small centrifugal compressor for automotive engines. *J. of Experimental Thermal and Fluid Science*, 32(3):818–826, 2008. *(Cited on p. **23, 37, 38, 39**)*

[59] J. Galindo, J.R. Serrano, C. Guardiola, and C. Cervelló. Surge limit definition in a specific test bench for the characterization of automotive turbochargers. *J. of Experimental Thermal and Fluid Science*, 30(5):449–462, 2006. *(Cited on p. **18, 24, 25**)*

[60] J. Galindo, J.R. Serrano, X. Margot, A. Tiseira, N. Schorn, and H. Kindl. Potential of flow pre-whirl at the compressor inlet of automotive engine turbochargers to enlarge surge margin and overcome packaging limitations. *I.J. of Heat and Fluid Flow*, 28(3):374–387, 2007. *(Cited on p. **40, 41**)*

[61] J. Galindo, A. Tiseira, F.J. Arnau, and R. Lang. On-engine measurement of turbocharger surge limit. *Experimental Techniques*, 37(1):47–54, 2013. *(Cited on p. **24, 25**)*

[62] S. García-Nieto, M. Martínez, X. Blasco, and J. Sanchis. Nonlinear predictive control based on local model networks for air management in diesel engines. *Control Engineering Practice*, 16(12):1399–1413, 2008. *(Cited on p. **31**)*

[63] P. Gautier, A. Albrecht, A. Chasse, P. Moulin, A. Pagot, L. Fontvieille, and D. Issartel. A simulation study of the impact of lp egr on a two-stage turbocharged diesel engine. *Oil & Gas Science and Technology - Rev. IFP*, 64(3):361–379, 2009. *(Cited on p. **28**)*

[64] Jan Tommy Gravdahl and Olav Egeland. Speed and surge control for a low order centrifugal compressor model. IEEE Int. Conf. on Control Applications, pages 344–349, 1997. *(Cited on p. **39, 40, 41**)*

[65] Jan Tommy Gravdahl and Olav Egeland. Centrifugal compressor surge and speed control. *IEEE Trans. on Control Systems Technology*, 7(5):567–579, Sept 1999. *(Cited on p. **22, 38, 39, 40, 41**)*

[66] Jan Tommy Gravdahl, Olav Egeland, and Svein Ove Vatland. Active surge control of centrifugal compressors using drive torque. volume 2 of *Proc. IEEE Conf. on Decision and Control*, 2001. *(Cited on p. **38, 44**)*

[67] Jan Tommy Gravdahl, Frank Willems, Bram de Jager, and Olav Egeland. Modeling for surge control of centrifugal compressors: comparison with experiment. In *Proc. IEEE Conf. on Decision and Control*, volume 2, pages 1341–1346, Dec 2000. *(Cited on p. **11, 24, 28, 38, 41**)*

[68] Jan Tommy Gravdahl, Frank Willems, Bram de Jager, and Olav Egeland. Modeling of surge in free-spool centrifugal compressors: experimental validation. *J. of Propulsion and Power*, 20(5):849–857, Sept-Oct 2004. *(Cited on p. **24, 38**)*

[69] Edward M. Greitzer. The stability of pumping systems - The 1980 Freeman Scholar Lecture. *J. of Fluids Engineering*, 103:193–242, 1981. *(Cited on p. **23, 24, 25, 37**)*

[70] Panagiotis Grigoriadis. *Experimentelle Erfassung und Simulation instantionärer Verdichterphänomene bei Turboladern von Fahrzeugmotoren.* PhD thesis, Technischen Universität Berlin, 2008. *(Cited on p. **22, 24, 25, 38**)*

[71] Fahua Gu, Abraham Engeda, Mike Cave, and Jean-Luc Di Liberti. A numerical investigation on the volute/diffuser interaction due to the axial distortion at the impeller exit. *J. of Fluids Engineering*, 123(3):475–483, 2001. *(Cited on p. **29**)*

[72] L. Guzzella and A. Amstutz. Control of diesel engines. *Control Systems Magazine, IEEE*, 18(5):53–71, Oct 1998. *(Cited on p. **32, 33, 34, 44, 45, 48**)*

[73] K. E. Hansen, P. Jørgensen, and P. S. Larsen. Experimental and theoretical study of surge in a small centrifugal compressor. *J. of Fluids Engineering*, 103:391–395, 1981. *(Cited on p. **23, 24, 38, 43**)*

[74] Fredrik Hellström. *Numerical computations of the unsteady flow in turbochargers*. PhD thesis, KTH, Fluid Physics, 2010. *(Cited on p. **25, 29, 41**)*

[75] Elbert Hendricks. A compact, comprehensive model of a large turbocharged, two-stroke diesel engine. Techn. Paper 861190, 1986. *(Cited on p. **28**)*

[76] Elbert Hendricks. Isothermal vs. adiabatic mean value SI engine models. In *3rd IFAC Workshop, Advances in Automotive Control, Preprints, Karlsruhe, Germany*, pages 373–378, March 2001. *(Cited on p. **28**)*

[77] F. Herbst, C.-P. Stöber-Schmidt, P. Eilts, T. Sextro, J. Kammeyer, C. Natkaniec, J. Seume, D. Porzig, and H. Schwarze. The potential of variable compressor geometry for highly boosted gasoline engines. In *SAE World Congr.*, Techn. Paper 2011-01-0376, 2011. *(Cited on p. **17**)*

[78] John B. Heywood. *Internal Combustion Engine Fundamentals*. McGraw-Hill series in mechanical engineering. McGraw-Hill, 1988. *(Cited on p. **3, 30**)*

[79] Hermann Hiereth and Peter Prenninger. *Charging the Internal Combustion Engine*. Springer Wien NewYork, 2007. *(Cited on p. **10, 12, 13, 14, 26, 30, 39**)*

[80] Ulrich Hopmann and Marcelo C. Algrain. Diesel engine electric turbo compound technology. In *SAE World Congr.*, Techn. Paper 2003-01-2294, 2003. *(Cited on p. **13**)*

[81] Xiao Hu and Patrik B. Lawless. Predictions of on-engine efficiency for the radial turbine of a pulse turbocharged engine. In *SAE World Congr.*, Techn. Paper 2001-01-1238, 2001. *(Cited on p. **27**)*

[82] K.A.R. Ismail, C.V.A.G. Rosolen, F.J. Benevenuto, and D. Lucato. Small radial compressors: Aerodynamic design and analysis. *I.J. of Rotating Machinery*, pages 189–200, 1998. *(Cited on p. **12, 41**)*

[83] J.-P. Jensen, A.F. Kristensen, S.C. Sorenson, N. Houbak, and E. Hendricks. Mean value modeling of a small turbocharged diesel engine. In *SAE World Congr.*, Techn. Paper 910070, Feb 1991. *(Cited on p. **28, 31, 32, 43, 45**)*

[84] Wei Jiang, Jamil Khan, and Roger A. Dougal. Dynamic centrifugal compressor model for system simulation. *J. of Power Sources*, 158(2):1333–1343, 2006. *(Cited on p. **41, 42**)*

[85] Merten Jung. *Mean-Value Modelling and Robust Control of the Airpath of a Turbocharged Diesel Engine*. PhD thesis, Sidney Sussex College, Department of Engineering, University of Cambridge, 2003. *(Cited on p. **18, 27, 28**)*

[86] Merten Jung, Richard G. Ford, Keith Glover, Nick Collings, Urs Christen, and Michael J. Watts. Parametrization and transient validation of a variable geometry turbocharger for mean-value modeling at low and medium speed-load points. In *Powertrain and Fluid Systems, Conference and Exhibition*, Techn. Paper 2002-01-2729, San Diego, California, USA, October 2002. *(Cited on p. **16, 18**)*

[87] N. Karamanis and R.F. Martinez-Botas. Mixed-flow turbines for automotive turbochargers: steady and unsteady performance. *I.J. of Engine Research*, 3(3):127–138, 2002. *(Cited on p. **27, 28**)*

[88] Y. Kim, A. Engeda, R. Aungier, and G. Direnzi. The influence of inlet flow distortion on the performance of a centrifugal compressor and the development of an improved inlet using numerical simulations. *Proc. of the IMechE, Part D: J. of Automobile Engineering*, 215, 2001. *(Cited on p. **22, 24**)*

[89] P. A. Konstantinidis, G. C. Koltsakis, and A. M. Stamatelos. Transient heat transfer modelling in automotive exhaust systems. *Proc. of the IMechE, Part C: J. of Mechanical Engineering, Science*, 211(1), 1997. *(Cited on p. **15**)*

[90] Eric Krivitzky and Louis Larosiliere. Aero design challenges in wide-operability turbocharger centrifugal compressors. In *SAE World Congr.*, Techn. Paper 2012-01-0710, 2012. *(Cited on p. **23, 41**)*

[91] Thierry Lamquin and Kostandin Gjika. Power losses identification on turbocharger hydrodynamic bearing systems: test and prediction. In *Proc. of ASME Turbo Expo*, GT2009-59599, June 2009. *(Cited on p. **17**)*

[92] Per-Inge Larsson, Fredrik Westin, Johannes Andersen, Joachim Vetter, and Alberto Zumeta. Efficient turbo charger testing. *MTZ*, 70(07-08):16–21, 2009. *(Cited on p. **56**)*

[93] B. Lee, Z. Filipi, D. Assanis, and D. Jung. Simulation-based assessment of various dual-stage boosting systems in terms of performance and fuel economy improvements. In *SAE World Congr.*, Techn. Paper 2009-01-1471, 2009. *(Cited on p. **4**)*

[94] Oskar Leufvén. Compressor modeling for control of automotive two stage turbocharg-

ers. Licenciate thesis, Division of Vehicular Systems, Department of Electrical Engineering, Linköping University, 2010. LiU-TEK-LIC-2010:32, Thesis No. 1463. *(Cited on p. **7**)*

[95] Oskar Leufvén and Lars Eriksson. Time to surge concept and surge control for acceleration performance. In *Proc. of IFAC World Congr.*, pages 2063–2068, 2008. *(Cited on p. **5**)*

[96] Oskar Leufvén and Lars Eriksson. Engine test bench turbo mapping. In *SAE World Congr.*, Techn. Paper 2010-01-1232, 2010. *(Cited on p. **5**)*

[97] Oskar Leufvén and Lars Eriksson. Surge and choke capable compressor model. In *Proc. of IFAC World Congr.*, pages 10653–10658, 2011. *(Cited on p. **5, 6**)*

[98] Oskar Leufvén and Lars Eriksson. Investigation of compressor correction quantities for automotive applications. *I.J. of Engine Research*, 13(6):588–606, December 2012. *(Cited on p. **5**)*

[99] Oskar Leufvén and Lars Eriksson. Measurement, analysis and modeling of centrifugal compressor flow for low pressure ratios. *Submitted to I.J. of Engine Research*, Under review. *(Cited on p. **6**)*

[100] Oskar Leufvén and Lars Eriksson. A surge and choke capable compressor flow model - validation and extrapolation capability. *Submitted to Control Engineering Practice*, Under review. *(Cited on p. **5**)*

[101] R. I. Lewis. *Turbomachinery Performance Analysis*. Arnold, 1996. *(Cited on p. **10, 18, 41**)*

[102] Per Erik Lindahl and William Sandqvist. *Mätgivare, mätning av mekaniska storheter och temperatur*. Studentlitteratur, 1996. *(Cited on p. **49**)*

[103] J. Macek, O. Vitek, and Z. Zak. Calibration and results of a radial turbine 1-D model with distributed parameters. In *SAE World Congr.*, Techn. Paper 2011-01-1146, 2011. *(Cited on p. **17, 29**)*

[104] J. Macek and O. Vítek. Simulation of pulsating flow unsteady operation of a turbocharger radial turbine. In *SAE World Congr.*, Techn. Paper 2008-01-0295, 2008. *(Cited on p. **15, 27**)*

[105] V. Macián, J. M. Luján, V. Bermúdez, and C. Guardiola. Exhaust pressure pulsation observation from turbocharger instantaneous speed measurement. *Measurement, Science and Technology*, 15(6):1185–1194, June 2004. *(Cited on p. **28**)*

[106] Silvia Marelli, Chiara Carraro, and Massimo Capobianco. Effect of pulsating flow characteristics on performance and surge limit of automotive turbocharger compressors. *SAE I.J. of Engines*, 5:596–601, 2012. *(Cited on p. **24, 25**)*

[107] Guillaume Martin, Vincent Talon, Pascal Higelin, Alain Charlet, and Christian Caillol. Implementing turbomachinery physics into data map-based turbocharger models. *SAE I.J. of Engines*, 2(1):211–229, 2009. *(Cited on p. **14, 22, 43, 45**)*

[108] J.R. McBride, P.W. Husak, J.A. Lockwood, and K.E. Nietering. High frequency measurements of pressure and temperature fluctuations in an automotive exhaust system during steady state and transient driving conditions. In *SAE World Congr.*, Techn. Paper 2001-01-0227, 2001. *(Cited on p. **27**)*

[109] Shishir Menon, Anthony Furman, and Michael Krok. Detection of surge precursors in locomotive turbocharger. In *Industrial Technology, 2006. ICIT 2006. IEEE International Conference on*, pages 3067–3071, Dec 2006. *(Cited on p. **18**)*

[110] R.B. Montgomery. Viscosity and thermal conductivity of air and diffusivity of water vapor in air. *J. of Meteorology*, 4:193–196, Dec 1947. *(Cited on p. **17**)*

[111] F.K. Moore and E.M. Greitzer. A theory of post-stall transients in axial compression systems: Part i - development of equations. *Trans. of ASME, J. of Engineering for Gas Turbines and Power*, (108):68–76, 1986. *(Cited on p. **37, 42**)*

[112] P. Moraal and I. Kolmanovsky. Turbocharger modeling for automotive control applications. In *SAE World Congr.*, Techn. Paper 1999-01-0908, March 1999. *(Cited on p. **16, 27, 31, 32, 44**)*

[113] Sayyed Mostafa Motavalli, Ali Hajilouy-Benisi, and Mahdi Nili-Ahmadabadi. Experimental and theoretical investigation of centrifugal compressor performance characteristics. In *Proc. of ASME Turbo Expo*, GT2008-50939, June 2008. *(Cited on p. **41**)*

[114] Matthias Mrosek and Rolf Isermann. On the parametrisation of turbocharger power and heat transfer models. In *IFAC AAC*, 2010. *(Cited on p. **15, 17, 33, 35**)*

[115] Matthias Mrosek, Sebastian Zahn, and Rolf Isermann. Parameter estimation for physical

based air path models of turbocharged diesel engines – an experience based guidance. *SAE I.J. of Engines*, 2(2):570–583, 2009. *(Cited on p. **51**)*

[116] M. Müller, S. Sumser, P. Fledersbacher, K. Rößler, K. Fieweger, and H.J. Bauer. Using the centrifugal compressor as a cold-air turbine. In *Int. conf. on turbochargers and turbocharging*, London, 2005. *(Cited on p. **26, 39**)*

[117] Martin Müller, Elbert Hendricks, and Spencer C. Sorenson. Mean value modelling of turbocharged spark ignition engines. In *SAE World Congr.*, Techn. Paper 980784, Detroit, USA, 1998. *(Cited on p. **40, 43**)*

[118] J. Nitta, A. Minato, and N. Shimazaki. Performance evaluation of three-stage turbocharging system for heavy-duty diesel engine. In *SAE World Congr.*, Techn. Paper 2011-01-0374, 2011. *(Cited on p. **28**)*

[119] Mattias Nyberg and Thomas Stutte. Model based diagnosis of the air path of an automotive diesel engine. *Control Engineering Practice*, 12(5):513–525, 2004. *(Cited on p. **28**)*

[120] W. Oakes, P. Lawless, and S. Fleeter. High-speed centrifugal compressor instabilities during speed transients. *J. of Aerospace Engineering*, 17(3):106–112, 2004. *(Cited on p. **25**)*

[121] Jan-Ola Olsson. Boost limitation in a torque based engine management system. In *IFAC Symposium*, Advances in Automotive Control, pages 609–616, 2007. *(Cited on p. **28**)*

[122] Rabih Omran, Rafic Younes, and Jean-Claude Champoussin. Optimal control of a variable geometry turbocharged diesel engine using neural networks: Applications on the ETC test cycle. *IEEE Trans. on Control Systems Technology*, 17(2):380–393, March 2009. *(Cited on p. **31, 33, 43, 46**)*

[123] J. Panting, K.R. Pullen, and R.F. Martinez-Botas. Turbocharger motor-generator for improvement of transient performance in an internal combustion engine. *Proc. of the IMechE, Part D: J. of Automobile Engineering*, 215:369–383, 2001. *(Cited on p. **15, 27**)*

[124] F. Payri, J. Galindo, H. Climent, and C. Guardiola. Measurement of the oil consumption of an automotive turbocharger. *Experimental Techniques*, 29(5):25–27, 2005. *(Cited on p. **15**)*

[125] Pentronic. Pentronics temperaturhandbok 1, 1997. *(Cited on p. **51**)*

[126] Alexandros Plianos and Richard Stobart. Modeling and control of diesel engines equipped with a two-stage turbo-system. In *SAE World Congr.*, Techn. Paper 2008-01-1018, 2008. *(Cited on p. **32, 43, 45**)*

[127] Helmut Pucher, Torsten Eggert, and Björn Schenk. Experimentelle Entwicklungswerkzeuge für Turbolader von Fahrzeugmotoren. 6. Aufladetechnische Konferenz, Dresden, pages 227–240, Oct 1997. *(Cited on p. **38**)*

[128] Xuwen Qiu, Dave Japikse, Jinhui Zhao, and Mark R. Anderson. Analysis and validation of a unified slip factor model for impellers at design and off-design conditions. In *GT2010-22164*, Proc. of ASME Turbo Expo, June 2010. *(Cited on p. **41**)*

[129] C.D. Rakopoulos, C.N. Michos, and E.G. Giakoumis. Study of the transient behavior of turbocharged diesel engines including compressor surging using a linearized quasi-steady analysis. In *SAE World Congr. Modeling of SI and Diesel Engine 2005 (SP-1969)*, Techn. Paper 2005-01-0225, 2005. *(Cited on p. **23, 38, 43, 45**)*

[130] K.G. Rochford. Series turbocharging - a requirement for high specific output, vehicular diesel engines. In *SAE*, Techn. Paper 790067, 1979. *(Cited on p. **11**)*

[131] Alessandro Romagnoli and Richard Martinez-Botaz. Heat transfer on a turbocharger under constant load points. In *Proc. of ASME Turbo Expo*, GT2009-59618, June 2009. *(Cited on p. **17**)*

[132] J.A. Röth and L. Guzzella. Modelling engine and exhaust temperatures of a mono-fuelled turbocharged compressed-natural-gas engine during warm-up. *Proc. of the IMechE, Part D: J. of Automobile Engineering*, 224(1), 2010. *(Cited on p. **15**)*

[133] SAE standard. J1826 – Turbocharger Gas Stand Test Code, 1995. *(Cited on p. **18**)*

[134] SAE standard. J922 – Turbocharger Nomenclature and Terminology, 1995. *(Cited on p. **18**)*

[135] J.Vicente Salcedo, Emanuele Pieroni, Emilio Pérez, Xavier Blasco, Miguel Martínez, and J. Vicente García. Real-time control and simulation of a non-linear model for air management in a turbocharged diesel engine. In *FISITA World Automotive Congress*, F2004-F373, 2004. *(Cited on p. **31**)*

[136] T. Sato, J. M. Oh, and A. Engeda. Experimental and numerical investigation of the flow in a vaneless diffuser of a centrifugal compressor stage. part 1: Experimental investigation. *Proc. of the IMechE, Part C: J. of Mechanical Engineering, Science*, 219(10), Sept 2005. *(Cited*

on p. ***41)***

[137] S. Schmitt, W. Schmid, G. Hertweck, and M. Schlegl. Hochpräzise Messungen der Reibleistungen von Abgasturboladern. In *Supercharging Conference, Dresden Germany*, pages 185–206, 2007. *(Cited on p.* ***14, 17, 33****)*

[138] Marc Sens, Jonas Nickel, Panagiotis Grigoriadis, and Helmut Pucher. Influence of sensors and measurement system configuration on mapping and the use of turbochargers in the vehicle. In *SAE World Congr.*, Techn. Paper 2006-01-3391, Detroit, USA, March 2006. *(Cited on p.* ***18, 22****)*

[139] Rodolphe Sepulchre and Petar Kokotovic. Shape signifiers for control of a low-order compressor model. *Automatic Control, IEEE Trans. on*, 43(11):1643–1648, Nov 1998. *(Cited on p.* ***43****)*

[140] J.R. Serrano, F.J. Arnau, V. Dolz, A. Tiseira, and C. Cervelló. A model of turbocharger radial turbines appropriate to be used in zero- and one-dimensional gas dynamics codes for internal combustion engines modelling. *I.J. of Energy Conversion and Management*, 49(12):3729–3745, 2008. *(Cited on p.* ***27, 30****)*

[141] J.R. Serrano, V. Dolz, A. Tisiera, and A. Páez. Influence of environmental conditions and thermodynamic considerations in the calculation of turbochargers efficiency. In *SAE World Congr.*, Techn. Paper 2009-01-1468, 2009. *(Cited on p.* ***17****)*

[142] J.R. Serrano, C. Guardiola, V. Dolz, A. Tiseira, and C. Cervelló. Experimental study of the turbine inlet gas temperature influence on turbocharger performance. In *SAE World Congr.*, Techn. Paper 2007-01-1559, Detroit, USA, 2007. *(Cited on p.* ***16****)*

[143] J.R. Serrano, B. Tormos, K.L. Gargar, and F. Bouffaud. Study of the effects on turbocharger performance generated by the presence of foreign objects at the compressor intake. *Experimental Techniques*, pages no–no, 2011. *(Cited on p.* ***22****)*

[144] S. Shaaban and J. Seume. Impact of turbocharger non-adibatic operation on engine volumetric efficency and turbo lag. *I.J. of Rotating Machinery*, 5, 2012. *(Cited on p.* ***15****)*

[145] Sameh Shaaban. *Experimental Investigation and Extended Simulation of Turbocharger Non-adiabatic Performance*. PhD thesis, Leibniz Universität Hannover, 2004. *(Cited on p.* ***11, 16, 21, 26, 27, 31, 39****)*

[146] Raef S. Shehata, Hussein A. Abdullah, and Fayez F.G. Areed. Variable structure surge control for constant speed centrifugal compressors. *Control Engineering Practice*, 17(7):815–833, 2009. *(Cited on p.* ***43****)*

[147] A. Sidorow, R. Isermann, F. Cianflone, and G. Landsmann. Model based fault detection of the air and exhaust path of diesel engines including turbocharger models. In *SAE World Congr.*, Techn. Paper 2011-01-0700, 2011. *(Cited on p.* ***15, 17, 18****)*

[148] C. H. Sieverding, T. Arts, R. Dénos, and J.-F. Brouckaert. Measurement techniques for unsteady flows in turbomachines. *Experiments in Fluids*, 28:285–321, 2000. *(Cited on p.* ***49****)*

[149] J.S. Simon, L. Valavani, A.H. Epstein, and Edward M. Greitzer. Evaluation of approaches to active compressor surge stabilization. *J. of Turbomachinery*, 115:57–67, Jan 1993. *(Cited on p.* ***23****)*

[150] Borislav Sirakov and Michael Casey. Evaluation of heat transfer effects on turbocharger performance. In *Proc. of ASME Turbo Expo*, GT2011-45887, June 2011. *(Cited on p.* ***16****)*

[151] Subenuka Sivagnanasundaram, Stephen Spence, Juliana Early, and Bahram Nikpour. An investigation of compressor map width enhancement and a detailed analysis of inducer flow field. *The Hong Kong Institution of Engineers Transaction*, 17(4):23–30, 2010. *(Cited on p.* ***13****)*

[152] A.A. Sokolov and S.T. Glad. Identifiability of turbocharged IC engine models. In *SAE World Congr.*, Techn. Paper 1999-01-0216, March 1999. *(Cited on p.* ***30, 45****)*

[153] Richard Stone. *Introduction to Internal Combistion Engines*. MacMillan London, 2nd edition, 1992. *(Cited on p.* ***3****)*

[154] Jan F. Suhrmann, Dieter Peitsch, Marc Gugau, Tom Heuer, and Uwe Tomm. Validation and development of loss models for small size radial turbines. In *GT2010-22666*, Proc. of ASME Turbo Expo, June 2010. *(Cited on p.* ***14, 30****)*

[155] E. Swain. Diesel engine transient performance prediction during sequential turbocharging operations. *Proc. of the IMechE, Part C: J. of Mechanical Engineering, Science*, pages 123–131, 1993. *(Cited on p.* ***31, 32****)*

[156] E. Swain. Improving a one-dimensional centrifugal compressor performance prediction method. *Proc. of the IMechE, Part A: J. of Power and Energy*, 219, 2005. *(Cited on p. **39**)*

[157] S. Szymko, N. R. McGlashan, R. Martinez-Botas, and K. R. Pullen. The development of a dynamometer for torque measurement of automotive turbocharger turbines. *Proc. of the IMechE, Part D: J. of Automobile Engineering*, 221(2):225–239, 2007. *(Cited on p. **22**)*

[158] M. Tancrez, J. Galindo, C. Guardiola, P. Fajardo, and O. Varnier. Turbine adapted maps for turbocharger engine matching. *J. of Experimental Thermal and Fluid Science*, 35(1):146–153, 2011. *(Cited on p. **31**)*

[159] X. Tauzia, J.F. Hetet, P. Chesse, G. Grosshans, and L. Mouillard. Computer aided study of the transient performances of a highly rated sequentially turbocharged marine diesel engine. *Proc. of the IMechE, Part A: J. of Power and Energy*, 212:185–196, 1998. *(Cited on p. **39**)*

[160] Edward S. Taylor. *Dimensional analysis for engineers*. Clarendon Press, Oxford, 1974. *(Cited on p. **18**)*

[161] G. Theotokatos and N.P. Kyrtatos. Diesel engine transient operation with turbocharger compressor surging. In *SAE World Congr.*, Techn. Paper 2001-01-1241, 2001. *(Cited on p. **38**)*

[162] Andreas Thomasson and Lars Eriksson. Model-based throttle control using static compensators and IMC based PID-design. In *IFAC ECOSM*, 2009. *(Cited on p. **28**)*

[163] Andreas Thomasson and Lars Eriksson. Modeling and control of co-surge in bi-turbo engines. In *Proc. of IFAC World Congr.*, pages 13010–13015, 2011. *(Cited on p. **39, 44**)*

[164] Andreas Thomasson, Lars Eriksson, Oskar Leufvén, and Per Andersson. Wastegate actuator modeling and model-based boost pressure control. In *IFAC ECOSM*, pages 87–94, 2009. *(Cited on p. **7, 28**)*

[165] Andreas Thomasson, Oskar Leufvén, Ivan Criscuolo, and Lars Eriksson. Modeling and validation of a boost pressure actuation system, for a series sequentially turbocharged SI engine. *Control Engineering Practice*, Accepted for publication, 2013. *(Cited on p. **6, 28**)*

[166] A.J. Torregrosa, J.R. Serrano, and J.A. Dopazo. Experiments on wave transmission and reflection by turbochargers in engine operating conditions. In *SAE World Congr.*, Techn. Paper 2006-01-0022, Detroit, USA, March 2006. *(Cited on p. **24**)*

[167] Johan Wahlström. *Control of EGR and VGT for Emission Control and Pumping Work Minimization in Diesel Engines*. PhD thesis, Linköping university, 2009. *(Cited on p. **28**)*

[168] Johan Wahlström and Lars Eriksson. Modelling diesel engines with a variable-geometry turbocharger and exhaust gas recirculation by optimization of model parameters for capturing non-linear system dynamics. *Proc. of the IMechE, Part D: J. of Automobile Engineering*, 225(7):960–986, 2011. *(Cited on p. **31, 44, 45**)*

[169] A.J. Ward-Smith. Critical flowmetering: The characteristics of cylindrical nozzles with sharp upstream edges. *I.J. of Heat and Fluid Flow*, 1(3):123–132, 1979. *(Cited on p. **30**)*

[170] N. Watson and M.S. Janota. *Turbocharging the internal combustion engine*. MacMillan London, 1982. *(Cited on p. **3, 4, 10, 11, 12, 13, 14, 15, 17, 22, 26, 27, 30, 32, 39, 40, 41**)*

[171] M.H. Westbrook and J.D. Turner. *Automotive sensors*. IOP Publishing, 1994. *(Cited on p. **49**)*

[172] Fredrik Westin. Accuracy of turbocharged SI-engine simulations. Licentiate thesis, Internal Combustion Engines, Department of Machine Design, Royal Institute of Technology, Stockholm, Sweden, 2002. *(Cited on p. **17, 26, 33**)*

[173] Fredrik Westin and Ragnar Burenius. Measurement of interstage losses of a twostage turbocharger system in a turbocharger test rig. In *SAE World Congr.*, Techn. Paper 2010-01-1221, 2010. *(Cited on p. **13, 24, 56**)*

[174] F.M White. *Fluid Mechanics*. McGraw-Hill, 2005. *(Cited on p. **18, 41**)*

[175] Frank Willems. Modeling and control of compressor flow instabilities. Report no. wfw 96.151, Faculty of Mechanical Engineering, Control Engineering Section, Eindhoven University of Technology, 1997. *(Cited on p. **11, 23, 25, 38**)*

[176] Frank Willems and Bram de Jager. Modeling and control of compressor flow instabilities. *Control Systems, IEEE*, 19(5):8–18, Oct 1999. *(Cited on p. **22, 23, 38**)*

[177] J. E. Ffowcs Williams and X. Y. Huang. Active stabilization of compressor surge. *Journal of Fluid Mechanics*, 204:245–262, 6 1989. *(Cited on p. **23, 43**)*

[178] D.E. Winterbone and R.J. Pearson. Turbocharger turbine performance under unsteady flow - a review of experimental results and proposed models. *Proc. of the IMechE, Part C: J. of Mechanical Engineering, Science*, pages 193–206, 1998. *(Cited on p. **27**)*

[179] A.M Wo and J.P. Bons. Flow physics leading to sytsem instability in a centrifugal pump. *J. of Turbomachinery*, 116:612–620, Oct 1994. *(Cited on p. **23**)*

[180] M. Yang, X Zheng, Y. Zhang, and Z Li. Improved performance model of turbocharger centrifugal compressor. In *Proc. of ASME Turbo Expo*, GT2008-50009, June 2008. *(Cited on p. **26, 42**)*

[181] Donghui Zhang, Jean-Luc Di Liberti, and Michael Cave. Blade thickness effect on impeller slip factor. In *Proc. of ASME Turbo Expo*, GT2010-22164, June 2010. *(Cited on p. **29**)*

[182] Zhe Zhang, Kangyao Deng, Zhenbiao Wang, and Xiangguo Zhu. Experimental study on the three-phase sequential turbocharging system with two unequal size turbochargers. *SAE I.J. of Fuels and Lubricants*, 1:1181–1186, 2008. *(Cited on p. **28**)*

[183] Karl Zinner. *Aufladung von Verbrennungsmotoren. Grundlagen, Berechnungen, Ausführungen*. Springer Verlag, 1985. *(Cited on p. **4, 10, 11**)*

Papers

Paper 1

1

Time to surge concept and surge control for acceleration performance†

Oskar Leufven and Lars Eriksson

Vehicular Systems, Department of Electrical Engineering, Linköping University, S-581 83 Linköping, Sweden.

Abstract

Surge is a dangerous instability that can occur in compressors. It is avoided using a valve that reduces the compressor pressure. The control of this valve is important for the compressor safety but it also has a direct influence on the acceleration performance.

Compressor surge control is investigated by first studying the surge phenomenon in detail. Experimental data from a dynamic compressor flow test bench and surge cycles measured on an engine is used to tune and validate a model capable of describing surge. A concept named *time to surge* is introduced and a sensitivity analysis is performed to isolate the important characteristics that influence surge transients in an engine. It is pointed out that the controller clearly benefits from a feed-forward term due to the small time frames associated with the transition to surge. In the next step this knowledge is used in the design of a novel surge controller. This surge controller is then compared to two other controllers and it is shown that it avoids surge and improves the acceleration performance by delivering both higher engine torque and turbo shaft speed after a gear change.

†This is a formatted version of "Time to surge concept and surge control for acceleration performance" by Oskar Leufven and Lars Eriksson, IFAC World Congress 2008, Seoul, Korea. The original version was published in ifac-papersonline.net, `http://ifac-papersonline.net`, doi: `10.3182/20080706-5-KR-1001.00350`. The formatting is restricted to changing the article into a single-column format, adjusting sizes of figures and tables, and adjusting the referencing style.

1 Introduction

From being used exclusively in sports and performance cars, turbochargers are now common even in ordinary family cars. Ever increasing fuel prices and focus on the environment have moved the automotive industry from using large bigbore engines to using the advantages of downsized and turbocharged engines instead [1].

An important component in the turbocharger is the compressor as it influences the engine power and thus acceleration performance. In the compressor a dangerous instability phenomenon called surge can occur. It is a small time frame phenomenon caused by the relatively slow dynamics of the turbo shaft. If an automotive turbocharger is driven in deep surge cycles for too long the turbo charger will break down. An effective fail safe method for avoiding surge using a surge valve is implemented in today's production cars. However, in order to ensure safety in all cases, this method wastes much of the valuable pressurized air and turbo shaft speed. Surge control is most important during a gear change since the compressor pressure directly influences the torque available when the new gear is engaged.

The approach is to use experimental surge data from both a compressor surge test stand and an engine test bench to build and validate a compressor and engine model that can describe surge. Then a sensitivity analysis is performed to investigate what properties are most important when considering the time to reach surge and then it is studied what can be done to increase the engine acceleration performance through surge valve control. Based on the knowledge gained from the surge investigation a novel control structure for surge control is developed. One important part is the feedforward term, motivated by the short time frames associated with surge control. The developed controller is then compared to two other controllers.

2 Modeling

To investigate surge and different control strategies a surge capable compressor model has been developed. It is implemented as part of a Mean Value Engine Model (MVEM) [2] of a turbocharged Spark Ignited (SI) engine in Simulink. The model structure is component based using restrictions (air filter, compressor, intercooler, throttle, engine, turbine, exhaust system) interconnected with control volumes, and further extended with surge and wastegate valves. Component based MVEM of turbocharged engines is outlined in [3] and [4] while the implemented model is developed and validated in [5]. The generel structure of the model is shown in Fig. 1 and the states and notation used is given in the appendix. There are in all 14 states; six pairs of control volume pressures and temperatures, shaft speed and, for the surge capability, compressor mass flow.

2.1 Surge region modeling

The original MVEM has been extended to handle surge [6, 7]. The extension utilizes the model by Moore-Greitzer [8, 4] and introduces a compressor mass

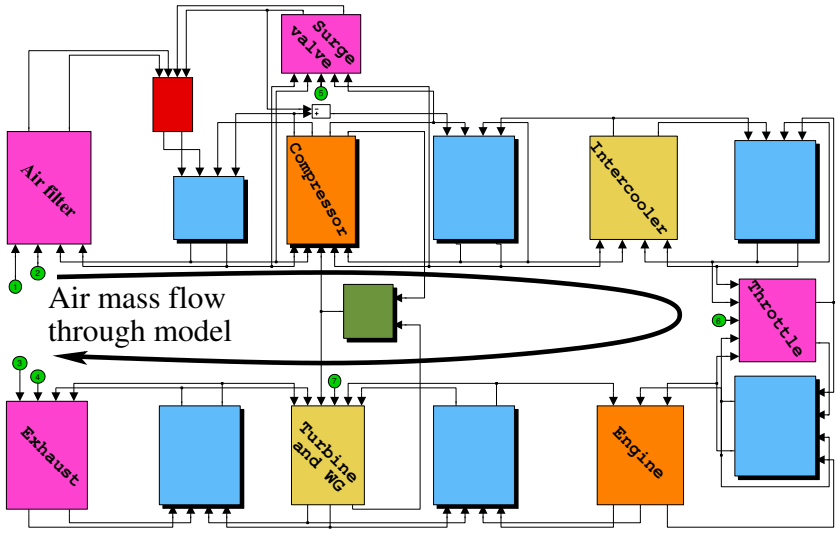

Figure 1: Engine model with a surge capable compressor model. The mass flow path starts in the air filter (upper left corner) and continues through the compressor, intercooler, throttle, intake manifold, cylinder(s), exhaust manifold, turbine to the exhaust system (lower left corner). These different components are interconnected with control volumes. The turbocharger shaft is seen between the compressor and the turbine. The model also contains a wastegate and a surge valve.

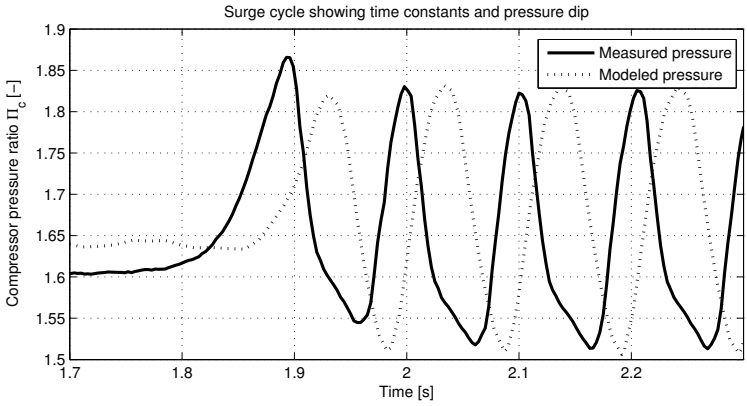

Figure 2: Measured (solid) and modeled (dashed) surge cycle pressures. The figure shows that the compressor model captures both the surge cycle time as well as pressure dynamics during surge as the measurements.

flow state, given by

$$\frac{dW_c}{dt} = \frac{\pi D_c^2}{4L_c} \cdot (\hat{p}_c - p_c) \tag{1}$$

Here $\hat{p}_c = \hat{p}_c(T_{af}, p_{af}, p_c, \omega_{tc}, W_c)$ describes the compressor pressure build up using the parameterized Ellipse model developed in [6] which handles both forward as well as backward (surging) compressor mass flows. Methods for determining and tuning the parameters of the surge capable compressor model are also described in [6].

2.2 Surge region validation

To ensure that the model captures real surge phenomena the implemented compressor model is validated against measured data. Validation data from both a separate compressor surge test stand and surge measurements on a real engine are used. The surge test stand validation is shown in Fig. 2. It is shown that the surge cycle time and compressor pressure ratio behavior during surge is well described by the model. The full MVEM is validated in Fig. 3 with respect to compressor pressure ratio and turbo shaft speed variations for a rapid throttle closing transient. The validations show that the model gives good description of surge properties, which will be important for the control development, in particular: where surge starts, cycle times, pressure fluctuations and also turbo shaft speed changes.

3 Time to surge – TTS

As a first step in the controller design the requirements are investigated. The surge phenomenon is very fast and thus puts stringent requirements on the nec-

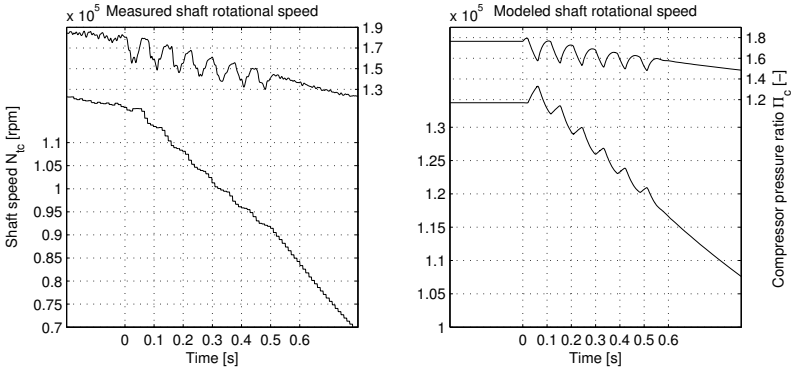

Figure 3: Turbo shaft speed and pressure variations for a rapid throttle closing transient. Left–measured, right–modeled for an operating point close to measured data. It is seen that the turbo shaft speed does not change much from the surge initiation until the compressor has entered the first surge cycle, which motivates the assumption that the shaft dynamics can be neglected when TTS is investigated.

essary controller reaction time. To facilitate an analysis of this requirement a concept called *Time To Surge* (TTS) is introduced. TTS describes how long time it takes for the compressor to enter surge for every operating point in the compressor map, thus showing the needed response time of the control system. Measured compressor pressure from two fast throttle closings are plotted together with the throttle area reference signal in Fig. 4. It is seen that the throttle closing is not instantaneous and that the TTS is slightly larger than 0.1s.

The most common cause for surge in an automotive turbocharged engine is a fast throttle closing, e.g. associated with a gear change. Therefore the calculation of TTS is based on the following scenario: the compressor starts in an initial operating point, then there is a sudden drop in throttle mass flow which will lead the compressor into surge. The compressor is said to enter surge when the compressor mass flow equals the surge mass flow for the current shaft speed. The surge mass flow is given by the compressor map and the line formed by the surge mass flows for all shaft speeds is called the surge line, SL.

TTS depends on many system properties and to study what is most important a sequence of increasingly complex systems are studied in the following sections.

3.1 System 1: Instantaneously zero throttle mass flow

In the first system both the intercooler restriction and temperature differences/dynamics are neglected. Furthermore the turbo shaft speed is assumed constant, due to the small time frames of the surge phenomenon compared to the turbo shaft dynamics (see Fig. 3). The conditions in the air filter control

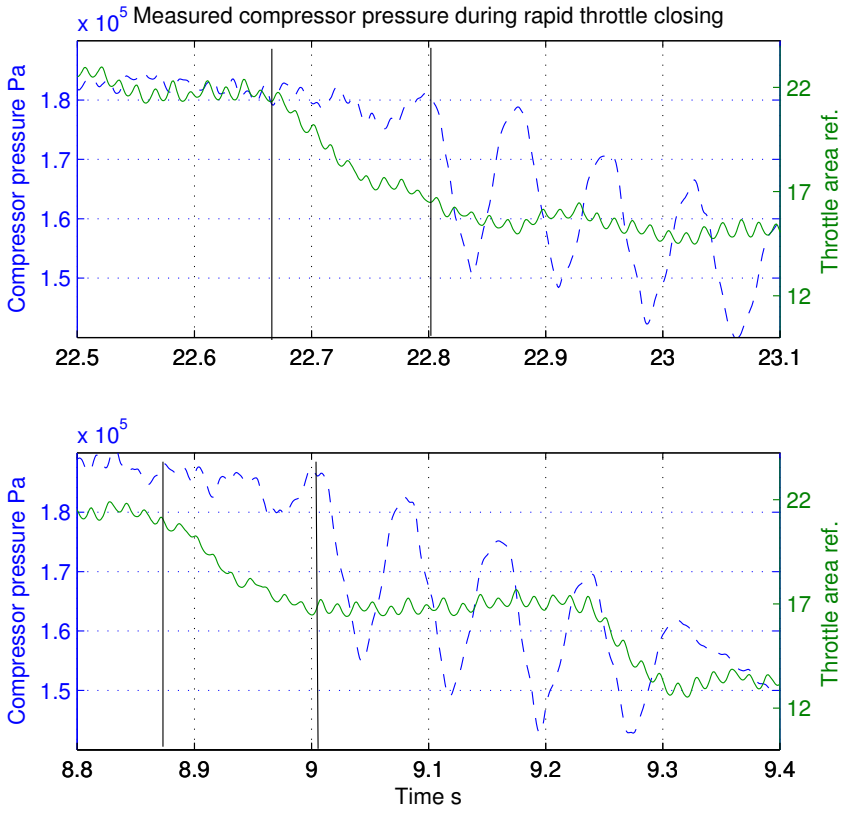

Figure 4: Pressure measured after the compressor (dashed) from two fast throttle closings are plotted together with the throttle area reference signal (solid). Lines are also shown to emphasize where the step is applied and where the compressor starts surging. For both these finite closing speed transients TTS is about 0.1s. The measured signals are filtered offline using a low pass filter with zero phase shift.

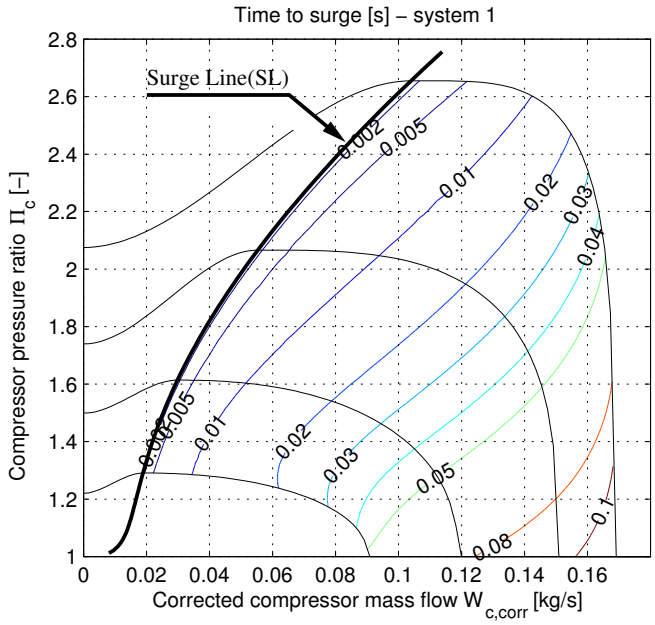

Figure 5: TTS for system 1. The approach assumes an instantaneous stop in throttle mass flow and underestimates the TTS, showing a worst case scenario.

volume (p_{af}, T_{af}) are also kept constant. Finally it is assumed that the throttle mass flow immediately goes to zero in the transient. The differential equations for this simple system now become

$$\frac{dp}{dt} = \frac{RT}{V}(W_c - W_{th}) \tag{2a}$$

$$\frac{dW_c}{dt} = \frac{\pi D_c^2}{4L_c}(\hat{p}_c - p_c) \tag{2b}$$

$$W_{th} = 0 \qquad \text{for } t > t_{init} \tag{2c}$$

where the assumption of an isothermal model, [9], for the lumped control volume is used. A normal temperature increase of 80K over the compressor is assumed as well as a constant control volume temperature before the compressor of 290K. The resulting TTS from this approach is shown in Fig. 5. The figure shows a worst case, smallest time, originating from a throttle mass flow instantaneously going from $W_{c,init}$ to 0. Even for large mass flows far away from the SL, the time is rather small and a feedback control system thus has to be fast and combined with fast actuators to be able to avoid surge.

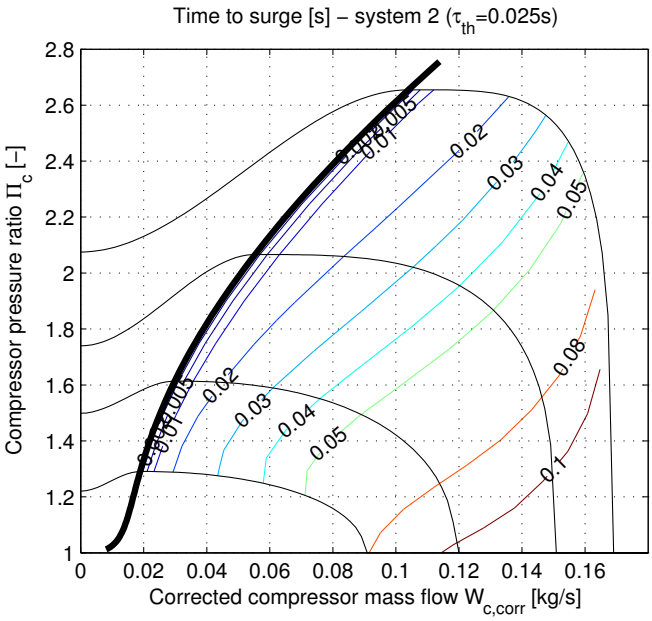

Figure 6: TTS for system 2. Shown is the TTS map for a throttle time constant of $\tau_{th} = 0.025$s. Larger constants have the same qualitative behavior but differs in the numerical values

3.2 System 2: Dynamic throttle behavior

In the next step the instantaneous stop in throttle mass flow is extended with a first order system for the throttle mass flow. This models the finite response time of a throttle system. The system is now described by (2) but where equation (2c) is exchanged for

$$\begin{aligned} \frac{dW_{th}}{dt} &= -\tau_{th} W_{th} + u_{th} \\ u_{th} &= \begin{cases} W_{th,init} & t < t_{init} \\ 0 & t \geq t_{init} \end{cases} \end{aligned} \tag{3}$$

Since the throttle dynamics is not known exactly, two different first order system time constants, τ_{th}, are used. The results from the calculations for $\tau_{th} = 0.025$s are shown in Fig. 6. Compared to system 1, Fig. 5, the TTS is larger for every operating point, which is expected. The differences between the two time constants, τ_{th}, are obvious. The behavior is similar but the slowly closing throttle has a much larger TTS. This shows that the throttle closing time constant has a significant impact on TTS.

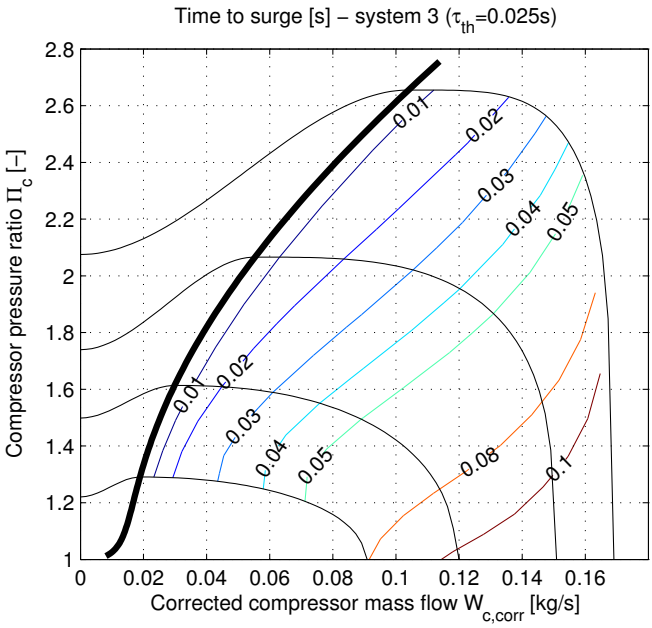

Figure 7: TTS for Approach 3 for the throttle time constant A comparison with Fig. 6 shows that the introduction of control volume temperature dynamics as a state has only very minor effect.

3.3 System 3: Temperature dynamics in intermediate control volumes

The next extension is to add the temperature dynamics, i.e. using the adiabatic model [9], of the lumped control volume. Compressor upstream conditions are still kept constant for this system, as is the turbo shaft speed. The states for this system are $W_c, p_{cv}, T_{cv}, W_{th}$. If TTS for this system, shown in Fig. 3.3, is compared to Fig. 6 it is easy to see that the extra temperature dynamics introduced has only minor effect. Also the qualitative behavior of the TTS is preserved. The temperature dynamics can thus be neglected.

3.4 System 4: Complete 14 states MVEM

As a final investigation the full 14 states MVEM is used to see if there are other effects that have a major impact on TTS. In the previously investigated systems three simplifying assumptions have been made; constant inlet conditions, lumped control volume and constant shaft speed. These will be addressed here. The first by adding an air filter restriction and control volume, which allows the compressor inlet conditions to vary. In particular the inlet pressure will be slightly lowered and mass flow dependent. The second by introducing the intercooler restriction and an extra control volume between compressor and throttle.

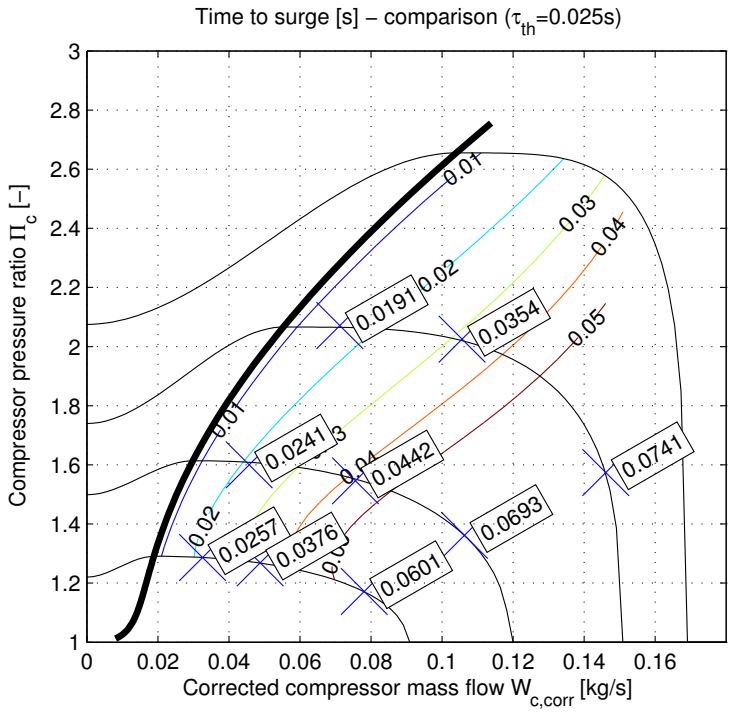

Figure 8: TTS using the full 14 states model, $\tau_{th} = 0.025$s. Isolines in the background are from system 3 with the same τ_{th}.

The third by the introduction of turbo shaft dynamics, allowing the compressor speed to vary (see Fig. 3).

For the complete model with $\tau_{th} = 0.025$s the TTS-map is shown in Fig. 8. TTS for $\tau_{th} = 0.1$s is as expected larger. Even for this multi state system it is obvious that the throttle closing speed, essentially τ_{th}, has a major effect on the time it takes before the compressor enters surge.

The differences between the complete MVEM model and the three simple approaches presented earlier are small. TTS is around $10-15\%$ larger throughout the compressor map compared to system 2 and 3. Using any of the simpler approaches to calculate TTS would thus give a control system some margin.

3.5 Conclusions of the TTS-investigation

Throughout the investigation a clear trend in parameter sensitivity can be seen. The single most important factor is how fast the throttle closes, due to the close connection between effective throttle area and throttle mass flow. In summary, these are the main results from the investigation

- ⋆ The most important parameter is the throttle time constant τ_{th}.

- ⋆ Shaft speed variations can be neglected with a good result because of the relatively slow dynamics.
- ⋆ Temperature dynamics can be neglected unless very small control volumes are being used.

As can be seen in the small differences between the full MVEM model and the three simpler approaches, even a less complex method for determining TTS gives satisfactory performance.

4 Construction of a surge control system

There are two actuators available for surge control, wastegate and surge valve. The wastegate valve effects the driving torque from the turbine and the surge valve releases pressurized air after to before the compressor. The wastegate has almost no effect due to the slow dynamics of the turbine shaft. The main actuator is therefore the surge valve.

4.1 Feedforward or feedback control

The discussion so far supports the claim that a feedforward control system is needed. The largest TTS for the throttle closings studied are all less than around 0.2s. If only real operating points are considered this maximum time is reduced even further and for normal operating points it is closer to 0.05s. The necessary reaction times of a control system are thus even faster. If feedback control is to be used, the reaction time of the control system can be divided into three parts: control system sample time, feedback sensor response time and actuator response time. Reducing any of these parts almost always implies a large increase in production costs.

One way to enhance the possibilities to avoid surge is to add a surge valve controlled not only by the Electronic Control Unit (ECU) but also controlled by a pressure difference. To add even more safety to the system the control system could be constructed to close the surge valve and leave the opening to a pressure difference system, see [6].

4.2 Surge valve characteristic

The surge valve of the MVEM is implemented as

$$\begin{aligned} T &= T_c \\ W_{sv} &= A_{sv} \frac{p_c}{\sqrt{T_c R}} \sqrt{\frac{2\gamma}{\gamma-1}\left(p_r^{\frac{2}{\gamma}} - p_r^{\frac{\gamma+1}{\gamma}}\right)} \end{aligned} \tag{4}$$

with $p_r = \max\left(\frac{p_{af}}{p_c}, \left(\frac{2}{\gamma+1}\right)^{\frac{\gamma}{\gamma-1}}\right)$. A surge valve has a maximum effective opening area and the surge valve maximum mass flow is shown in Fig. 9 for two different effective areas. Only surge control for cases where the surge valve

can recycle the compressor surge mass flow are considered, thus meaning shaft speeds where

$$W_{sv,max} > W_{c,surge,noncorr} \tag{5}$$

effectively giving an upper limit for the shaft speeds to be considered.
$W_{c,surge,noncorr}$ is the real mass flow, i.e. not corrected, at the surge line for the given shaft speed. Due to the fact that the maximum mass flow through the surge valve is also inversely proportional to the square root of the compressor control volume temperature, the possible control region is further reduced. The air filter control volume temperature is also assumed to vary little from the ambient temperature due to the heated recycled air, effectively meaning that the recycled air mass is considered small compared to the control volume mass.

4.3 Formulation of control goal

To retain high turbo shaft speeds, during e.g. gear changes, the goal for the control system is to keep the operating point on the highest possible shaft speed. The spool up time for the turbo is then reduced when the new gear is engaged and the demand for engine torque rises again. Retaining turbo shaft speed means keeping the driving torque from the turbine high and keeping the torque consumed by the compressor low. This can be seen in the turbo shaft dynamics

$$\begin{aligned} \frac{d(N_{tc}\frac{\pi}{30})}{dt} &= \frac{d\omega_{tc}}{dt} = \frac{1}{J_{tc}}(Tq_t - Tq_c - Tq_{tc,f}) \\ Tq_c &= \frac{30}{\pi}\frac{(T_c - T_{af})\cdot c_p \cdot W_c}{N_{tc}} \end{aligned} \tag{6}$$

The consumed torque is proportional to both the temperature difference over the compressor as well as the compressor mass flow. Further it is inversely proportional to the shaft speed. To be able to find the most interesting compressor operating point consumed compressor torque isolines are shown in Fig. 9. It can be seen that for every shaft speed the least amount of torque is consumed for operating points at the surge line.

4.4 Control algorithm

The control algorithm for the feedforward controller is as follows: when the throttle closing is commanded, calculate the time it takes for the operating point to reach the surge line, TTS. When the surge line (SL) is reached open the surge valve directly to a mass flow according to the following

$$\begin{aligned} W_{sv} &= 0 & t_{init} < t < t_{init} + t_{TTS} \\ W_{sv} &= W_{th} - W_{c,surge} & t = t_{init} + t_{TTS} \end{aligned} \tag{7}$$

meaning that the surge valve is closed for the first TTS seconds and thereafter opened to stabilize W_c at the SL. When this is done, engage a PI(D)-controller that follows the SL.

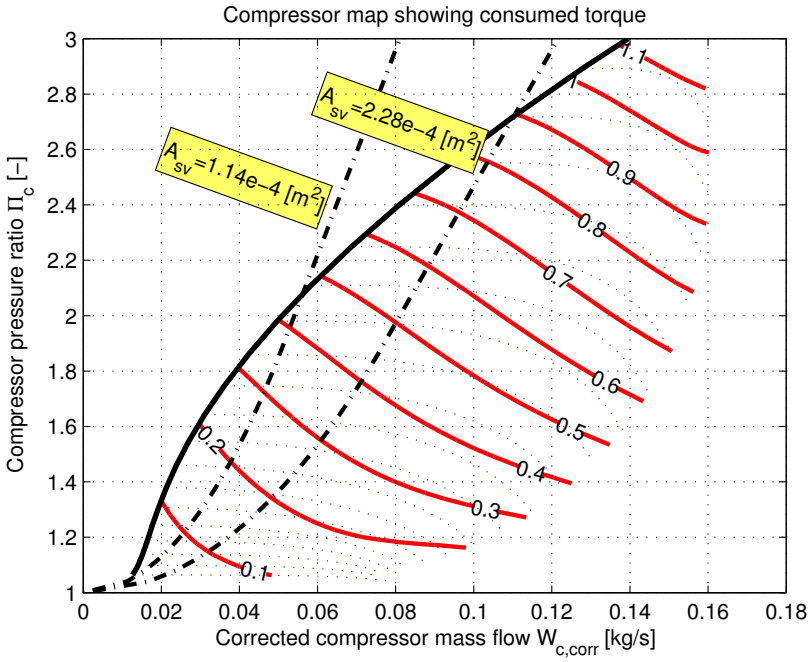

Figure 9: Consumed compressor torque shown with solid line. Dashed line shows compressor speed line. Seen is that for every speed line the minimum consumed torque is to be found at the surge line (or left of this). Surge valve characteristics are also shown for two different effective areas, $1.14 \cdot 10^{-4}\text{m}^2$ and $2.28 \cdot 10^{-4}\text{m}^2$, from [7].

5 Controller evaluation

A test scenario is used for evaluation. It consists of a one second long gear change where the throttle area is dropped to a minimum. The time constant used for the throttle is $\tau_{th} = 0.025$s giving a fast system to control. The controller described in the previous section is compared to two other controllers, one using a simple blow-off-technique that keeps the surge and waste gate valve fully open and one using feedback from mass flows and utilizing a PI-controller. A first order system surge valve, having a time constant of $\tau_{sv} = 0.02$s was used for all three controllers as well as a maximum effective surge valve area of $1.14 \cdot 10^{-4}\text{m}^2$, see [7]. The effect from more realistic cases having pulse width modulated control signals and time delays in the system is studied in [6].

The results from the gear change test case is shown in Fig. 10. It is seen that the feedforward controller has a up to 8% higher engine output torque and up to 20% higher turbo shaft speed. The difference is, as expected, decreasing slowly after the gear change and in the long run the operating points of all three systems will converge.

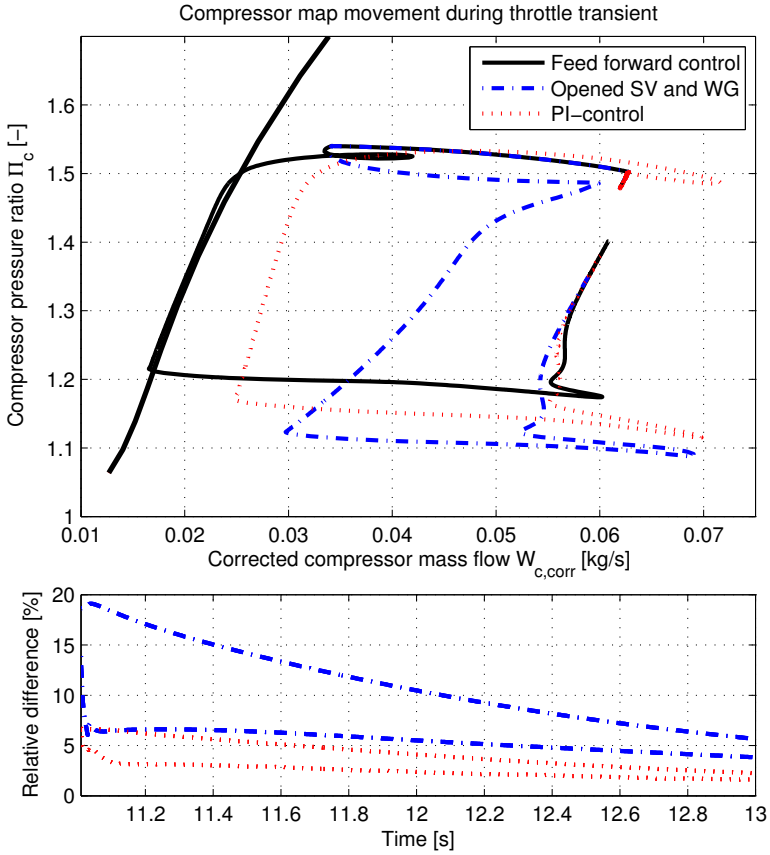

Figure 10: The figure shows differenct compressor map movements in corrected quantities for the three different controllers described in section 5. The feedforward controller map movement is closest to the SL and the corresponding relative increase in both shaft speed as well as engine torque after the gear change is seen. The shaft speed difference is at most 20% between the feedforward controller and the simple "blow open"-controller.

6 Conclusions

A measurement, called Time To Surge (TTS), of how long time it takes for a compressor to enter surge after a fast throttle closing is proposed. Different methods, of increasing complexity, for determining TTS are compared through the usage of a validated surge capable mean value engine model, having 14 states. The MVEM model is parameterized and validated using experimental data. The TTS parameter sensitivity is studied and TTS is found to depend mainly on throttle closing speed. There are no significant changes when taking the temperature or turbo shaft dynamics into account. A system that uses only three states (p_c, W_c, W_{th}) and an isothermal assumption gives a good description and has only a maximum deviation of 10% compared to the complete MVEM model. The largest TTS for normal compressor operating points is found to be around 0.1s which gives a strong motive for a feedforward loop in the control system.

An investigation is conducted to find the optimal compressor map movement that will maintain as high turbo shaft speeds as possible during rapid throttle transients. The investigation shows that, for every shaft speed, the path of least consumed torque coincides with the surge line.

A throttle transient during a gear change is used as a test case in a simulation setup. A new controller based on feedforward and the TTS concept is compared to two other controllers; a fast control system using feedback and a simple "blow-open"-controller. Comparisons show the gains with a feedforward system. The increase in shaft speed and engine net torque when the next gear is engaged is found to be 20% and 8% respectively compared to the simplest "blow-open"-controller.

References

[1] L. Guzzella, U. Wenger, and R. Martin. IC-engine downsizing and pressure-wave supercharging for fuel economy. In *SAE World Congr.*, Techn. Paper 2000-01-1019, 2000.

[2] Elbert Hendricks. The analysis of mean value engine models. In *SAE*, Techn. Paper 890563, 1989.

[3] Lars Eriksson, Lars Nielsen, Jan Brugård, Johan Bergström, Fredrik Pettersson, and Per Andersson. Modeling of a turbocharged SI engine. *Annual Reviews in Control*, 26(1):129–137, 2002.

[4] Lars Eriksson. Modeling and control of turbocharged SI and DI engines. *Oil & Gas Science and Technology - Rev. IFP*, 62(4):523–538, 2007.

[5] Per Andersson. *Air Charge Estimation in Turbocharged Spark Ignition Engines*. PhD thesis 989, Linköping University, 2005.

[6] Johan Bergström and Oskar Leufvén. Surge modeling and control of automotive turbochargers. Master's thesis LiTH-ISY-EX-3999, Linköping University, 2007.

[7] E. Wiklund and C. Forssman. Bypass valve modeling and surge control for turbocharged SI engines. Master's thesis LiTH-ISY-EX-3712, Department of Electrical Engineering, Linköpings Universitet, Linköping, Sweden, Aug 2005.

[8] Edward M. Greitzer. The stability of pumping systems - The 1980 Freeman Scholar Lecture. *J. of Fluids Engineering*, 103:193–242, 1981.

[9] Elbert Hendricks. Isothermal vs. adiabatic mean value SI engine models. In *3rd IFAC Workshop, Advances in Automotive Control, Preprints, Karlsruhe, Germany*, pages 373–378, March 2001.

A Nomenclature

State	Description	Unit
p_{af}	Air filter control volume pressure	Pa
T_{af}	Air filter control volume temperature	K
p_c	Compressor control volume pressure	Pa
T_c	Compressor control volume temperature	K
p_{ic}	Intercooler control volume pressure	Pa
T_{ic}	Intercooler control volume temperature	K
p_{im}	Intake manifold control volume pressure	Pa
T_{im}	Intake manifold control volume temperature	K
p_{em}	Exhaust manifold control volume pressure	Pa
T_{em}	Exhaust manifold control volume temperature	K
p_{es}	Exhaust system control volume pressure	Pa
T_{es}	Exhaust system control volume temperature	K
N_{tc}	Turbo shaft speed	$\frac{1}{min}$
W_c	Compressor mass flow	$\frac{kg}{s}$
Symbol	**Description**	**Unit**
V	Volume	m^3
CV	Control Volume subscript	
R	Specific gas constant	$\frac{J}{kgK}$
D_c	Compressor diameter	m
L_c	Compressor duct length	m
η_c	Compressor efficiency	$-$
γ	Ratio of specific heats	$-$
Π_c	Compressor pressure ratio	$-$
W_{th}	Throttle mass flow	$\frac{kg}{s}$
τ	1st order system time constant	
$init$	Initial condition subscript	
Tq_c	Compressor torque	Nm

Paper 2

Engine Test Bench Turbo Mapping[†]

2

Oskar Leufvén and Lars Eriksson

Vehicular Systems, Department of Electrical Engineering,
Linköping University, S-581 83 Linköping, Sweden.

Abstract

A method for determining turbocharger performance on installations in an engine test bench is developed and investigated. The focus is on the mapping of compressor performance but some attention is also given to the turbine mapping. An analysis of the limits that an engine installation imposes on the reachable points in the compressor map is performed, in particular it shows what corrected flows and pressure ratios can be reached and what these limitations depend on. To be able to span over a larger region of the corrected flow a throttle before the compressor is suggested and this is also verified in the test bench.

Turbocharger mapping is a time consuming process and there is a need for a systematic process that can be executed automatically. An engine and test cell control structure that can be used to automate and monitor the measurements by controlling the system to the desired operating points is also proposed.

In experiments, used for constructing the compressor speed lines, it is virtually impossible to control the turbocharger to the exact corrected speed that is postulated by the speed line. To overcome this two methods that compensate for the deviation between measured speed and the desired speed are proposed and investigated. Detailed data from a gas stand is used to evaluate the measurements compared to those that are generated in the engine test cell installation. The agreements are generally good but there is more noise in the engine data and there are also some small systematic deviations.

[†]This is a formatted version of "Engine Test Bench Turbo Mapping" by Oskar Leufvén and Lars Eriksson, SAE Technical Paper 2010-01-1232, SAE World Congress and Exhibition 2010, Detroit, USA. Reprinted with permission ©2010 SAE International. This paper may not be printed, copied, distributed or forwarded without prior further permission from SAE. The original paper can be found at `http://papers.sae.org/2010-01-1232/`, doi: `10.4271/2010-01-1232`. The formatting is restricted to changing the article into a single-column format, adjusting sizes of figures and tables, and adjusting the referencing style.

1 Introduction

Downsizing and turbocharging of SI engines plays an important role when developing fuel efficient vehicles. To further reduce fuel consumption and emissions more advanced and complicated concepts are being investigated and used, such as for example two-stage charging. In the development of the engine and its control system the information about turbocharger performance plays an important role. Turbocharger performance is expressed using maps, as representations and tabulated data, that are often provided by the compressor and turbine manufacturers or they can also be determined in a gas stand.

Turbocharger performance characteristics are not always readily available, and the manufacturer gas stand measurements are, in some cases, not reliable or can be influenced by the engine installation. Differences occur between stationary gas stand maps and on-engine performance, due to for example flow pulsations, flow geometry differences, and heat transfer. Another situation that frequently occurs when modeling turbocharged engines is that the provided manufacturer map is insufficient, i.e. it only covers a small portion of the operating region. There is thus a demand for turbocharger maps among researchers and engine developers.

To meet this demand this paper develops and investigates methods for measuring and determining turbocharger performance on installations in an engine test bench. This has wide applicability. For example the procedure helps determine the performance on the engine test stand and the mapping also provides valuable input to the modeling where the interaction between the engine and turbocharger is also visible.

1.1 Contributions

The main contribution is the method for determining turbocharger maps in an engine test cell installation, which is an integration of the following four parts:

i: A theoretical investigation of the reachable region of a turbo map, given the installation, is presented.

ii: Considering the limitations that an engine installation impose on the attainable flows, an extra throttle is proposed to increase the corrected compressor mass flow whilst keeping the actual engine flow within limits. This throttle is installed upstream the first compressor stage and is shown to increase the reachable region of the compressor mapping procedure.

iii: A controller structure for automated turbo mapping that can utilize the proposed extra throttle setup, is also presented.

iv: Two methods are proposed for handling slight offsets between actual measured corrected shaft speed and that which is desired.

1.2 Outline

A general description of the turbocharger performance and its determination is given in Section 2. In addition some related background information about the

selected performance quantities is provided in Appendix A. The measurement setup and engine installation is described in Section 3.

When a turbocharger is installed on an engine it is not possible to span the complete operating region of the turbocharger. Sections 4 and 5 contribute with an analysis of how an engine installation influences the reachable region of the compressor and turbine maps. An extra throttle is proposed to increase the reachable mapping region. A control structure is proposed in Section 6 that allows for easy mapping.

Section 7 develops methods for how the accuracy of the speed lines can be improved when the measured data points have speeds that deviate from the desired. The proposed method is investigated experimentally in Section 8 where the engine test bench results are shown to agree well with those of the gas stand. Finally Section 8 summarizes the conclusions of the paper.

2 System description and turbo maps

This section describes the engine test cell system that is used in the study as well as general compressor and turbine maps with examples. A detailed turbo map that is larger than normal manufacturer maps will be presented.

2.1 System description

The engine test bench used is an electric dynamometer that is capable of both motoring and braking the engine as well as emulating driveline transients. It is however, in the mapping, only run in brake mode and under constant speeds. The engine is a 4 cylinder, 2 liter, direct injected, spark ignited engine that is equipped with variable cam phasing for both intake and exhaust valves. Furthermore it has a two stage prototype turbo system fitted to it. However the two stage system is only used in single stage mode in the turbo mapping investigation here.

The engine control system is a prototype system capable of changing all relevant control signals in real time. Compared to a standard turbo-charged gasoline engine this particular engine is equipped with an extra butterfly valve throttle upstream of the first compressor stage. This throttle is also controlled by the control system. An overview of the system is shown in Fig. 1.

2.2 Compressor and turbine maps

A typical compressor map is shown in Fig. 2, which is a graphical representation of the measurement data that is provided by the manufacturer, see [14, 15] for more examples of maps. Procedures for determining turbo performance, in gas stands, are given in for example [10, 11].

The compressor map in Fig. 2 is not the same as the one on the engine, but it is larger than a normal manufacturer map. It thus both gives a better view of the turbo characteristics and is also more suitable for the analysis of the reachable region. The performance variables $\Pi_c = \frac{p_{02}}{p_{01}}$ and η_c in (25) are described using

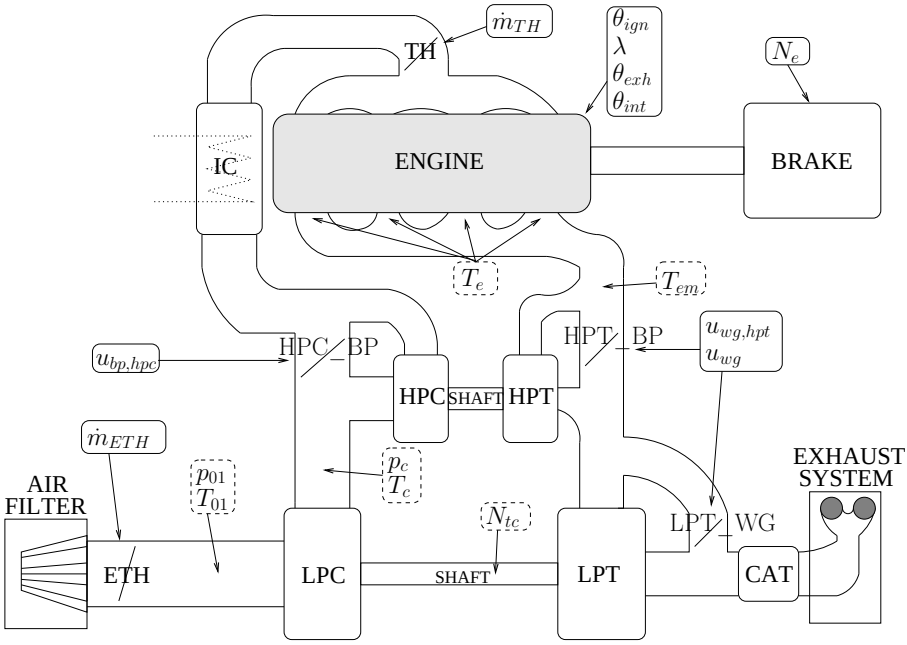

Figure 1: Illustration of the two stage system connected to the engine brake. Note especially the location of the extra throttle at the inlet of the first compressor stage. Also shown in the figure are the, main, available control signals (in solid rectangles) as well as the important system states (in dashed rectangles).

the corrected quantities in (26). In the compressor map corrected flow $\dot{m}_{c,corr}$,

$$\dot{m}_{c,corr} = \dot{m}_c \frac{\sqrt{\frac{T_{01}}{T_{std}}}}{\frac{p_{01}}{p_{std}}} \tag{1}$$

is on the x-axis, pressure ratio, Π_c on the y-axis, solid lines show constant corrected speed $N_{tc,corr}$

$$N_{tc,corr} = N_{tc} \frac{1}{\sqrt{\frac{T_{01}}{T_{std}}}} \tag{2}$$

The dotted lines show iso-efficiency lines for η_c.

A turbine map is shown in Fig. 3, which shows expansion ratio $1/\Pi_t$, efficiency η_t, and corrected compressor mass flow $\dot{m}_{t,corr}$.

3 Measurements

3.1 Gas stand measurements

The gas stand turbo map, used for experimental validation of the proposed method, has 12 operating points on each of the total 9 constant compressor

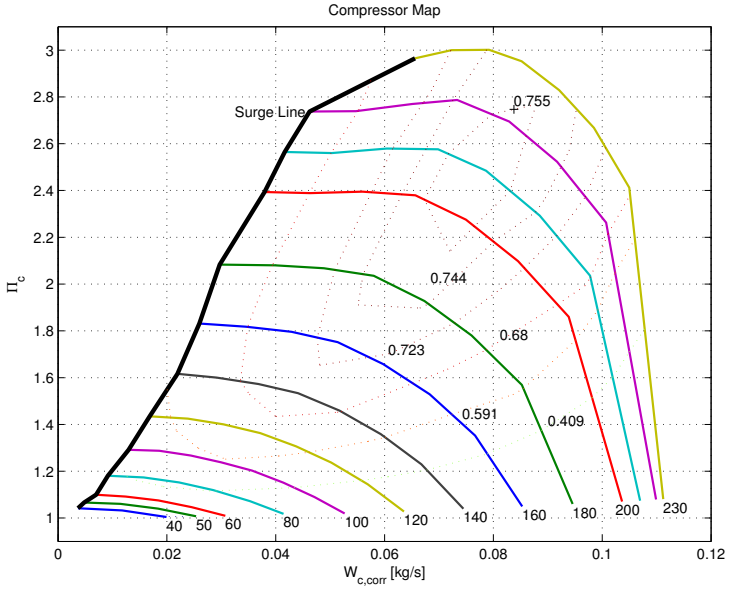

Figure 2: Compressor map showing the compressor efficiency map as a function of the pressure ratio Π_c and corrected mass flow $\dot{m}_{c,corr}$, with lines of constant corrected speed, and the surge line. The numbers $40 - 230$ are the shaft speeds given in $kRPM$.

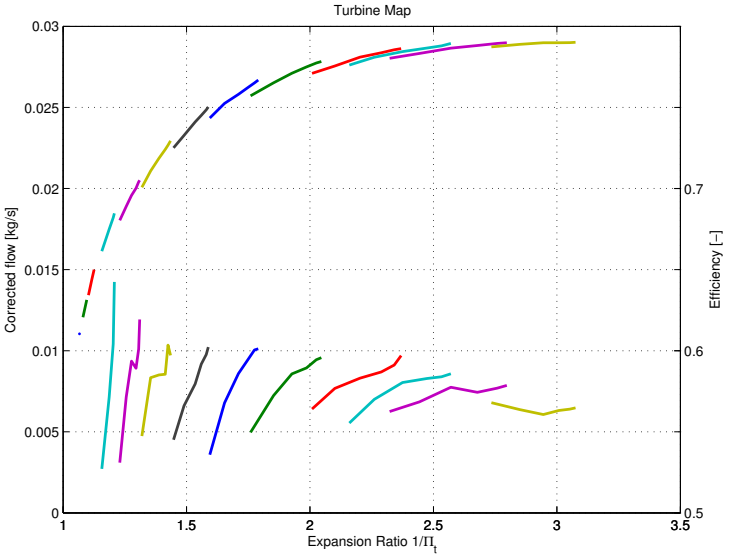

Figure 3: Turbine map showing the flow characteristic and the efficiency, for various lines of constant corrected speed. The x-axis gives the expansion ratio $1/\Pi_t$, the left y-axis the corrected mass flow $\dot{m}_{t,corr}$, and the right y-axis gives the efficiency.

speed lines. The measurements were done on another turbo individual but of the same model as the one installed on the engine, there can however be discrepancies between different individuals.

3.2 Engine test stand measurements

The measurements were conducted using both a MicroAutoBox (dSPACE) as well as a VXi (HP) system with Kistler pressure sensors and Pentronic thermoelements and the data was bias compensated using cold measurements. The sampling frequencies used were 80[Hz] and 1[kHz] depending on signal measured. Mass flow was measured with both a hot wire sensor as well as a laminar flow meter on the cold inlet air. The turbine mass flow was estimated using the compressor air mass flow and fuel flow calculated from a wide-band lambda signal. Furthermore the wastegate spring was assumed to fully close the wastegate valve in the turbine mapping measurements.

No extra thermal insulation was provided, the installation was kept as close to a production system as possible. This implies that temperatures measured in the engine test stand were influenced by heat transfer, both due to convection, conduction as well as radiation.

Pressures were measured with static pressure taps and the total pressure was calculated using the pipe area and mass flow. For cross sections where exact measurements were not available the areas were approximated, given outer dimensions and estimated thickness.

The measurements were taken when the system was stabilized, which took up to 10-15 minutes depending on operating point. Data was recorded during multiple days and using the same fuel quality. The signals were low pass filtered using non-phase-shifting filters offline.

4 Engine test bench imposed limits

Compared to gas stand turbo mapping there are obviously some differences when mapping a turbo system on an engine test stand. These limits are described in this section. This is followed by a theoretical investigation as well as a experimental investigation. The limits are

- $T_{exh} < T_{exh,lim}$, exhaust temperature limit for turbine protection
- $p_c > p_{amb}$, due to that soft pipes, after the compressor stage, would otherwise collapse
- $N_{tc} < N_{tc,lim}$, turbocharger over speeding protection
- $\Delta T_c = T_c - T_{af}$, temperature rise over compressor stage
- $\lambda_{min} < \lambda < \lambda_{max}$, air-fuel-ratio limitations due to stable combustion and stable power delivery to the turbine
- The variable cam-phasing were actuated in order to ensure stable combustion and stable power delivery to the turbine
- $N_e < N_{e,lim}$, engine speed upper bound

- ⋆ $Tq_e < Tq_{e,lim}(N_e)$, engine torque limit
- ⋆ $A_{wg} \leq A_{wg,max}$ wastegate opening area is limited
- ⋆ $\dot{m}_t$-determination, no mass flow measurements on the "hot" side

Listed limits are imposed on the system by the test stand setup and not by the proposed method.

5 Theoretical investigation of limits

This section presents a theoretical investigation of the reachable operating region for the turbo setup given an engine setup with its limits.

5.1 Turbine inlet temperature

The temperature of the gases leaving the engine, T_e is in [4] well described by an affine function in mass flow

$$T_e = T_{cyl,0} + \dot{m}_e K_t \tag{3}$$

where $(T_{cyl,0}, K_t)$ are tuning constants. This holds as long as the air-to-fuel-ratio is kept at unity ($\lambda = 1$). The exhaust temperature is reduces through heat transfer when passing the exhaust valves and through the exhaust manifold. This leads to a lower turbine inlet temperature than predicted by Eq. (3). This temperature loss is modeled in [4], and it is described by

$$T_{em} = T_a + (T_e - T_a)\, e^{-\frac{h(\dot{m}_e)\, A}{\dot{m}_e\, c_p}} \tag{4}$$

where T_a is the external temperature, $h(\dot{m}_e)$ effective heat transfer coefficient, A pipe wall surface area, and c_p specific heat at constant pressure.

To avoid turbine damage the control system tries to control the gas temperature through fuel enrichment, i.e. $\lambda < 1$. This cools the gases through increased fuel vaporization as well as increasing the mass that is heated by the combustion. Fig. 4 shows the turbine inlet temperature as function of mass flow where fuel enrichment has been used to limit the temperature for larger mass flows.

This insufficient exhaust enthalpy limits the reachable compressor region, in particular a lower temperature moves the limit away from the surge line as shown in Fig. 5.

For small mass flows though, it is possible to increase T_e by moving away from optimal ignition angle and simply start the combustion later. This lowers the engine efficiency since less energy is extracted from the gas during the expansion stroke, thus increasing the temperature of the gas that enters the exhaust system T_e, see e.g. [7, 9].

5.2 Turbine mass flow

The turbine will extract power even for a fully opened wastegate valve. This is due to the fact that the effective opening area of the wastegate valve is limited.

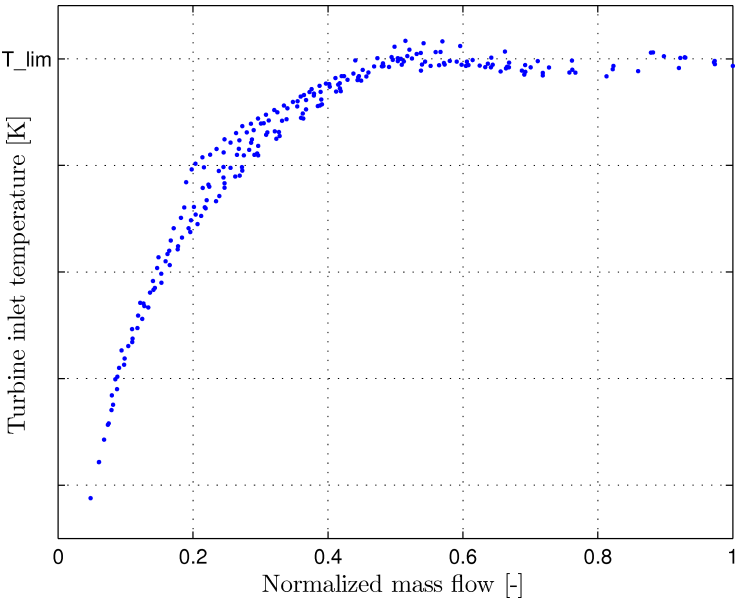

Figure 4: Measured exhaust temperature with temperature control through fuel enrichment.

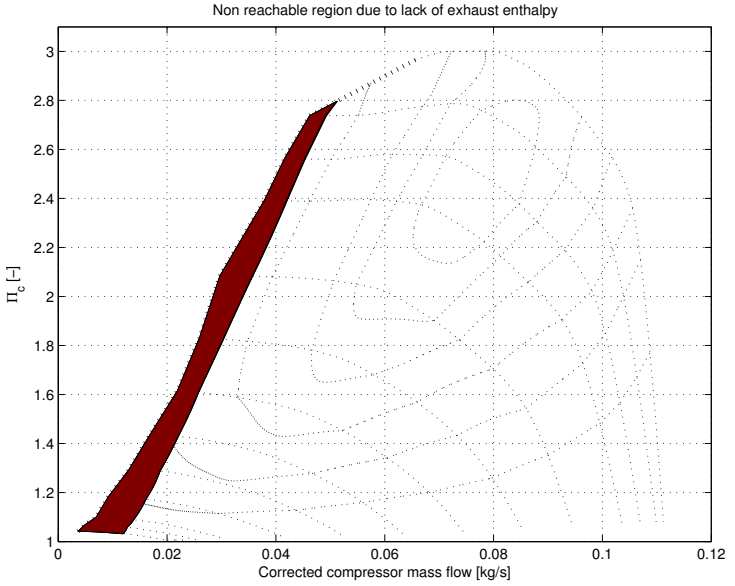

Figure 5: The limited exhaust temperature limits the amount of energy that can be provided for the compressor and thereby reduces the reachable region. The dark region, is due to this, unreachable.

A pressure ratio will thus effectively be established as soon as there is a mass flow in the system, putting a restriction on how small turbo speed that is achievable given a mass flow. On the other hand, for a fully closed wastegate valve the compressor could be driven into the unstable region for some mass flow. Using the equation for a compressible restriction [7] to describe the wastegate mass flow

$$\dot{m}_{wg} = \frac{p_{em}}{\sqrt{RT_{em}}} A_{wg} C_d \Psi(\Pi_t) \tag{5}$$

it is easy to see how a finite A_{wg} will limit the control of how much power that is extracted by the turbine. For a stable turbo operating points the compressor power P_c and the turbine power P_t must be equal, i.e.

$$\underbrace{\dot{m}_c c_{p,c} T_{01} \frac{\Pi_c^{\frac{\gamma_c - 1}{\gamma_c}} - 1}{\eta_c}}_{=P_c} = \underbrace{\dot{m}_t c_{p,t} T_{03} (1 - \Pi_t^{\frac{\gamma_t - 1}{\gamma_t}}) \eta_t}_{=P_t} \tag{6}$$

where the mechanical efficiency is included in η_t. This equation can be used together with a model for the compressor and turbine and Eq. (5) to gain insight into how the wastegate area limits the reachable operating points in the compressor map. In Fig. 6 these equations are solved for different values of A_{wg}. It is assumed that the turbine inlet temperature is kept at the maximum allowable. This is normally not the case for smaller mass flows as shown in Fig. 4, but can be achieved through later ignition angles as discussed previously. The region to the left of $A_{wg} = 0$ in Fig. 6 is restricted due to that even with fully closed wastegate there is not enough power to reach larger speeds. The left most line corresponds to fully closed wastegate and the other have increasing area. For a given system the maximum area $A_{wg,max}$ gives a limit on how far down in the compressor map the system can operate. For a given maximum value of $A_{wg,max}$ there is therefore a lowest turbo speed given for a given mass flow.

5.3 Turbine mass flow measurement

The wastegate valve has to be closed, since the air mass flow is only measured on the intake side giving the following turbine mass flow

$$\dot{m}_t = \dot{m}_a + \dot{m}_f = \dot{m}_a \left(1 + \frac{1}{(A/F)_s \lambda}\right) \tag{7}$$

Note that this flow can be distributed through both the wastegate and turbine unless the wastegate is closed. This restriction, combined with the fact that the wastegate valve spring is unable to close the valve for large expansion ratios, limits the reachable turbine map considerably. Large deviations from $\lambda = 1$ were avoided in the turbine mapping, due to the possible introduction of measurement errors and uncertainties in the calculation of γ. This limits the turbine mapping since the exhaust temperature limit is reached earlier when fuel enrichment is not allowed.

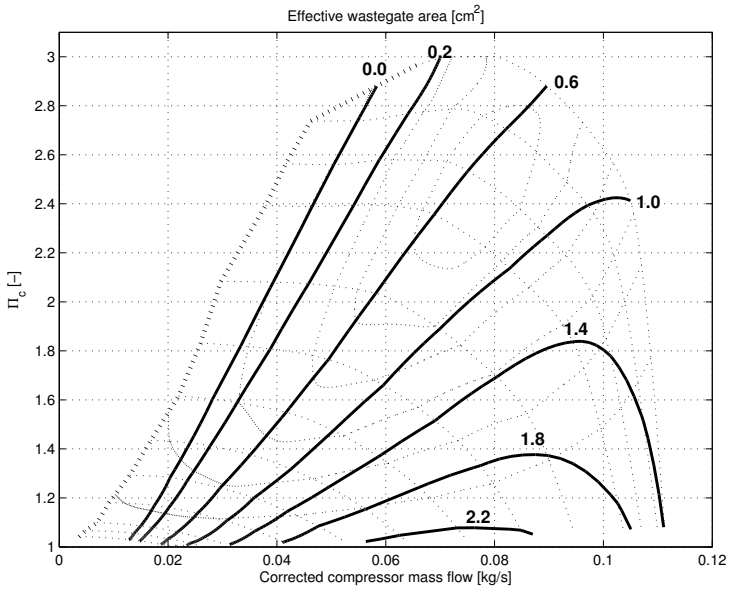

Figure 6: A figure showing the coupling between wastegate area and the position in the compressor map. The left most line depends on the turbine inlet temperature and it has been selected as the highest allowed turbine temperature.

5.4 Compressor temperature increase

If the compressor is driven in an operating point with too large pressure ratio in combination with a too small efficiency the temperature rise over the compressor stage, $\Delta T_c = T_c - T_{01}$, will exceed the allowable limit for the system.

$$\Delta T_c = T_{01} \frac{\Pi_c^{\frac{\gamma-1}{\gamma}} - 1}{\eta_c} \tag{8}$$

The allowable region of the compressor map can be determined using this equation and the compressor map that contains the pressure ratio and efficiency. The result is presented in Fig. 7.

5.5 Flexible pipes

Due to that the pipes downstream of the compressor are flexible there will be a minimum absolute compressor pressure, p_c. This is due to the deformation of the pipes when $p_c < p_{amb}$. The following must therefore hold for all operating points

$$p_{01} \cdot \Pi_c = p_c > p_{amb} \tag{9}$$

This limit can be reached for lower turbo speeds since these have smaller Π_c for a given mass flow.

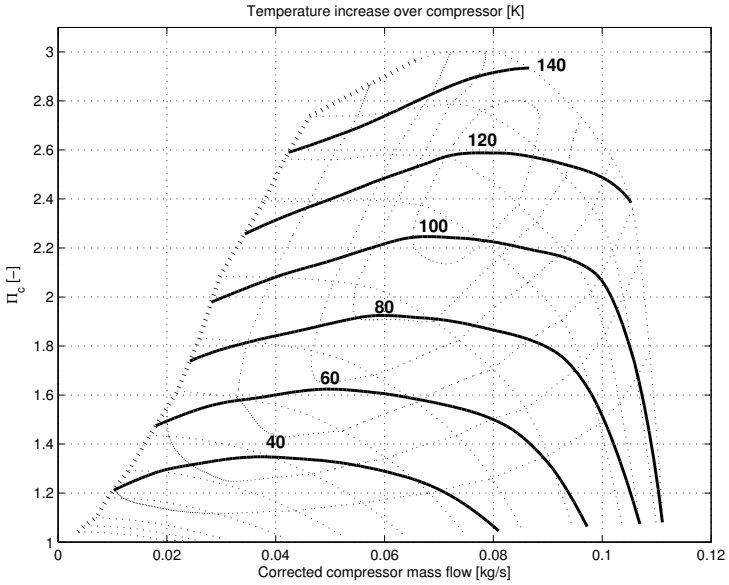

Figure 7: The plots shows the limit in compressor map resulting from the restriction in temperature rise over the compressor stage. Shown are lines of constant temperature increase.

5.6 All Constraints Overlaid

When combining the constraints that have been discussed one will receive a map similar to Fig. 8. In this figure the limits have been chosen to be very restrictive, to better show the contributions from each restriction. There are three limiting factors shown in the figure. The first one to the left, comes from the limited reachability using fully closed wastegate combined with maximum exhaust system temperature. The upper limit is due to the temperature increase limit of the compressor stage. The lower limit is due to a limited opening area of the wastegate valve.

Apart from these limitations there are also others that have to be accounted for. The combustion must be stable to supply a stable enough mass flow to the turbine. This restricts the control of fuel enrichment and spark timing as well as the cam phasing. There is also a limit due to the extra throttle combined with the need to keep $p_c > p_{amb}$; for small Π_c, the pressure at the compressor inlet can not be too low. The combustion engine may not exceed its limits on power and torque. Other natural limits are surge, choke and over speeding of the turbo. However these last ones are also equally applicable in a gas stand and are therefore not further discussed.

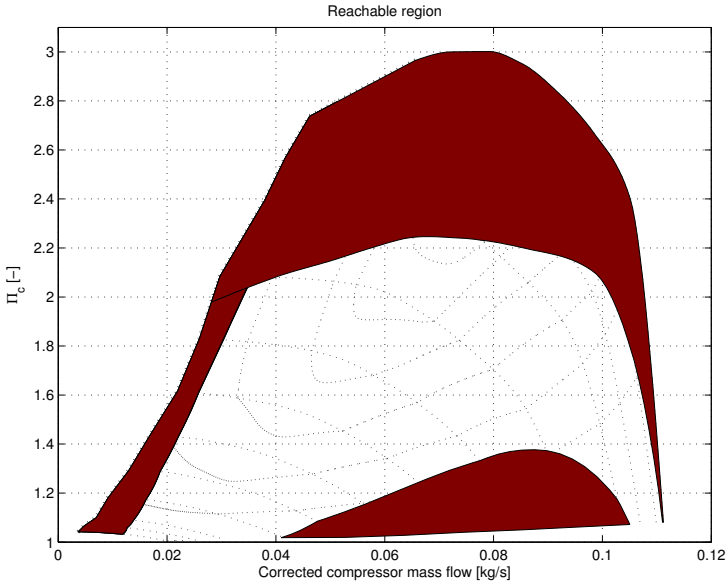

Figure 8: All constraints that have been discussed are now overlaid in the compressor map, showing the reachable set of operating points.

5.7 Extensions using pre-compressor throttle

Here it is assumed that the SAE-correction equation can be used, i.e. Eq. (1) and (2). (It is worth to note that there are typesetting errors in the SAE-standards [10, 11] that are derived from the normal quantities in [3].) A larger region of the compressor map can spanned, using the $\frac{p_{01}}{p_{std}}$-factor in the denominator, compared to maintaining the inlet conditions close to the standard pressure and temperature (p_{std} and T_{std}). This is here recognized as an opportunity and used as a key feature of the proposed method. A pre-compressor throttle is used to lower the pressure before the compressor inlet, thus effectively increasing the corrected mass flow while keeping the actual mass flow within its limits.

The ability to change p_{01}, and thus P_c through Eq. (6), can also be used to achieve turbine speeds unreachable for standard conditions. This applies to small mass flows where P_t would otherwise be too small to reach the desired speed given the loading P_c with $p_{01} \approx p_{amb}$.

6 Turbo Mapping Method

Gas stand turbo mapping normally measures speed lines from choke to surge. As seen in section 4 and 5 this is not achievable for all speed lines when the turbo is mounted in an engine test stand. The engine test stand mapping therefore starts with finding the extreme points that are reachable, i.e. points 1 and 4 or 5 in Fig. 10. It is then decided how many points that are to be measured on the current desired corrected speed line ($N_{tc,corr,des}$), and starting at point 1 the

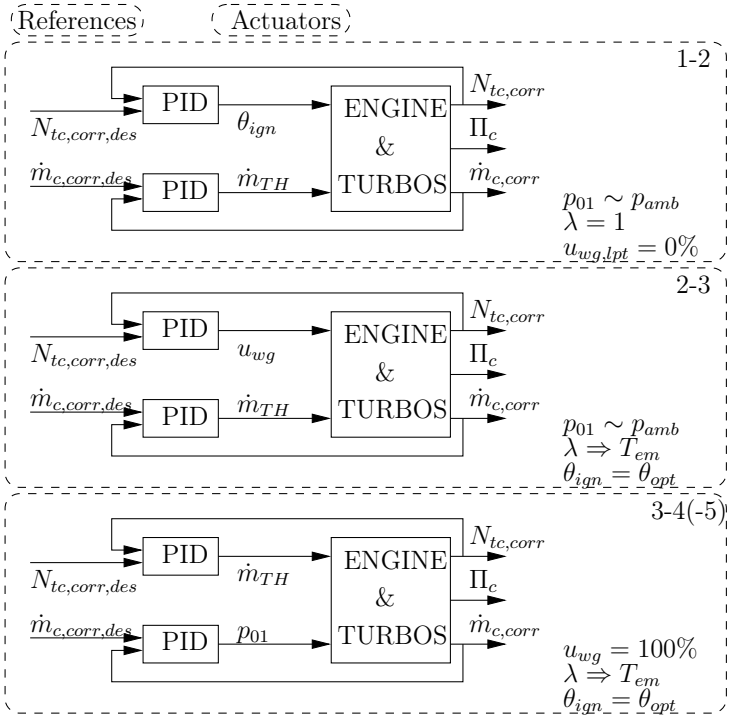

Figure 9: A control structure for the engine test stand turbo mapping. The numbers (e.g. 1-2) are presented in Fig. 10 and described in section 6. Three different controllers are used on different parts of a speed line. For example the top most controller is used between points 1-2 where θ_{ign} is used to effectively control exhaust enthalpy and thus, with fully closed wastegate valve ($u_{wg} = 0\%$), controlling turbo shaft speed ($N_{tc,corr}$). $\dot{m}_{c,corr}$ is controlled using the main throttle mass flow ($\dot{m}_{TH}$) since the pressure upstream of the compressor is kept at ambient ($p_{01} = p_{amb}$). The proposed structure uses feedback and PID controllers for ($\dot{m}_{c,corr}, N_{tc,corr}$).

reference values for corrected compressor mass flow ($\dot{m}_{c,corr,des}$) are fed to the control structure, seen in Fig. 9. Depending on mass flow, different actuators are used for control.

The overall structure of the mapping controller consists of three different controllers and they are all shown in Fig. 9. The proposed structure uses feedback and PID controllers for the desired points on the speed line specified by ($\dot{m}_{c,corr,des}, N_{tc,corr,des}$). The function of each controller is described in the list below (where the numbers referred to are shown in Fig. 10)

(1-2): $\theta_{ign} \neq \theta_{opt}$ to increase available turbine energy is used combined with $u_{wg} = 0\%$ to achieve the desired corrected shaft speed, $N_{tc,corr,des}$. λ is kept at the standard conditions given by the engine control system. $\dot{m}_{c,corr}$ is controlled using $\dot{m}_{TH}$. The extra throttle keeps the pressure upstream of the compressor stage at maximum, i.e. $p_{01} \approx p_{amb}$.

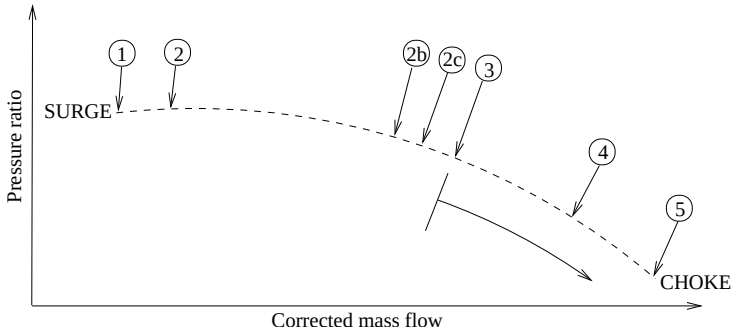

Figure 10: A generic compressor speed line, showing the different controller regions used in the compressor mapping, limited by the surge and choke point. The x-axis is the corrected mass flow, the y-axis shows pressure ratio. The regions made up by the encircled numbers are given by different system limitations and are explained in section 6. The extra throttle upstream of the first compressor stage is used from point 3 and on down to choke, marked with an arrow.

(2-2b-2c-3): nominal engine conditions, where u_{wg} controls $N_{tc,corr,des}$. $\dot{m}_{c,corr}$ is controlled using $\dot{m}_{TH}$. At point 2b the temperature forces the use of $\lambda < 1$ to control the exhaust temperature (when $\theta_{ign} = \theta_{opt}$). For higher $N_{tc,corr,des}$ an increase in mass flow can be limited due to difficulties in keeping a stable combustion caused by too small λ, indicated by 2c in Fig. 10.

(3-4): At point 3 the engine utilizes fully opened wastegate valve. $\dot{m}_{c,corr}$ is instead controlled using the extra throttle which controls the inlet pressure, $p_{01} < p_{amb}$.

(4-5): For smaller turbo speeds, $N_{tc,corr}$, there is a limitation caused by the intake system of the engine that makes the measuring of larger mass flows, given the reference compressor speed, impossible. This is due to the soft pipes of the engine that forces the pressure after the compressor to always be greater than the ambient ($p_c > p_{amb}$).

During the turbine mapping the control signals are limited to, mainly, main throttle mass flow, $\dot{m}_{TH}$. This is due to the restrictions described in the Sections 4 and 5. The major limiting factor is the decision to keep $\lambda \approx 1$ and $u_{wg,lpt}$. The extra throttle has only a small influence on the achievable mass flow for the turbine mapping as it can reduce the compressor power by decreasing p_{01} below p_{amb}.

7 Correction Factors for Measurements

Compressor speed lines give a good description of the compressor flow characteristics and therefore plays an important role when selecting a compressor for a particular system. However when performing experiments and building up a speed line in engine tests it is virtually impossible to control the system to the exact corrected speed as is postulated by the speed line. Variations around the

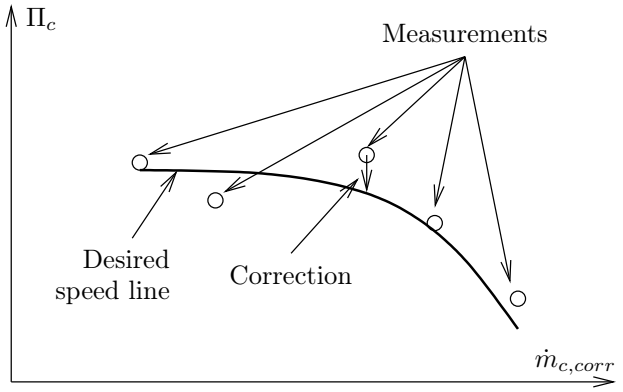

Figure 11: Example of a speed line and measurement points scattered around this line. The correction is desirable to perform such that the final product of the mapping will give a correct picture of the device performance.

nominal speed is inevitable when constructing the maps, and depending on the variations it might be necessary to compensate for these variations. See Fig. 11 for an illustration. The amount of variations differs and for a gas stand the variations are small but for an engine installation the variations are larger and they distort the speed lines.

To solve this problem of map generation two methods are proposed and investigated for how to correct a measured data point with $N_{tc,corr}$ to the desired speed $N_{tc,corr,des}$. In the first method the compressible dimensionless numbers are utilized and gives an adjustment that is motivated from the physics, that does not rely on any model parameters. The other utilizes a model when performing the correction. There are also other corrections that have been proposed for measurements of stationary machines, e.g. in [2].

7.1 Correction by Dimensionless Numbers

It is well known that the dimensional analysis gives valuable insight into the dominating effects and characteristics of turbomachinery and it is also the basis for the corrected quantities that are used in the maps. The two most important quantities are the energy transfer coefficient

$$\Psi = \frac{c_p\, T_{01} \left[\Pi_c^{\frac{\gamma-1}{\gamma}} - 1 \right]}{N^2\, D^2} \tag{10}$$

and the flow coefficient

$$\Phi = \frac{\dot{m}_c}{\rho_{01}\, N\, D^3} \tag{11}$$

Some material about the dimensionless numbers is collected in Appendix A.

The cornerstone in this method comes from the observation that both Ψ and Φ have only a very weak dependence on N (or equivalently the Mach number).

This observation has been utilized in several models [1, 13, 5] for compressor modeling. Since these dimensionless numbers have only a weak dependence on N this can be used to adjust the map data. This is now utilized to determine how a speed change will influence the mass flow and pressure ratio for the same values of Ψ and Φ. This can be expressed mathematically as

$$\Delta\Psi = 0 \tag{12}$$

$$\Delta\Phi = 0 \tag{13}$$

It is worth to comment that one could allow Ψ and Φ to change and for example determine the variation along a constant flow path (as will be done in the pressure ratio model below). However this would require a model (i.e. an assumption) for how Ψ and Φ are connected along a speed line. A less restrictive assumption is that Ψ and Φ remain the same (i.e. Eq. (12) and (13)).

The changes in pressure ratio and mass flow can now be approximated with the aid of the Taylor expansion of Eq. (10) and (11) with respect to the corresponding changes in $\Delta\Pi_c$, $\Delta\dot{m}_c$, and ΔN. The first order Taylor expansion yields

$$\Delta\Psi = \frac{c_p\, T_{01}}{N_{tc}^2\, D^2}\left(\frac{\gamma-1}{\gamma\,\Pi_c^{\frac{1}{\gamma}}}\Delta\Pi_c - 2\left[\Pi_c^{\frac{\gamma-1}{\gamma}}-1\right]\frac{\Delta N_{tc}}{N_{tc}}\right)$$

$$\Delta\Phi = \frac{1}{\rho_{01}\, N_{tc}\, D^3}\left(\Delta\dot{m}_c - \dot{m}_c\frac{\Delta N_{tc}}{N_{tc}}\right)$$

Using Eq. (12) and (13) now yield the changes in pressure ratio and mass flow that are associated with a change in speed

$$\frac{\Delta\Pi_c}{\Pi_c} = 2\frac{\gamma_c}{\gamma_c-1}\left[1-\Pi_c^{-\frac{\gamma_c-1}{\gamma_c}}\right]\frac{\Delta N_{tc}}{N_{tc}} \tag{14}$$

$$\frac{\Delta\dot{m}_c}{\dot{m}_c} = \frac{\Delta N_{tc}}{N_{tc}} \tag{15}$$

These expressions directly give the change from measurable quantities and are easy to apply directly to the data. For example when adjusting the data to a certain desired corrected speed line we get $N_{tc,des} = N_{tc,corr,des}\sqrt{\frac{T_{01}}{T_{std}}}$ and $\Delta N_{tc} = N_{tc,des} - N_{tc}$. In summary this correction relies upon measured quantities and the dimensional analysis together with the assumption of weak dependence of speed in the dimensionless quantities.

A correction that has a similar structure is proposed in [2], where the correction terms are expressed as

$$\frac{\Pi_{c,2}}{\Pi_{c,1}} = \left(\frac{N_2}{N_1}\right)^2 \tag{16}$$

$$\frac{\dot{V}_{c,2}}{\dot{V}_{c,1}} = \left(\frac{N_2}{N_1}\right) \tag{17}$$

where these relate the pressure ratio and volume flows to the rotational speed. For small changes these two expressions are similar to those in Eq. (14) and (15),

which can be seen by Taylor expanding the expressions, but they are not identical.

7.2 Corrections With a Pressure Ratio Model

Another option for performing the correction analysis is to use a model for the connection between the pressure ratio, corrected mass flow, and corrected speed. Such a model can be expressed as follows

$$\Pi_c = f_{\Pi_c}(\dot{m}_{c,corr}, N_{tc,corr}) \tag{18}$$

This model structure also covers surge capable models, where the speed line expresses the ideal pressure that the compressor can generate. Here the user of the model can select among a variety of models, e.g. physically based models, curve fitting models, interpolation models. When the model structure has been determined its parameters can be determined (as long as the model is identifiable) with the aid of the least squares method.

Now it is straight forward to calculate the partial derivative of

$$\Pi_c = f_{\Pi_c}(\dot{m}_{c,corr}, N_{tc,corr})$$

with respect to $N_{tc,corr}$ and we have the resulting expression

$$\Delta\Pi_c = \frac{\partial f_{\Pi_c}(\dot{m}_{c,corr}, N_{tc,corr})}{\partial N_{tc,corr}} \Delta N_{tc,corr} \tag{19}$$

This is a straight forward approach as long as there is a model available and that it is differentiable with respect to the corrected speed. The model structure should be selected such that it gives a good description of the data and it is of course beneficial if it is easily differentiable w.r.t. $N_{tc,corr}$.

Looking at Eq. (18) it is tempting to think that one could also use a model that has the following structure

$$\dot{m}_{c,corr} = f_{\dot{m}_{c,corr}}(\Pi_c, N_{tc,corr})$$

However this does not turn out to be a good choice, which is easily seen near the surge line or at higher speeds where it is difficult to define a unique function $f_{\dot{m}_{c,corr}}$. If one is successful in defining such a model in any way the flat lines close to the surge line will give a large partial derivative with respect to $N_{tc,corr}$ and this will make the transformation very sensitive to noise in measurement data and model parameters.

8 Experimental results

First the two correction approaches are illustrated, then the compressor flow and efficiency characteristics are examined, and finally the turbine map is investigated.

8.1 Correction factors

In the first approach everything is given while in the second approach a model structure is necessary. As model a simple polynomial is selected, that has a third order dependence in corrected mass flow and second order dependence in compressor speed.

$$f_{\Pi_c}(x,y) = \; a_9\,x^3 + a_8\,x^2\,y + a_7\,x\,y^2 + a_6\,x^2 + a_5\,x\,y + \\ +a_4\,y^2 + a_3\,x + a_2\,y + a_1$$

This model is easily tuned to the measurement data with the aid of the (linear) least squares method and the partial derivative is also easy to calculate. For the compressor gas stand map the proposed polynomial gives a mean relative Π_c-error between model and mapped value of $< 3\%$ with a largest value of 14%. The resulting partial derivative with respect to $N_{tc,corr}$ is

$$\Delta\Pi_c \;\; = (a_8\dot{m}_{c,corr}^2 + 2a_7\dot{m}_{c,corr}N_{tc,corr} + a_5\dot{m}_{c,corr} + \\ +2a_4N_{tc,corr} + a_2)\cdot\Delta N_{tc,corr}$$

The results are shown in Fig. 12 and presented in the following table

$\frac{\Delta N_{tc,corr}}{N_{tc,corr}}$ [-]	$\frac{\Delta N_{tc}}{N_{tc}}$ [-]	$\Delta\Pi_{c,1}$ [-]	$\Delta\dot{m}_{c,1}$ [g/s]	$\Delta\Pi_{c,2}$ [-]
−0.04	−0.04	−0.001	−0.032	−0.001
0.04	0.04	0.001	0.032	0.001
−0.37	−0.37	−0.005	−0.277	−0.008
1.19	1.19	0.015	0.879	0.024

The table shows the last 4 points of the upper speed line of Fig. 13. $\Delta\Pi_{c,1}$[-] and $\Delta\dot{m}_{c,1}$[g/s] are the correction quantities calculated using the dimensionless numbers, i.e. Eq. (14) and (15) and $\Delta\Pi_{c,2}$[-] is calculated using Eq. (19). Since $N_{tc,corr}\,C = N_{tc}$[-] and $N_{tc,corr,des}\,C = N_{tc,des}$[-] with $C = \sqrt{T_{01}/T_{std}}$ the following holds

$$\frac{\Delta N_{tc}}{N_{des}} = \frac{N_{tc,des} - N_{tc}}{N_{des}} = \frac{N_{tc,corr,des}\,C - N_{tc,corr}\,C}{N_{tc,corr}\,C} = \\ = \frac{N_{tc,corr,des} - N_{tc,corr}}{N_{tc,corr}} = \frac{\Delta N_{tc,corr}}{N_{tc,corr}}$$

and the two first columns in the table will be the same. A negative $\Delta N_{tc,corr}$ for example produces a negative correction, $\Delta\Pi_{c,2}$[-] for the pressure ratio as expected. The largest deviation, ΔN_{tc} for this turbo shaft speed was 1.19%.

8.2 Compressor map

The measured and corrected compressor map is shown in Fig. 13 and parts are magnified in Fig. 12. Both the pressure characteristics as well as the efficiency curves agree well for the speed lines shown. The major restrictions for reaching

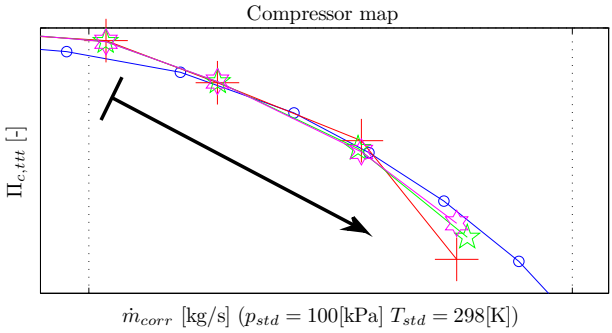

Figure 12: Illustration of the two correction methods. Blue circles show the measurement points from the gas stand. Red crosses show the measured data, green pentagrams corrections according to Eq. (14) and (15), and magenta hexagrams represent corrections according to Eq. (19). The point with largest mass flow is measured at a too small N_{tc} as well as $N_{tc,corr}$ which is seen in the figure were both correction methods increase Π_c, as expected. The first method (pentagrams) shows also deviation in corrected flow.

larger mass flows on these speed lines was the fully opened throttle utilized combined with the problem with keeping $p_c > p_{amb}$ to ensure that the soft pipes were kept intact. The mean absolute relative errors in efficiency and pressure ratio for the two speed lines presented are $\Delta\eta_c = (3.1, 1.7)\%$ and $\Delta\Pi_c = (0.7, 0.6)\%$ for the smaller and larger speed respectively.

In Fig. 12, the uppermost engine test stand point has the largest actual mass flow from the engine test stand mapping. From that point on the extra throttle is used to decrease upstream pressure and thus increasing the corrected mass flow, marked with an arrow (see Fig. 10). The lowest pressure ratio point, with largest corrected mass flow, has about 3% lower actual flow and about 30% lower upstream pressure. This clearly shows the benefit of the proposed additional throttle.

It has to be noted that the measurements were on purpose conducted without any extra insulation which, at least for small speeds, affects especially η_c (see [12]). Other aspects affecting the result is that the installation restricted the sensor placement and number of sensors which can lead to errors, in the pressure and temperature measurements, due to flow patterns.

8.3 Turbine map

The turbine map is shown in Fig. 14 where it is seen that the mass flow is slightly underestimated for small flows and slightly overestimated for large. As seen in the figure the turbine map agrees acceptable for the measured points. The turbine efficiency was calculated using

$$\eta_t = \frac{\dot{m}_c c_{p,c}(T_c - T_{01})}{\dot{m}_t c_{p,t} T_{em} \left(1 - (\Pi_t)^{\frac{\gamma_t - 1}{\gamma_t}}\right)}$$

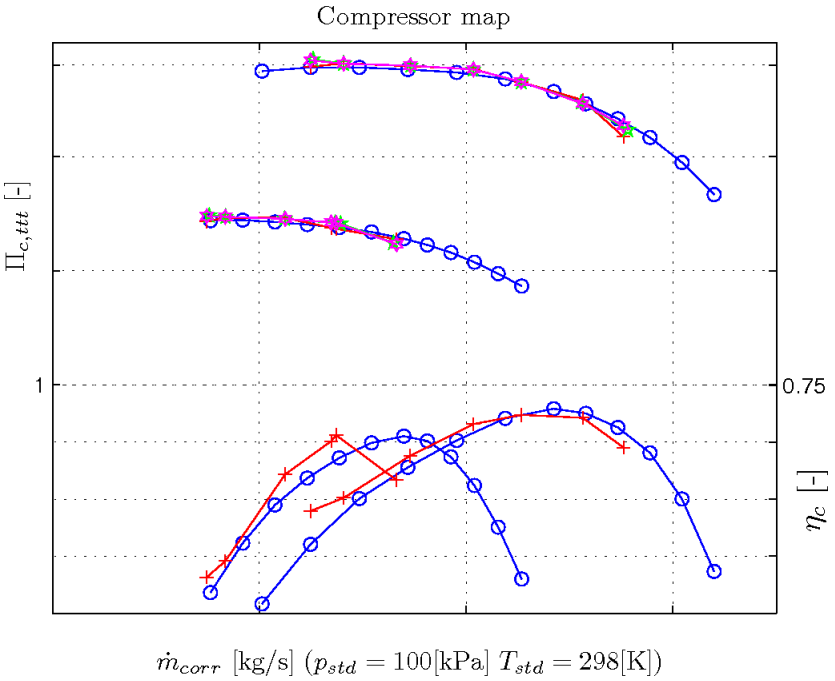

Figure 13: The compressor map measured using the proposed method compared to the gas stand map. Compared to the standard compressor map presentation it has here been chosen to not plot the compressor efficiency as contours. A "turbine map" approach is chosen instead to better see the differences. The upper two curves are the speed lines, whereas the lower lines show the efficiency. Two different constant corrected speed lines are shown. The pressure characteristics agree well for lower mass flows but start to differ for larger mass flows. Both proposed correction methods are shown. The efficiency curves are also well represented but differ slightly for the smallest and largest mass flows as well. $\Pi_c = 1$ as well as $\eta_c = 0.75$ are shown for reference on respective side.

from e.g. [7], where the mechanical efficiency is included in the turbine efficiency, η_t. This however overestimated η_t. Values exceeding 1 and in general 15% or more too large values were estimated, which is a well known problem for low flows in turbines. These values are therefore left out of Fig. 14. Note though that, due to the limitations only a small turbine map was measured. The largest limitation was the decision to maintain $\lambda = 1$ and not use fuel enrichment to not exceed the exhaust system temperature limit.

9 Conclusions and comments

A procedure for turbo mapping in engine test benches has been proposed and the potential of such a setup has been analyzed and investigated. The setup has been implemented in an engine test cell and the performance has been studied.

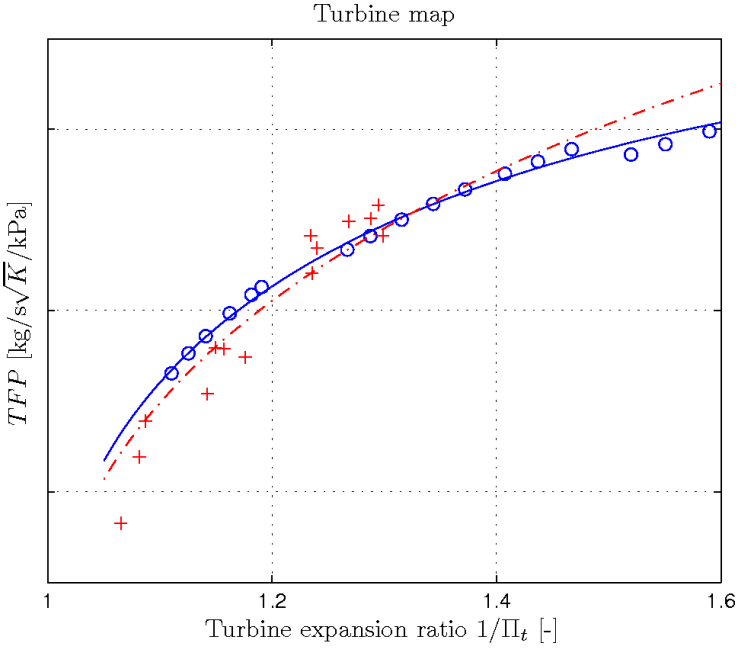

Figure 14: This figure shows the turbine map measured in the engine test stand (red crosses and dashed dotted line) compared to the map measured in the gas stand (blue circles and solid line). The reachable pressure ratios are though, as described in the text, rather limited. The two lines are a least squares fitted standard model ($\dot{m}_t = c_1\sqrt{1-\Pi_t^{c_2}}$, see e.g. [6]) to better show the differences.

The added extra throttle upstream of the first compressor stage is shown to increase the reachable region of the turbo map.

It is shown that the procedure produces turbocharger performance data that matches well with those from a gas stand. The compressor map has been given most attention in the paper, but the turbine flow capacity is also studied.

A theoretical analysis shows how the engine operating limits are transformed to the reachable points in the compressor performance map. One important result is that it is beneficial to have a throttle at the compressor inlet, which will increase the reachable region in terms of the corrected compressor mass flow. The results from the theoretical analysis are confirmed experimentally.

A control structure based on SISO controllers is also proposed and it shows how the turbocharger and engine test bench can be controlled in a systematic manner to support the performance mapping procedure. This control structure has been applied in the engine test cell.

Two methods for adjusting the measured compressor data, when there are deviations between the measured speed and that which is desired when constructing a speed-line, have been proposed and investigated. The results show that the description of the speed line is improved and it was most clear for higher flows.

References

[1] Andersson, P. (2005). *Air Charge Estimation in Turbocharged Spark Ignition Engines*. PhD thesis 989, Linköping University.

[2] Chapman, K. S. & Shultz, J. (2003). *Guidelines for: Testing Large-Bore Engine Turbochargers*. Technical report, The National Gas Machinery Laboratory, Kansas State University, 245 Levee Drive.

[3] Dixon, S. (1998). *Fluid Mechanics and Thermodynamics of Turbomachinery*. Butterworth-Heinemann, 4th edition.

[4] Eriksson, L. (2002). Mean value models for exhaust system temperatures. *SAE I.J. of Engines*, 111(3).

[5] Eriksson, L. (2007). Modeling and control of turbocharged SI and DI engines. *Oil & Gas Science and Technology - Rev. IFP*, 62(4), 523–538.

[6] Eriksson, L., Nielsen, L., Brugård, J., Bergström, J., Pettersson, F., & Andersson, P. (2002). Modeling of a turbocharged SI engine. *Annual Reviews in Control*, 26(1), 129–137.

[7] Heywood, J. B. (1988). *Internal Combustion Engine Fundamentals*. McGraw-Hill series in mechanical engineering. McGraw-Hill.

[8] Lewis, R. I. (1996). *Turbomachinery Performance Analysis*. Arnold.

[9] Nilsson, Y., Eriksson, L., & Gunnarsson, M. (2006). Modelling for fuel optimal control of SI VCR engines. In *Proc. of New Trends in Engine Control, Simulation and Modelling* IFP, Rueil-Malmasison, France.

[10] SAE standard (1995a). J1826 – Turbocharger Gas Stand Test Code.

[11] SAE standard (1995b). J922 – Turbocharger Nomenclature and Terminology.

[12] Shaaban, S. (2004). *Experimental Investigation and Extended Simulation of Turbocharger Non-adiabatic Performance*. PhD thesis, Leibniz Universität Hannover.

[13] Sorenson, S. C., Hendricks, E., Magnusson, S., & Bertelsen, A. (2005). Compact and accurate turbocharger modelling for engine control. In *SAE World Congr. Electronic Engine Controls 2005 (SP-1975)*, Techn. Paper 2005-01-1942.

[14] Watson, N. & Janota, M. (1982). *Turbocharging the internal combustion engine*. MacMillan London.

[15] Zinner, K. (1985). *Aufladung von Verbrennungsmotoren. Grundlagen, Berechnungen, Ausführungen*. Springer Verlag.

A Dimensionless Numbers

For compressible flows there is a set of dimensionless numbers that are used in a central way when describing the compressor performance. Their properties and the way that they are used to introduce the corrected quantities are summarized in this appendix.

Dimensional analysis

Dimensional analysis gives insight into what effects and dependencies are important for the performance. In particular the measurements and determination of the turbo charger performance rely upon these to reduce the number of necessary measurements and to give a compact description of the performance.

A major benefit of using dimensionless numbers is that they reduce the amount of expensive measurements needed for determining turbocharger performance. A turbochargers performance is determined from measurements taken at several operating points with given inlet pressure, inlet temperature, mass flow, etc. To be able to use the measured performance we want to know how it changes with for example the inlet pressure, covering low and high altitudes, or temperature covering winter and summer driving. Dimensionless numbers give insight into many of these dependencies and reduces the number of necessary measurements. Furthermore, dimensionless numbers are also directly useful when modeling compressors and turbines.

Dimensionless numbers and their usage for determining turbo-machinery performance is given in [14, 8], and they are summarized below. The three performance parameters: isentropic stagnation enthalpy

$$\Delta h_{01} = c_p\, T_{01} \left[(p_{02}/p_{01})^{(\gamma-1)/\gamma} - 1 \right]$$

efficiency η, and delivered power P have the following functional expressions for a turbo-machine that operates with a compressible working fluid

$$[\Delta h_{01}, \eta, P] = f(D, N, \dot{m}, \rho_{01}, a_{01}, \mu, \gamma)$$

here the performance depends upon D–diameter, ρ_{01}–inlet density, $\dot{m}$–mass flow, N–rotational speed, a_{01}–inlet stagnation speed of sound, μ–dynamic viscosity, γ–ratio of specific heats. Modeling of the compressor is the task of determining the three functions $f(\ldots)$ above. This task is promoted by the dimensional analysis which reduces the dimensions to the following quantities (see e.g. [3])

$$\Psi = \frac{\Delta h_{0s}}{N^2\,D^2} = \quad f_1(\frac{\dot{m}}{\rho_{01}\,N\,D^3}, \frac{\rho_{01}\,N\,D^2}{\mu}, \frac{N\,D}{a_{01}}, \gamma) \tag{20}$$

$$\eta = \qquad\qquad f_2(\frac{\dot{m}}{\rho_{01}\,N\,D^3}, \frac{\rho_{01}\,N\,D^2}{\mu}, \frac{N\,D}{a_{01}}, \gamma) \tag{21}$$

$$\hat{P} = \frac{P}{\rho\,N^3\,D^5} = f_3(\frac{\dot{m}}{\rho_{01}\,N\,D^3}, \frac{\rho_{01}\,N\,D^2}{\mu}, \frac{N\,D}{a_{01}}, \gamma) \tag{22}$$

where $Re = \frac{\rho_{01}\,N\,D^2}{\mu}$ is a form of Reynolds number, ND/a_{01} is called the blade Mach number, and

$$\Phi = \frac{\dot{m}}{\rho_{01}\,N\,D^3} \tag{23}$$

is called the flow coefficient. The full expression for the head coefficient expressed using measured quantities is

$$\Psi = \frac{c_p\,T_{01}\left[\left(\frac{p_{02}}{p_{01}}\right)^{\frac{\gamma-1}{\gamma}} - 1\right]}{N^2\,D^2} \tag{24}$$

Corrected quantities

For an ideal gas the third dimensionless group is substituted into the first, and Ψ is exchanged for pressure ratio. The power parameter is also exchanged for the temperature quotient. With these manipulations the following expressions and variables are used.

$$\frac{p_{02}}{p_{01}}, \eta, \frac{\Delta T_0}{T_{01}} = f(\frac{\dot{m}\,\sqrt{R\,T_{01}}}{D^2\,p_{01}}, \frac{N\,D}{\sqrt{R\,T_{01}}}, Re, \gamma) \tag{25}$$

The influence of the Reynolds number is usually small, so it is often disregarded. Finally, when the performance is studied for a machine of given size and given fluid then R, γ, D remain constant and are therefore left out

$$\frac{p_{02}}{p_{01}}, \eta, \frac{\Delta T_0}{T_{01}} = f(\frac{\dot{m}\,\sqrt{T_{01}}}{p_{01}}, \frac{N}{\sqrt{T_{01}}})$$

Note that the independent variables in the last expression are not dimensionless and these quantities are named *corrected mass flow* and *corrected speed*

$$\dot{m}_{corr} = \frac{\dot{m},\sqrt{T_{01}}}{p_{01}}, \qquad N_{corr} = \frac{N}{\sqrt{T_{01}}}$$

Compressor and turbine data are represented using maps with either those corrected quantities given above or the following ones that are also called *corrected mass flow* and *corrected speed*

$$\dot{m}_{corr} = \frac{\dot{m}, \sqrt{(T_{01}/T_{ref})}}{(p_{01}/p_{ref})}, \qquad N_{corr} = \frac{N}{\sqrt{(T_{01}/T_{ref})}} \tag{26}$$

where T_{ref} and p_{ref} are reference conditions. In the majority of the turbocharger data reported in this paper the last one is most common but both are used. It is thus important to be very careful when interpreting the performance maps that are provided by manufacturer.

Paper 3

Investigation of compressor correction quantities for automotive applications[†]

3

Oskar Leufvén and Lars Eriksson

Vehicular Systems, Department of Electrical Engineering, Linköping University, S-581 83 Linköping, Sweden.

Abstract

Turbo performance is represented using maps, measured for one set of inlet conditions. Corrections are then applied to scale the performance to other inlet conditions. A turbo compressor for automotive applications experiences large variations in inlet conditions, and the use of two stage charging increases these variations. The variations are the motivation for analyzing the correction quantities and their validity. A novel surge avoidance strategy is found in the correction equations, where the result is that a reduction in inlet pressure can increase the surge margin of eight studied maps. The method for investigating the applicability of the strategy is general.

An experimental analysis of the applicability of the commonly used correction factors, used when estimating compressor performance for varying inlet conditions, is presented. A set of experimental measurements from an engine test cell and from a gas stand shows a small, but clearly measurable trend, with decreasing compressor pressure ratio for decreasing compressor inlet pressure. A method is developed, enabling measurements to be analyzed with modified corrections.

An adjusted shaft speed correction quantity is proposed, incorporating also the inlet pressure in the shaft speed correction. The resulting decrease in high altitude engine performance, due to compressor limitations, are quantified and shows a reduction in altitude of $200 - 600$ m, for when engine torque has to be reduced due to limited compressor operation.

[†]This is a formatted version of "Investigation of compressor correction quantities for automotive applications" by Oskar Leufvén and Lars Eriksson, and the final, definite version of this paper has been published in International Journal of Engine Research Volume 13/Issue 6, December/2012 by SAGE Publications Ltd, All rights reserved. ©Oskar Leufvén and Lars Eriksson. The original paper can be found at `http://online.sagepub.com`, doi: `10.1177/1468087412439018`. The formatting is restricted to changing the article into a single-column format, adjusting sizes of figures and tables, and adjusting the referencing style.

1 Introduction

Downsizing with turbocharging is a common way to decrease vehicle fuel consumption [9, 19], where the turbo performance is important for retaining vehicle drivability and consumer acceptance [1]. Turbo compressor performance is characterized by a map, describing the properties of the compressor. The goal with the map, is to describe turbocharger performance, so that it covers the full operating region of the compressor. However, when turbocharger performance is measured, the characteristics obtained are valid for the inlet conditions under which the measurements were conducted. To overcome this deficiency, different correction factors are applied to scale the performance variables to cover other inlet conditions.

The correction factors are based on dimensional analysis of the compression system [18], and are used in the SAE standards [22, 23]. The SAE standards for measuring and correcting turbo data are commonly used in the automotive community. This paper investigates compressor inlet variations and evaluates the accuracy of the SAE correction quantities for the compressor side.

1.1 Outline and contributions

Section 1.2 presents compressor maps, the commonly used inlet corrections, and a compressor model used in the paper. Section 2 contributes with an investigation of inlet conditions for automotive compressors, showing that compressors, especially in a two stage system, experience large variations in correction quantities. Section 2.2 highlights the increase of up to 50 % in air filter pressure drop, due to the decreasing ambient gas density with altitude.

Section 3 contributes with a novel surge avoidance method, and presents altitude dependent engine torque lines, using the nominal corrections. Section 4 presents measurements of compressor performance, at different inlet conditions, from an engine test stand and a gas stand. Section 5 proposes modifications to the commonly used correction quantities, based on the experimental findings and develops a method for analyzing measured data, if the correction quantities are changed. The key result is that an increased fit to measured data is found if also inlet pressure is included in the compressor shaft speed correction.

The effect on the altitude dependent engine torque lines, due to modifications of the corrections are quantified in Section 6. A reduction in altitude of 200 – 600 m, for when engine torque has to be reduced to due limited compressor operation is found.

1.2 Compressor map and inlet correction

A compressor map presents compressor performance data normalized to a reference standard compressor inlet temperature, T_{std} and pressure, p_{std}. These reference conditions are a key component of the map, and must be provided with the map. Frequently used standard conditions are $p_{std} = 100$ kPa and $T_{std} = 298$ K. Standardization documents for how to measure and present corrected map data are given in e.g. [4, 22], and Fig. 1 presents an example of a

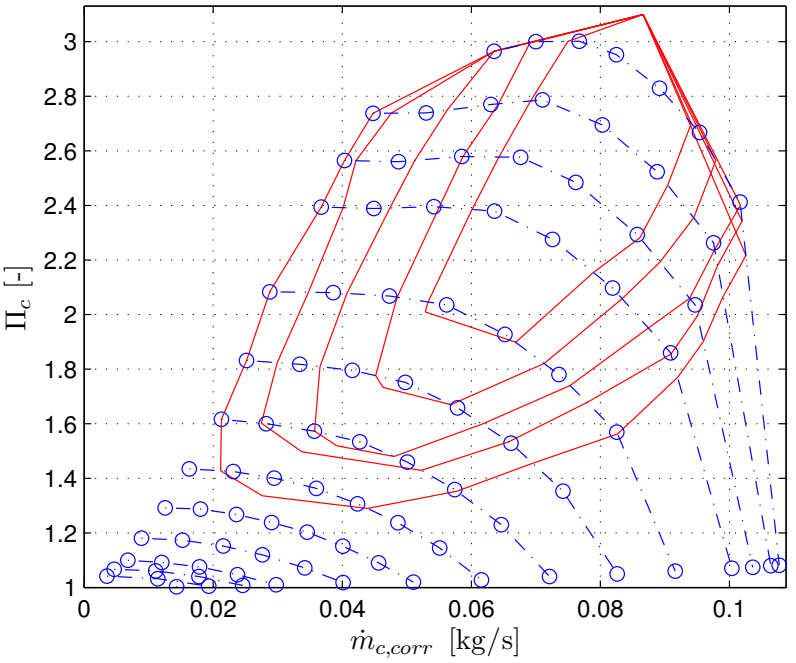

Figure 1: Compressor speed lines shown as dash dotted lines, connecting map points $(\dot{m}_{c,corr}, \Pi_c)$, marked with circles, with equal corrected compressor speed $N_{tc,corr}$. Solid lines show contours of constant compressor adiabatic efficiency η_c.

compressor map. The basis for these correction factors come from dimensional analysis (see e.g. [26]), and derivations of the correction factors can be found in e.g. [27, 12]. The ratio of actual inlet pressure and temperature to these standard states are used to adjust the performance variables, and are here defined

$$\begin{aligned} \delta &= {}^{\mathrm{p}_{01}}/_{\mathrm{p}_{\mathrm{std}}} \\ \theta &= {}^{\mathrm{T}_{01}}/_{\mathrm{T}_{\mathrm{std}}} \end{aligned} \tag{1}$$

where p_{01} and T_{01} are the compressor inlet pressure and temperature, respectively. Compressor pressure ratio is given by

$$\Pi_c = \frac{p_{02}}{p_{01}} \tag{2}$$

where p_{02} is the outlet pressure. The corrected compressor mass flow is given by

$$\dot{m}_{c,corr} = \dot{m}_c \frac{\sqrt{{}^{\mathrm{T}_{01}}/_{\mathrm{T}_{\mathrm{std}}}}}{({}^{\mathrm{p}_{01}}/_{\mathrm{p}_{\mathrm{std}}})} = \dot{m}_c \frac{\sqrt{\theta}}{\delta} \tag{3}$$

where $\dot{m}_c$ is the compressor mass flow. The corrected compressor speed is given by

$$N_{tc,corr} = N_{tc} \frac{1}{\sqrt{\mathrm{T}_{01}/\mathrm{T}_{\mathrm{std}}}} = N_{tc} \frac{1}{\sqrt{\theta}} \tag{4}$$

with actual turbo speed N_{tc}. Points of equal $N_{tc,corr}$ in the compressor map, are usually connected to form what is known as a compressor speed line. Speed lines are measured from the surge line, to the left in the compressor map, to a choked flow, or until η_c has dropped too much, to the right. Connecting the points of each speed line with lowest mass flow approximates the surge line of the compressor, and indicates the boundary of stable compressor operation. Turbo shaft speeds are measured up to the maximum allowable, $N_{tc,max}$. Raising the speed further, known as over speeding [21], can destroy the turbo.

The adiabatic efficiency, η_c, is also presented for each point, describing how efficiently the compression process is, compared to an adiabatic. Contours of constant η_c are superimposed on the speed lines in Fig. 1.

The connection between inlet conditions and correction quantities is shown in Fig. 2, where solid lines show constant mass flow scaling factor $\sqrt{\theta}/\delta$, and dash dotted lines show constant shaft speed scaling factor $1/\sqrt{\theta}$, as function of inlet conditions.

Compressor speed line modelling

An Ellipse compressor model, described in detail in [15, 17], will be used in the following sections. The equation to model a single speed line is

$$\Pi_c = \left[1 - \left(\frac{\dot{m}_{c,corr} - c_4}{c_3 - c_4}\right)^{c_1}\right]^{1/c_2} c_5 \tag{1.5a}$$

where the $c_i,\ i \in [1, 5]$ are the speed line model parameters. A complete compressor model results, if c_i are instead basis functions according to

$$c_1 = c_{1,0} + c_{1,1} N_{tc,corr} \tag{1.5b}$$
$$c_2 = c_{2,0} + c_{2,1} N_{tc,corr}^{c_{2,2}} \tag{1.5c}$$
$$c_3 = c_{3,0} + c_{3,1} N_{tc,corr} \tag{1.5d}$$
$$c_4 = 0 + c_{4,1} N_{tc,corr}^{c_{4,2}} \tag{1.5e}$$
$$c_5 = 1 + c_{5,1} N_{tc,corr}^{c_{5,2}} \tag{1.5f}$$

where $c_{i,j}$ are the 11 model parameters for a compressor model (1.5a-f). Eight compressor maps (A-H) will be used in the analysis, in the following sections. The mean relative model errors for $\eta_c > 60$ %-points are < 1 %, and the corresponding standard deviations are < 3 %, with further improvement if fitted to a single speed line. The maximum mass flow for the maps range from $\approx$0.1 kg/s (A), up to $\approx$0.3 kg/s (H), and Fig. 3 shows the model fit.

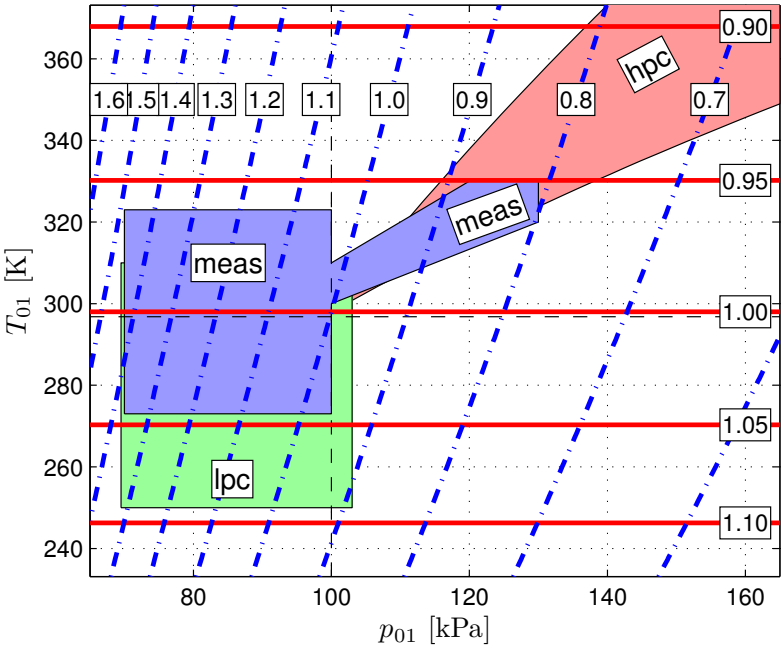

Figure 2: Isolines of compressor performance variable scaling values, as function of inlet conditions. Solid, horizontal, lines show $1/\sqrt{\theta}$ and dash dotted lines show $\sqrt{\theta}/\delta$. The standard reference states $p_{std} = 100$ kPa and $T_{std} = 298$ K are also marked as dashed lines. Corrected and actual quantities are equal only at the intersection of these lines. Inlet conditions associated with a significant coverage of single stage automotive compressors is marked with "lpc", and high pressure stage compressor operation (for a two stage system) is marked "hpc". The region marked with "meas" is the grid for measurements in Section 4.

2 Inlet conditions for automotive compressors

The compressor inlet gas state depends on both changes in ambient conditions, as well as on the engine subsystems affecting the gas before the compressor inlet.

2.1 Variations in ambient conditions

In order to find what values of (p_{amb}, T_{amb}) that are common for automotive turbochargers one needs to know how and where the system is used.

Ambient pressure variations

Roads are found at altitudes from below -400 m to more than 5000 m. Most vehicles are found at less extreme altitudes, and for a significant coverage of

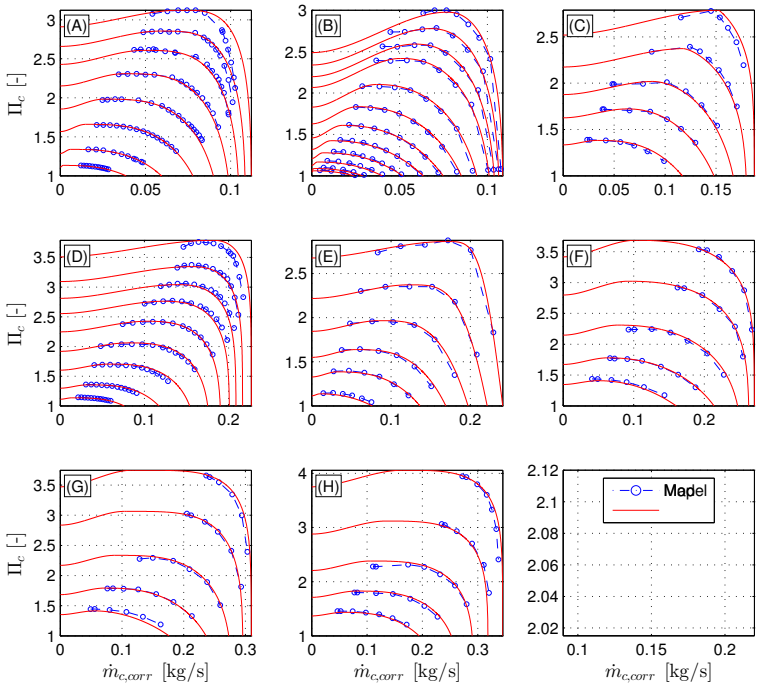

Figure 3: Eight compressor maps shown with circles connected by dash dotted lines, and the fit of the Ellipse model in (1.5a-f).

automotive engine applications

$$h_{sig} \in [-100, 3000] \text{ m} \tag{6}$$

is assumed to be sufficient. This smaller interval also helps reduce the cost of the experimental tests that cover the intervals. The close connection between altitude and pressure can be modeled [20]

$$p_{amb}(h) = p_b \left\{ T_b / \left[T_b - L_b (h - h_b) \right] \right\}^{\left(\frac{g_b M_b}{R L_b} \right)} \tag{7}$$

with $p_b = 101.3$ kPa, $T_b = 288.15$ K, $R = 8.31$ J/(mol K), $h =$ altitude m, $h_b = 0$ m, $g_b = 9.807$ m/s^2, $L_b = -0.0065$ K/m and $M_b = 28.96$ kg/ (k mol). The ambient pressure variations due to altitude can be found using (7), and for the interval (6) this is

$$p_{amb,sig} \in [70, 103] \text{ kPa} \tag{8}$$

and is presented in Fig. 4.4(b). It is seen that $p_{amb}(h)$ is approximately a straight line. Normal ambient pressure variations due to weather, are smaller than those due to altitude, see Fig. 4.4(a), and are for the following investigations considered to be included in the interval (8).

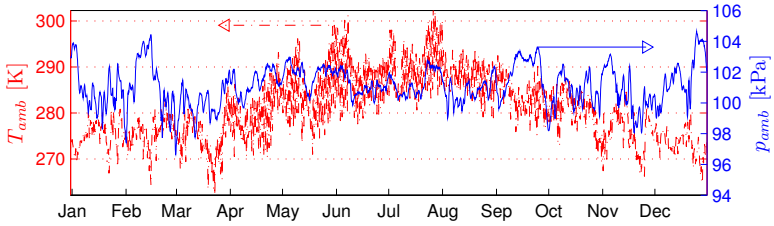

(a) Measurements of ambient conditions during one year.

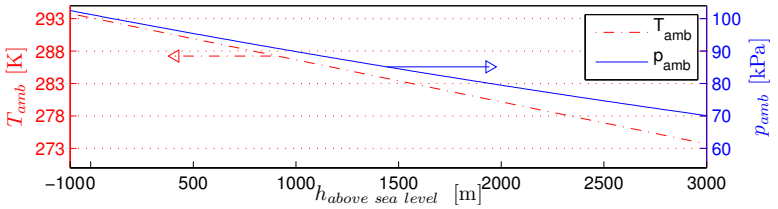

(b) $T_{amb}(h)$ and $p_{amb}(h)$ according to (7) and (10).

Figure 4: Summary of the variations in ambient pressures and temperature due to altitude and seasonal changes. Upper: Measurements of ambient conditions of Malmen meteorological station. Both T_{amb} and p_{amb} vary approximately 10% over the year. Lower: Temperature and pressure vs. altitude using (7) and (10).

Ambient temperature variations

Extremes in measured ambient temperature shows values of $T_{amb} \in [184, 331]$ K. Significant coverage of engine operations is reached for a narrower temperature interval

$$T_{amb,sig} \in [250, 310] \text{ K} \tag{9}$$

Ambient temperature can be modelled as [13]

$$T_{amb} = T_{ref,sea} + L_b h \tag{10}$$

where $T_{ref,sea} = 293.15$ K. The result of using (10) for the intervall given in (6) is presented in Fig. 4.4(b), and is a straight line. Fig. 4.4(a) presents an example of a temperature trace for one year, of Malmen meteorological station.

Two stage system

The temperature and pressure after the first compressor stage, are the inlet conditions of the second stage. For a two stage system the quotient between the pressure ratio of the high pressure stage, Π_{hpc}, and the pressure ratio of the low pressure stage, Π_{lpc}, is defined

$$\Gamma = {}^{\Pi_{\mathrm{hpc}}}/_{\Pi_{\mathrm{lpc}}} \tag{11}$$

and the total compression system pressure ratio is given by the ratio of high pressure stage outlet pressure p_{hpc} to first stage inlet pressure p_{01}

$$\Pi_{tot} = \Pi_{lpc} \cdot \Pi_{hpc} = {}^{\mathrm{p_{hpc}}}/_{\mathrm{p_{01}}} \tag{12}$$

where p_{01} is the total pressure at the first stage inlet. The Γ-value describes how much of the total pressure increase that is done by the second stage compared to the first. To avoid a pressure loss over either of the compressor stages, the following must hold

$$\frac{1}{\Pi_{tot}} < \Gamma < \Pi_{tot} \tag{13}$$

Compressor outlet temperature, T_{01}, can be modeled

$$T_{02} = \left(\frac{\Pi_c^{\frac{\gamma-1}{\gamma}} - 1}{\eta_c} + 1 \right) T_{01} \tag{14}$$

with $\Pi_c = p_{02}/p_{01}$.

2.2 Air filter and intercooler

Apart from changes in p_{amb} and T_{amb}, the engine installation also affects the gas on its way to the compressor inlet. p_{01} for automotive applications, is expected to be slightly lower than p_{amb}, because the air filter and pipes between compressor inlet and ambient restrict the air flow, resulting in a pressure loss $\Delta p_{af} = p_{amb} - p_{01}$. A general restriction for a compressible flow [12] can be used to model an air filter restriction as

$$\dot{m} = \frac{C_d A p_{amb}}{\sqrt{R T_{amb}}} \left(\frac{p_{01}}{p_{amb}} \right)^{\frac{1}{\gamma}} \sqrt{\frac{2\gamma}{\gamma - 1} \left[1 - \left(\frac{p_{01}}{p_{amb}} \right)^{\frac{\gamma-1}{\gamma}} \right]} \tag{15}$$

where $C_d A$ is normally lumped together and referred to as effective flow area, and it is important to note that the resulting pressure drop depends on the ambient gas state. The pressure drop, for a system having $\Delta p_{af} = 3$ kPa at $T_{amb} = T_{std}$, $p_{amb} = p_{std}$, increases 50 % at $p_{amb} = 70$ kPa, due to the decreased ambient gas density. The largest increase in Δp_{af} from varying T_{amb} according to (9), is 7 %.

The upper plot of Fig. 5 shows the result of (15) for different values of $C_d A$ as a function of $\dot{m}$, with $p_{amb} = 100$ kPa and $T_{amb} = 298$ K. Values of Δp_{af} can be found in the literature [3, 10, 14], and are usually in the range of $\Delta p_{af} \in [3, 8]$ kPa.

Also the intercooler and pipes after the compressor are important when establishing the map operating point. The temperature of the gas after the compressor depends on the operating point, according to (14). Values of pressure drops caused by the intercooler can be found in the literature [3, 10], and are usually in the range of $\Delta p_{ic} \in [5, 15]$ kPa.

Fig. 2 presents a summary of the expected changes in ambient conditions, as well as estimated changes in the second stage inlet conditions covering $\delta \in$

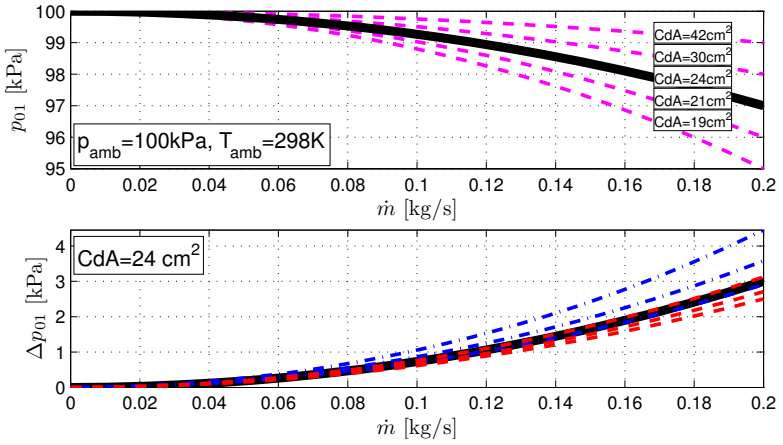

Figure 5: Pressure drop from ambient to compressor inlet, $\Delta p_{af} = p_{amb} - p_{01}$. Upper plot: p_{01} as function of mass flow for different C_dA-values and constant (p_{amb}, T_{amb}). Lower plot: dash dotted line shows Δp_{af} as a function of different $p_{amb} \in [70, 103]$ kPa (with $T_{amb} = 298$ K), and dashed as a function $T_{amb} \in [250, 310]$K (with $p_{amb} = 100$ kPa). The thick solid line in both plots is for $C_dA = 24\,cm^2$, $p_{amb} = 100$ kPa and $T_{amb} = 298$ K as a reference.

$[0.9, 1.5]$ and in $\theta \in [0.9, 1.1]$. Note however that pressure is expected to be even lower due to e.g. an air filter restriction, and the effect from heat transfer is not included in the figure. Fig. 2 also shows inlet conditions for the second stage compressor marked with hpc, calculated as first stage outlet states using (2) and (14) with $\eta_c \in [40, 90]$ %, $p_{01} = p_{std}$ and $T_{01} = T_{std}$.

3 Automotive examples

The corrections (3) and (4) and a map have direct automotive control implications, and this section exemplifies it through two applications. Opportunities for a novel way to control surge is presented first. Secondly, the investigations from Section 2, and a map, are used to calculate an altitude dependent engine torque line. Three different limits are taken into account: Compressor surge (CS), turbo over speed (TOS), and the extreme point where the maximum allowable pressure ratio of the map is utilized (Π_{max}). Π_{max} is always at the TOS-limit and at max Π_c of the map. The second example is used again in Section 6, with modified corrections (3) and (4).

3.1 Opportunities for novel surge control

The change in operating point coming from a decrease in p_{01} is given by (2) and (3), and the dash dotted lines in Fig. 6 show the associated translation in the map. It is seen that the lines have a large positive slope, and all go through

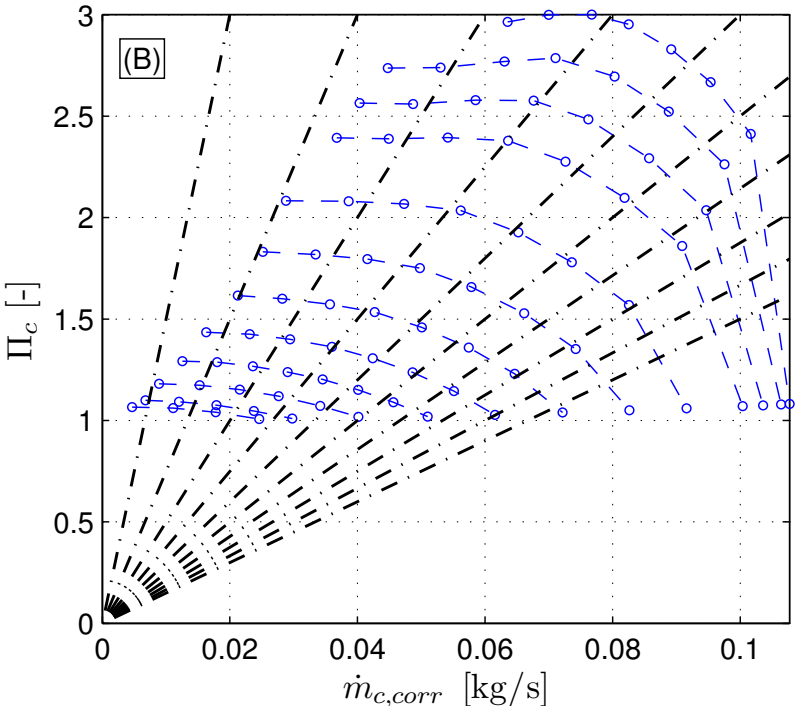

Figure 6: The dash dotted lines represent the translation asymptote in a map, due to a change in p_{01}, and are superimposed on Compressor map (B). The straight dash dotted lines are given by holding p_{02}, T_{01} and $\dot{m}_c$ constant and calculating $\dot{m}_{c,corr}$ and Π_c in (2) and (3), thus giving the change in compressor map operating point from throttling the compressor inlet.

$(\dot{m}_{c,corr}, \Pi_c) = (0, 0)$ for $p_{01} = \infty$. The lines also reveal that decreasing p_{01} can give a novel way to increase the margin to the surge line. If a new operating point, after a decrease in p_{01}, is further away from the surge line depends on the surge line slope, for the studied Π_c.

The question is whether there exist map points, where a decrease in p_{01} increases the surge margin. The method to answer this question is as follows. Find the line from Fig. 6, that has the same slope as the surge line, for the studied Π_c-range. Superimpose this line on the compressor map, and any point in the map, that is right of this dash dotted line, for the studied Π_c-range, will see an increase in surge margin for a decrease in p_{01}. Fig. 7 presents areas, for maps A-H, were the surge margin is increased for a decrease in p_{01}. It can be seen that such areas exist, also close to the surge line. The method to use the dash dotted lines of Fig. 6 and a map is general, and can be used for any map.

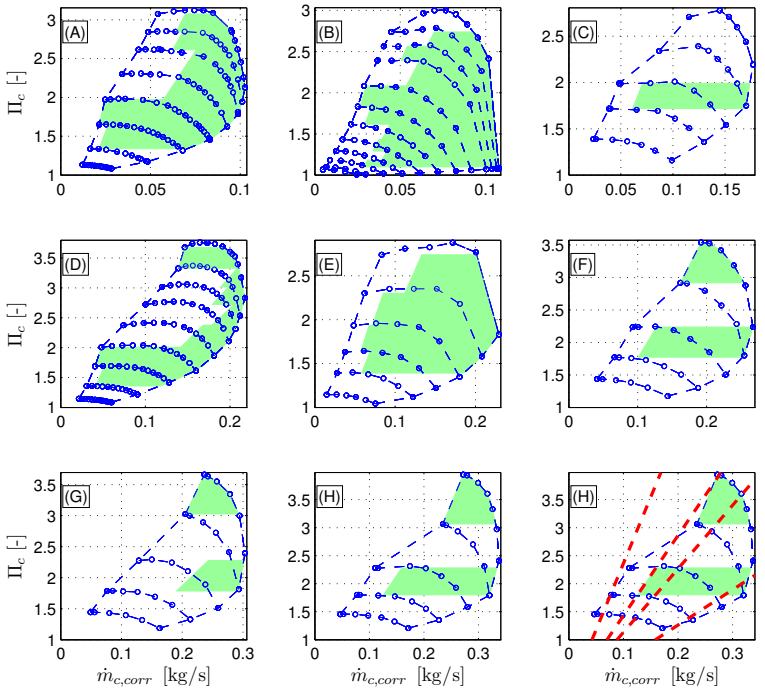

Figure 7: Map areas were the points are such that a decrease in p_{01} increases the surge margin. The lower right plot shows the lines with the same slope, as the straight lines making up the surge line, for map (H), but originating in (0,0). Corresponding lines are used to assess the marked areas of all maps (A-H).

3.2 Max torque line vs. altitude

The compressor map can be used to calculate an altitude dependent maximum engine torque line, using e.g. a volumetric efficiency engine model. This section presents such calculations with the correction quantities given by (3) and (4) for the maps (A-H). This issue will be returned to in Section 6, where modified corrections are used. The allowable map region, giving the potential engine torque, is limited by CS, TOS and Π_{max}. p_{amb} and T_{amb} are connected to altitude using (7) and (10).

The outer contour of the stable compressor operating region, gives the maximum allowable Π_c, for a mass flow. The outer contour consists of the maximum allowable corrected shaft speed, $N_{tc,corr,max}$ and the surge line. Maximum allowable corrected shaft speed is given by $N_{tc,corr,max} = {}^{\mathrm{N_{tc,max}}}/\sqrt{{}^{\mathrm{T_{01}}}/_{\mathrm{T_{std}}}}$, and depends on T_{01}. This speed line is modeled using (1.5a). The surge line is given by each map.

Maximum engine torque is assumed achievable, if an intake manifold pres-

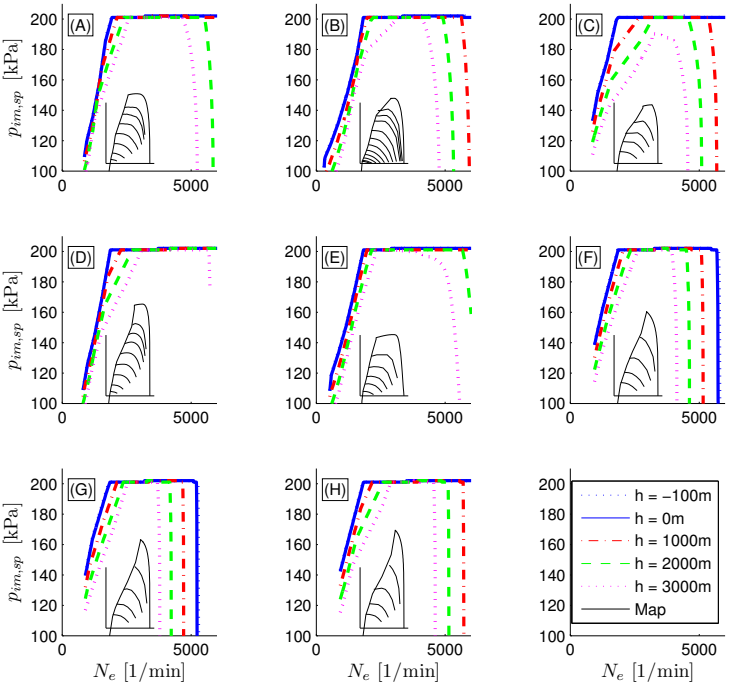

Figure 8: Lines showing for which N_e a $p_{im,sp} = 200$ kPa is achievable as a function of altitude $h \in [-100, 0, 1000, 2000, 3000]$ m. Each subplot contains a picture of the corresponding map, to show the close coupling of the allowable map region and the achievable $p_{im,sp}$.

sure set point of $p_{im,sp} = 200$ kPa, is achievable. Different engine models, based on volumetric efficiency, are assumed for each map (A-H). The volumetric efficiency is assumed to give an mass flow, $\dot{m}_{2k}$, at an engine speed of $N_e = 2000$ 1/min and at $p_{im,sp} = 200$ kPa. $\dot{m}_{2k}$ is taken from each map (A-H), as 110 % of the surge mass flow at $\Pi_c = 2, \theta = 1, \delta = 1$. The volumetric efficiency is further assumed to give $2.5 \cdot \dot{m}_{2k}$ at $N_e = 5000$ 1/min and $p_{im,sp} = 200$ kPa. This N_e-range corresponds to torque/speed characteristics commonly found in modern TC engines. Π_c is given by air filter and intercooler models according to Section 2.2. Fig. 8 shows the resulting engine torque lines, along with a small map in each subplot, to emphasize the coupling of the allowable map region and the achievable $p_{im,sp}$. Table 1 presents the altitudes where engine torque has to be reduced, due to the CS, TOS, or Π_{max}-limit. CS gives the altitude where $p_{im,sp}$ no longer can be reached for $N_e = 2000$ 1/min, TOS the corresponding value for $N_e = 5000$ 1/min and Π_{max} finally gives the limit where $p_{im,sp}$ has to be reduced independent of $N_e \in [2000, 5000]$ 1/min. CS restricts engine torque before $h = 3000$ m, for all maps. TOS restricts all

Table 1: Altitude where engine torque is reduced, due to the limits (CS, TOS, Π_{max}) discussed in Section 3.2, for maps (A-H).

Map limits		(A)	(B)	(C)	(D)	(E)	(F)	(G)	(H)
CS	m	480	1240	230	460	1310	820	610	620
TOS	m	2660	1900	1490	4040	2650	1150	390	2200
Π_{max}	m	3840	3290	2550	5510	3030	4920	5210	5870

but map (D). Map (C) is restricted by the Π_{max}-limit before $h = 3000$ m. A narrow map width means difficulties with a wide mass flow range, e.g. map (G). The maps with best estimated low engine speed torque, have a surge line with steep positive slope, e.g. map (B) or (E). To be least limited by Π_{max}, a map needs a large maximum Π_c at $N_{tc,max}$, e.g. map (F). It is important to note that these calculations are given by, not only the compressor map, but also by the corrections (3) and (4).

4 Experimental investigation of correction quantities

This section presents speed lines, measured at different compressor inlet conditions. An engine test stand measurement is first presented, focusing on the low pressure stage inlet conditions from Section 2. A presentation of measurements, from an independent gas stand, focusing on high pressure stage inlet conditions, then follows.

4.1 Engine test stand measurements

The test setup consists of a 2 L spark ignited direct injected engine with a two stage turbo system installed in an engine test cell. A schematic picture of the laboratory and measurement setup, used to vary the compressor inlet conditions, is presented in Fig. 9. The temperature and pressure of the air surrounding the compressors under study were not changed during the experiments, only the conditions in the straight pipe leading up to the compressor inlet. The effect from changes in heat transfer were therefore considered negligible. Sensors used were Kistler pressure sensors (models 4295/4260), Pentronic K-type thermocouples, PicoTurn shaft speed sensors, a Laminar Flow Element (LFE) mass flow sensor (custom built by the Technical University Denmark), and a Bosch HFM2C hot film air mass flow sensor. All signals were sampled using an HPE1415-module in an HP VXi main frame.

Low inlet temperature measurements are achieved using cold outside air. High inlet temperatures are created using electrical heating. Compressor inlet pressures are reduced using an extra throttle upstream the compressor inlet. An air filter follows the extra throttle. A straight pipe, approximately 80 cm in length, then leads up to the first stage compressor inlet. The instrumentation for the first stage inlet conditions is fitted to the straight pipe, to minimize influence from uneven distributed flow. Multiple sensors $(p, T, \dot{m})$ were fitted, to enable

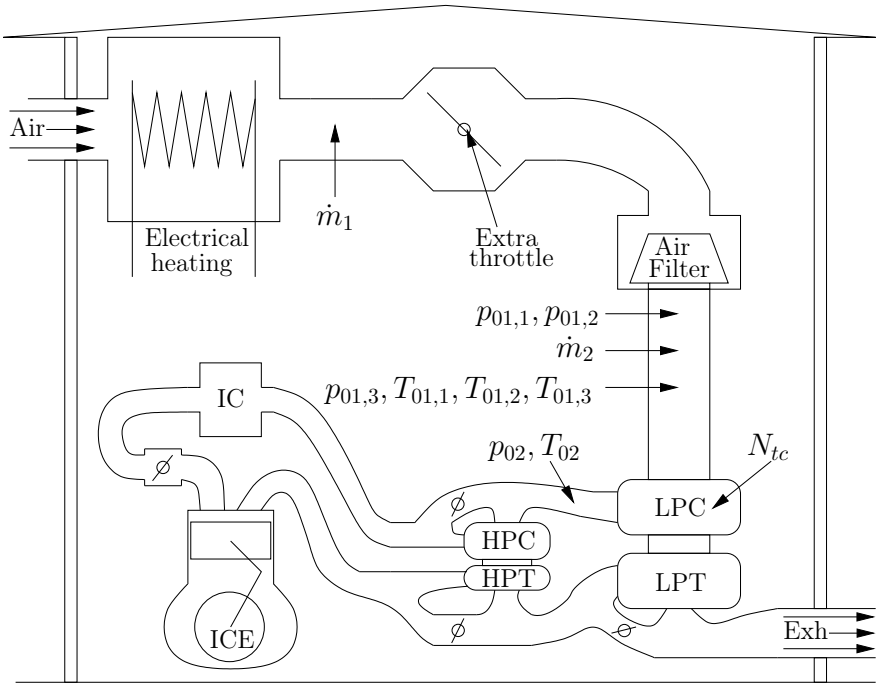

Figure 9: Schematic picture of the laboratory and engine test stand setup. Ambient air comes in from top left and can be electrically heated. The extra throttle is used to decrease p_{01}. An air filter is followed by three pressure ($p_{01,i}$) and temperature sensors ($T_{01,i}$), and a mass flow sensor ($\dot{m}_2$) before the compressor inlet. An extra mass flow sensor is installed before the extra throttle for diagnosis purposes. p_{02} and T_{02} are measured at the lpc outlet, and turbo shaft speed N_{tc} is measured on the lpc. The air flow runs through the engine, catalyst and the exhaust is expelled to the outside.

diagnose of the sensors. Pressure and temperature after the first compressor stages are measured using a single pair of sensors, since the sensor placement is limited due to packaging constraints. Further, the degrees of freedom are reduced when measuring compressor speed lines in an engine test stand [16].

It is not possible to increase p_{01} during the engine test stand measurements. The pipes and air filter cause a pressure drop, see Section 2.2. This means that it is difficult to reach $p_{01} = 100$ kPa for large mass flows, where the pressure drop is up to 5 kPa. The variation in Reynolds number is commonly assumed to be negligible. Appendix C presents an investigation of the relative changes in Reynolds numbers for the experiments, where the result is that the Reynolds number varies by a factor of two, which is considered to be a small variation.

Table 2: The corrected shaft speeds measured in the engine test stand $N_{tc,corr,sp}$, number of points measured #, and measured grid of inlet conditions. The two last columns show mean absolute relative error $|(\mathrm{N_{tc,corr,sp}}/\mathrm{N_{tc,corr,meas}}) - 1|$, and standard deviation.

$N_{tc,corr,sp}$	#	p_{01} [kPa]	δ [-]	T_{01} [K]	θ [-]	mean	std
103869	275	70–100	0.7–1	273–323	0.92–1.08	0.20%	0.26%
77064	179	80–100	0.8–1	273–323	0.92–1.08	0.18%	0.26%

Low pressure compressor stage - lpc

The speed lines are measured for different combinations of $T_{01} \in [273, 323]$ K and $p_{01} \in [70, 100]$ kPa. All speed lines are measured with constant $N_{tc,corr}$, calculated using (4). The measured grid is schematically shown in Fig. 2 and the resulting speed lines are shown in Fig. 10 with corresponding gas stand speed lines as reference. The compressor performance differs between the engine test stand measurements and in the reference gas stand map. Installation dependent compressor performance is frequently encountered, and is also reported in [21, 5, 11]. The data for the two speed lines presented here, is summarized in Table 2. It can be seen that the mean absolute relative error for the shaft speeds presented was 0.2%, or lower. These small deviations are adjusted for using the techniques, based on dimensionless numbers, developed in [16] (i.e $\Delta\Phi = 0, \Delta\Psi = 0$ for small $\Delta N_{tc} = N_{tc,meas} - N_{tc,sp}$).

The lower speed line of Fig. 10, is limited to measurements with compressor inlet pressure $p_{01} > 80$ kPa, since otherwise $p_{01} \cdot \Pi_c < p_{amb}$, which causes the soft pipes of the engine intake system to collapse as discussed in [16]. Not all T_{01} in the $T_{01,grid}$ of Table 2 are measured for both shaft speeds presented here, a total of nine different T_{01} are measured within the $T_{01,grid}$.

Speed line dependence on p_{01} and T_{01}

Fig. 10 shows measured speed lines, where different symbols are used to indicate measurements from different p_{01}. The points with the lowest p_{01} are generally below these of the second smallest p_{01}, with the trend also visible for the larger p_{01}-points. The speed line model (5a) is therefore used to investigate and visualize a potential p_{01}-dependence. The parameters $c_i, i \in [1, 5]$ of (5a) are fitted to measurements with equal p_{01}, but different T_{01}, to see if there are any trends in the modeled speed lines. The resulting speed lines are presented in Fig. 11. The data shows a clear trend; for the smallest corrected shaft speed the $p_{01} = 100$ kPa-model has the largest Π_c, and the $p_{01} = 80$ kPa-model has the lowest Π_c. The larger $N_{tc,corr}$-lines display the same trend, largest Π_c is found for largest p_{01} given a $\dot{m}_{c,corr}$.

Applying the same methodology to points with equal T_{01}, reveals no trends. For the small corrected shaft speed the lowest temperature line is at the bottom, but then the second highest temperature line follows. The same mixed order is also found for the large corrected speed.

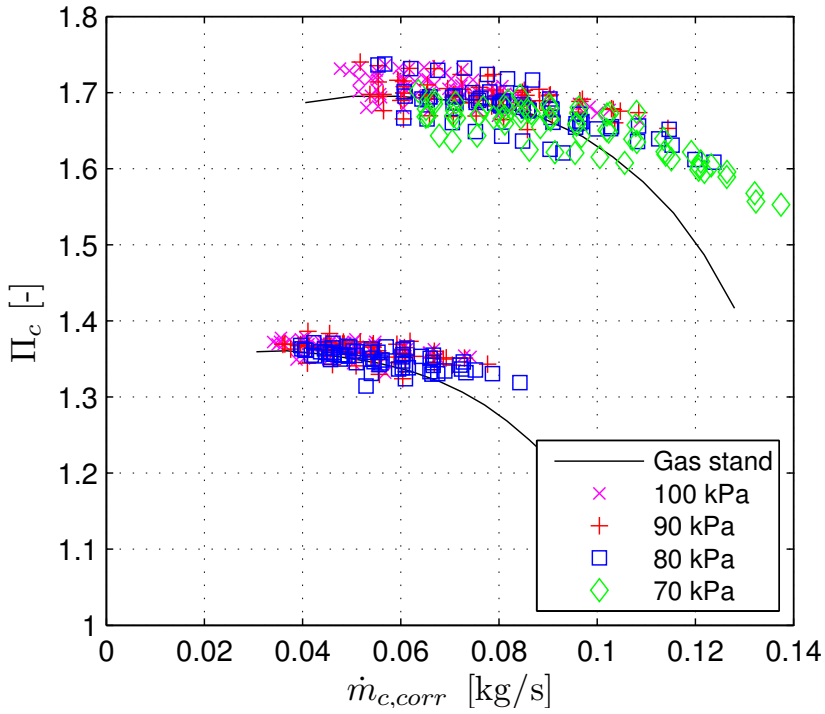

Figure 10: Measured map points from the engine test stand, at different inlet conditions. Solid line are gas stand speed lines as reference. Points with equal $p_{01} = \{70, 80, 90, 100\}$ kPa are marked by equal symbol. The upper speed line will be referred to as the large shaft speed, and the lower as the small shaft speed.

Points with $(\dot{m}_{c,corr}, N_{tc,corr}) = const$

Π_c for points with equal $(\dot{m}_{c,corr}, N_{tc,corr})$, but with different (p_{01}, T_{01})-pairs, are compared to further investigate possible trends in Π_c. Automotive compressors have small speed line slopes over a wide range of mass flows [10, 16]. The data is therefore divided into groups at multiples of 5 g/s, where map points with $\Delta\dot{m}_{c,corr} = \pm 1.5$ g/s around the desired multiple of 5 g/s, are accepted, i.e. for the 70 g/s case, points with $\dot{m}_{c,corr} \in [68.5, 71.5]$ g/s. A model is estimated, for each $\dot{m}_{c,corr}$-group using

$$a_0 = a_1 p_{01} + a_2 T_{01} + a_3 \Pi_c \tag{16}$$

to make any trend in Π_c, for changing p_{01} and/or T_{01}, more prominent. The intersection between the model (16) and the axes of the plot is given in Fig. 12. The equations for the planes were bias adjusted for better visibility, which does not alter the conclusions, since it is the slope that is of interest.

The result from the investigation is that for both corrected shaft speeds

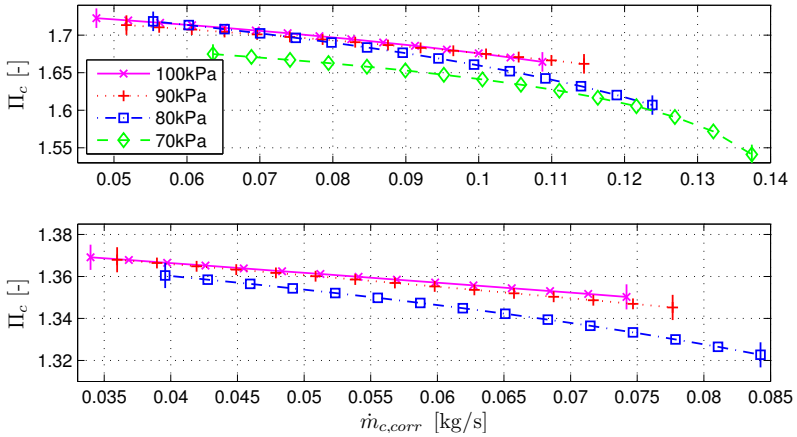

Figure 11: Speed line models (1.5a) fitted to measured data with constant $(N_{tc,corr}, p_{01})$, for the large and small shaft speed presented in Fig. 10. The extra vertical lines on each modeled speed line shows the range of data points for that particular p_{01}. There is a small discrepancy between Π_c for different p_{01} with the general trend showing larger Π_c for larger p_{01}.

measured, a decreasing trend in Π_c for decreasing p_{01} is found, supporting the results from previous section. No clear trend in T_{01} is found. A large positive slope of the model (16) with T_{01} is found for the smallest corrected mass flow point presented for the small corrected shaft speed. The opposite case is found for the same corrected shaft speed, for the largest corrected mass flow presented.

4.2 Gas stand data

The gas stand data is measured independently and according to industrial practice (see e.g. [22, 23, 4]), and more details are found in [28]. The same two stage system as in the engine test stand, but another individual, is used. Two different data sets are measured. The first consists of individual maps of the two stage system compressors, measured with inlet conditions $\theta \approx 1, \delta \approx 1$. The two turbos are then mounted together for the second data set, and second stage speed lines are measured for small Γ, see (11). This map has inlet conditions $\theta > 1, \delta > 1$, see Section 2.1, and will be referred to as the interstage map.

The individual high pressure stage map, referred to as the individual map, will be compared to the interstage high pressure map in this section, since they are maps of the same turbo, but with different inlet conditions.

High pressure compressor stage - hpc

The interstage temperature is measured in close proximity to the second stage impeller, which, for mass flows close to surge, can show an increase in temperature [2]. This is indeed seen for the smallest mass flow point of each speed line,

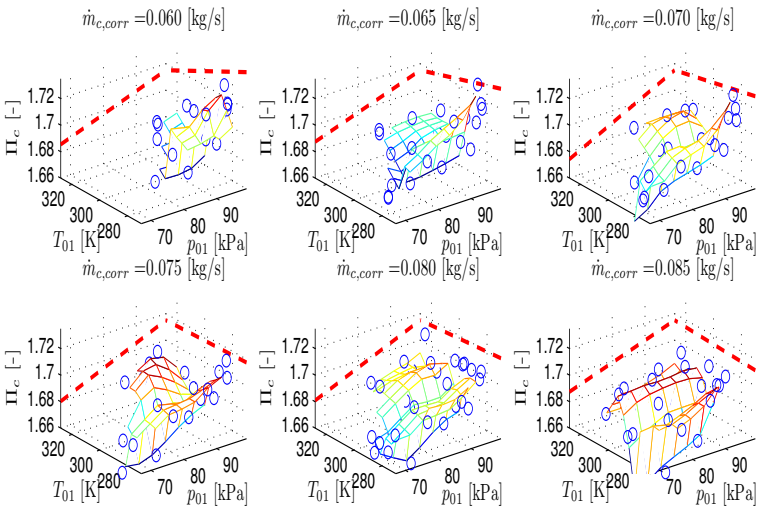

(a) Large shaft speed

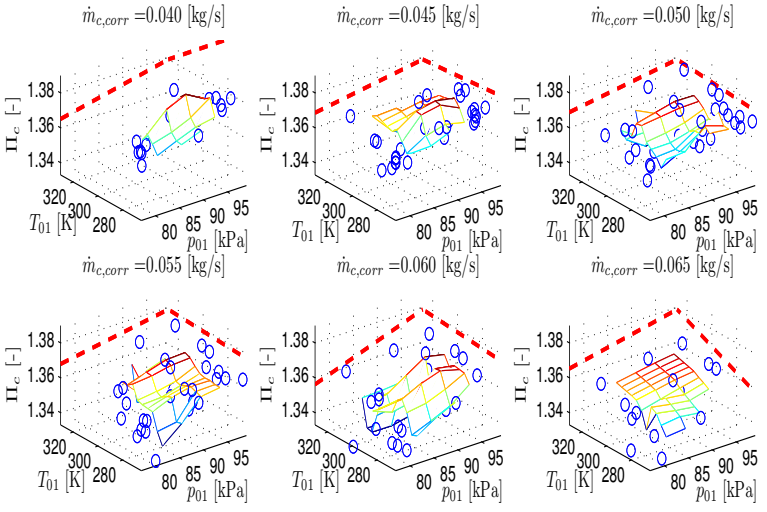

(b) Small shaft speed

Figure 12: Variations in measured Π_c for different $(\dot{m}_{c,corr}, p_{01}, T_{01})$ for two shaft speeds. A trend with decreasing Π_c for decreasing p_{01} is seen. The dashed line gives a bias adjusted LSQ-fitted plane (16), and its intersection with the axes, to better visualize trends.

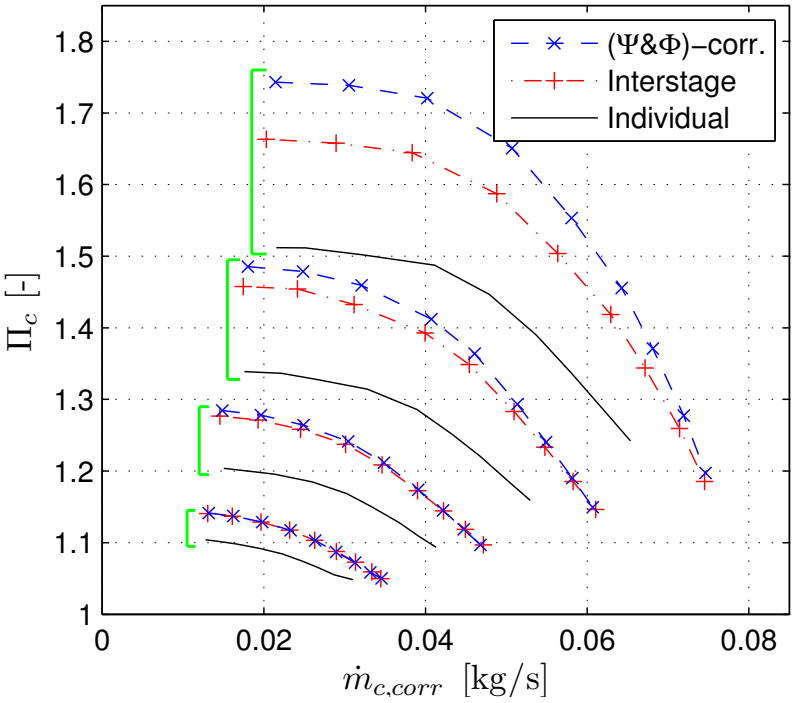

Figure 13: Dash dotted lines show underlying interstage measurement, which is measured at constant N_{tc}. Dashed line: adjusted interstage measurement using the techniques in [16], to give the corresponding $N_{tc,corr}$-line of the dash dotted line. The solid line presents the individual gas stand map as reference. The square brackets indicate which speed lines that should be compared.

which has a temperature increase of $15-20$ K, compared to the second smallest mass flow point. The temperature for the smallest mass flow point is therefore adjusted, and set equal to the temperature of the second smallest mass flow point on that speed line. The interstage data is further measured at constant N_{hpc} and not constant $N_{hpc,corr}$. The (Ψ&Φ)-approach in [16] is therefore used to adjust the measurements. The result is shown in Fig. 13, where the solid lines show the individual gas stand map as a reference. The dashed dotted lines represent the performance map calculated using the modeled inlet temperature, and measured inlet pressure, but with $N_{hpc} = const$. The dashed lines represent the $N_{hpc,corr} = const$ speed lines calculated using the (Ψ&Φ)-approach.

The inlet conditions for the interstage map are presented in Table 3, and represent from left to right, low to high shaft speed. A large discrepancy exists between the individual and the interstage hpc-map. Since $T_{01} > T_{std}$, i.e. $\theta > 1$, of the hpc inlet, the corresponding $N_{tc,corr}$ of the interstage map, is smaller than for the individual hpc-map, given the same N_{tc}-line. Even so, all interstage speed lines have larger Π_c given a $\dot{m}_{c,corr}$, than the corresponding

Table 3: Measured shaft speeds, number of points #, and inlet conditions for the interstage hpc-map, presented with dash dotted lines in Fig. 13.

N_{tc}	#	p_{01} [kPa]	δ [-]	T_{01} [K]	θ [-]
144597	9	118–128	1.18–1.28	318–331	1.09–1.13
118795	9	107–113	1.07–1.13	308–317	1.05–1.08
92959	9	102–106	1.02–1.06	303–310	1.04–1.06
67081	9	100–102	1.00–1.02	302–308	1.03–1.05

lines measured in the individual hpc-map.

5 Modifying the corrections

The correction factors are applied to scale the compressor performance variables, to cover also different inlet conditions, than those used during the performance measurement. Π_c of two points, with the same corrected mass flow (3) and corrected shaft speed (4), measured at different inlet conditions should be equal. This is not the case for the measurements presented in the previous sections.

This section investigates if the corrections, (3) and (4), can be modified, to better fit the measured data. The corrections are modified separately. This reduces the analysis complexity, and is deemed as an adequate approach to find trends in the data without risking over fitted parameters. Further, the structure of the corrections is kept, and the following shaft speed correction is proposed

$$N_{tc,corr,K} = \frac{N_{meas}}{\theta^m}\delta^n \tag{17}$$

where, compared to (4), also δ is included, and the parameters (m, n) are allowed to vary, and $K \in \{\text{I,II,III,IV}\}$ represents the different corrections that are tested, and are further presented in Section 5.2. A case with $m = 0.5, n = 0$ corresponds to the nominal correction, i.e. (4). For the mass flow correction the following modification is proposed

$$\dot{m}_{c,corr,J} = \dot{m}_{c,meas}\frac{\theta^r}{\delta^s} \tag{18}$$

where a case with $r = 0.5, s = 1$ corresponds to the nominal correction (3). The $J \in \{\text{I,II,III,IV}\}$ are further presented in Section 5.2. Assuming that most maps are measured with $\theta \approx 1, \delta \approx 1$, this correction structures also have the advantage that no change is needed to most maps. To avoid unreasonable correction quantities, (m, n) and (r, s) are allowed to vary in the range $[-2, 2]$.

The conclusions drawn are from the changes in pressure ratio given a change in inlet conditions, since the mass flow to pressure ratio characteristic has been shown to be insensitive to heat transfer [24, 7, 6, 25].

5.1 Connecting a change $dN_{tc,corr}$ to a change $d\Pi_c$

In order to see how a modification to the shaft speed correction, changes a map point, the modification needs to be connected to either, or both, of the

other variables of the map: $\dot{m}_{c,corr}$ and Π_c. This section connects $dN_{tc,corr}$ to $d\Pi_c$, and develops a tool to adjust measured Π_c, due to a modified shaft speed correction.

For any function $\tilde{f} = \tilde{f}(\dot{m}_{c,corr}, N_{tc,corr}, \Pi_c) = 0$, e.g. using (1.5a-f)

$$\tilde{f} = \Pi_c - \left[1 - \left(\frac{\dot{m}_{c,corr} - c_4}{c_3 - c_4}\right)^{c_1}\right]^{1/c_2} c_5 = 0 \tag{19}$$

where the c_i are functions of $N_{tc,corr}$ according to (5b-f), the implicit function theorem can be used to calculate the quantity $dN_{tc,corr}/d\Pi_c$, according to

$$d\tilde{f} = \frac{\partial \tilde{f}}{\partial \Pi_c} d\Pi_c + \frac{\partial \tilde{f}}{\partial \dot{m}_{c,corr}} d\dot{m}_{c,corr} + \frac{\partial \tilde{f}}{\partial N_{tc,corr}} dN_{tc,corr} = 0 \tag{20}$$

The variation of interest is how a speed line changes, for a given $\dot{m}_{c,corr}$. This variation can be deduced by setting $d\dot{m}_{c,corr} = 0$ in (20), giving the sensitivity

$$\left.\frac{dN_{tc,corr}}{d\Pi_c}\right|_{\dot{m}_{c,corr}} = -\frac{\frac{\partial \tilde{f}}{\partial \Pi_c}}{\frac{\partial \tilde{f}}{\partial N_{tc,corr}}} \tag{21}$$

An analytical derivation of (21), for the model (1.5a-f), is found in Appendix B. A change $dN_{tc,corr}$ can thus be connected to a change $d\Pi_c$ for constant $\dot{m}_{c,corr}$. This means that a point measured at erroneous $N_{tc,corr}$ can be adjusted vertically in the map, if the partial derivatives can be calculated. The quantity, given by (21), gives the corrected shaft speed change associated with a unit increase in Π_c, for a point in the map.

Also $dN_{corr}/d\dot{m}_{c,corr}$ can be calculated. This is however neglected, due to the high sensitivity caused by the small slopes of the speed lines, pointed out in [10, 16].

Modelling $dN_{tc,corr}/d\Pi_c$

The model (1.5a-f) is used to calculate (21) for the eight maps (A-H) presented in Fig. 3. The calculations show that the largest values of (21) are found at the surge line of the lowest speed line for all maps, and decreasing for increasing $\dot{m}_{c,corr}$. The sensitivity (21) is also decreasing with increasing shaft speeds, and found to be approximately affine in corrected mass flow, given a $N_{tc,corr}$. Equation (21) is always positive, since speed lines never cross.

An affine model in $\dot{m}_{c,corr}$ according to

$$\frac{dN_{tc,corr}}{d\Pi} = d_1 \dot{m}_{c,corr} + d_0 \tag{22}$$

where (d_1, d_0) are model parameters, is proposed to model (21). Fig. 14 presents four models (22) parametrized to the four corrected shaft speed of the individual hpc-map, and the model fit is good. The model (22) is used in the next sections to analyze modifications of the corrections according to (17) and (18).

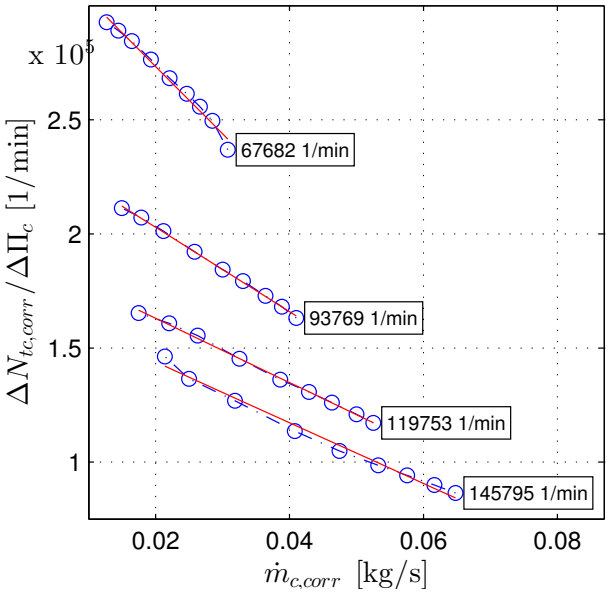

Figure 14: Modeled $dN_{tc,corr}/d\Pi_c|_{\dot{m}_{c,corr}}$ as a function of $\dot{m}_{c,corr}$ for the individual hpc map. An affine function in $\dot{m}_{c,corr}$ is also shown for each line to motivate the simple model used in the investigation of the correction quantities.

5.2 Low pressure stage data

The low pressure stage data is analyzed first, since this data is more comprehensive than the high pressure stage data. The high pressure stage data is then used to test the hypothesis that has been built using the low pressure stage measurements. The objective with the investigation presented in this section, is to estimate a speed line with unknown shape and corrected shaft speed, modeled using (1.5a). Note that the engine test stand measured speed lines are not compared to the reference gas stand speed lines. The parameters (d_1, d_0) in (22) are calculated using the reference gas stand speed lines, and are considered representative also for the engine test stand speed lines. The parameters (d_1, d_0) can be included in the estimation, but this was neglected here, due to the increase in the number of parameters to fit to the data.

Modifying the shaft speed correction

This section assumes that (3) is valid, and investigates if there are gains in modifying (4), according to (17). Four shaft speed corrections were tested, $K \in \{\text{I,II,III,IV}\}$. Correction I uses $m = 0.5, n = 0$, and corresponds to the nominal correction quantity (4). Correction II has $m \in [-2, 2], n = 0$, Correction III $m = 0.5, n \in [-2, 2]$, and Correction IV varies both parameters, $m \in [-2, 2], n \in [-2, 2]$. Given a desired corrected shaft speed $N_{tc,corr,sp}$, it is possible to correct

Table 4: Changes in fit of measured data to a speed line model (1.5a), for modified shaft speed corrections (17). It is seen that an increase of the fit is achieved if also δ is included in the correction. An even better fit is obtained if also the θ-exponent is allowed to change, though the increased fit associated is small. The most notable increase in fit comes from going from Correction II to Correction III, meaning that also δ is included in the calculation of $N_{tc,corr}$.

	Corr.	m	n	$N_{tc,corr,sp}$	mean($\|e\|$)	std(e)	$\sum(\|e\|)$
103869	I	0.5	0	103867	0.0156	0.0206	4.30
	II	0.540	0	103870	0.0155	0.0203	4.27
	III	0.5	0.041	103862	0.0140	0.0190	3.85
	IV	0.562	0.045	103862	0.0140	0.0184	3.84
77064	I	0.5	0	76973	0.0078	0.0102	1.39
	II	0.460	0	77039	0.0074	0.0100	1.33
	III	0.5	0.053	77025	0.0066	0.0094	1.18
	IV	0.476	0.051	76995	0.0064	0.0093	1.14

the measured Π_{meas} using (22)

$$\Pi_{corr} = \Pi_{meas} + \frac{dN_{tc,corr}}{d_1 \dot{m}_{c,corr} + d_0} \tag{23}$$

where (d_1, d_0) are parametrized using a speed line model (1.5a), for the reference gas stand map data and

$$dN_{tc,corr} = N_{tc,corr,sp} - N_{tc,corr,K} \tag{24}$$

A non linear least squares estimation method is used to find $(m, n, N_{tc,corr,sp})$ and $c_i,\ i \in [1, 5]$ of (1.5a), minimizing

$$e = (\Pi_{mod} - \Pi_{corr}) \tag{25}$$

or more explicit

$$\left[1 - \left(\frac{\dot{m}_{c,corr} - c_4}{c_3 - c_4}\right)^{c_1}\right]^{\frac{1}{c_2}} c_5 = \Pi_{meas} + \frac{N_{tc,corr,sp} - {\mathrm{N_{meas}}}/{(\mathrm{T_{01}}/\mathrm{T_{std}})^{\mathrm{m}}\,(\mathrm{p_{01}}/\mathrm{p_{std}})^{n}}}{d_1 \dot{m}_{c,corr,meas} + d_0} \tag{26}$$

The fitted parameters $(m, n, N_{tc,corr,sp})$ of (26), are given in Table 4, along with standard deviation and mean for the error e (25). A better fit to the speed line model (1.5a) is found, when the shaft speed correction also contains p_{01}. The most notable increase in fit come from going from Correction II to Correction III, meaning to allow $n \neq 0$ and thus also include δ in the shaft speed correction. The best fit values for n are small and positive, corresponding to a correction with decreasing corrected shaft speed with decreasing inlet pressure.

Table 5: Change in fit of measured data to an Ellipse speed line if the mass flow correction factor (3) is changed according to (18), with the error to be non linear least squares minimized given by (27).

Corr.		r	s	mean($\|e\|$)	std(e)	$\sum(\|e\|)$
103869	I	0.5	1	0.0131	0.0174	3.60
	II	0.393	1	0.0131	0.0174	3.60
	III	0.5	0.974	0.0131	0.0174	3.60
	IV	0.361	0.944	0.0131	0.0174	3.60
77064	I	0.5	1	0.0070	0.0093	1.25
	II	-0.753	1	0.0061	0.0088	1.10
	III	0.5	1.725	0.0066	0.0091	1.18
	IV	-0.711	1.327	0.0060	0.0088	1.07

Modifying the mass flow correction

This section modifies the mass flow correction (3) according to (18). The objective is to improve the fit to a speed line model (1.5a), for the engine test stand measured speed lines. $N_{tc,corr}$ is assumed to be constant, see Table 2. Four mass flow corrections are tested, $J \in \{\text{I,II,III,IV}\}$. Correction I has $r = 0.5, s = 1$, which is the standard correction (3), Correction II: $r \in [-2, 2], s = 1$, Correction III: $r = 0.5, s \in [-2, 2]$, and Correction IV varies both parameters $r \in [-2, 2], s \in [-2, 2]$.

A minimization of $e = \Pi_{mod} - \Pi_{meas}$ with Π_{mod} given by (1.5a) using the different versions of (18) is first investigated. The estimation problem is formulated; find the parameters of the speed line model (1.5a), and m and n minimizing

$$e = \Pi_{meas} - \left[1 - \left(\frac{\dot{m}_{c,corr,J} - c_4}{c_3 - c_4}\right)^{c_1}\right]^{\frac{1}{c_2}} c_5 \tag{27}$$

where $\dot{m}_{c,corr,J}$ is given by (18).

The result is presented in Table 5, and shows that the increase in fit to the speed line model, from allowing (r, s) to vary, is minimal. The deviations in (r, s) from standard values $(r = 0.5, s = 1)$ are large for the small shaft speed. The large shaft speed shows smaller deviations in (r, s), compared to the standard values. The estimated r with best fit, for the small shaft speed, are negative, while positive for the large shaft speed. These inconclusive results are connected to the high parameter sensitivity caused by the small slope of the speed lines, discussed in [10, 16].

A mass flow correction modification can also be analyzed, if the causality of (1.5a) is changed according to

$$\dot{m}_{c,corr,mod} = \left[1 - \left(\frac{\Pi_c}{c_5}\right)^{c_2}\right]^{1/c_1} \cdot (c_3 - c_4) + c_4 \tag{28}$$

and (18) is formulated as

$$\dot{m}_{c,mod} = \frac{\dot{m}_{c,corr,mod}}{\frac{\theta^r}{\delta^s}} \tag{29}$$

Table 6: Change in fit of measured data to a speed line model (1.5a), for modified mass flow corrections (3), using the error e (30).

	Corr.	r	s	mean($\|e\|$)	std(e)	$\sum(\|e\|)$
103869	I	0.5	1	0.0148	0.0184	4.07
	II	0.197	1	0.0144	0.0179	3.95
	III	0.5	0.611	0.0129	0.0160	3.56
	IV	-0.404	0.664	0.0121	0.0151	3.32

The error between the measured $\dot{m}_c$ and the modeled $\dot{m}_{c,mod}$

$$e = \dot{m}_c - \dot{m}_{c,mod} \tag{30}$$

is used in the analysis. This corresponds to a horizontal translation of the measured points, in order for the points to better fit the speed line shape given by (1.5a).

Table 6 presents the result for the large shaft speed, since the investigation of the small shaft speed is too sensitive to initial parameter values, and is therefore discarded. The small slope of the speed lines, means that the horizontal translation in the map has to be large, to move a point close to the speed line modeled using (1.5a). The fit can be improved if $s < 1$.

5.3 High pressure stage data

Both the interstage data and the individual map data are measured for the same compressor in the gas stand. Therefore, compared to Section 5.2, this section investigates the corrections needed to minimize the vertical distance between the interstage speed lines and the speed lines of the individual map. Note however, that there are other inlet/outlet geometries associated with the two stage setup, for the interstage data, compared to the individual measured map. Different surrounding systems can lead to different compressor performance [21, 5, 11].

The parameters (d_1, d_0) of (22) are estimated using the individual hpc-map. Compared to Section 5.2, due to the large discrepancy between the individual hpc-map and the interstage map, the parametrization of (22) using the individual hpc-map can lead to substantial modelling errors for (21). The parameters (d_1, d_0) can be included in the parameter estimation, but this is discarded to avoid over fitting.

Further, since all speed lines from the interstage map have larger Π_c, investigating horizontal translation is neglected and only modifications to the shaft speed correction are investigated in this section.

Modifying the shaft speed correction

This section does not modify (3), and investigates potential gains in modifying (4) according to (17). A model of (21) according to (22), is used.

The objective is to minimize $e = \Pi_{mod} - \Pi_{corr}$. Each individual hpc map speed line is used to parametrize (1.5a), giving Π_{mod}. The individual hpc map can be used in the parametrization, independent of tested correction, since $\theta \approx 1$

Table 7: The estimated parameters m, n using Corrections I-IV from Section 5.3, for the high pressure stage measurements. The small (δ, θ) of the interstage speed lines, see Table 3, combined with the large discrepancy between the individual and the interstage hpc-map give the large magnitudes of m and n. Estimated m is always negative.

N_{tc}	Corr.	m	n	mean($\|e\|$)	std(e)	$\sum(\|e\|)$
144597	I	0.5	0	0.1991	0.0076	1.7914
	II	-0.885	0	0.0177	0.0217	0.1589
	III	0.5	0.696	0.0134	0.0181	0.1205
	IV	-0.150	0.418	0.0107	0.0148	0.0967
118795	I	0.5	0	0.1244	0.0102	1.1192
	II	-1.856	0	0.0062	0.0072	0.0561
	III	0.5	1.543	0.0142	0.0192	0.1277
	IV	-1.391	0.350	0.0028	0.0033	0.0250
92959	I	0.5	0	0.0680	0.0062	0.6102
	II	-2.000	0	0.0088	0.0022	0.0796
	III	0.5	2.000	0.0362	0.0124	0.3261
	IV	-2.000	0.418	0.0032	0.0038	0.0289
67081	I	0.5	0	0.0299	0.0067	0.2691
	II	-2.000	0	0.0055	0.0044	0.0498
	III	0.5	2.000	0.0273	0.0020	0.2453
	IV	-2.000	1.548	0.0040	0.0035	0.0358

and $\delta \approx 1$, for the individual hpc map, in combination with the structure of the tested corrections (17), as discussed in the ingress of Section 5. The speed line model fit to the individual map speed lines is excellent, which is expected since 5 parameters are fitted to the 9 data points. A good model fit is needed to calculate Π_{mod} for the $\dot{m}_{c,corr}$ found in the interstage map, since the $\dot{m}_{c,corr}$ of the interstage map are larger than the $\dot{m}_{c,corr}$ found in the individual hpc map, and the model thus extrapolates the corresponding Π_c.

Π_{corr} is calculated using (23) with different parameters (m, n) in (17). The four Corrections I-IV presented in Section 5.2 are used in this investigation.

As seen in Fig. 13, the interstage speed lines need to be shifted vertically downwards to minimize the distance to the individual map speed lines. Since (21) always is positive, a shift downwards is produced only if (24) is negative. Due to $\theta \approx 1$ and $\delta \approx 1$, for the individual hpc-map, $N_{tc,corr,sp}$ is readily found in the individual map, independent of shaft speed correction. Since $\theta > 1$ and $\delta > 1$ for the interstage map (see Table 3), the shaft speed corrections estimated are expected to be $m < 0$ and $n > 0$.

The result of modifying the shaft speed corrections for the hpc-data is presented in Fig. 15, and Table 7 gives the numerical values. Correction I corresponds to, adjusting the measurements, using the default shaft speed correction (4). The lines are shifted upwards, since the data is measured with $\theta > 1$. Note the close coupling between the (Ψ&Φ)-corrected dashed lines in Fig. 13 and Correction I marked with crosses in Fig. 15. Correction I does not, however, adjust $\dot{m}_{c,corr}$. Corrections II and IV show $m < 0$ for all speed lines presented.

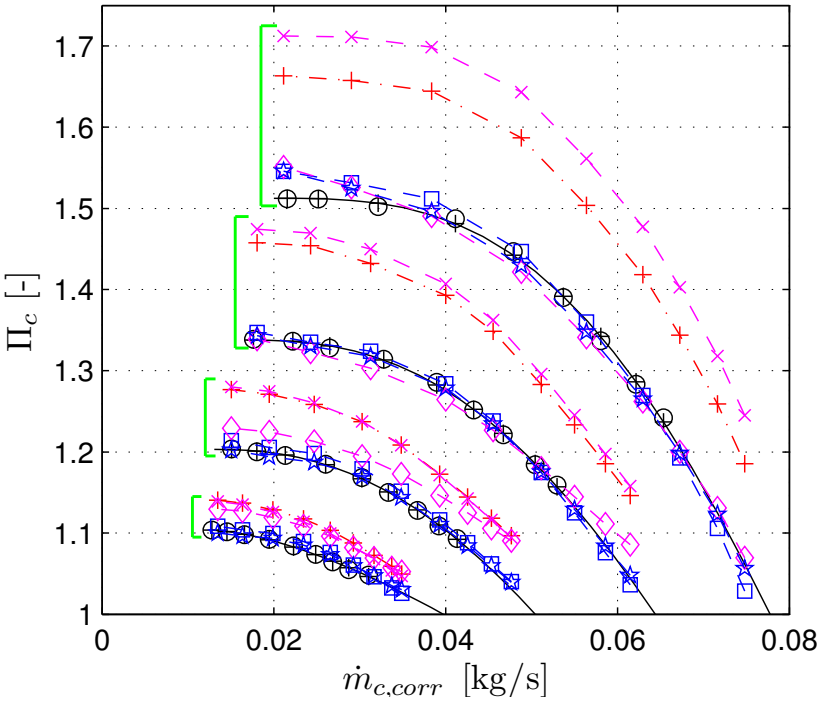

Figure 15: Resulting speed lines from modified shaft speed corrections (17) for the hpc-data. The Corrections I-IV are shown with: cross (I), square (II), diamond (III), and pentagram (IV). Plus represents the interstage speed lines, measured at constant N_{tc}. The individual hpc-map is shown with circles, and the solid line is the fit of the speed line model (1.5a). The square brackets indicate which lines that are comparable.

Since θ and δ are closer to unity for the smaller interstage shaft speeds (see Table 3), the magnitude of m and n are larger for these shaft speeds. Since (21) is large for small shaft speeds (see Fig. 14), a large $dN_{tc,corr}$ of (23) is needed to adjust the measurements, and thus a large exponent of the tested shaft speed correction quantities is needed. That is, if $T_{01}/T_{std} = 1.02$, a large m is needed to make any adjustment of the interstage measurement. The analysis of the smaller shaft speeds is therefore more sensitive to measurement errors, or errors in the parameters (d_1, d_0) of (22), and the parameter estimations converge to the tested limits (-2 and 2).

Table 8: Altitude where engine torque is reduced, due to the compressor limits (CS, TOS, Π_{max}) discussed in Section 3.2, for maps (A-H), shown in Fig. 3. The first part repeats the results of Table 1 for convenience, followed by a part where the shaft speed correction is modified. The last part presents calculations using two modified mass flow corrections.

m/n	r/s	Map limits		(A)	(B)	(C)	(D)	(E)	(F)	(G)	(H)
std/std	std/std	CS	m	480	1240	230	460	1310	820	610	620
		TOS	m	2660	1900	1490	4040	2650	1150	390	2200
		Π_{max}	m	3840	3290	2550	5510	3030	4920	5210	5870
1/0.05	std/std	CS	m	490	1230	220	460	1350	860	610	610
		TOS	m	2450	1740	1360	3810	2430	1090	360	2110
		Π_{max}	m	3560	3080	2380	5030	2810	4500	4690	5280
1/0.7	std/std	CS	m	620	1220	170	380	1280	890	590	1030
		TOS	m	1140	740	540	1980	1150	560	90	1200
		Π_{max}	m	1890	1660	1280	2520	1490	2230	2240	2540
std/std	0.5/0.6	CS	m	330	830	200	390	810	560	450	500
		TOS	m	3100	2560	2000	4810	2680	2010	1030	3600
		Π_{max}	m	3680	3070	2400	5150	2960	4540	4710	5290
std/std	-0.7/1	CS	m	660	1810	240	520	1860	1110	760	720
		TOS	m	2380	1660	1320	3460	2480	970	330	1850
		Π_{max}	m	3900	3380	2630	5640	3070	5050	5370	6080

6 Engine torque line with modified correction quantities

The same investigations of engine torque line versus altitude, as presented in Section 3.2, is presented here, with modified correction quantities. The change in altitude where the engine torque has to be reduced due to the limits, correlated to safe compressor operation, is discussed and quantified. The result is presented in Table 8, where the result from Table 1 is repeated in the first part of the table, to simplify the comparison. The next part of the table is calculated using adjusted shaft speed corrections and are discussed in the next section. The last part of the table uses modified mass flow corrections.

6.1 Modified shaft speed correction

The θ-exponent m of (17) is found to be slightly smaller than the standard value of $m = 0.5$ for the engine test stand measurements, and largely negative for the gas stand data. The negative values of m from the gas stand data are neglected, since no such clear trend is found in the more comprehensive engine test stand data. Further, the gas stand data contained only $\theta > 1$ measurements, while the engine test stand has $\theta \in [0.92, 1.08]$. The δ-exponent n of (17) is found to be between $n = 0.05$ for the engine test stand measurements, and $n = 0.7$ for the gas stand measurements.

Two combinations of (m, n): $(0.5, 0.05)$ and $(0.5, 0.7)$, are thus investigated.

The resulting engine torque calculations are presented in the second section of Table 8. The calculations generally show that, if also p_{01} is included in the shaft speed correction, through a non-zero n, a decrease in estimated engine performance with increasing altitude results.

$n = 0.05$-case

Compared to the case with nominal correction presented in the first section of Table 8, the low engine speed torque is not affected much, since the surge line is defined in Π_c and $\dot{m}_{c,corr}$. The map limits connected to the maximum corrected shaft speed, TOS and Π_{max}, are affected by the modified shaft speed correction. Compared to the nominal case, also map (E) is limited by the largest Π_c available before $h = 3000$ m is reached. High engine speed torque is severely affected by the modifications. It is only map (D) that can reach the maximum torque for $N_e = 5000$ 1/min at $h = 3000$ m. If Table 8 is compared to Table 1, it can be seen that the largest altitude, where it is at all possible to reach maximum torque, is reduced by approximately $200 - 600$ m.

Larger n

For the case where n is increased to $n = 0.7$ from Table 7, an even worse estimated engine performance is found. The reduction in maximum corrected shaft speed, coming from using (17) with a constant max N_{tc}, gives severely restricted high altitude performance. The restriction comes mainly from the reduced maximum shaft speed, meaning that engine torque has to be reduced due to TOS and Π_{max}. The change in altitude for when CS restricts engine torque is much smaller, except for map (H).

6.2 Modified mass flow correction

For the mass flow correction, contradicting trends were found. Two different combinations of (r, s) are used in the analysis. The first case use $r = -0.7$ and $s = 1$ from Table 5. The second uses $r = 0.5$ and $s = 0.6$ from Table 6.

6.3 Modifying θ-exponent

A reduction in corrected mass flow results from reducing s in (18) from 1 to 0.6. This reduces the CS-limiting altitude, but increases the TOS-limiting altitude. This is so since the map operating points are moved left in the map, and thus closer to the surge line, and away from the TOS-line. The altitude where the Π_{max}-limit affects engine torque is also reduced for the maps studied.

6.4 Modifying δ-exponent

The large modification of (18), in going from a $r = 0.5$ of the standard mass flow correction (3), to a negative $r = -0.7$ increases the altitude for when CS restricts engine torque, since the operating point change in the map, is away from the surge line. The TOS-limiting altitude is reduced by $50 - 600$ m, and

the altitude when Π_{max} restricts engine torque is increased slightly, compared to the altitude calculated using the standard mass flow correction.

7 Conclusions

The importance of having correct inlet condition correction for the compressor performance variables were discussed and motivated, especially for a two stage system where the correction quantities are large, due to large ratio between inlet and standard states. The additional increase in air filter pressure drop, due to the reduced ambient gas density with increasing altitude, was up to 50 %. The novel surge avoidance method presented, using the increase in corrected mass flow coming from a decrease in compressor inlet pressure, was shown to be applicable to increase the surge margin of eight compressor maps.

Engine test stand measurements showed a trend of decreasing Π_c for decreasing p_{01}, for two shaft speeds presented. No clear trends in Π_c was found for variations in T_{01}. A remarkable discrepancy existed between the interstage map and the individual map from the gas stand measurements. The interstage map have larger Π_c given a $\dot{m}_{c,corr}$, for all four speed lines presented.

An affine model in corrected mass flow was sufficient to model the sensitivity $dN_{tc,corr}/d\Pi_c$, given constant corrected mass flow, and could be used to adjust measured speed lines if the mass flow correction or shaft speed correction were modified. The sensitivity calculated for all eight maps showed largest values for the smallest corrected mass flow at the smallest shaft speed, and then decreased with increasing mass flow and corrected shaft speed. Further, the sensitivity was positive for all points in the eight maps.

Modifications to the standard mass flow and shaft speed corrections were presented and, using the proposed structure of the modifications, maps measured at standard conditions need no adjustment. A better fit to the measured maps, for both low pressure and high pressure stage, could be found if also compressor inlet pressure ratio δ was included in the shaft speed correction quantity. A good fit to the measurements was obtained if the factor $\delta^{0.05}$ was included in the shaft speed correction.

Already the small modification $\delta^{0.05}$ to the shaft speed correction, was shown to have large impact on an altitude dependent engine torque line. Reductions in engine torque were encountered at altitudes $200 - 600$ m below the altitudes calculated using the standard shaft speed corrections. Modifications to the mass flow correction, based on the measured data, also had large impact on engine performance limits.

Funding acknowledgment

This work was supported by the Vinnova Industry Excellence Center: LINK-SIC Linköping Center for Sensor Informatics and Control.

Declaration of conflicting interests

The authors declare that there is no conflict of interest.

References

[1] Adams, T. (1984). Comparison of a turbocharger to a supercharger on a spark ignited engine. Techn. Paper 841285.

[2] Andersen, J., Lindström, F., & Westin, F. (2009). Surge definitions for radial compressors in automotive turbochargers. *SAE I.J. of Engines*, 1(1), 218–231.

[3] Andersson, P. (2005). *Air Charge Estimation in Turbocharged Spark Ignition Engines*. PhD thesis 989, Linköping University.

[4] ASME (1997). PTC 10-1997, Performance test code on compressors and exhausters. American Society of Mechanical Engineers, New York.

[5] Benvenuto, G. & Campora, U. (2002). Dynamic simulation of a high-performance sequentially turbocharged marine diesel engine. *I.J. of Engine Research*, 3(3), 115–125.

[6] Casey, M. & Fesich, T. (2009). On the efficiency of compressors with diabatic flows. In *Proc. of ASME Turbo Expo*, GT2009-59015.

[7] Cormerais, M., Hetet, J., Chesse, P., & Maiboom, A. (2006). Heat transfer analysis in a turbocharger compressor: modeling and experiments. In *SAE World Congr.*, Techn. Paper 2006-01-0023 Detroit, USA.

[8] Dixon, S. (1998). *Fluid Mechanics and Thermodynamics of Turbomachinery*. Butterworth-Heinemann, 4th edition.

[9] Emmenthal, K., Hagemann, G., & Hucho, W. (1979). Turbocharging small displacement spark ignition engines for improved fuel economy. In *SAE*, Techn. Paper 790311.

[10] Eriksson, L., Nielsen, L., Brugård, J., Bergström, J., Pettersson, F., & Andersson, P. (2002). Modeling of a turbocharged SI engine. *Annual Reviews in Control*, 26(1), 129–137.

[11] Galindo, J., Climent, H., Guardiola, C., & Tiseira, A. (2009). On the effect of pulsating flow on surge margin of small centrifugal compressors for automotive engines. *J. of Experimental Thermal and Fluid Science*, 33(8), 1163–1171.

[12] Heywood, J. B. (1988). *Internal Combustion Engine Fundamentals*. McGraw-Hill series in mechanical engineering. McGraw-Hill.

[13] International Civil Aviation Organization (1993). ICAO Doc 7488-cd – manual of the ICAO standard atmosphere (extended to 80 kilometres (262 500 feet)), ISBN 92-9194-004-6. ICAO standard.

[14] Jung, M., Ford, R., Glover, K., Collings, N., Christen, U., & Watts, M. (2002). Parametrization and transient validation of a variable geometry turbocharger for mean-value modeling at low and medium speed-load points. In *Powertrain and Fluid Systems, Conference and Exhibition*, Techn. Paper 2002-01-2729 San Diego, California, USA.

[15] Leufvén, O. & Eriksson, L. (2008). Time to surge concept and surge control for acceleration performance. In *Proc. of IFAC World Congr.* (pp. 2063–2068).

[16] Leufvén, O. & Eriksson, L. (2010). Engine test bench turbo mapping. In *SAE World Congr.*, Techn. Paper 2010-01-1232.

[17] Leufvén, O. & Eriksson, L. (2011). Surge and choke capable compressor model. In *Proc. of IFAC World Congr.* (pp. 10653–10658).

[18] Lewis, R. I. (1996). *Turbomachinery Performance Analysis.* Arnold.

[19] Manz, P. (1984). Passenger car diesel engines charged by different systems for improved fuel economy. Techn. Paper 841301.

[20] NASA (1976). U.S. standard atmosphere, 1976. NASA standard.

[21] Olsson, J. (2007). Boost limitation in a torque based engine management system. In *IFAC Symposium*, Advances in Automotive Control (pp. 609–616).

[22] SAE standard (1995a). J1826 – Turbocharger Gas Stand Test Code.

[23] SAE standard (1995b). J922 – Turbocharger Nomenclature and Terminology.

[24] Shaaban, S. (2004). *Experimental Investigation and Extended Simulation of Turbocharger Non-adiabatic Performance.* PhD thesis, Leibniz Universität Hannover.

[25] Sirakov, B. & Casey, M. (2011). Evaluation of heat transfer effects on turbocharger performance. In *Proc. of ASME Turbo Expo*, GT2011-45887.

[26] Taylor, E. (1974). *Dimensional analysis for engineers.* Clarendon Press, Oxford.

[27] Watson, N. & Janota, M. (1982). *Turbocharging the internal combustion engine.* MacMillan London.

[28] Westin, F. & Burenius, R. (2010). Measurement of interstage losses of a twostage turbocharger system in a turbocharger test rig. In *SAE World Congr.*, Techn. Paper 2010-01-1221.

[29] White, F. (2005). *Fluid Mechanics.* McGraw-Hill.

A Nomenclature

Variables and parameters		Subscripts	
C_dA	effective area	01	compressor inlet
c_i	speed line model param.	02	compressor outlet
$c_{i,j}$	compressor model param.	af	air filter
e	error	amb	ambient
g	gravitational constant	b	ambient pressure model
h	altitude	c	compressor
$\dot{m}$	mass flow	$corr$	corrected
M	molar mass of air	e	engine
N	speed	hpc	high pressure stage compr.
L	temperature lapse rate	ic	intercooler
p	total absolute pressure	im	intake manifold
R	gas constant	lpc	low pressure stage compr.
T	total absolute temperature	max	maximum
Γ	quotient of pressure ratios	$meas$	measurement
γ	ratio of specific heats	mod	modeled
δ	inlet temperature ratio	ref	reference
η	adiabatic efficiency	sig	significant
θ	inlet pressure ratio	sp	set points
Π	pressure ratio	std	standard
Φ	dimensionless flow param.	tc	turbocharger
Ψ	Head coefficient	$2k$	at $N_e = 20001/\text{min}$

The variables a, d, m, n, r and s are submodel parameters.

B Derivation of $\left.\frac{dN_{tc,corr}}{d\Pi_c}\right|_{\dot{m}_{c,corr}}$

The sensitivity $\left.\frac{dN_{tc,corr}}{d\Pi_c}\right|_{\dot{m}_{c,corr}}$ is used in Section 5, and is interesting since it gives information about how a change in $N_{tc,corr}$ is connected to a change in Π_c. Defining $\tilde{f}$ using the Ellipse model structure (1.5a-f) gives the following $\tilde{f}$

$$\tilde{f} = \Pi_c - \left[1 - \left(\frac{\dot{m}_{c,corr} - c_4}{c_3 - c_4}\right)^{c_1}\right]^{1/c_2} c_5 = 0 \tag{31}$$

where $c_i(N),\ i \in [1,5]$. With $\frac{\partial \tilde{f}}{\partial \Pi_c} = 1$, and using $d\dot{m}_{c,corr} = 0$, (20) becomes

$$1 \cdot d\Pi_c + \frac{\partial \tilde{f}}{\partial N_{tc,corr}} dN_{tc,corr} = 0 \tag{32}$$

which gives the following expression for (21)

$$\left.\frac{dN_{tc,corr}}{d\Pi_c}\right|_{\dot{m}_{c,corr}} = -\frac{1}{\frac{\partial \tilde{f}}{\partial N_{tc,corr}}} \tag{33}$$

Defining the following functions

$$K(N_{tc,corr}, \dot{m}_{c,corr}) = \frac{\dot{m} - c_4(N_{tc,corr})}{c_3(N_{tc,corr}) - c_4(N_{tc,corr})} \tag{34}$$

$$H(N_{tc,corr}, \dot{m}_{c,corr}) = 1 - K^{c_1(N_{tc,corr})} \tag{35}$$

$$G(N_{tc,corr}, \dot{m}_{c,corr}) = H^{1/c_2(N_{tc,corr})} = \Pi_c / c_5 \tag{36}$$

and the derivative is then calculated according to

$$-\frac{\partial \tilde{f}}{\partial N_{tc,corr}} = \frac{\partial c_5}{\partial N_{tc,corr}} G + c_5 \frac{\partial G}{\partial N_{tc,corr}} \tag{37}$$

We now have

$$\frac{\partial G}{\partial N_{tc,corr}} = G\left(-\frac{1}{c_2}\frac{\partial c_2}{\partial N_{tc,corr}}\ln(G) + \frac{1}{c_2 H}\frac{\partial H}{\partial N_{tc,corr}}\right) \tag{38}$$

$$\frac{\partial H}{\partial N_{tc,corr}} = -K^{c_1}\left(\frac{\partial c_1}{\partial N_{tc,corr}}\ln(K) + \frac{c_1}{K}\frac{\partial K}{\partial N_{tc,corr}}\right) \tag{39}$$

with

$$\frac{\partial K}{\partial N_{tc,corr}} = \frac{\frac{\partial(\dot{m}_{c,corr}-c_4)}{\partial N_{tc,corr}}(c_3-c_4) - (\dot{m}_{c,corr}-c_4)\frac{\partial(c_3-c_4)}{\partial N_{tc,corr}}}{(c_3-c_4)^2} \tag{40}$$

where $\frac{\partial \dot{m}_{c,corr}}{\partial N_{tc,corr}} = 0$ gives

$$\frac{\partial K}{\partial N_{tc,corr}} = \frac{(c_4-\dot{m}_{c,corr})\frac{\partial c_3}{\partial N_{tc,corr}} - c_3\frac{\partial c_4}{\partial N_{tc,corr}}}{(c_3-c_4)^2} \tag{41}$$

Combining (38)-(41) and inserting it into (37) together with the partial derivatives of the basis functions $c_i,\ i \in [1,5]$ from (1.5b-f) gives the following

$$\begin{aligned}-\frac{\partial \tilde{f}}{\partial N_{tc,corr}} = {} & c_{5,1}c_{5,2}N_{tc,corr}^{c_{5,2}-1}G - \frac{\Pi_c}{c_2}\Bigg[c_{2,1}c_{2,2}N_{tc,corr}^{c_{2,2}-1}\ln(G) \\ & + \frac{1}{H}K^{c_1}\Bigg(c_{1,1}\ln(K) \\ & + \frac{c_1}{K}\frac{(c_4-\dot{m}_{c,corr})c_{3,1} - c_3c_{4,1}c_{4,2}N_{tc,corr}^{c_{4,2}-1}}{(c_3-c_4)^2}\Bigg)\Bigg]\end{aligned} \tag{42}$$

which now can be used to calculate $\left.\frac{dN_{tc,corr}}{d\Pi_c}\right|_{\dot{m}_{c,corr}}$.

C Reynolds number variation

Dimensionless numbers and their usage for determining turbo-machinery performance [27, 18] are summarized below. Isentropic stagnation enthalpy, efficiency and delivered power, for a turbo-machine that operates with a compressible fluid are given by

$$[\Delta h_{01}, \eta, P] = \tilde{f}(D, N, \dot{m}, \rho_{01}, a_{01}, \mu, \gamma)$$

where D is the diameter, ρ_{01} is the density, a_{01} is the stagnation speed of sound and μ is the dynamic viscosity. Dimensional analysis reduces the dimensions to [8]

$$\Psi, \eta, \hat{P} = f\left(\frac{\dot{m}}{\rho_{01}\,N\,D^3}, \frac{\rho_{01}\,N\,D^2}{\mu}, \frac{N\,D}{a_{01}}, \gamma\right) \tag{43}$$

where $Re = \frac{\rho_{01} N D^2}{\mu}$ is a form of Reynolds number. Using Sutherland's law [29], the relative variation in Re for the experiments presented in Section 4.1 is

$$\frac{Re}{\hat{Re}} = \frac{\rho \mathrm{N}/\mu}{\hat{\rho}\hat{\mathrm{N}}/\hat{\mu}} = \frac{\rho/\mu}{\hat{\rho}/\hat{\mu}\sqrt{\mathrm{T}_{01}/\mathrm{T}_{\mathrm{std}}}} \in [0.628, ..., 1.22] \tag{44}$$

where $\hat{Re}$ is calculated for compressor inlet conditions $T_{01} = T_{std}$ and $p_{01} = p_{std}$. Thus Re for the experiments varies approximately by a factor of two, which is considered to be a small variation.

Paper 4

A surge and choke capable compressor flow model - Validation and extrapolation capability[†]

Oskar Leufvén and Lars Eriksson

Vehicular Systems, Department of Electrical Engineering, Linköping University, S-581 83 Linköping, Sweden.

4

Abstract

Increasingly stringent emissions legislation combined with consumer performance demand, have created the need for complex automotive engines. The control of these complex system rely heavily on control oriented models. Models capable of describing all operating modes of the systems are beneficial, and the models should be easily parametrized and enable extrapolation. A large database of automotive compressor maps is characterized, and used to develop, validate and automatically parametrize a compressor flow model capable of describing reversed flow, normal operation and choke. Measurement data from both an engine test stand, and a surge test stand, is used to parametrize and validate the surge capability of the model. The model is shown to describe all modes of operation with good performance, and also to be able to extrapolate to small turbo speeds. The extrapolation capability is important, since compressor maps are shown to lack information for low speeds, even though they frequently operate there in an engine installation.

[†]This is a formatted version of "A surge and choke capable compressor flow model - Validation and extrapolation capability" by Oskar Leufvén and Lars Eriksson, submitted to Control Engineering Practice and under review second stage of review. The formatting is restricted to changing the article into a single-column format, adjusting sizes of figures and tables, and adjusting the referencing style.

1 Introduction

Efficiency demands and emissions legislation have lead both heavy duty and car manufacturers to develop ever more advanced turbocharged engines [**?** **?** **?**]. The complexity of the charging systems are increasing. Currently e.g. series sequential ([**?** **?** **?**]), parallel sequential ([**?** **?**]) systems or a combination of a turbo and a mechanical compressor are in production. Both more stages [**?**], as well as the inclusion of electric machines connected to a turbo or mechanical compressor shaft are being investigated [**?**].

The engine control system plays an important role in achieving the desired turbocharged system behavior. The control system, in turn, relies on good control oriented models for numerous applications e.g. observer design [**?**], control [**?** **?** **?** **?**], and diagnosis [**?** **?**]. The aim with this paper is to collect the state of the art in compressor knowledge and develop a control oriented compressor model, that is directly useful in control, estimation and diagnosis applications.

In automotive applications, a turbocharged (TC) engine operates its turbo, or turbos, with turbo speeds from stand still up to roughly half of capacity in the manufacturer map. At higher altitudes, a higher pressure ratio (Π_c) is needed, which means that also higher speeds can be reached, see e.g. [**?**]. The range of maximum engine torque of a TC engine, is related to the flow range of the compressors used, where surge limits the torque at low engine speeds, and choke and over-speeding limits the torque at high engine speeds (see e.g. [**?**]). Further, a single stage system can be operated with Π_c below unity, e.g. during engine transients before it has overcome inertia effects [**?**]. The, for multi-stage systems, commonly used passive high pressure stage (HP) by-pass (BP) valve (a spring pre-loaded valve that opens for a large enough pressure drop across it) will, in fact, force the HP stage compressor to operate at $\Pi_c < 1$ when charging with the low pressure (LP) stage. This operation also exists as a fail-safe mode for an actively controlled BP valve, see e.g. Fig. 4.4(a) where the HP stage is operated stationary with $\Pi_c < 1$.

Turbo performance is commonly measured by the turbo manufacturer and represented using maps, see Fig. 1 for a sketch. Normally the map focuses on regions of high engine performance, i.e. torque and power, while the majority of engine operation is spent in regions that are not covered in the standard maps. Neither surge nor choke operation is covered in a standard map. A control oriented model should thus preferably be able to describe all modes of operation, have good extrapolation capability, and be easy to tune with the restricted available map data.

1.1 Contributions and outline

This paper analyzes and extends the control oriented Ellipse compressor model that was proposed for car applications in [**?**]. The model is capable of capturing all modes of operation (normal, surge and choke/restriction), and avoids heat transfer modeling through its emphasis on mass flow to pressure ratio characteristics.

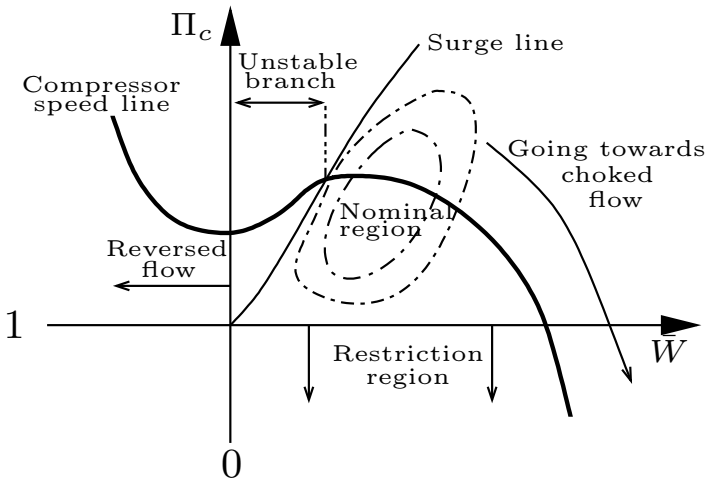

Figure 1: All three turbo compressor operation quadrants important to model for automotive control applications. One speed line with constant $\bar{N}$ is shown. The islands show contours of constant adiabatic efficiency. Some important speed line points are also marked: pressure ratio at zero flow point $(0, \hat{\Pi}_{c0})$, corrected mass flow and pressure ratio at the zero slope (ZSL) point with positive flow $(\bar{W}_{\text{ZSL}}, \hat{\Pi}_{\text{ZSL}})$, and the maximum flow point at zero pressure ratio $(\bar{W}_{max}, 0)$. These will be used in the Ellipse flow model structure presented in Section 5.2. Note also that the surge line does not necessarily pass through the ZSL point of a speed line.

This paper contributes with an analysis of map properties for a database with 236 maps, with applications ranging from small automotive to large heavy duty applications. The data distribution is discussed, and what a practicing engineer can encounter when working with modeling and parameter estimation of compressor data is highlighted. The knowledge generated in the analysis of the compressor maps are later used for the parametrization process of the proposed model structure. A compressor flow modeling literature survey covering all operating modes, is then presented. An in-depth analysis of the Ellipse model structure follows. The analysis presents a novel automated parametrization process used on the database maps. The Ellipse model structure is extended and further validated, to also include heavy duty application maps. The model structure is validated on the database of compressor maps, and an analysis focusing on the model structure extrapolation capability is presented. Summary and conclusions end the paper.

2 The compressor map

The goal with the map is to describe the compressor performance, for all operating conditions. When turbocharger performance is measured, the characteristics

obtained are valid for the inlet conditions under which the measurements were conducted. To overcome this deficiency, different correction factors are applied to scale the performance variables to cover other inlet conditions. The correction factors are based on dimensional analysis of the compression system [**?**]. Most maps use corrected mass flow

$$\bar{W} = W_c \frac{\sqrt{\mathrm{T_{01}}/\mathrm{T_{std}}}}{\mathrm{p_{01}}/\mathrm{p_{std}}} \tag{1}$$

and corrected shaft speed

$$\bar{N} = \frac{N_{tc}}{\sqrt{\mathrm{T_{01}}/\mathrm{T_{std}}}} \tag{2}$$

where p_{std} and T_{std} are referred to as reference conditions, T_{01} and p_{01} are the temperature and pressure at the compressor inlet respectively, and W_c and N_{tc} are the compressor mass flow and shaft speed respectively (the nomenclature is provided in Appendix A). The reference conditions are a key component, and must be provided with the map. The bar denotes a corrected quantity, and the compressor model of this paper is given in corrected quantities. An experimental investigation of compressor correction quantities for automotive applications is presented in [**?**], demonstrating the importance and correctness of equations (1) and (2).

The compressor map, see e.g. Fig. 1, shows what stationary pressure ratio, $\Pi_c = \mathrm{p_{02}}/\mathrm{p_{01}}$, and adiabatic efficiency, η_c, a compressor achieves as a function of $\bar{W}$ and $\bar{N}$. Here p_{02} is the pressure in the control volume after the compressor. When the compressor is installed as part of an engine, these pressures are commonly referred to the air filter control volume pressure $p_{af}(= p_{01})$ and compressor control volume pressure $p_c(= p_{02})$. Points of equal $\bar{N}$ are normally connected, giving a compressor speed line, denoted SpL. Points are measured from the smallest mass flow, found at the surge line, to the largest mass flow where choking can occur. Choke can lead to a pressure drop over the compressor. Surge is a dangerous instability and can occur e.g. during a gear shift under acceleration, where a throttle closing causes a fast reduction in mass flow.

2.1 Map measurement

The common way to measure a turbo map is in a gas stand [**? ? ?**]. However, also other facilities can be used, see e.g. [**? ?**]. Methods for both single stage, as well as multiple stage systems are present [**?**]. A compressor map is usually measured as follows. Turbine inlet pressure and temperature are controlled to maintain a desired $\bar{N}$. A valve on the compressor discharge side is used to vary the back pressure of the compressor, and thereby $\bar{W}$ and Π_c. The system is given an appropriate time to stabilize all components thermally at a fixed discharge valve position, before a stationary compressor map point is measured. Points are then measured from surge and up to choke. Different standards on how to measure and present map data exist, see e.g. [**? ? ? ?**].

The definition of surge from [**?**] has been analyzed in [**? ?**], and different measures can be used e.g. pressure or shaft speed oscillations, or increasing

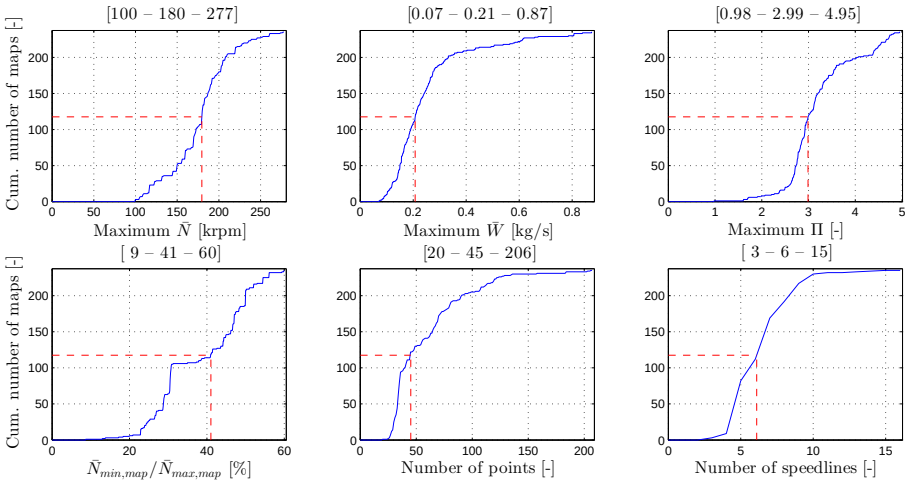

Figure 2: Cumulative distribution of: maximum shaft speed, maximum corrected mass flow, maximum pressure ratio, ratio between minimum and maximum corrected shaft speed, number of map points, number of speed lines, for the compressor map database. The title of each plots gives the minimum, and maximum value, and the cumulative sum equal to 50% of the number of maps in the database, respectively.

temperature of air close to the impeller entry. A unique, broadly accepted definition seems to be lacking. Surge is, in fact, a system property [**?**], and compressor characteristics can well be measured down to zero flow [**?**], and also reversed flow [**?**]. Down to what Π_c a speed line should be measured for larger flows, is also an open question.

3 Experimental data

This section describes the stationary map database, and the dynamic measurements that are used to generate knowledge and form the rationale for the control oriented model. A first analysis, that serves as a preparation for the parametrization, is performed using the database.

3.1 Compressor map database

A database of compressor maps, with maps from the main manufacturers of turbos for automotive application, has been prepared. Fig. 2 summarizes the database, and presents cumulative distribution of: maximum shaft speed, maximum corrected mass flow, maximum pressure ratio, ratio between minimum and maximum corrected shaft speed, number of map points, number of speed lines, for the compressor map database. It can be seen that half of the maps have: (i) a minimum speed that is 41% or more of the maximum, (ii) 45 or more points, (iii) 6 or more speed lines. This is the type of data that one can expect

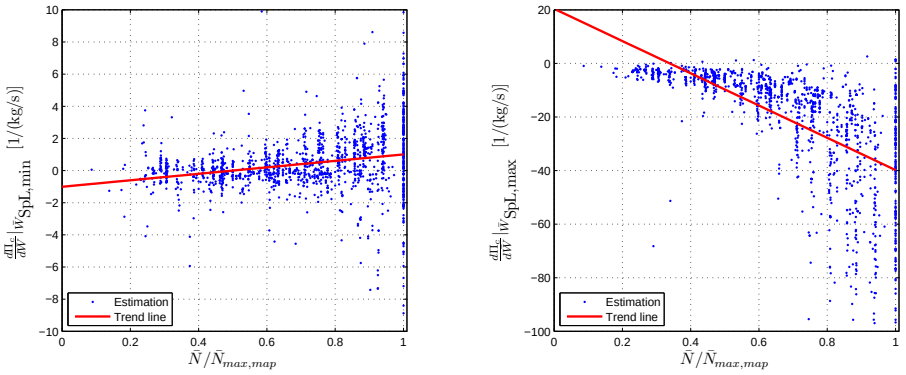

Figure 3: Estimated speed line slope ($^{d\Pi_c}/_{d\bar{W}}$) for the points with smallest $\bar{W}$ of a SpL (*left*) and with largest $\bar{W}$ (*right*), for all maps in the database. The x-axis is $\bar{N}$ normalized by the maximum $\bar{N}$ found in each map. A line is fitted to the data, to illustrate the general trends.

when parametrizing a compressor model. A control oriented model structure should be capable of describing relevant performance from the average size map, given by roughly: 6 speed lines with roughly 7 points on each, where the lowest mapped speed line is 41% of the maximum found in the map. The typical map, of the 236 maps used to support the analysis of this paper, has: (1) a maximum $\bar{N}$ of 180krpm, (2) a maximum $\bar{W}$ of 0.21$^{kg}/_{s}$, and (3) a maximum Π_c of 2.99. The map database is thus biased towards car sized compressor maps. Some of the maps contain points measured down to a pre-defined minimum η_c. More rare are maps measured the whole way down to the discharge line characteristics of the gas stand. This line corresponds to the flow restriction the gas stand piping itself has, and is a function of the gas stand construction.

The slope $^{d\Pi_c}/_{d\bar{W}}$ of a SpL will be important in the latter analysis. Especially the slopes at the end points of a SpL are interesting, since these contain information of how a SpL can be extrapolated. For example, if a large negative slope exists at the maximum $\bar{W}$ of a SpL, the extrapolation of this SpL down to $\Pi_c = 0$ (below which compressor operation is physically impossible, since pressures can not be negative) will be of good accuracy.

Fig. 3 shows the estimated speed line slope ($^{d\Pi_c}/_{d\bar{W}}$) for the points with smallest $\bar{W}$ of a SpL (*left*) and with largest $\bar{W}$ (*right*), for all maps in the database. The slopes were estimated as the slope of a straight line passing through the outer most two $\bar{W}$ points of each SpL. The x-axis is $\bar{N}$ normalized by the maximum $\bar{N}$ found in each map. A line is fitted to the data, to illustrate the general trends. If these trend-lines are studied, it can be seen that the upper $40 - 50\%$ of the $\bar{N}$ have a zero slope point between maximum and minimum flow, and thus that a zero slope point exists on that SpL-measurement. Further only the upper 40% of the speed lines have a significant negative slope at the maximum flow point, and thus enables an extrapolation of that SpL down to $\Pi_c = 0$. These observations will be important when selecting initial values for

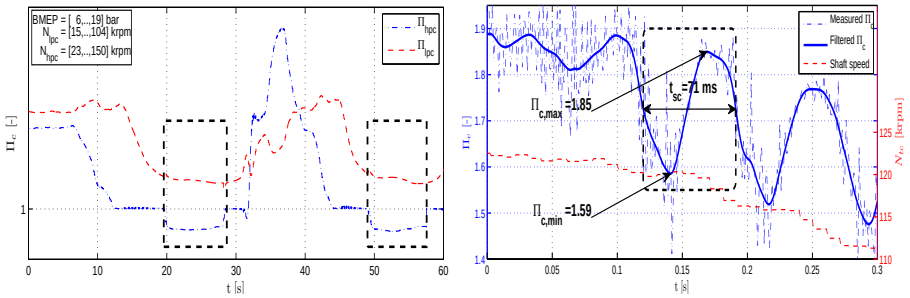

(a) $\Pi_c < 1$-operation. (b) Π_c for two surge cycles.

Figure 4: *Left:* Two stage system operating with the high pressure stage compressor as a restriction (with $\Pi_{c,HP} < 1$). *Right:* Two measured surge cycles from a single stage test stand installation, indicating the surge properties discussed in Section 5.1. The solid line is zero phase shift low pass filtered Π_c to easier separate the measurement signal (dash dotted) from the noise. Dashed line shows turbo shaft speed. The dashed box shows one surge cycle. The surge properties are: $t_{sc} = 71$ms and $\Gamma_{\Pi_{cs}} = {}^{(1.85-1.59)}/_{(1.85-1)} = 31\%$.

the optimization of the Ellipse flow model parameters, detailed in Section 5. There, e.g. the initial model parameters for $\bar{W}$ at the zero slope point of a SpL will be estimated from only the upper 40% of the map (since the lower part does not have a zero slope point).

3.2 Test stand experimental data

Test stand experimental data is collected from three different platforms: (i) a two stage turbocharged engine test stand (see Fig. 4.4(a)); (ii) a single stage engine test stand (see Fig. 4.4(b)); (iii) a compressor driven by a separate electric motor in a surge test stand (see Fig. 5). Details of the measurement chain of the engine test stands can be found in [**?**].

The surge test stand consists of a turbocharger where the turbine side has been removed. The driving torque is instead supplied from an electric motor via a gearbox, see Fig. 4.5(a). The compressor side piping consists of a straight inlet pipe with measurement stations for pressure and temperature. The discharge pipe contains a throttle used to control the operating point and measurement stations for temperature, pressure and mass flow. N_{tc} is measured and controlled using the electric motor. Continuous surge operation was possible for long periods of time, see Fig. 4.5(b). The reader is referred to [**?**] for more details on the surge test rig setup and measurement chain.

4 Control oriented compressor models & MVEM

This section reviews related flow models available in the literature, and introduces the mean value engine modeling (MVEM) used in Section 5.5 and

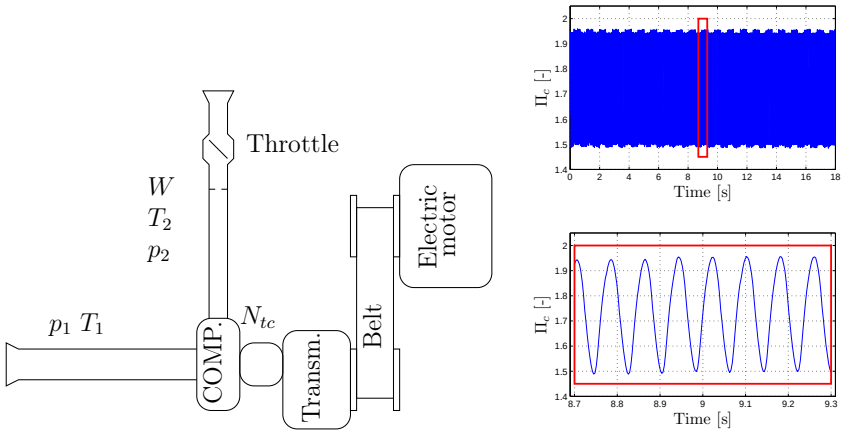

(a) Schematic overview.

(b) Measurement of continuous surge.

Figure 5: *Left:* Schematic overview of the surge test stand. *Right:* example of continuous surge operation in the surge test stand. The lower plot shows the rectangle marked area of the upper plot enlarged.

Section 6.

4.1 Modeling normal, choke and surge operation

The basic operation of automotive turbochargers are presented in e.g. [**?** **?**], and a vast range of compressor flow models for the *normal* operating region are available in the literature, see [**?**] for a control oriented summary. For control applications, the modeling approaches used range from pure curve fitting based models (e.g. [**?** **?** **?**]), dimensionless number modeling (e.g. [**?** **?**]), and physics based models of different computational cost (e.g. [**?** **?** **?**]).

Choking is discussed and modeled in [**?**]. [**?**] and [**?**] model the inducer, impeller and diffuser choke flow, assuming that all flow processes are adiabatic and that the fluid is a perfect gas. The choke mass flow, assuming that choking occurs in the impeller and that the flow is isentropic, is modeled in [**?** **?**], and is still an active field, see e.g. [**?**]. Restriction compressor operation is discussed in a number of papers, see e.g. [**?** **?** **?**], where the compressor is modeled as a typical turbine nozzle characteristic with poor efficiency.

Surge modeling is described in numerous papers. Compressor characteristic during surge is modeled e.g. in [**?** **?** **?** **?** **?**], where the most common model is a third order polynomial which is also used here. The process for reversed flow is modeled as isothermal [**?** **?**]. Another important point of a full compressor characteristic is the zero flow pressure build up (denoted as $\hat{\Pi}_{c0}$ in the sequel), which is modeled e.g. in [**?** **?** **?** **?** **?** **?** **?**] using radial equilibrium theory. The radial equilibrium models have also been shown to give good fit to measured data in [**?** **?**].

The model presented in this paper belongs to the grey-box family, where

the physics is used in the basis functions to ensure sound extrapolation. Compared to previous efforts, all modes of operation are incorporated into the model structure, and no detailed geometric information is needed. The empirical basis functions improves the model fit, compared to pure physics based models, while still enabling automated parametrization and low computational cost.

4.2 Mean Value Engine Modeling (MVEM)

The full system validation in this paper relies on MVEM, originally coined in [**?** **?**]. Component based MVEM of TC spark ignited (SI) engines is outlined in [**?**] and [**?**]. The baseline model is developed and validated in [**?**] and has been extended to handle surge in [**?** **?**]. The extension utilizes the model by Moore-Greitzer [**?**] that introduces a compressor mass flow state.

The TCSI model structure, uses restrictions (air filter, compressor, intercooler, throttle, engine, turbine, exhaust system) interconnected with control volumes, and further extended with surge and wastegate valves. There are 14 states: six pairs of control volume pressures and temperatures, turbo shaft speed and compressor mass flow.

5 The compressor model

This section starts with a brief description of sub-models that commonly makes up a compressor model, and the deep surge cycle properties that will be the goal of the surge modeling. The rest of the section is then devoted to the main contribution of the paper, the Ellipse compressor $\hat{\Pi}$-model.

To include surge capability in the compressor flow model, the approach in [**?**] is used, introducing a state for the compressor mass flow W_c according to

$$\frac{dW_c}{dt} = \frac{\pi D_c^2}{4L_c} \cdot (\hat{p} - p_c) \tag{3}$$

where

$$\hat{p} = \hat{\Pi} \cdot p_{af} \tag{4}$$

and D_c is the compressor diameter, L_c is the duct length. p_c and p_{af} are set by the system, while $\hat{p}$ (and $\hat{\Pi}$) is a measure of the pressure the compressor builds given an operating point, and only for stationary operation is $p_c = \hat{p}$. This has implications for the highly non-stationary surge cycle. Here the rapid changes in $\bar{W}$ means that there must be a large difference between the pressure measured in the control volume after the compressor (p_c) and $\hat{p}$ (the pressure in the control volume before the compressor times the modeled $\hat{\Pi}$), see the discussions in Section 5.5.

The compressor model has further sub-models describing: outlet temperature, T_c

$$T_c = T_{af} \left(\frac{\Pi_c^{\frac{\gamma-1}{\gamma}} - 1}{\eta_c} + 1 \right) \tag{5}$$

and consumed torque, Tq_c

$$Tq_c = {}^{30}/_{\pi} \frac{(T_c - T_{af})\, c_p W_c}{N_{tc}} \tag{6}$$

where γ, c_p are gas properties taken as constants due to the small variations in inlet gas properties, and η_c is the compressor adiabatic efficiency. The η_c-model for all compressor operating regions from [**?**] is used here. The dynamics for the shaft speed N_{tc} is given by the turbo shaft torque balance

$$\frac{d(N_{tc}\pi/30)}{dt} = \frac{1}{J_{tc}}(Tq_t - Tq_c - Tq_{tc,fric}) \tag{7}$$

where Tq_t is torque supplied from the turbine, $Tq_{tc,fric}$ is the shaft friction and J_{tc} is the turbocharger inertia.

5.1 Deep surge cycle properties

Two deep surge cycle properties, identified in [**?**], will be the goal of the surge modeling. A deep surge cycle is defined as a break down of flow through the compressor, followed by a rapid transition to fully reversed flow. The pressure after the compressor (p_c) than rapidly decreases, and the compressor is again able to maintain positive flow. A rapid transition to forward flow occurs, and p_c increases to end the cycle. The two deep surge cycle properties are

$$t_{sc}, \text{ Cycle time of a deep surge cycle [s]}$$
$$\Gamma_{\Pi_{cs}} = \frac{(\Pi_{c,max} - \Pi_{c,min})}{(\Pi_{c,max} - 1)} \text{ [–]}$$

where $\Pi_{c,max}$ and $\Pi_{c,min}$ are the largest and smallest Π_c during a surge cycle. The properties are exemplified using engine test stand surge measurements in Fig. 4.4(b), which shows also pressure and shaft speed variations for a typical surge cycle.

5.2 Ellipse compressor $\hat{\Pi}$-model

The model is divided into three distinct regions, depending on $\bar{W}$, to cover all operating modes. With reference to Fig. 1, these regions approximately correspond to: negative flow, unstable branch, and nominal & choke.

In this distinction, the point on a SpL with zero slope (ZSL) is important. This point is not necessarily at the surge line, but is for most maps found close to the surge line [**?**]. Thus most map points have $\bar{W}$ larger than that at the ZSL. Two basis functions of the model structure describe the ZSL-points of a map; $\bar{W}$ at ZSL ($=\bar{W}_{\text{ZSL}}$), and $\hat{\Pi}$ at ZSL ($=\hat{\Pi}_{\text{ZSL}}$). It is then recognized that a compressor SpL falls of gradually for increasing $\bar{W}$. For large $\bar{W}$ the SpL tends to be vertical. This behavior is modeled as a generalized ellipse (motivating the model name) starting at the ZSL-point and having a vertical slope at a maximum $\bar{W}$ found at $\Pi_c = 0$. The maximum mass flow is described by a basis function in the model structure ($=\bar{W}_{max}$). The eccentricity of the ellipses ("the

SpL") is modeled using two basis functions (=C_1, C_2), and the model does have similarities, but does not strictly speaking correspond, to an ellipse.

The model structure extends from the ZSL-point to a vertical slope at $\bar{W}_{max}$. The flow model, for normal operating, is thus made up by a generalized ellipse with its major and minor axis, as well as the eccentricity parametrized as function of $\bar{N}$. The ellipse starts in the $(\bar{W}, \Pi_c)$-point $(\bar{W}_{\mathrm{ZSL}}, \hat{\Pi}_{\mathrm{ZSL}})$ and ends in $(\bar{W}_{max}, 0)$, with eccentricity given by C_1, C_2, see Fig. 1.

For positive $\bar{W}$ smaller than the ZSL, a third order polynomial is used as a model between the ZSL point and $\hat{\Pi}_{c0}$. The pressure build up at zero flow is in its turn modeled using $\Gamma_{\Pi_{cs}}$.

A turbine like behavior is used as a model for negative $\bar{W}$. This model is parametrized as three constants, independent of $\bar{N}$. The constants $\bar{W}_t$, $\hat{\Pi}_{ct}$ and K_{ct} give the shape of this turbine like characteristic.

To model equations are summarized as

$$
\begin{cases}
\bar{W} > \bar{W}_{\mathrm{ZSL}} & \begin{cases}
\hat{\Pi} & = \left(1 - \left(\frac{\bar{W} - \bar{W}_{\mathrm{ZSL}}}{\bar{W}_{max} - \bar{W}_{\mathrm{ZSL}}}\right)^{C_1}\right)^{1/C_2} \hat{\Pi}_{\mathrm{ZSL}} \\
C_1 & = f_{C_1}(\bar{N}) \\
C_2 & = f_{C_2}(\bar{N}) \\
\bar{W}_{max} & = f_{\bar{W}_{max}}(\bar{N}) \\
\bar{W}_{\mathrm{ZSL}} & = f_{\bar{W}_{\mathrm{ZSL}}}(\bar{N}) \\
\hat{\Pi}_{\mathrm{ZSL}} & = f_{\hat{\Pi}_{\mathrm{ZSL}}}(\bar{N})
\end{cases} \\
0 < \bar{W} < \bar{W}_{\mathrm{ZSL}} & \begin{cases}
\hat{\Pi} & = \hat{\Pi}_{c0} + b_2 \bar{W}^2 + b_3 \bar{W}^3 \\
b_2 & = {}^{3(\hat{\Pi}_{\mathrm{ZSL}} - \hat{\Pi}_{\mathrm{c0}})}/_{\bar{\mathrm{W}}^2_{\mathrm{ZSL}}} \\
b_3 & = {}^{-2(\hat{\Pi}_{\mathrm{ZSL}} - \hat{\Pi}_{\mathrm{c0}})}/_{\bar{\mathrm{W}}^3_{\mathrm{ZSL}}} \\
\hat{\Pi}_{c0} & = \hat{\Pi}_{\mathrm{ZSL}} - f_{\Gamma_{\Pi_{cs}}}(\bar{N})(\hat{\Pi}_{\mathrm{ZSL}} - 1) \\
\Gamma_{\Pi_{cs}} & = f_{\Gamma_{\Pi_{cs}}}(\bar{N})
\end{cases} \\
\bar{W} < 0 & \begin{cases}
\hat{\Pi} & = \hat{\Pi}_{c0} + \left(1 - \left({}^{\bar{\mathrm{W}}}/_{\mathrm{b_1}}\right)^2\right)^{-1/\mathrm{K_{ct}}} - 1 \\
b_1 & = \frac{\bar{W}_t}{\sqrt{1 - \left(\hat{\Pi}_{ct} - \hat{\Pi}_{c0} + 1\right)^{-K_{ct}}}}
\end{cases}
\end{cases}
\tag{8}
$$

where the parameters ($b_i, i \in 1, 2, 3$ and $\hat{\Pi}_{c0}$) are only intermediate variables, enabling the model SpL to be continuous in $\hat{\Pi}$ and the first derivative ${}^{\mathrm{d}\hat{\Pi}}/_{\mathrm{d}\bar{\mathrm{W}}}$, at the two model region switching points ($\bar{W} = 0$ and $\bar{W} = \bar{W}_{\mathrm{ZSL}}$).

The Ellipse flow model contains 14 parameters (denoted c) within the different basis function, to describe all the three quadrants of compressor operation. The following subsections will first describe the basis function f_i

$$
i \in \left\{ C_1, C_2, \bar{W}_{max}, \bar{W}_{\mathrm{ZSL}}, \hat{\Pi}_{\mathrm{ZSL}}, \Gamma_{\Pi_{cs}} \right\} \tag{9}
$$

and an automated model parametrization process will then be described. The normal operating region is first discussed, followed by surge modeling discussions.

It should be noted that the Ellipse model describes the connection between $\bar{W}$ and $\hat{\Pi}$. The motivation for this is that, while η_c presented in a map is largely affected by heat transfer, the flow/pressure-behavior is insensitive to changes in heat transfer, see e.g. [**? ? ? ?**]. Thus, a detailed heat transfer modeling effort is avoided.

5.3 Normal region ($\bar{W} > \bar{W}_{\mathbf{ZSL}}$)

Both $\bar{W}_{\mathrm{ZSL}}$ and $\hat{\Pi}_{\mathrm{ZSL}}$ are expected to increase with $\bar{N}$. For $\bar{N} = 0$, $\bar{W}_{\mathrm{ZSL}} = 0$ and $\hat{\Pi}_{\mathrm{ZSL}} = 1$ are expected. An increasing $\bar{W}_{max}$ with increasing $\bar{N}$ is expected, until the inducer chokes, see [**? ?**].

Eccentricity: f_{C_1} and f_{C_2}

The first two Ellipse model functions enable an $\bar{N}$-dependent eccentricity of the ellipse (compare $\left(\left(\bar{\mathrm{W}}-\bar{\mathrm{W}}_{\mathrm{ZSL}}\right)/\left(\bar{\mathrm{W}}_{\max}-\bar{\mathrm{W}}_{\mathrm{ZSL}}\right)\right)^{C_1} + \left(\hat{\Pi}/\hat{\Pi}_{\mathrm{ZSL}}\right)^{C_2} = 1$). Five different versions of the eccentricity basis functions C_1 and C_2 were tested: a single constant $C_1 = C_2 = c_0$; a single affine function in $\bar{N}$ as $C_1 = C_2 = c_0 + c_1\bar{N}$; $C_1 = C_2 = c_0 + c_1\bar{N}^{c_2}$; $C_1 = C_2 = c_1 + c_2\bar{N} + c_2\bar{N}^2$; and finally the proposed structure as $C_1 = c_{1,0} + c_{1,1}\bar{N}$ and $C_2 = c_{2,0} + c_{2,1}\bar{N}^{c_{2,2}}$. The following f_{C_1} and f_{C_2} were found to balance model simplicity and descriptive capabilities for the map database

$$\begin{array}{ll} f_{C_1}(\bar{N}) & = c_{1,0} + c_{1,1}\bar{N} \\ f_{C_2}(\bar{N}) & = c_{2,0} + c_{2,1}\bar{N}^{c_{2,2}} \end{array} \tag{10}$$

where $c_{i,j}$ are real valued constants.

Maximum corrected mass flow: $f_{\bar{W}_{max}}$

A first order polynomial is proposed to model maximum corrected mass flow $\bar{W}_{max}$

$$f_{\bar{W}_{max}}(\bar{N}) = c_{3,0} + c_{3,1}\bar{N} \tag{11}$$

where $c_{3,0} > 0$ gives a positive flow also for $\bar{N} = 0$ (i.e. a standstill turbo), and $c_{3,1} > 0$ gives an increasing maximum $\bar{W}$ for increasing $\bar{N}$. A minimum selector can be added to physically correspond to a choked inducer flow, $\bar{W}_{ci}$, according to

$$\tilde{f}_{\bar{W}_{max}} = \min(\bar{W}_{ci}, f_{\bar{W}_{max}})$$

where the minimum selector emphasizes that no further increase in $\bar{W}$ is possible, independent of increases in $\bar{N}$. This was not used here.

If an ellipse SpL is fitted to each SpL of a map, the $\bar{W}_{max}$-values can be plotted against $\bar{N}$. Here it is important to note that in order for the Ellipse SpL to give reasonable extrapolation (down to $\Pi_c = 0$) focus should be on SpL with higher $\bar{N}$. This since these SpL will have the steeper slope at high $\bar{W}$. Fig. 6 presents normalized estimated maximum $\bar{W}$ (found at $\Pi = 0$) vs. normalized $\bar{N}$. Since the estimation relies on extrapolation using the slope of a SpL, only the upper SpL (with $\bar{N} > 60\% \cdot \max(\bar{N})$) are plotted. These SpL have a large slope, see Fig. 3. For smaller $\bar{N}$, with typically small slope also at the maximum $\bar{W}$ of the SpL, the SpL-model parameter optimization typically resulted in a $\bar{W}_{max}$-estimate only slightly larger than the maximum $\bar{W}$ of that SpL, and with a very sharp eccentricity (C_1 and C_2).

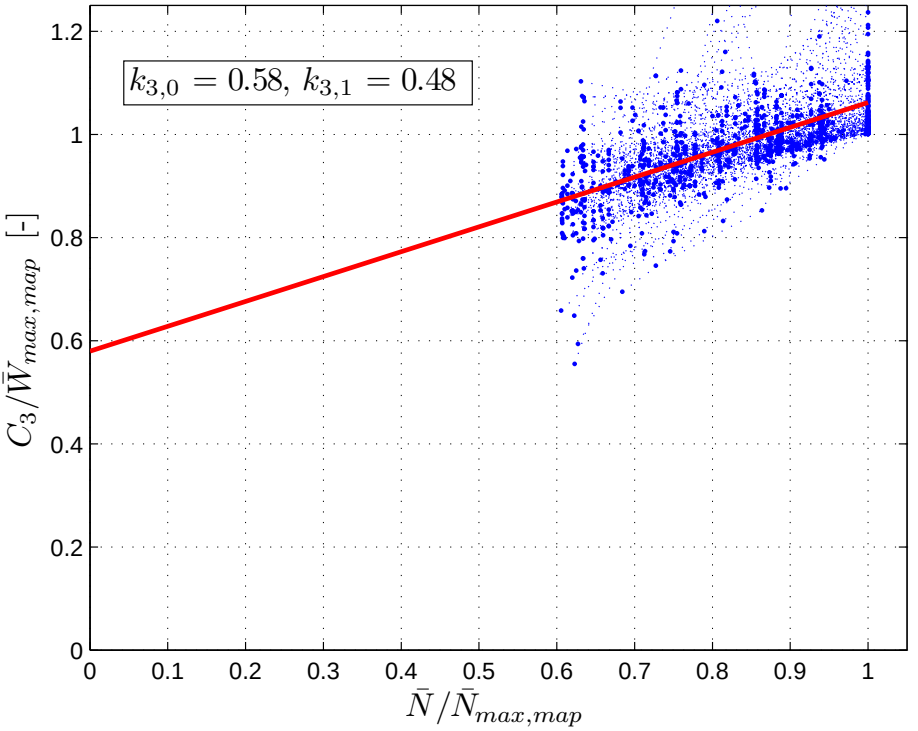

Figure 6: Normalized estimated maximum $\bar{W}$ (found at $\Pi = 0$) vs. normalized $\bar{N}$. Since the estimation relies on extrapolation using the slope of a SpL, only the upper SpL (with $\bar{N} > 60\% \cdot \max(\bar{N})$) are plotted. These SpL have a large slope, see Fig. 3. A function of the form (11) is also fitted to all these normalized data points, and marked with a solid line (together with the function parameters).

An affine function is also fitted to the data and marked with a solid line (together with the best least squares fit parameters)

$$\frac{\bar{W}_{max}}{\bar{W}_{max,map}} = k_{3,0} + k_{3,1}\frac{\bar{N}}{\bar{N}_{max,map}} \tag{12}$$

Note that the indicated parameters $k_{3,0}$ and $k_{3,1}$ are deliberately indicated with k to separate them from the Ellipse basis function parameters c. The parameters k indicate the best fit between the C_3 normalized by the maximum flow of each map, to $\bar{N}$ normalized by the maximum $\bar{N}$ of each map. The parameters are also fitted to all the maps of the database. However, the indicated parameters ($k_{3,0}$ and $k_{3,1}$) can be used as initial estimates for a model parameter optimization over all map points, given only $\bar{W}_{map,max}$ and $\bar{N}_{max,map}$.

Zero slope corrected mass flow: $f_{\bar{W}_{\mathbf{ZSL}}}$

The equations for the zero slope mass flow model is

$$f_{\bar{W}_{\mathrm{ZSL}}}(\bar{N}) = 0 + c_{4,1}\bar{N}^{c_{4,2}} \tag{13}$$

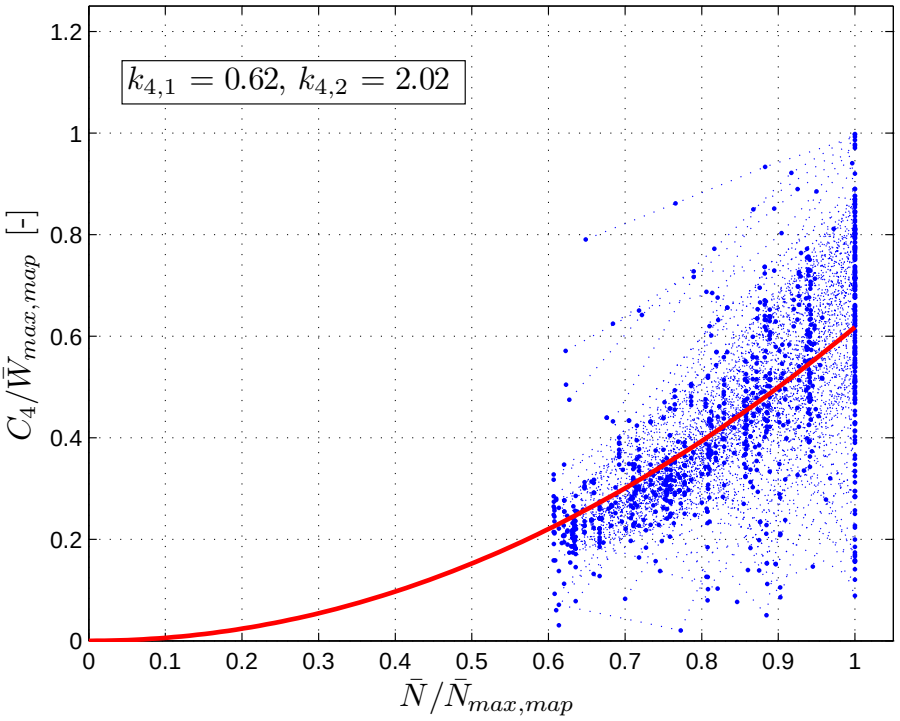

Figure 7: Normalized $\bar{W}$ at the zero slope point of maps vs. normalized $\bar{N}$. Since the estimation tries to find the zero slope $\bar{W}$, only higher $\bar{N}$ (with $\bar{N} > 60\% \cdot \max(\bar{N})$) are plotted. This since lower SpL do not have a zero slope point, see Fig. 3. A basis function of the form (13) fitted to all the normalized data points is also shown.

where the 0 emphasizes physically sound $\bar{W} = 0$ for $\bar{N} = 0$. An Ellipse SpL-model was parametrized to each map SpL (thus neglecting the $\bar{N}$-dependence in the model equations), using nonlinear least squares. Obtained $\bar{W}_{\text{ZSL}}$-points are presented in Fig. 7. Since the estimation tries to find the zero slope $\bar{W}$, only higher $\bar{N}$ (with $\bar{N} = 60\% \cdot \max(\bar{N})$) are plotted. This since lower SpL do not have a zero slope point, see Fig. 3.

The $\bar{W}_{\text{ZSL}}$ and $\bar{N}$ are here normalized by the maximum $\bar{W}$ and maximum $\bar{N}$ found in each map, respectively. In Fig. 7, each point represents a single speed line of a map. The points for each SpL of a map are connected with a dashed line. The proposed basis function (13) gives a good description. The red solid line is the least squares fit to all points of all maps of the database, and can be used as initial parameter estimates given only $\bar{W}_{map,max}$ and $\bar{N}_{max,map}$. It is important to note that the proposed Ellipse structure basis function $\bar{W}_{\text{ZSL}}$ is parametrized to a single map in applications, while the figure shows all maps together (thereby giving the "noisy" look). As in Section 5.3, the model parameters indicated in the figure can be used as initial values in an optimization using the maximum flow and speed found in a map (to go from k_{4j} to c_{4j}).

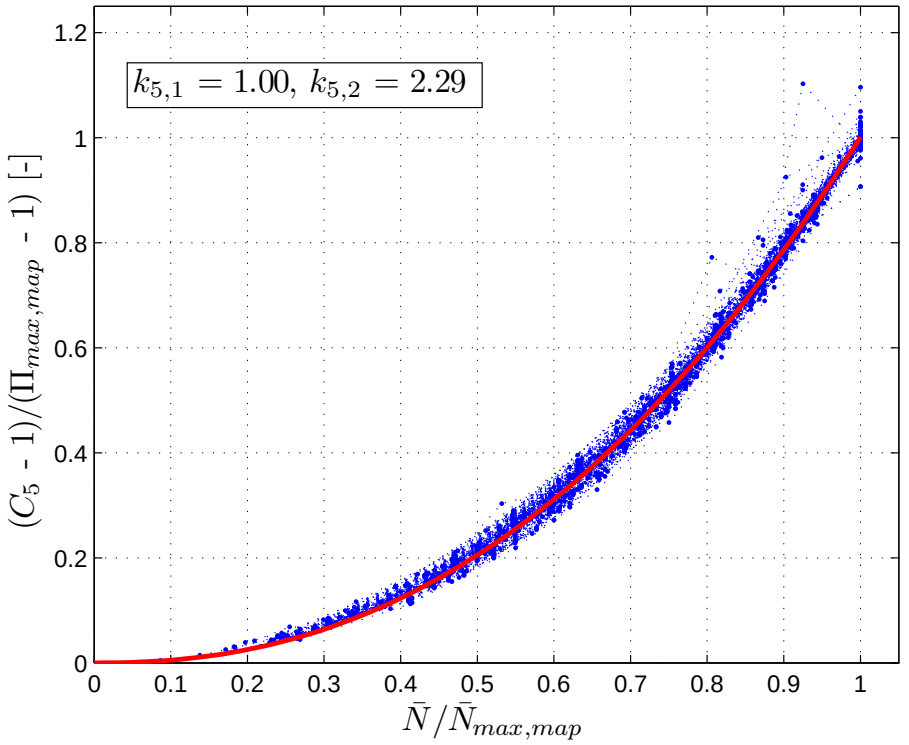

Figure 8: $\frac{\hat{\Pi}_{\mathrm{ZSL}}-1}{\hat{\Pi}_{max,MAP}-1}$ for each SpL of each map in the database vs. (map) normalized $\bar{N}$. Each point in the plot represents estimation on a single SpL of each map.

Zero slope pressure ratio: $f_{\hat{\Pi}_{\mathbf{ZSL}}}$

The pressure ratio at the zero slope point is modeled as

$$f_{\hat{\Pi}_{\mathrm{ZSL}}}(\bar{N}) = 1 + c_{5,1}\bar{N}^{c_{5,2}} \tag{14}$$

where the 1 emphasizes physically sound $\hat{\Pi} = 1$ for $\bar{N} = 0$. As in Section 5.3, Ellipse model parameters were estimated for each SpL of each map in the database. All $\bar{N}$ were used, since all SpL contain a maximum Π_c, either as a local maximum or in the point near the surge that is a point with small slope.

The pressure ratio at the zero slope point is shown in Fig. 8. In the figure each point represents a single SpL of each map, and the points of each map are connected using dashed lines. The solid red line represents the least squares best fit for all maps of the database. Given the normalization as indicated by the axis, the line shows remarkable agreement for all points. As in the previous two sections, the indicated parameter values can be used as initial values for a model parameter optimization (using the maximum Π_c and $\bar{N}$ of a map to go from k_{5j} to c_{5j}). Two points can be made here. Since normal compressor operation is mainly in regions with small SpL slope, the basis function (14) can

in itself be used as a compressor flow model for this region, e.g. assuming the speed lines to be horizontal. Further, given only values of $\Pi_{c,max}$ and $\bar{N}_{max}$ the parameter values indicated in Fig. 8, together with the normalization, can be used if no map at all exist as

$$\hat{\Pi} = (\Pi_{c,max} - 1)\left(1 + k_{5,1}\left(\frac{\bar{N}}{\bar{N}_{max}}\right)^{k_{5,2}}\right) + 1$$

For compressor models making use of interpolation, it is recommended to exploit the inherent curvature seen in Fig. 8, especially if the map grid is sparse in $\bar{N}$. This since using a linear interpolation can result in poor approximation.

Zero flow pressure ratio: $f_{\hat{\Pi}_{c0}}$

The experimental data indicates that $\Gamma_{\Pi_{cs}} \approx 30 - 35\%$ is a good approximation if no surge data exists. $\Gamma_{\Pi_{cs}} = 30\%$ is also chosen as the initial value for the parametrization process described in next section. For compressor maps having points with lower mass flow than the zero slope line, another method can be used to shape the speed lines. Given the model structure from (8), nonlinear optimization can be used to find the parameters of $f_{\hat{\Pi}_{c0}}$ to obtain best fit to the map points. If no surge data is available for a map, the recommendation would be to use $\Gamma_{\Pi_{cs}} = 30\%$. This is indeed chosen for most of the maps of the database, due to lack of surge data.

5.4 Parametrization for normal region

This section presents the automated parametrization process used to enable a quantitative analysis of the model structure. The process was necessary to avoid manually setting initial values for the full nonlinear least squares parameter optimization.

The process was divided into the following steps: (i) estimate the parameters of (9) for each $\bar{N}$; (ii) fit initial estimates of the C_{3-6} model parameters (denoted $\tilde{C}_{3-6}$); (iii) considering the initial estimates $\tilde{C}_{3-6}$ as locked, estimate initial C_{1-2}; and finally (iv) a full nonlinear least squares optimization starting at the initial values.

In the first step, a nonlinear least squares method was used. The initial conditions for the optimization were found from map values at the current SpL: $\tilde{C}_3 = 1.05 \cdot \max(\bar{W}_{\mathrm{SpL}})$, $\tilde{C}_4 = \min(\bar{W}_{\mathrm{SpL}})$, $\tilde{C}_5 = \max(\Pi_{c,\mathrm{SpL}})$. The initial value for $\Gamma_{\Pi_{cs}}$ was set to 0.3, see Section 5.3. The initial values of the eccentricity parameters were put equal, and an iterative search with $\tilde{C}_1 = \tilde{C}_2 \in [1, 9]$ was conducted. To avoid having less points than parameters to optimize over for a given SpL, eight points were added in close vicinity of the map points. The points were evenly distributed at a maximum distance of $\Delta\bar{W} = 0.5\% \cdot \max(\bar{W}_{\mathrm{SpL}})$ from the map points. The pressure ratio of these additional points were calculated using estimates of the SpL slope for each map point.

The parameters $\tilde{C}$ estimated for each individual SpL were then used to make initial estimates of the corresponding basis function parameters $\tilde{c}_{ij}$, $i \in [1, 6]$.

The parameters $\tilde{C}_j, j \in \{1,2,3,4,6\}$ were considered to be uncertain for SpL having $\bar{N} < 60\% \cdot \bar{N}_{max}$. This uncertainty in the parameters stem from the small slope of these lower SpL, thus making the nonlinear least squares insensitive to parameter changes for these $\bar{N}$. However, the $\hat{\Pi}_{\text{ZSL}}$-estimation is considered to be of good quality, since all SpL (of most maps) have their maximum Π at a point with small slope, and the estimation of the $\hat{\Pi}_{\text{ZSL}}$-model parameters $\tilde{c}_{5,i}, i = 1,2$ was conducted over all $\bar{N}$ of the maps.

The initial parametrization of the eccentricity basis functions was conducted using least squares.

The criterion in the optimization for the fourth, and last step, was to minimize the squared distance between $\Pi_{map} - \hat{\Pi}_{model}$ for all map points. Modeled $\hat{\Pi}$ for $\bar{W}$ larger than the modeled maximum flow C_3 is not defined in the structure, and was taken as 0.

The initially estimated $\tilde{C}_{3-5}$ are presented in Figures 6, 7 and 8. These figures thus show a single point for each individual SpL in all maps of the database, and the points from each map estimation are connected using dashed lines.

5.5 Surge modeling parametrization

This section first discusses surge modeling properties in general, and then describes how experimental data can be used to further analyze the model properties.

First it is recognized that the exact SpL shape, for $\bar{W} \in [0, \bar{W}_{\text{ZSL}}]$, is not of great importance for the surge behavior, see [**?**]. It can also be seen in (3), where the change in p_c is given by the emptying and filling dynamic of the downstream control volume, and $\hat{p}$ is given by the compressor model. The slope of a SpL is positive in this region, [**?** **?** **?**], and the difference $(\hat{p} - p_c)$ is therefore large, and the region is passed quickly. The, for surge, important parameter $\hat{\Pi}_{c0}$ (pressure ratio at zero flow) has been recognized in e.g. [**?**], and is here modeled as a function of the parameter $\Gamma_{\Pi_{cs}}$, see (8).

The importance of $\hat{\Pi}_{c0}$ comes from the fact that the Π_c-trajectory, during deep surge, has to enclose the point $(\bar{W} = 0, \hat{\Pi}_{c0})$. This is seen in (3), where $\hat{p}$ has to lead p_c to increase W_c and take the compressor out of reversed flow. The trajectory is given by the compressor characteristics and the system properties.

If surge simulations are studied in detail, it is revealed that $\Pi_c \approx \hat{\Pi}$ is a good approximation, apart from during the rapid transition periods when the compressor flow changes sign. Hence, maximum and minimum Π_c during a surge cycle approximately give $\hat{\Pi}_{\text{ZSL}}$ and $\hat{\Pi}_{c0}$ of the model, respectively. Measurement data of Π_c during surge can therefore be used to assess $\Gamma_{\Pi_{cs}}$. Further, the pressure $\hat{p}_0 = p_{af} \cdot \hat{\Pi}_{c0}$ is the pressure of the downstream control volume needed for the compressor to go from negative to positive W_c, which will affect t_{sc}.

Effect from $\Gamma_{\Pi_{cs}}$, $\bar{W}_t$, $\hat{\Pi}_{ct}$, K_{ct} on the surge properties

The intermediate variable b_1 is given by algebraic constraints (8), forcing all SpL through $(\bar{W}_t, \hat{\Pi}_{ct})$. To investigate how the other Ellipse model parameters

	$\Gamma_{\Pi_{cs}}$	$\bar{W}_t$	$\hat{\Pi}_{ct}$	K_{ct}	Param. change
Δt_{sc}	19%(-20%)	-4%(5%)	0%(-1%)	-1%(1%)	+30%(-30%)
	6%(-7%)	-1%(1%)	0%(-0%)	-0%(0%)	+10%(-10%)
$\Delta\Gamma_{\Pi_{cs}}$	26%(-27%)	1%(-1%)	-0%(0%)	0%(-0%)	+30%(-30%)
	9%(-9%)	0%(-0%)	-0%(0%)	0%(-0%)	+10%(-10%)

Table 1: Sensitivity of the surge properties with respect to changes in the Ellipse model parameters. The parameters are varied $\pm\{10\%, 30\%\}$ from nominal, $t_{sc} = 81$ms and $\Gamma_{\Pi_{cs}} = 54\%$.

N_{tc} [krpm]	$mean(W_{th})$ [g/s]	$\Pi_{c,max}$ [-]	$\Pi_{c,min}$ [-]	$\Gamma_{\Pi_{cs}}$ [-]
80	15.0	1.35	1.17	51%
91	17.8	1.45	1.23	49%
99	21.9	1.53	1.26	51%
110	25.0	1.66	1.33	50%
120	28.5	1.79	1.39	50%
131	30.4	1.96	1.48	50%
140	38.5	2.10	1.54	51%
130	55.1	1.88	1.87	2%
130	49.0	1.89	1.88	2%
130	42.9	1.90	1.87	3%
131	42.6	1.91	1.87	4%
131	37.9	1.94	1.82	13%
131	33.0	1.94	1.48	49%
131	30.4	1.96	1.48	50%

Table 2: Surge test stand measurements in normal and continuous surge operation. Upper part: deep surge at different $\bar{N}$. $\Gamma_{\Pi_{cs}} \approx 50\%$ independent of $\bar{N}$. Lower part: one $\bar{N}$ with different $mean(W_{th})$. The two last rows show that, for deep surge, an increase in $mean(W_{th})$ with 10% only decreases $\Gamma_{\Pi_{cs}}$ with $< 1\%$.

affect the surge properties from Section 5.1, an MVEM of the surge test rig is used. Each of the four model parameters $(\Gamma_{\Pi_{cs}}, \bar{W}_t, \hat{\Pi}_{ct}, K_{ct})$, describing the characteristics for $\bar{W}$ less than the ZSL-point, are varied $\pm\{10\%, 30\%\}$ from nominal values of $\Gamma_{\Pi_{cs}} = 49\%$, $\bar{W}_t = -0.059$, $\hat{\Pi}_{ct} = 10$ and $K_{ct} = 0.5$. Measurement of deep continuous surge is compared to a simulation with the nominal values in Fig. 12, showing good agreement.

The resulting sensitivity in the surge properties are summarized in Table 1. The most important parameters are found to be $\Gamma_{\Pi_{cs}}$ (giving $\hat{\Pi}_{c0}$) and $\bar{W}_t$.

Surge rig data

The test rig is further described in [**?**], and some of the data is presented in Table 2. $\Gamma_{\Pi_{cs}}$ is calculated using continuous surge measurements at constant $\bar{N}$, see Fig. 12, where the compressor is operated at a typical "limit cycle". $\Gamma_{\Pi_{cs}}$ is found to be $\approx 50\%$ for a wide range of $\bar{N}$ for this compressor. Further, if several data sets with $\bar{N} = const$ are studied in more detail, it is found that once deep surge is established, $\Gamma_{\Pi_{cs}}$ shows only a small dependence of mean mass flow. Note that the third last row of Table 2 shows $\Gamma_{\Pi_{cs}}$ for mild surge, and that also points with larger flow have a non-zero $\Gamma_{\Pi_{cs}}$.

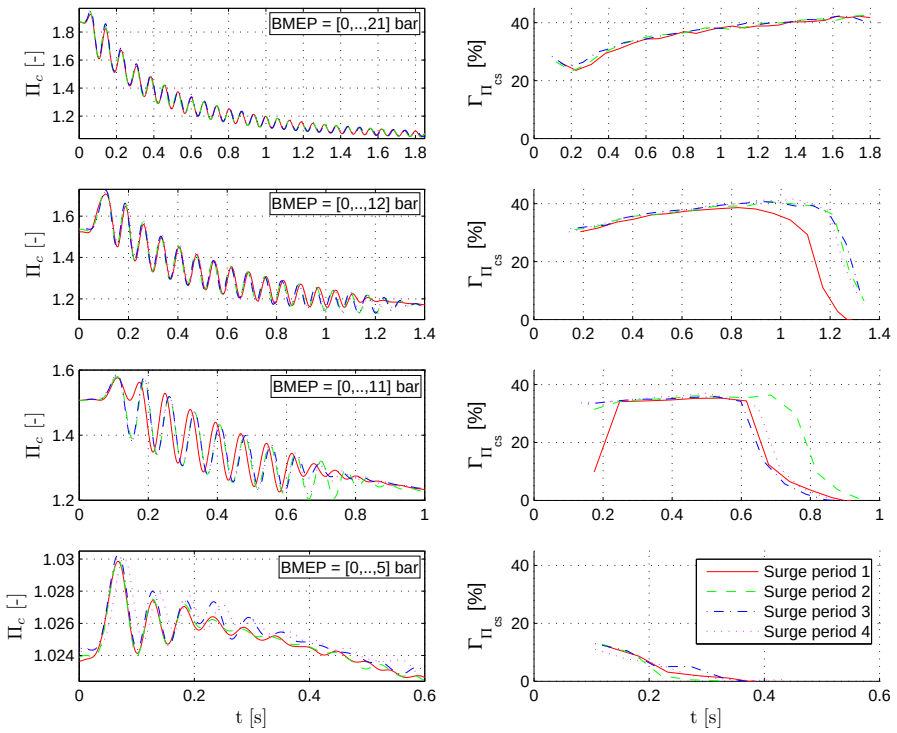

Figure 9: Measured surge in an engine test stand. Each row shows multiple surge periods initiated from the same engine operating point. Initial Π_c decreases from top to bottom. Left: Π_c-traces. Right: Calculated $\Gamma_{\Pi_{cs}}$.

Engine test stand data

Fig. 9 presents multiple typical surge measurements, seen as oscillations in e.g. pressures and turbo speed, at tip-out from an engine test stand. A number of tip-outs were initiated for each initial engine operating point, and a number of initial engine operating points were tested.

It can be seen that when deep surge is established, surge is repeatable with remarkable accuracy, although the behavior of the first and last cycles of the surge periods can differ, where some cycles show a mild surge behavior. The right plots show $\Gamma_{\Pi_{cs}}$, where an increasing trend in $\Gamma_{\Pi_{cs}}$ for decreasing Π_c can be seen. When the surge period is over $\Gamma_{\Pi_{cs}}$ goes to zero. Since N_{tc} decreases during the tip-outs, it is not possible to get a correct value of $\Gamma_{\Pi_{cs}}$. The maximum pressure ratio during a surge cycle ($\Pi_{c,max}$ of Section 5.1) is here taken as the peak following an associated $\Pi_{c,min}$-value, giving an approximation of $\Gamma_{\Pi_{cs}}$. An increasing trend in $\Gamma_{\Pi_{cs}}$ can be seen for decreasing Π_c.

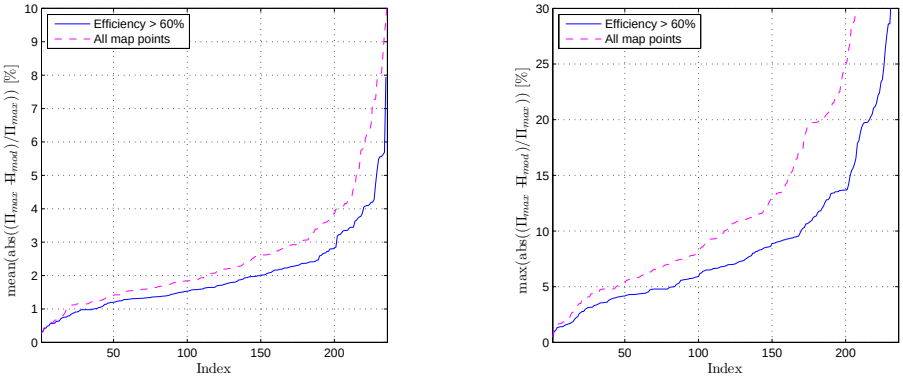

Figure 10: Left: mean absolute relative error for map points with $\eta_c > 60\%$ ("normal" operating region), and for all map points. Right: maximum absolute relative error.

6 Validation

The validation is divided into three parts. Normal operation modeling is first validated. The low speed extrapolation capability is then validated, followed by a surge modeling validation. Note that the models are parametrized on component level, and that small component model errors might result in large errors on a system level. This can be handled following the methodology presented in e.g. [**?**], for which the model structure is well suited.

6.1 Normal operation

Normal operation was considered to be represented by the operating points in the compressor maps of the database. One should though keep in mind that some of the maps contained SpL measured down to very low η_c. Since the parametrization process of the model structure was automated, all maps in the database were used. A summary of the mean and maximum relative model errors is first presented. Three representative maps are then selected, and presented to show the model structure properties.

The model is compared to the map in Fig. 10. The left plot shows mean absolute relative error for map points with $\eta_c > 60\%$ ("normal" operating region), and for all map points. The right plot shows maximum absolute relative error. Note the different y-axis scalings of the plots. It can be seen that the mean errors are less than 2.5% and 4% for the $\eta_c > 60\%$ ("normal operating range") and for all points respectively, for most of the maps. Also the maximum relative error for the normal operating range is small. It can also be seen that the Ellipse structure struggles for a few of the maps in the database. This can be a consequence of the least squares estimation getting stuck in a local minimum or a "strangely" shaped map.

Further validations are presented in Fig. 11. The figure presents what was considered to be three representative model fits (not the best, and not the worst

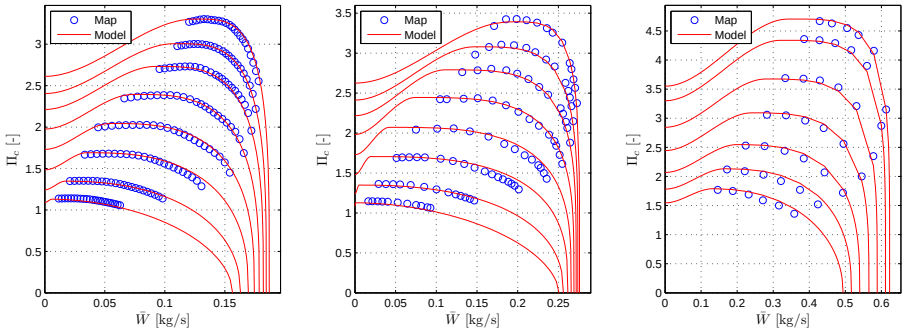

Figure 11: Representative model fits for three different sized (from small car to truck application) compressors. The circles represent map points, and the solid line is the Ellipse model. Very good agreement is found throughout the entire map. The model SpL are also extended down to maximum flow, and also down to zero flow.

fit models). Three compressors of different size were selected, representing flow ranges from (from left to right) a small car compressor up to a truck compressor. The circles represent map points, and the solid line is the Ellipse model. The model SpL are also extended down to maximum flow, and also down to zero flow to show the extrapolation. Very good agreement is found throughout the entire map for the small and large compressor, while the center model seems to underestimate $\bar{W}$ at ZSL of the map.

6.2 Surge operation

Mean Value Engine Models (MVEM) are used to validate the surge modeling. Two models were constructed; one for the surge test stand, and one engine test stand.

Surge test stand surge

The surge test stand MVEM consists of a compressor, two control volumes and a restriction. These are parametrized to correspond to the geometries and physical behavior from measurements. The results are shown in Fig. 12, where it is seen that measured and modeled t_{sc} and pressure oscillations are in good agreement. The upper plot shows a stable operating close to surge, where a good agreement between stationary modeled and measured Π_c is demonstrated. The lower plot shows an operating points in deep surge, where both the modeled t_{sc} and $\Gamma_{\Pi_{cs}}$ are in good agreement.

Engine test stand surge

The full TCSI MVEM developed in [**?**] is extended with the Ellipse compressor model. The same engine used to parametrize the MVEM, was driven in surge and measured. These measurements are here compared to the extended MVEM.

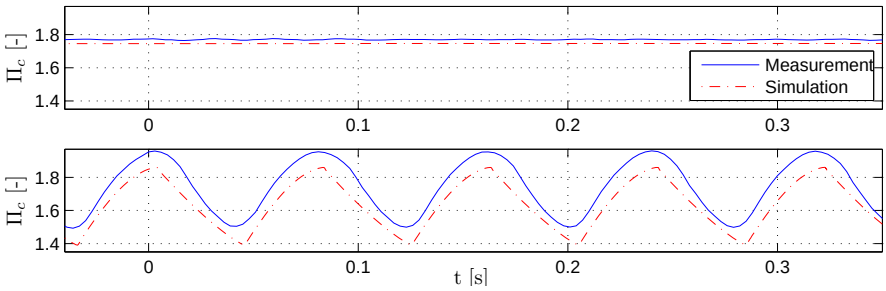

Figure 12: Modeled and measured surge rig Π_c, for a constant $\bar{N} = 130$krpm for two W_{th}. Upper: W_{th} close to surge. Lower: Operating point with deep surge.

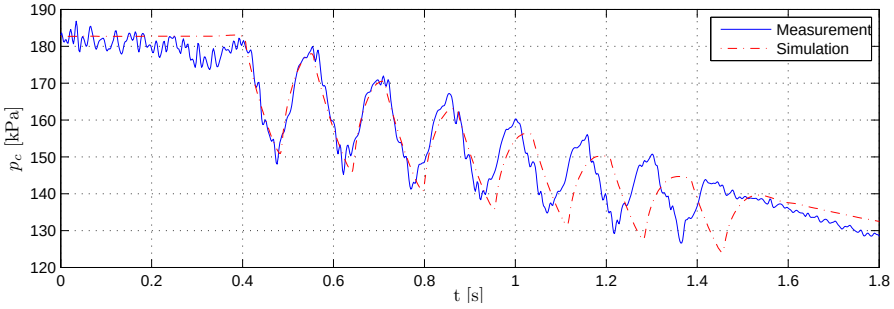

Figure 13: Engine test stand measured and MVEM simulated compressor control volume pressure for a surge transient.

The measured and modeled pressure oscillations are well modeled both in amplitude and frequency, both for stable operation before surge is initiated and during deep surge, see Fig. 13. The last modeled surge cycle deviates slightly from the measured, indicating a small error in t_{sc}.

7 Low speed extrapolation capability

Many of the available compressor maps contain measured points starting at approximately half of $\bar{N}_{max}$, see Fig. 2. All compressors, though, are started from standstill at some occasion, and many automotive applications make use of only the lower part of the compressor map (unless operated at altitude, see e.g. [**?** **?**]). The extrapolation capability of the model structure is thus important, in particular since compressor speed lines found in a map commonly represent only the upper half of the compressor $\bar{N}$ range, see Fig. 2.

This investigation makes use of the compressor maps, where measurements for low speed lines are available. An Ellipse model is parametrized using only the upper half $\bar{N}$ of the map, and the extrapolation capability of the model is

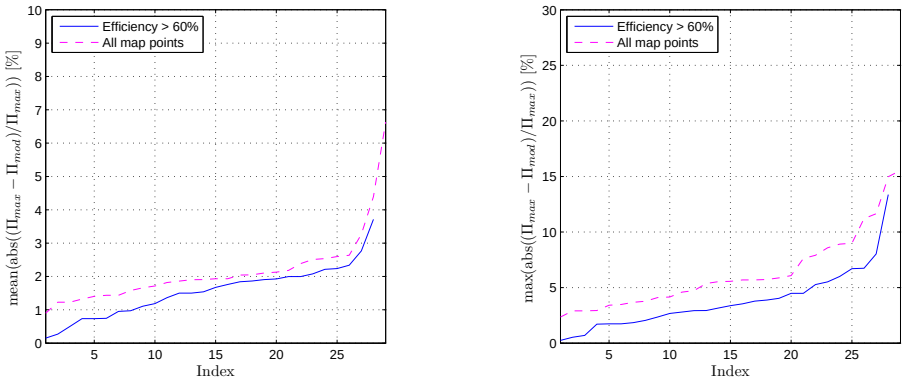

Figure 14: Absolute relative errors for extrapolated low speed points. Left: mean values for map points with $\eta_c > 60\%$, and for all map low $\bar{N}$ points. Right: maximum absolute relative error. Note the different y-axis scalings of the plots. One of the maps did not have any points with $\eta_c > 60\%$ at the small $\bar{N}$ investigated.

then validated against the measured lower SpL of the maps.

A total of 29 compressor maps were extracted out of the database. The selection criteria were that the maps should have: $\min(\bar{N}_{map}) < 0.3 \cdot \max(\bar{N}_{map})$, at least 90 points, and $\max(\Pi_{map}) > 2.8$. The maps passing these criteria were having $\bar{W}_{max,map} \in [0.1, 0.34]^{\mathrm{kg/s}}$, and thus mainly of car or small truck sizes. The model parameter re-optimization to only the upper $\bar{N}$ was conducted using nonlinear least squares. The starting point for this optimization was the optimized parameters for all $\bar{N}$. During the re-optimization, the model parameters that changed the most were: c_{41} and c_{51} (indicating a high model parameter sensitivity for these parameters).

The resulting mean and maximum absolute relative errors are presented in Fig. 14. It can be seen that the extrapolation capability of the Ellipse model structure is good, but for a few of the maps the extrapolation is less accurate. The lower SpL points (which was not included in the parametrization) have mean relative errors of less than 3% for most of the maps, for both map points with more than $\eta_c > 60\%$ and for all points. Also the maximum errors found are small.

8 Summary and conclusions

A database of 236 compressor maps has been analyzed, showing several interesting properties. A normal compressor map contains approximately 45 points over 6 speed lines, with shaft speeds starting at 41% of maximum shaft speed. A zero slope point and significant negative slope at the maximum mass flow is normally only found for speed lines with $\bar{N} > 60\% \cdot \max(\bar{N})$. The knowledge generated from the database is used to build a compact but descriptive control oriented compressor model.

Normal and choke compressor operation can be modeled using ellipses, and extended to describe surge. The parametrization can be automated given a compressor map and data from surge. The proposed basis functions for the curve fitting are validated on a database of compressor maps, and are shown to give good description for a wide range of automotive compressors, both single stage and two stage. The basis functions are physically motivated, and ensure a sound extrapolation capability. The ellipse model has good performance for normal operation, as well as for surge and operation with pressure ratios less than unity.

The automated parametrization is shown to give less than 3% mean absolute relative error for the normal operating region, for more than 200 of the maps. The corresponding maximum absolute relative error is less than 15% for all normal points, for more than 200 of the maps. Good extrapolation capability is important since no data is available for lower turbo speeds. Linear interpolation between different speed lines is an approximation, and the interpolation is better handled using the proposed Ellipse structure. Especially the very good fit of the $\hat{\Pi}_{\text{ZSL}}$-basis function can be exploited. The Ellipse model structure is shown to extrapolate to small turbo speeds with good performance.

The conclusions of the surge rig and engine test stand experiments are that $\Gamma_{\Pi_{cs}}$ can be used to model $\hat{\Pi}_{c0}$. If no available surge data exists, a constant value of $\Gamma_{\Pi_{cs}} \in [30, 50]\%$ will give a good approximation. Further, deep surge cycles are highly repeatable, and $\Gamma_{\Pi_{cs}}$ shows only a small dependency of mean mass flow. Surge pressure oscillations can be seen in measured data down to pressure ratios of close to unity, and are not limited to high pressure ratios/high shaft speeds. The deep surge cycle frequency is mainly given by the emptying and filling dynamics in combination with the compressor characteristics, where pressure build up at zero mass flow is most important. An MVEM together with the proposed Ellipse model can used to model compressor surge with good accuracy.

A Nomenclature

Symbol	Description
map	Compressor map
01	Compressor inlet station
02	Compressor outlet station
af	Air filter
c	Compressor
$c0$	Compressor at zero flow
cs	Compressor surge
ct	Compressor as turbine
$fric$	Friction
hpc	High pressure stage
lpc	Low pressure stage
max	Maximum
min	Minimum
$\Pi_{c,max/min}$	Max/Min Π_c during sc
sc	Surge cycle
std	Standard/reference
t	Turbine
ci	Choked inducer
tc	Turbocharger
th	Throttle
$\Gamma_{\Pi_{cs}}$	$\frac{(\Pi_{c,max}-\Pi_{c,min})}{(\Pi_{c,max}-1)}$ for sc
ZSL	Zero Slope Line, $\bar{W} > 0$
SpL	Speed Line
Π_{c0}	Pressure ratio at zero flow
$\hat{\Pi}$	Pressure build up ratio
$\hat{p}$	$\hat{\Pi} \cdot p_{01}$
$\hat{p}_0$	$\hat{p}$ at zero flow
$\hat{\Pi}_{c0}$	$\hat{\Pi}$ at zero flow

Symbol	Description
η	Adiabatic efficiency
p	Pressure
Π	Pressure ratio
$\hat{p}$	Pressure build up
$\hat{\Pi} = {}^{\hat{p}}/_{p_{af}}$	Pressure build up ratio
Γ	Π-ratio during surge
T	Temperature
Tq	Torque
W	Mass flow
$\bar{W}$	Corrected mass flow
N	Shaft speed
$\bar{N}$	Corrected shaft speed
D_c, L_c	Characteristic dia. & length
γ, c_p	Gas properties
J	Inertia
t	Time
$\bar{W}_t$	$\bar{W}$ at turbine-asymptote
$\hat{\Pi}_{ct}$	$\hat{\Pi}$ at turbine-asymptote
K_{ct}	Turbine-asymptote parameter
C_1, C_2	Ellipse eccentricity
$\bar{W}_{max}$	Maximum flow at $\Pi_c = 0$
$\bar{W}_{ZSL}$	$\bar{W}$ at ZSL
$\hat{\Pi}_{ZSL}$	$\hat{\Pi}$ at ZSL
$\Gamma_{\Pi_{cs}}$	Modeled $\Gamma_{\Pi_{cs}}$
$c_{i,j}$	Ellipse model parameters
k_{ij}	Model parameters fitted normalized data from all maps of the database

Paper 5

Measurement, analysis and modeling of compressor flow for low pressure ratios[†]

Oskar Leufvén and Lars Eriksson

Vehicular Systems, Department of Electrical Engineering, Linköping University, S-581 83 Linköping, Sweden.

5

Abstract

Increasingly stringent emissions legislation combined with consumer performance demands, have driven the development of downsized engines with complex turbocharger arrangements. To handle the complexity model-based methods have become a standard tool, and these methods need models that are capable of describing all operating modes of the systems. The models should also be easily parametrized and enable extrapolation. Both single and multiple stage turbo systems can operate with a pressure drop over their compressors, both stationary and transient. The focus here is to develop models that can describe centrifugal compressors that operate both in normal region and restriction region from standstill to maximum speed. The modeling results rely on an analysis of 305 automotive compressor maps, whereof five contain measured restriction operation, and two contain measured standstill characteristic. A standstill compressor is shown to choke at a pressure ratio of approximately 0.5, and the corresponding choking corrected mass flow being approximately 50% of the compressor maximum flow capacity. Both choking pressure ratio and flow are then shown to increase with corrected speed, and the choking pressure ratio is shown to occur at pressure ratios larger than unity for higher speeds. Simple empirical models are proposed and shown to be able to describe high flow and pressure ratios down to choking conditions well. A novel compressor flow model is proposed and validated to capture the high flow asymptote well, for speeds from standstill up to maximum.

[†]This is a formatted version of "Measurement, analysis and modeling of compressor flow for low pressure ratios" by Oskar Leufvén and Lars Eriksson, submitted to International Journal of Engine Research. The formatting is restricted to changing the article into a single-column format, adjusting sizes of figures and tables, and adjusting the referencing style.

1 Introduction

Efficiency demands and emissions legislation have lead both heavy duty and car manufacturers to develop ever more advanced turbocharged engines [9, 12, 25]. The flora of boosting system layouts is increasing, see e.g. [10]. Currently e.g. series sequential [33, 6, 11], parallel sequential systems [2], sequential series and parallel systems [8], or a combination of turbo and mechanical compressor are in production. Both more stages [24], as well as the inclusion of electric machines connected to a turbo or mechanical compressor shaft are investigated [10]. A promising path to handle the increased system complexity is model based control and diagnosis, which in turn relies on good control oriented models capturing relevant behavior.

The normal operating region of a turbo is well known and modeled in the industry, see e.g. [15] or [22]. Also surge modeling is found in the literature, see e.g. [32] or [17]. Current models, however, rarely describe component performance for operation close to, and below, a compressor pressure ratio (Π_c) of unity. Some investigations for low Π_c operation has been presented. In [28], the compressor is said to work as a poor turbine if a positive torque results, and else work as a throttle, for operation with corrected compressor mass flow $\bar{W} > 0$ and $\Pi_c < 1$. In [23], a typical nozzle discharge characteristic is said to be apparant, and a cold air turbine efficiency of the compressor of 20% is assumed. Compressor speedline extensions below $\Pi_c < 1$ are presented in [14]. In [4] an extrapolation methodology is presented, down to where the impeller inlet temperature equals the outlet. From this point downwards the compressor is said to work as a rather poor turbine, with excessive kinetic energy in the outlet.

Single stage system can be operated with $\Pi_c < 1$, e.g. during engine transients. Multi-stage turbo system can operate stationary with $\Pi_c < 1$ [4]. Thus, also this operating region is important to incorporate into a control oriented model.

This paper presents experimental data for compressor restriction operation, and methods to model this behavior. The knowledge gained in the investigation is generally applicable, and is useful for validation of the high flow extrapolation capability of a given model. The focus is on the mass flow to pressure ratio characteristics, since this has been shown to be insensitive to changing heat transfer conditions, see e.g. [28, 7, 3, 29]. The modeling efforts are hence simplified.

1.1 Outline and contributions

The compressor map, the gas stand used to measured maps, and how restriction map points can be measured are discussed first. The compressor map database used is then presented, and the maps are categorized into three types: normal, full, or extended. The extended maps contain compressor restriction operation. Characteristics of a compressor map, and a speedline (SpL), are highlighted. The measured extended maps are then presented focusing on the highlighted characteristics, and the operation outside of the normal operating range is an-

alyzed and modeled. A compressor flow model is then presented and validated as an extrapolation tool to evaluate operation outside the measured range. The model is exploited to deepen the understanding of compressor flow at unity pressure ratio, resulting in the development of models for this flow. A novel extension to the model is presented, and it is exemplified how the experimental findings can be incorporated into a model that describes the high flow and low pressure ratio operation of centrifugal compressors.

2 Experimental setup and data

2.1 Compressor map

The goal with the compressor map is to describe the compressor performance, for all operating conditions. When turbo performance is measured, the characteristics obtained are valid for the inlet conditions under which the measurements were conducted, see [30, 34]. To overcome this deficiency, different correction factors are applied to scale the performance variables to cover other inlet conditions. The correction factors are based on dimensional analysis of the compression system [21], and are fundamental to the map, see e.g. [20].

A compressor map consists of a number of stationary measurements of compressor inlet total temperature T_{01}, outlet total temperature T_{02}, inlet total pressure p_{01}, outlet total pressure p_{01}, mass flow W_c, and shaft speed N_{tc}. The compressor pressure ratio Π_c and adiabatic efficiency η_c are then directly calculated from measurement data

$$\Pi_c = {}^{\mathrm{p_{02}}}\!/_{\mathrm{p_{01}}} \tag{1}$$

$$\eta_c = \frac{\Pi_c^{\frac{\gamma_c - 1}{\gamma_c}} - 1}{{}^{\mathrm{T_{02}}}\!/_{\mathrm{T_{01}}} - 1} \tag{2}$$

A compressor inlet pressure reference $p_{c,ref}$, and a compressor inlet temperature reference $T_{c,ref}$, are then used to calculate corrected compressor mass flow $\bar{W}$ and corrected compressor speed $\bar{N}$ as calculated as

$$\bar{W} = W_c \cdot \frac{\sqrt{{}^{\mathrm{T_{01}}}\!/_{\mathrm{T_{c,ref}}}}}{{}^{\mathrm{p_{01}}}\!/_{\mathrm{p_{c,ref}}}} \tag{3}$$

$$\bar{N} = N_{\mathrm{tc}} \cdot \frac{1}{\sqrt{{}^{\mathrm{T_{01}}}\!/_{\mathrm{T_{c,ref}}}}} \tag{4}$$

Most discussions will be made in corrected quantities, but to keep the presentation compact "corrected compressor mass" will commonly be omitted in the text, and e.g. "flow" should then be read as "corrected compressor mass flow", unless otherwise explicitly stated. A number of points with equal $\bar{N}$ are measured from a small flow (referred to as the "surge line"), to a large flow point. The large flow point is most commonly given by a lower threshold in η_c, or to a given value of discharge throttle valve position (S2 in Fig. 1). Points with equal $\bar{N}$ are connected, and the lines formed are referred to as compressor speedlines.

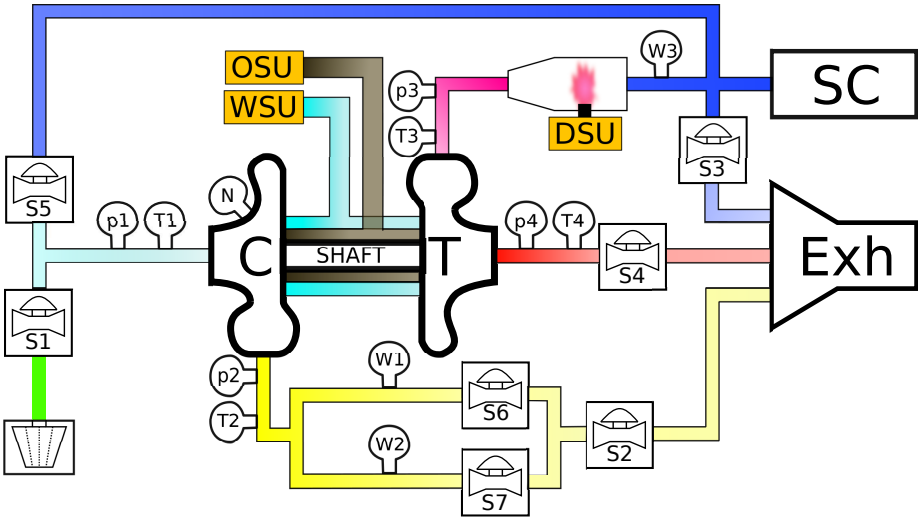

Figure 1: Schematic overview of the gas stand layout used to measure the extended maps. The abbreviations are: C compressor, T turbine, SC screw compressors, Exh exhaust chimney, DSU/OSU/WSU diesel/oil/water supply unit respectively, and S are valves to control flow. p, T, W, and N indicate measurement locations. Restriction operation of the compressor was enabled through closing S1 and using S5 to control p_{01}. The compressor discharge line is attributed to gas stand components after the compressor consisting of pipes, pressure, temperature, and mass flow measurement stations, and the compressor throttling valve. The discharge line ends in the chimney where the air is discharged to ambient.

2.2 Gas stand and normal map measurement

Compressor maps are commonly measured in a gas stand [30, 34]. Procedures for determining turbo performance in gas stands, are given in e.g. [26, 27, 1, 5]. An overview of the gas stand used to measure the extended maps presented in this paper, is shown in Fig. 1. Further details of this gas stand can be found in e.g. [16, 31], and in Appendix A.

A gas stand consists of a diesel burner (DSU), where diesel is burned in pressurized air, which is fed to the turbine (T) of the turbo. A closed loop controller uses the turbine feeding pressure (p_{03}) to control speed. Conditioned air at ambient pressure and temperature is fed to the compressor (C). A throttle valve (S2) loads the compressor discharge side. The S2 position is varied resulting in different compressor operating points, and when the system has stabilized, mean values of measured signals are stored for that particular map point.

Extended map measurement in a gas stand

Two different types of restriction measurements were made in the gas stand depicted in Fig. 2: (i) $p_{01} = 200$kPa and p_{02} varying, and (ii) $p_{02} = 100$kPa

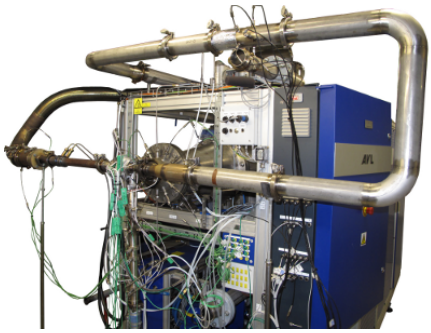
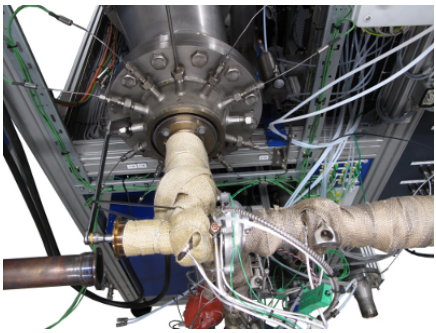

Figure 2: Installation pictures for restriction operation measurement, and standstill measurement respectively.

with p_{01} varying. For both measurement types, a maximum $p_{01} = 200$kPa was used, since a higher differential pressure from compressor to turbine side can brake the axial bearings of the chargers. Even with this limit, one of the axial bearings broke, and had to be replaced. The pressurized air fed to the compressor inlet, was conditioned to have a temperature close to ambient. The limit on p_{01}, along with the discharge line characteristics, meant that the lowest achievable Π_c also increased with increasing $\bar{W}$ (and hence $\bar{N}$).

To balance map grid density and time consumption, points for each $\Delta\Pi_c = 0.08$ starting at $\Pi_c = 1$ were measured (i.e. first measure $\Pi_c = 1$ then $\Pi_c = 0.92$ and so on). The two types of measurements converges to the same points for the lowest Π_c, since then the maximum $p_{01} = 200$kPa and a fully opened S2 (see Fig. 1) are used for both types of measurement. The largest difference occurs for the $\Pi_c = 1$ point, where the first measurement type is performed with $p_{01} = p_{02} = 200$kPa, and the second type with $p_{01} = p_{02} = p_{amb} = 100$kPa. Standstill speedlines were measured, naturally only with $\Pi_c < 1$, by locking the turbine nut using a device that minimized any radial displacement of the rotor assembly. The same two types of measurement presented above were then used.

The screw compressors of the gas stand commonly supplies only the turbine with pressurized air, but for the $\Pi_c < 1$ measurements the majority of this air flow went through the compressors tested. The combined maximum flow of the screw compressors are approximately 500g/s, which meant that neither of the measured extended maps have $\Pi_c < 1$ measurements up to maximum $\bar{N}$.

During the measurements, the gas stand was controlled to maintain a constant $\bar{N}$. However, small variations in speed are inevitable, and the method from [18] was used to post process the data to create speedlines. The adjustments were almost neglectable, due to the accurate gas stand speed control.

2.3 Three types of compressor maps

Three types of compressor maps are used in this paper: (I) normal map, (II) full map, and (III) extended map. The distinction between the types are discussed below, and an overview of the map types is shown in Fig. 3.

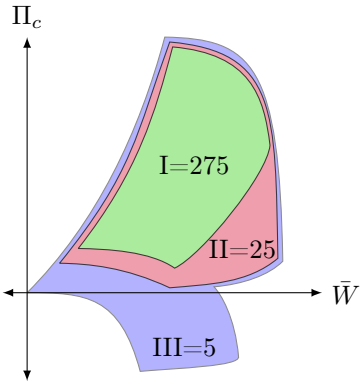

Figure 3: Overview of the three types of compressor maps; (I) Normal maps; measured down to reasonable efficiency for larger speeds or constant setting of throttling valve (S2, in Fig. 1), (II) Full maps; measured to test stand discharge characteristics with S2 fully opened, (III) Extended maps; measured below pressure ratio of unity and also for standstill operation. The numbers of the different types of maps of the map database are also indicated.

Normal maps have points measured with reasonably high compressor efficiencies, hence only the higher Π_c part of a SpL. This means that points measured for high flows deviate largely from a pressure ratio of unity, and that the S2-valve is never fully opened. ***Full*** maps have points measured down to the discharge line characteristic of the test stand, with a fully opened S2-valve. A well designed gas stand discharge line then enables measurement of compressor maps down to a pressure ratios close to unity, also for large flows. However, the gas stand discharge line characteristics gives a lower pressure ratio threshold. This means that a SpL with smaller flow can be measured closer to $\Pi_c = 1$. ***Extended*** maps have points with $\Pi_c < 1$.

Points of an extended map can be removed to create a full map, and points of a full map can be removed to create a normal map. The information contents of maps are thus, in some sense

$$\text{normal} \subset \text{full} \subset \text{extended} \tag{5}$$

as illustrated in Fig. 3. This classification will be used during the validation process of the extrapolation tools presented later.

2.4 Compressor map database

A database of compressor maps with compressor sizes for automotive applications has been prepared for this paper, and a summary of the entries is found in Fig. 4. The maps of the database will be systematically classified, and analyzed in the following subsections.

The compressors cover small car applications (with a maximum $\bar{W} < 100$g/s and a corresponding maximum $\bar{N} > 300$krpm), and up to heavy truck ap-

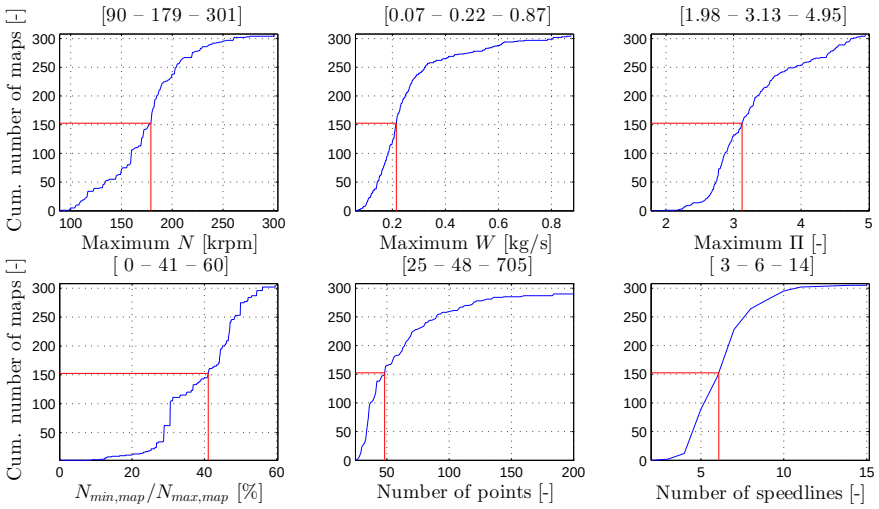

Figure 4: Summary of the map database. The top row shows distribution of maximum $\bar{N}$, $\bar{W}$ and Π_c for each map, respectively. The bottom row shows accordingly: ratio of minimum to maximum $\bar{N}$, number of points, and number of SpL. The titles give the lowest, median, and maximum values for each plot.

plications (with maximum $\bar{W} > 800$g/s and a corresponding maximum $\bar{N} <$ 100krpm). As can be seen in Fig. 4, the database is biased towards car sized compressor maps. The titles of each subfigure gives the minimum, median, and maximum value for the particular variable presented in that subfigure. A "median map" of the database has a maximum $\bar{N}$ of roughly 180krpm, maximum $\bar{W}$ of roughly 220g/s and a maximum pressure ratio of roughly 3.1. The "median map" further contains SpL from roughly 40% of maximum $\bar{N}$ up to maximum, and 48 points spread over 6 SpL. For some of the plots the maximum or minimum points are not shown. This is due to that, e.g. one of the maps contained more than 700 points, and including this point in the plot would stretch the axis and hide other information.

Classification of the maps

The map entries were classified as belonging to either of the three types presented in Section 2.3. The extended maps were easily classified as those with $\Pi_c < 1$-points. Since the control signal to the S2-valve was not available for most map database entries, the following method was used to distinguish between normal and full maps. For each map, the highest SpL was selected, and the flow at $\Pi_c = 2$ was then linearly interpolated. Maps that did not contain values with $\Pi_c < 2.0$ at maximum $\bar{N}$, used the maximum $\bar{W}$ of the map instead. An equivalent effective throttle area was then estimated from the gas

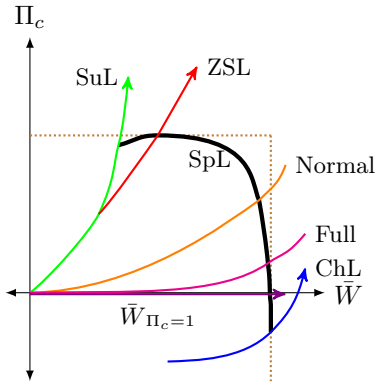

Figure 5: Overview of a speedline (SpL) passing through, from low to high flow: the surge (Su) point at the surge line (SuL), the zero slope (ZS) point at the zero slope line (ZSL), a point where measurements of normal maps (Normal) stops, the gas stand discharge side characteristic line that defines the lower Π_c-limit for the full maps (Full), the unity pressure ratio ($\bar{W}_{\Pi_c=1}$) point, and ending in the choke (Ch) point at the choke line (ChL) where an infinite slope is found. Low SpL commonly have no zero slope (ZS) point. The surge point (Su) coincides with the ZS point at an intermediate speed. Points below the $\Pi_c = 1$-line (the x-axis) are referred to as restriction operation points.

flow through a restriction equation (see e.g. [13])

$$A_{eff,\mathrm{S2}} = W_{\mathrm{S2}} \cdot \frac{\sqrt{\frac{R \cdot T_{\mathrm{S2}}}{p_{\mathrm{S2}}}}}{\frac{1}{\Pi_{\mathrm{S2}}^{1/\gamma}} \cdot \sqrt{\frac{2 \cdot \gamma}{\gamma - 1}} \cdot \left(1 - \left(\frac{1}{\Pi_{\mathrm{S2}}}\right)^{\frac{\gamma-1}{\gamma}}\right)} \tag{6}$$

where T_{S2} is an assumed fluid temperature at the throttle, and constant values of $R = 287^{\mathrm{J}}/_{\mathrm{kg\,K}}$, $T_0 = 298\mathrm{K}$, $\gamma = 1.4$ were used. $\Pi_{\mathrm{S2}} = 2$ was considered a reasonable limit between normal and full maps, and $T_{\mathrm{S2}} = T_0 \cdot \Pi_{\mathrm{S2}}^{(\gamma-1)/\gamma} = 363.3\mathrm{K}$ was used, and $p_{02} = 200\mathrm{kPa}$ was assumed.

The measured points below this limiting line are then studied. A map was considered a full map if: (1) at least 20% of the points were under the line or (2) at least 20 points under the line combined with at least 50% of the SpL having a point under the line or (3) at least 5 SpL with points under the line. Maps that did not satisfy any of (1), (2), or (3), were classified as a normal map. In summary, the number of maps from each map type are: 275 normal, 25 full, and 5 extended.

Characteristic points on a compressor speedline

A number of characteristic properties of a compressor speedline (SpL) will be discussed, and are exemplified in Fig. 5. A lower SpL is measured at smaller $\bar{N}$. The ***slope*** of a SpL is defined as $^{\Delta\Pi_c}/_{\Delta\bar{W}}$. The point of each SpL with zero slope

is referred to as the Zero Slope (ZS) point, and the point with infinite slope is referred to as the Choke (Ch) point. If the ZS, or the Ch, points are connected to lines and these are referred to as the Zero Slope Line (ZSL) or Choke Line (ChL), respectively. The minimum flow point of a SpL is referred to as the surge point (Su), and if these points are connected the Surge Line (SuL) is constructed. A restriction point is a point where the compressor operates with $\Pi_c < 1$.

An analysis of the database shows the following properties of a regular map: lower SpL have no ZS point, the point for ZS coincides with the point for Su for intermediate SpL, and higher SpL have a positive slope close to the SuL with a ZS at higher flows. It is not common to measure SpL down to the Ch point, nor to measure restriction operation.

A regular SpL shows increasing $\bar{W}$ for a decrease in Π_c, for points with higher flow than the ZS flow. A "backwards" turning SpL gives a smaller $\bar{W}$ for a decreasing Π_c, where a given $\bar{W}$ and $\bar{N}$ give two different Π_c, see e.g. [4]. The backwards bending SpL-property is found in all five extended maps, and twelve of the other maps in the database. The maps with this property were from different turbo manufacturers, measured in different test setups, and of different sizes. The phenomenon with backwards bending SpL is thus not associated with the measurement of the extended maps presented here.

3 Analyzing the extended maps

Extended maps were measured for three turbo models referred to as; TD04, K04, and KP35 (though these names really refer to the turbine frame sizes), and are exemplified for the TD04 turbo in Fig. 6. Manufacturer maps (manu), measured in independent gas stands, were also available for all three turbo models. Two different KP35-individuals were measured, to investigate any spread in the characteristics between individuals. The measurements were further repeated for one of the KP35-individuals at a later occasion, to investigate the measurement repeatability. The standstill SpL of the K04 turbo was repeated at two different wheel orientations, to investigate if there is an influence from wheel orientation on the standstill characteristics.

Some calibration dependent deviations with the gas stand mass flow sensor system for $p_{01} >> p_{amb}$ occured when the gas stand changed between the two Vcones used to measure different mass flow ranges, i.e. changing from W1 to W2 using valves S6 and S7 in Fig. 1. The calibrations of the gas stand Vcones were therefore re-estimated off-line. The re-estimation process is detailed in Appendix B, and presented in Fig. 6 where it can be seen that the scattering of the restriction operation points decreases after the re-estimation.

The five extended maps are summarized in Table 1. The ":"-operator compacts the table, and for example: "81:31:236" means every 31th krpm from 81krpm to 236krpm (with numbers rounded). The maximum $\bar{N}$ and $\bar{W}$ of the maps are also presented, where the numbers in parenthesis indicate corresponding data from manufacturer maps. It can be seen that it is only the K04 and TD04 maps that contain standstill measurement. The KP35-1, KP35-2 and

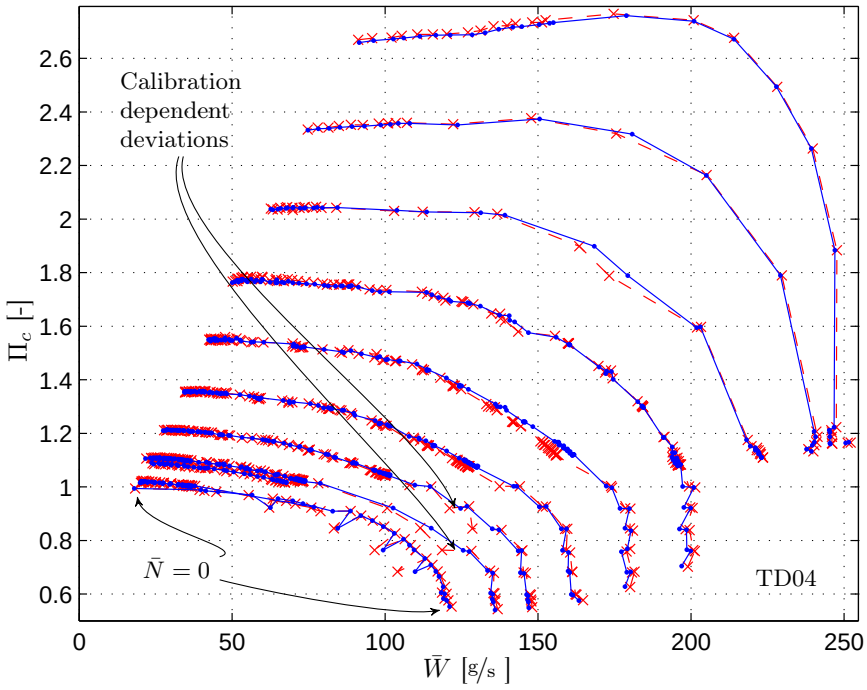

Figure 6: Extended map for the TD04 turbo. The dots connected with solid lines show the offline re-estimated map, and the crosses connected dashed lines show the raw data from the gas stand. The stand-still speedline at the lowest left, is discussed more in-depth in Section 3.1.

Map	Meas $\bar{N}$ [krpm] $\Pi_c < 1$	$p_{01} = 100$kPa, S2 = 100%	Maximum $\bar{N}$ [krpm]	$\bar{W}$ [g/s]	$\Pi_c < 1$ $\bar{N}$-range [%]
KP35-1	93:26:144, 196:26:248	248	273(263)	105(102)	35-94
KP35-2	68, 111, 142, 206, 236	49, 68, 81:31:236, 270, 300	300(263)	107(102)	22-90
KP35-3	41, 57, 67, 93, 144, 196	41, 57, 67, 93, 120, 144, 172 196, 247	247(263)	103(102)	16-75
K04	0, 43:16:126	23, 33, 43:16:159	159(174)	209(209)	(0)25-72
TD04	0, 44:17:113	0, 20, 40, 44:17:181, 185	185(170)	252(239)	(0)26-66

Table 1: Summary of the extended map measurements for $\Pi_c < 1$ and S2 = 100%. The ":"-operator compacts the table, and for example: "81:31:236" means every 31th krpm from 81krpm to 236krpm (with numbers rounded). The maximum $\bar{N}$ and $\bar{W}$ of the extended maps are also presented, where the numbers in parenthesis indicate corresponding data from manufacturer maps. The last column shows the $\bar{N}$-range of the SpL with $\Pi_c < 1$. For example: The lower value for the TD04 is calculated as $^{44}/_{170}$, and reference is hence made to the maximum $\bar{N}$ of the corresponding manufacturer map.

TD04 maps are measured beyond the manufacturer $\bar{N}$-limit. Studying the K04 manufacturer map reveals that the higher SpL measured still have a finite slope at the highest $\bar{W}$, and it is expected that these SpL would have a larger maximum $\bar{W}$ if measured down to $\Pi_c = 1$. The last column presents the $\bar{N}$-range of the extended SpL, as compared to the maximum $\bar{N}$ of the corresponding manufacturer map.

The following four subsections will highlight and model important asymptotic characteristics of compressor flow, and demonstrates the importance of verifying the validity limits of a given model. The models will further be used for extrapolation, i.e. to estimate outside the range of data that was used to parametrize the model. Interpolation in data will also be used, i.e. to estimate within the range of data used to parametrize a model.

3.1 Standstill compressor speedline

The standstill SpL naturally defines a lower asymptotic limit for any compressor model. Measurements of SpL with $\bar{N} = 0$ are presented in Fig. 7. The squares represent measurements where $p_{01} = 200$kPa (blue for K04, and red for TD04). The measurements with $p_{01} = 200$kPa consistently show a larger $\bar{W}$ than the points measured with $p_{01} = p_{amb}$ (indicated by the crosses), for both turbo models. The cause for these deviations is still an open issue. Note also the small but visible jump in the data for the TD04 around $\bar{W} = 90$g/s, which is due to the change from Vcone1 to Vcone2 as discussed in previous section.

The two blue lines consist of two lines each, where the orientation of the compressor wheel was altered between the measurement series, to investigate whether the wheel position affected the characteristics. No difference between the SpL for different wheel orientations is seen.

Three models were tested to model the standstill characteristics. First A_{eff} of (6) was estimated using least squares. This model was though not capable of describing the characteristics especially for lower Π_c, and different A_{eff} were estimated for each type of measurement. Therefore, two others models are proposed. An empirical model as

$$\Pi_{c,mod,1}(\bar{N} = 0) = \left(1 - \left(\frac{\bar{W}}{c_{1,2}}\right)^{c_{1,1}}\right)^{\frac{1}{c_{1,1}}} \cdot (1 - c_{1,3}) + c_{1,3} \tag{7}$$

as well as a model commonly used as for turbine flow, as

$$\Pi_{c,mod,2}(\bar{N} = 0) = \left(1 - \left(\frac{\bar{W}}{c_{2,1}}\right)^{2}\right)^{c_{2,2}} \tag{8}$$

were tested. Both models are shown in Fig. 7, were they are hardly distinguishable from the measurements. The first model is preferred due to the increased flexibility and especially the ability to have vertical SpL slope at $\Pi_c > 0$.

3.2 Corrected compressor choking line mass flow - $\bar{W}_{\mathbf{ChL}}$

Measured choking flow are presented with circles in Fig. 8. For all maps, an increasing choking flow with $\bar{N}$ can be seen. The choking flow for lower speeds

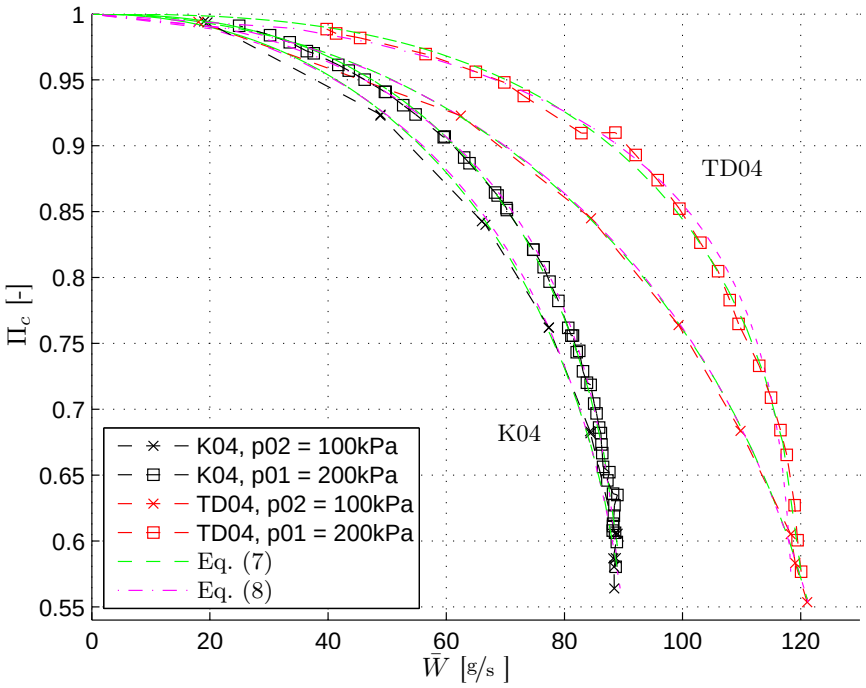

Figure 7: Standstill characteristics for the TD04 and K04 turbos. The squares represent measurements where $p_{02} = 200$kPa. These measurements consistently show a larger $\bar{W}$ than the points measured with $p_{01} = p_{amb}$, indicated by the crosses. The characteristic lines for the K04 are measured for two different wheel orientations, with a neglectable difference.

can be well described by a power law model as

$$\bar{W}_{\mathrm{ChL},pow}(\bar{N} \leq \bar{N}_{s,1}) = c_{3,0} + c_{3,1} \cdot \bar{N}^{c_{3,2}} \tag{9}$$

or a polynomial model as

$$\bar{W}_{\mathrm{ChL},poly}(\bar{N} \leq \bar{N}_{s,1}) = c_{4,0} + c_{4,1} \cdot \bar{N} + c_{4,2} \cdot \bar{N}^2 \tag{10}$$

where $c_{3,0}$ and $c_{4,0}$ can be physically interpreted as choking flow at standstill, for both models. $\bar{N}_{s,1}$ is referred to as the switching speed, where switch refers to that the characteristics switches behavior. An abrupt change in a characteristic line as this will lead to definitions of further switching points in the following sections. The data is not enough to support a model for higher speeds but an extension as

$$\bar{W}_{\mathrm{ChL},pow}(\bar{N} > \bar{N}_{s,1}) = c_{5,0} + c_{5,1} \cdot \bar{N} \tag{11}$$

is proposed for completeness. Validating model fits are presented in Fig. 8, where it can be seen that both the power law and the polynomial model have

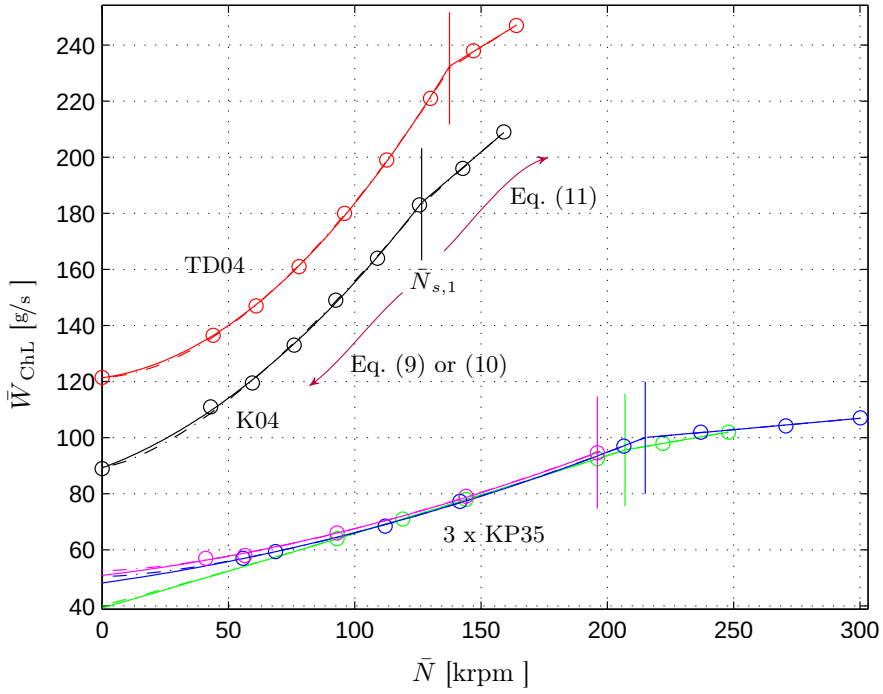

Figure 8: Measured corrected compressor choking mass flow (circles). Two low speed models: (9) (solid) and (10) (dash dotted) are shown, as well as corresponding continuations for high speed using the model (11). The models are almost indistinguishable. The switching point between choking flow models for low $\bar{N}$ and high $\bar{N}$ that defines $\bar{N}_{s,1}$ are also indicated with horizontal lines.

good fit for low to medium speeds, and the affine model has good fit for higher speeds.

The parametrization of (10) to the maps resulted in no extremum within the $\bar{N}$ ranges of each map. However, the strictly monotonic behavior of the power law model (9) makes it the preferred model. No choking line flow measurement for the upper speeds was found for the KP35-3 map. The other four maps have 2-3 flow points with $\bar{N} > \bar{N}_{s,1}$ are naturally well described by the two parameter affine models (fitting a two parameter model to 2-3 points).

The intersection speeds, $\bar{N}_{s,1}$, between the low speed and the high speed choking flow models, normalized with the maximum $\bar{N}$ of corresponding manufacturer map, were: 79% (KP35-1), 82% (KP35-2), 75% (KP35-3), 73% (K04), and 81% (TD04). This means that for speeds above roughly 75-80% of maximum speed the increase in choking flow characteristics, found for lower speeds, is broken off, and the increase is then relatively smaller. The maximum speed of the manufacturer maps were considered to be a more representative normalization compared to taking the maximum speed of the extended maps, since the extended maps were measured at speeds above the manufacturer recommenda-

Map	$\bar{W}_{\mathrm{ChL,meas}}$	Eq. (9)(rel.err)	Eq. (10)(rel.err)
K04	89g/s	97g/s (8%)	93g/s (4%)
TD04	122g/s	122g/s (0%)	119g/s (-2%)

Table 2: Comparison of measured corrected compressor standstill choking mass flow, and extrapolation using (9) and (10) (i.e. $c_{3,0}$ and $c_{4,0}$ respectively), parametrized to $0 < \bar{N} \leq \bar{N}_{s,1}$. The relative errors are indicated in parenthesis.

Map	$\bar{W}_{\mathrm{max,manu}}$	Eq. (9)(rat.)	Eq. (10)(rat.)
KP35-1	102g/s	40g/s (39%)	39g/s (38%)
KP35-2	102g/s	50g/s (50%)	48g/s (47%)
KP35-3	102g/s	53g/s (52%)	51g/s (50%)
K04	209g/s	97g/s (46%)	93g/s (44%)
TD04	239g/s	122g/s (51%)	119g/s (50%)

Table 3: Comparison of extrapolated standstill choking mass flow using (9) and (10) (i.e. $c_{3,0}$ and $c_{4,0}$ respectively), parametrized to $0 < \bar{N} \leq \bar{N}_{s,1}$, and the maximum flow of a corresponding manufacturer map $\bar{W}_{\mathrm{max,manu}}$. The ratios between modeled flow and maximum manufacturer map flow are also indicated in parenthesis.

tions, see Table 1.

The extrapolation capability of the proposed low speed models (9) and (10) were studied, using the two maps that contained standstill choking flow (K04 and TD04). The models were parametrized to SpL having $0 < \bar{N} \leq \bar{N}_{s,1}$. The measured standstill $\bar{N} = 0$ choking flow was then compared to the values resulting from extrapolating the models to standstill. The result is presented in Table 2. It can be concluded that the models (9) and (10) capture the standstill choking flow well, and that the models can accurately extrapolate standstill choking.

Models for choking flow for $\bar{N} < \bar{N}_{s,1}$ were then parametrized for all maps, and the modeled standstill choking flow (i.e. $c_{3,0}$ of (9) and $c_{4,0}$ of (10)) was compared to the maximum flow of a corresponding manufacturer map ($\bar{W}_{\mathrm{max,manu}}$). The result is presented in Table 3. The ratio $\bar{\mathrm{W}}_{\mathrm{Ch}}(\bar{\mathrm{N}}=0)/\bar{\mathrm{W}}_{\mathrm{max,manu}}$ is approximately 50%, for all but the first map (KP35-1) which both models underestimate. Since the restriction operation measurements starts from 93krpm for this map (see Table 1), the small extrapolated standstill choking flow is believed to be due to an overfit to the data for higher speeds. Thus, to ensure small errors in the extrapolation to standstill choking flow, measurements of choking flow need to be conducted at relatively small $\bar{N}$.

3.3 Choking line pressure ratio - $\Pi_{c,\mathbf{ChL}}$

The choking line pressure ratios are extracted from the measured extended maps, using visual inspection. The reason to perform the process manually, is the high sensitivity to small errors in either the control of $\bar{N}$ (the gas stand), the measurement of mass flow or the gas stand mass flow measurement calibration. The measured choking line pressure ratios are shown with circles in Fig. 9. It

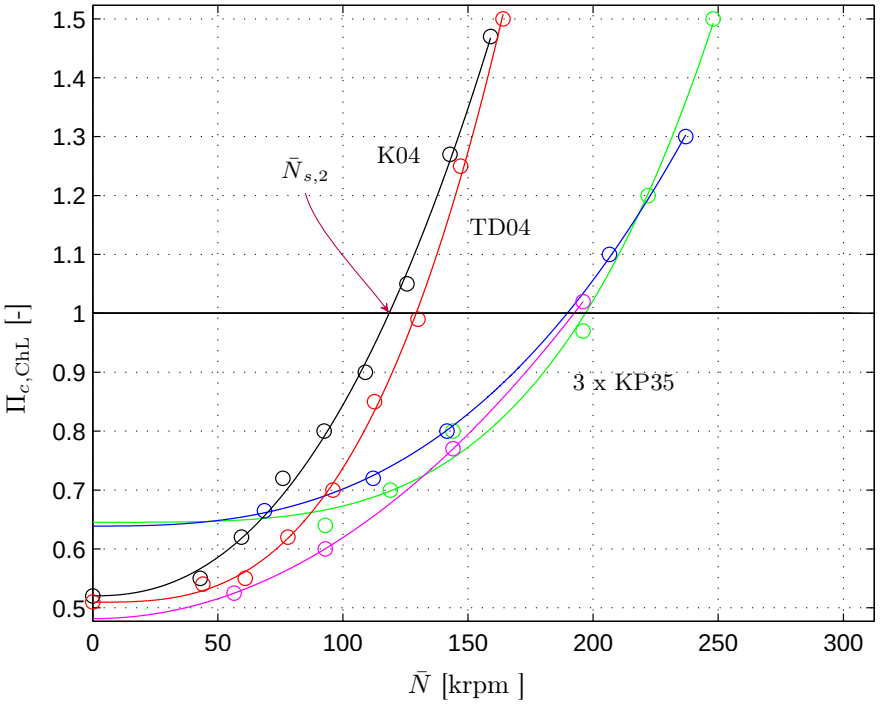

Figure 9: Measured and modeled (12) choking pressure ratio $\Pi_{c,\mathrm{ChL}}$ for the extended maps. The intersection speed between the models and the, with a solid line marked, $\Pi_c = 1$ line defines $\bar{N}_{s,2}$.

can be seen that the choking line pressure ratio starts at a Π_c of well below unity for all maps. For the K04, TD04, and KP35-3 maps $\Pi_{c,\mathrm{Ch}}$ is approximately 0.5 for standstill or low speed operation, while it is larger for the KP35-1 and KP35-2 maps. Choking line pressure ratio then increases monotonically with $\bar{N}$, and no abrupt change, as for the choking line flow, is visible. The choking pressure ratios are above one for all maps, at higher speeds. All the three maps with choking pressure ratio measurements at close to maximum manufacturer speeds (KP35-1, K04, TD04), have approximately a choking pressure ratio of 1.5 for the highest speed. Having choking pressure ratio above unity, can be explained by that a compressor stage is comprised of several components, and a particular component can be choked even though the compressor stage globally operates with a pressure increase over it. Thus, the minimum Π_c for when a SpL tends to be vertical can be found at $\Pi_c > 1$ (see also the discussion in Section 2.4).

The following power law model is proposed for choking line pressure ratio

$$\Pi_{c,\mathrm{ChL},pow}(\bar{N}) = c_{6,0} + c_{6,1} \cdot \bar{N}^{c_{6,2}} \tag{12}$$

where the parameter $c_{6,0}$ is interpreted as standstill choking pressure ratio. Model fits to each map and extrapolation to stand still are shown as solid lines in Fig. 9, where it can seen that the model captures the choking line pressure

ratio well. A second order polynomial model was also tested, but was rejected due to poor fit and the potential of having a minimum within the speed range of interest (and hence violating the monotonic behavior seen in the measurements).

Another switching speed $\bar{N}_{s,2}$ is here defined as the speed for which the model (12) is equal to one, and is hence the speed for when the model lines in Fig. 9 cross the $\Pi_c = 1$-line. $\bar{N}_{s,2}$ for each map normalized with the maximum $\bar{N}$ of corresponding manufacturer map were: 75% (KP35-1), 72% (KP35-2), 73% (KP35-3), 68% (K04), and 76% (TD04). This means that choking occurs above unity pressure ratio for speeds higher than approximately 70% of maximum allowable speed. One can note that these numbers are close to the switching speed of the choking line flow models presented in Section 3.2.

Map	$\Pi_{c,\mathrm{ChL,meas}}$	Eq. (12) (rel.err)
K04	0.520	0.521(0.1%)
TD04	0.510	0.509(-0.2%)

Table 4: Measured and modeled standstill choking pressure ratio. The models were parametrized to all $0 < \bar{N}$, and choking Π_c for $\bar{N} = 0$ was then extrapolated using the models (i.e. $c_{6,0}$ of (12)).

To investigate the low speed extrapolation capability of the model, the standstill SpL is then removed from the TD04 and K04 extended maps. The model (12), is then parametrized to all $\bar{N} > 0$, and choking pressure ratios at standstill (i.e. c_0 of (12)) are extrapolated using the models. The extrapolated values are compared to the measured in Table 4. The model shows remarkable small errors.

The standstill choking pressure ratios for the three KP35 maps, are extrapolated using the model (12). The extrapolated standstill choking pressure ratios were 0.645, 0.639, and 0.482 respectively. The large spread in the estimates for the KP35 maps, highlights the uncertainty from extracting the choking pressure ratio.

3.4 Corrected compressor mass flow at unity pressure ratio – $\bar{W}_{\Pi_c=1}$

Flow for unity pressure ratio $\bar{W}_{\Pi_c=1}$, maximum flow for the full map ($\bar{W}_{\mathrm{max,full}}$) part of the extended maps, and choking line flow ($\bar{W}_{\mathrm{ChL}}$), are compared and analyzed in this section.

The different flows are presented in Fig. 10. It is seen that the flows converge for higher speeds. Since choking pressure ratio is found for larger than unity pressure ratio at higher speeds, the converging of the flows are expected for these speeds. If the converged flows are extrapolated to higher than measured speeds, a saturation (indicated by the dotted line for the TD04-map) is visible for all but the K04-map.

Fig. 11 shows the choking flow and full map flow, relative to the flow at unity pressure ratio. It can be seen that full map flow agrees well with unity pressure ratio flow for high speeds, but also for the lowest speeds measured. Hence, a good approximation of unity Π_c flow can be found in full maps, using

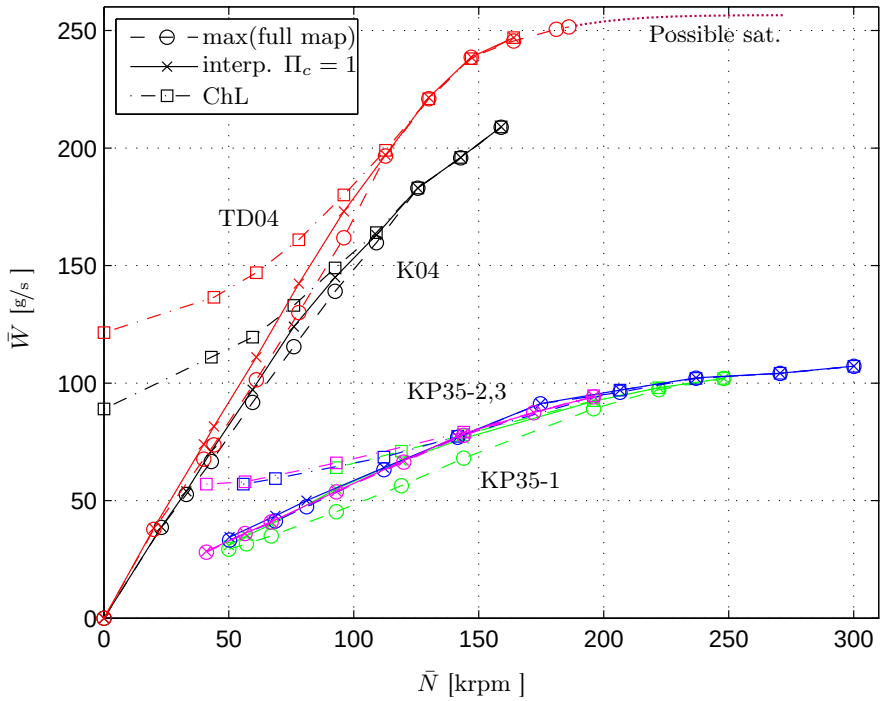

Figure 10: Characteristic corrected mass flow $\bar{W}$ points of the extended maps. The squares indicate choking $\bar{W}_{\mathrm{Ch}}$, the crosses indicate interpolated mass flow at unity pressure ratio $\bar{W}_{\Pi_c=1}$, and the circles indicate maximum $\bar{W}$ of the full map part of the extended maps $\bar{W}_{\mathrm{max,full}}$. A possible saturation flow can be seen, for all but the K04 map, if the converged flows are extrapolated to higher speeds.

the maximum measured $\bar{W}$ of these SpL. The good agreement between $\bar{W}_{\Pi_c=1}$ and $\bar{W}_{\mathrm{max,full}}$ for low $\bar{N}$, is due to that the discharge line of the gas stand causes a small backpressure for a fully opened S2-valve, for the lower flows associated with lower speeds. Thus, points can be measured down to almost unity pressure ratio. For higher speeds, the choking pressure ratio is larger than the gas stand discharge side flow resistance curve, which means that for high speeds $\bar{W}_{\Pi_c=1} = \bar{W}_{\mathrm{max,full}} = \bar{W}_{\mathrm{Ch}}$, if backwards bending speedlines are neglected. For intermediate speeds however, the last measured point with fully opened S2 is found relatively far from $\Pi_c = 1$ combined with a small negative slope, which causes larger difference between full map choking flow and unity pressure ratio flow. Further, the relative difference between full map flow and flow at unity pressure ratio at intermediate speeds, is largest for the TD04 map, followed by the K04 map and smallest for the KP35 maps. This is explained by the differences in measured flows, where the TD04 is the charger with the largest flow (see Table 1). Hence, while approximating $\bar{W}_{\Pi_c=1}$ for intermediate $\bar{N}$ with $\bar{W}_{\mathrm{max,full}}$ can be a good approximation for a small compressor on a

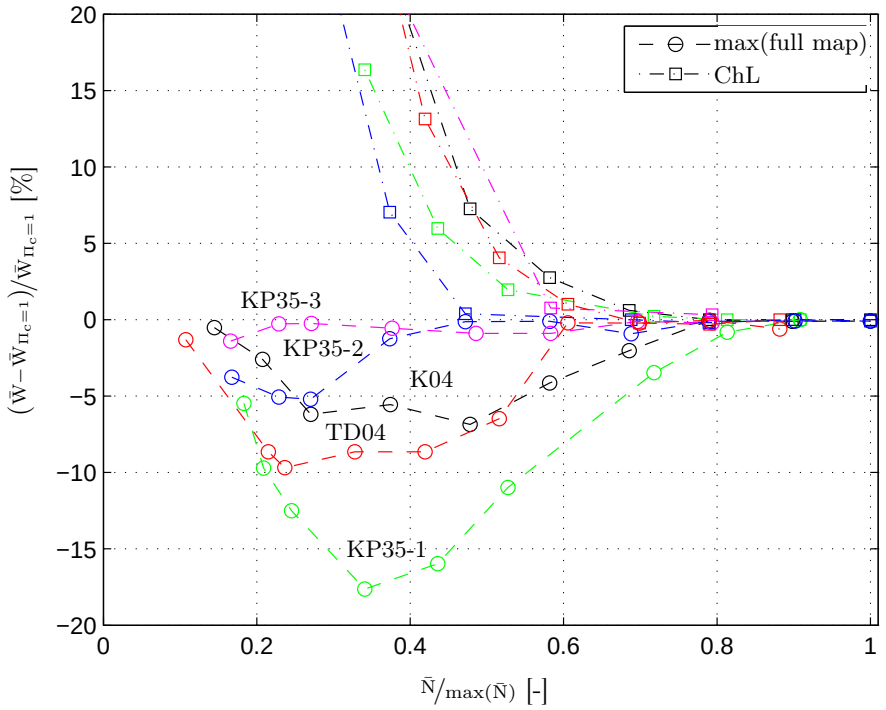

Figure 11: Measured choking flow and full map flow relative to interpolated flow at unity pressure ratio. The circles indicate full map flow, and crosses indicate choking flow.

given gas stand, a less satisfying result is expected for a larger compressor on the same gas stand.

For lower speeds the data indicates that a linear model as

$$\bar{W}_{\Pi_c=1}(\bar{N} \leq \bar{N}_{s,3}) = c_{7,1} \cdot \bar{N} \tag{13}$$

fits the measurements well, while balancing model complexity. A simple model for higher speeds is difficult to deduce from the data. An affine model as

$$\bar{W}_{\Pi_c=1}(\bar{N} > \bar{N}_{s,3}) = c_{8,0} + \cdot c_{8,1} \cdot \bar{N} \tag{14}$$

is proposed, and describes $\bar{W}$ at $\Pi_c = 1$ data well, while balancing model complexity. An upper saturation could be added to model (14), to agree with the experimental findings. $\bar{N}_{s,3}$ is defined as the speed where the low and high speeds model are equal, i.e. where (13)=(14).

Normalizing the $\bar{N}_{s,3}$ for each map, with the maximum $\bar{N}$ of the corresponding manufacturer map gives: 42% (KP35-1), 38% (KP35-2), 30% (KP35-3), 49% (KO4), and 70% (TDO4), of maximum measured $\bar{N}$.

The slopes $c_{7,1}$ of (13) and $c_{8,1}$ of (14) indicate the increase in $\bar{W}$ (at $\Pi_c = 1$) given a unity increase in $\bar{N}$. A larger compressor will generally have a larger

gain in $\bar{W}$ at unity pressure ratio per $\bar{N}$. The ratio of the slopes however indicate the severity of the choking. If $c_{7,1}/c_{8,1}$ is close to one, almost as much flow is gained on both sides of $\bar{N}_{s,3}$. The other way around, a slope ratio approaching infinity indicates that no extra flow is gained when the speed is increased beyond $\bar{N}_{s,3}$. The ratios of the slopes of the models, i.e. $c_{7,1}/c_{8,1}$, were: 2.2 (KP35-1), 2.1 (KP35-2), 1.6 (KP35-3), 1.7 (KO4), and 2.4 (TDO4). The small ratios of slopes for the KP35-2, KP35-3 and K04 maps indicate that the characteristics are not changing significantly at the switching $\bar{N}$.

Comment on model (13)

The simple model (13) can be motivated as follows. The energy and flow coefficient equations are given by

$$\Phi_c = \frac{W_c}{\rho_{01} \cdot \pi/4 \cdot d_c^2 \cdot U_c} \tag{15}$$

$$\Psi_c = \frac{c_p \cdot T_{01}}{0.5 \cdot U_c^2} \cdot \left[\Pi_c^{\frac{\gamma_c - 1}{\gamma_c}} - 1 \right] \tag{16}$$

where ρ is the density, d_c is the compressor diameter, U_c is the compressor blade speed, and c_p and γ_c are gas constants. Assuming that Φ_c and Ψ_c manifest only a weak dependence of N_{tc} gives the following

$$W_c|_{\Pi_c=1} = \underbrace{\Phi_c|_{\Psi_c=0} \cdot \rho_{01} \cdot \frac{\pi^2 \cdot d_c^3}{4 \cdot 60}}_{const} \cdot N_{\mathrm{tc}} \tag{17}$$

for some, unknown, value of $\Phi_c|_{\Psi_c=0}$ (which should then be independent of N_{tc}). Here it is clear that flow for pressure ratios equal to unity is proportional to N_{tc}, and if a constant T_{01} is assumed proportional to $\bar{N}$.

4 The Ellipse compressor model

The Ellipse model, see e.g. [17, 19], is commonly parametrized to describe the full operation range of a compressor. However, here it is only used to model a single SpL. The model and the parametrization process is first introduced and the high flow extrapolation capability is then studied.

4.1 Ellipse model overview

An overview of the model is presented in Fig. 12. A quarter of generalized ellipse is used to model a speedline from the zero slope point to the choking point. The zero slope line, the choke line, and the curvature of the ellipse are then functions of $\bar{N}$. For positive flows smaller than the zero slope flow, the following third order polynomial model is used

$$\Pi_{c,El} = \Pi_{c0} + 3\frac{\Pi_{c,\mathrm{ZS}} - \Pi_{c0}}{\bar{W}_{\mathrm{ZS}}^2} \cdot \bar{W}^2 - 2\frac{\Pi_{c,\mathrm{ZS}} - \Pi_{c0}}{\bar{W}_{\mathrm{ZS}}^3} \cdot \bar{W}^3 \tag{18}$$

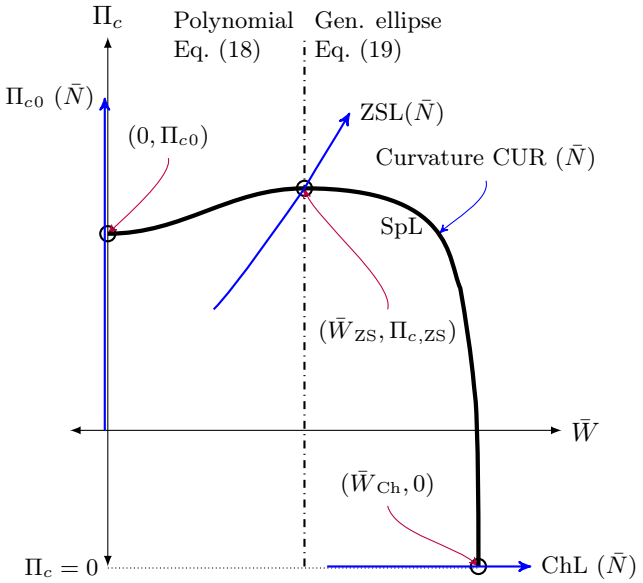

Figure 12: A generalized ellipse is used as a speedline model, from the zero slope point and to the choking point. A full compressor flow model is given by parameterizing the ZSL, the ChL, and the curvature of the generalized ellipse as functions of $\bar{N}$. A third order polynomial in $\bar{N}$ is used as model from zero flow to the ZSL, where zero flow pressure ratio (Π_{c0}) is a function of $\bar{N}$.

where Π_{c0} is the pressure ratio at zero flow. For flows between zero slope and choke ($\bar{W}_{\mathrm{ZS}} < \bar{W} \leq \bar{W}_{\mathrm{Ch}}$), the following model is used

$$\Pi_{c,El} = \left(1 - \left(\frac{\bar{W} - \bar{W}_{\mathrm{ZS}}}{\bar{W}_{\mathrm{Ch}} - \bar{W}_{\mathrm{ZS}}}\right)^{\mathrm{CUR}}\right)^{\frac{1}{\mathrm{CUR}}} \cdot \Pi_{c,\mathrm{ZS}} \tag{19}$$

where the zero slope pressure ratio and flow are modeled as

$$\Pi_{c,\mathrm{ZS}} = 1 + c_{9,1} \cdot \bar{N}^{c_{9,2}} \tag{20}$$

$$\bar{W}_{\mathrm{ZS}} = 0 + c_{10,1} \cdot \bar{N}^{c_{10,2}} \tag{21}$$

The 1 and 0 in these equations emphasize that zero slope is found at $(\bar{W}, \Pi_c) = (0, 1)$ for a standstill compressor. The choking line flow $\bar{W}_{\mathrm{Ch}}$ and curvature CUR are commonly a function of $\bar{N}$, and the choking line pressure ratio is set constant (usually at 0 to simplify the equation). CUR is commonly close to 2, in which case the model is an ellipse (which motivates the name), but since CUR is not necessarily equal to 2 the model does not strictly mathematically correspond to an ellipse. The flow for pressure ratios of unity and zero are given

by

$$\bar{W}_{\Pi_c=1} = \left(1 - \left(\frac{1}{\Pi_{c,\mathrm{ZS}}}\right)^{\mathrm{CUR}}\right)^{\frac{1}{\mathrm{CUR}}} \cdot (\bar{W}_{\mathrm{Ch}} - \bar{W}_{\mathrm{ZS}}) + \bar{W}_{\mathrm{ZS}} \tag{22}$$

$$\bar{W}_{\Pi_c=0} = \bar{W}_{\mathrm{Ch}} \tag{23}$$

For $\bar{W} > \bar{W}_{\mathrm{Ch}}$ the model saturates at $\Pi_c = 0$.

4.2 Model parametrization

In the parametrization of the model, nonlinear least squares are usually applied that minimizes $\sum_j \left(\Pi_{c,\mathrm{meas},j} - \Pi_{c,El,j}\right)^2$, where j runs over all measured points. However, normal least squares can give poor parameters due to the infinite slope at the choking point. Another approach was therefore followed here that, instead minimizing the total weighted least squares of $\sum_j e_j^2$ where

$$e_j = p \cdot \left(\frac{\Delta\bar{W}_j}{\max \bar{W}_{\mathrm{meas}}}\right)^2 + \left(\frac{\Delta\Pi_{c,j}}{\max \Pi_{c,\mathrm{meas}}}\right)^2 \tag{24}$$

$$\Delta\bar{W}_j = \bar{W}_{\mathrm{meas},j} - \bar{W}_{El,j} \tag{25}$$

$$\Delta\Pi_{c,j} = \Pi_{c,\mathrm{meas},j} - \Pi_{c,El,j} \tag{26}$$

The distance between measured data and model is normalized by the maximum measured $\bar{W}$ and Π_c on that SpL respectively. The total least squares is built by for each measured map point j constructing a line through the origin $(\bar{W},\Pi_c) = (0,0)$ and the measured map point $(\bar{W}_{\mathrm{meas},j}, \Pi_{c,\mathrm{meas},j})$. Where the constructed lines intersects the modeled speedline, is taken as $(\bar{W}_{El,j}, \Pi_{c,El,j})$. p is here introduced to emphasize or attenuate $\bar{W}$-errors, important for the high flow asymptote, and here $p = 1000$ was used. The parameter optimization was then conducted using the `lsqcurvefit` in matlab.

4.3 Validation of $\Pi_c > 1$-extrapolation

To validate the extrapolation capability of the Ellipse SpL-model, the full maps were used. The points on each SpL of the full maps were removed so that only the normal part of the SpL remained. An Ellipse SpL-model was then parametrized to the normal map part. The model extrapolation was then compared to the lowest point measured on that SpL in the full map.

The result is presented in Fig. 13. It can be seen that in general an underestimate of $\bar{W}$ of approximately 5% results. The relative errors are positive and larger for higher speeds. The large resulting relative errors for higher speeds can be explained by that many of the full maps contain only one point measured at low pressure ratio for higher speeds. When this point is removed, the remaining points form a SpL with small slope, which naturally overestimates the maximum flow of a SpL.

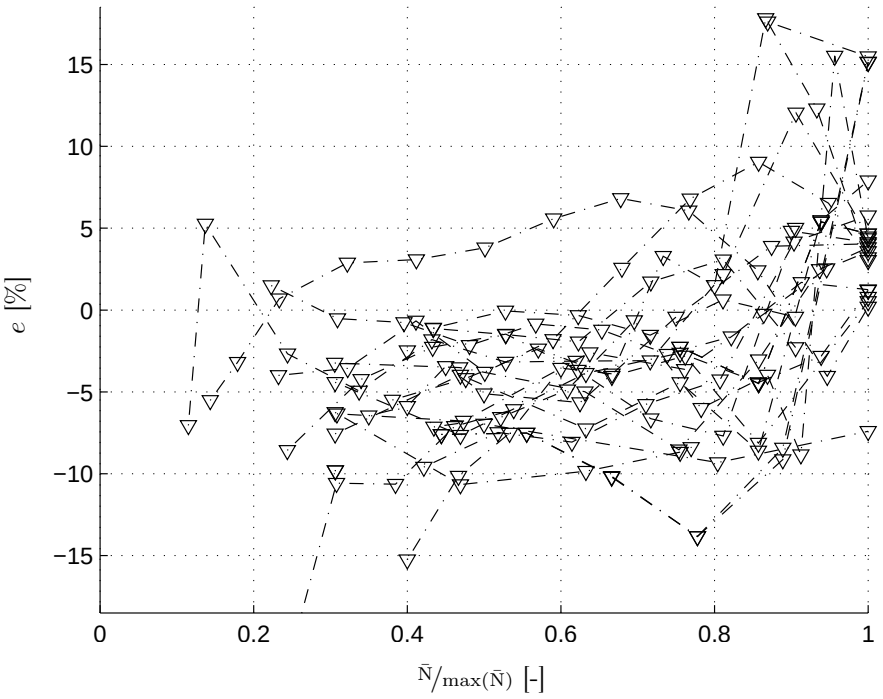

Figure 13: Validation of the Ellipse SpL model extrapolation. Models are parametrized to only the normal part of the full maps, and the models are then used to extrapolate $\bar{W}$ of the lowest Π_c of the full map. The resulting extrapolated $\bar{W}$ is compared to the measured, and the relative absolute errors as $e = {}^{(\bar{\mathrm{W}}_{\mathrm{mod}} - \bar{\mathrm{W}}_{\mathrm{meas}})}/_{\bar{\mathrm{W}}_{\mathrm{meas}}}$ are presented.

4.4 Comment on extrapolation to $\Pi_c < 1$

To analyze the extrapolation to $\Pi_c < 1$, the full map part of the extended maps were extracted, and used to parametrize SpL-models. The $\Pi_c < 1$-points were then used as validation data, for extrapolation to restriction operation. The resulting extrapolation showed large errors and highlights the importance of measurements, if models are to be used with high accuracy in restriction operation.

5 Analysis and modeling of $\bar{W}_{\Pi_c=1}$

The Ellipse SpL-model is here used to analyze flow at unity pressure ratio for the full and normal maps of the map database.

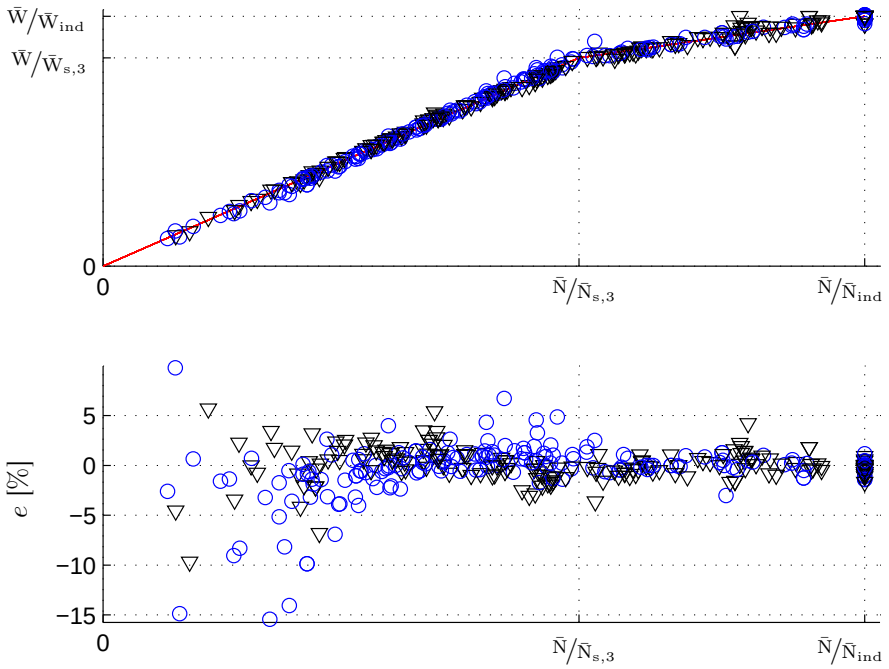

Figure 14: Validation of model (13) and (14), parametrized for $\bar{W}_{\Pi_c=1}$ estimated for each SpL using (22) (black triangles), and to the maximum $\bar{W}$ of each SpL (blue circles). For $\bar{N} < \bar{N}_{s,3}$ the data is normalized by the switching $\bar{N}$ and $\bar{W}$, respectively. All map individual model hence collapse to a single line (shown in red). A map individual ($\bar{N}_{\text{ind}}$ and $\bar{W}_{\text{ind}}$) normalization has been conducted to collapse all models to a single line (shown in red) for the higher speeds. The lower plots shows the relative errors. The 25 full maps are used.

5.1 Extrapolation to $\Pi_c = 1$ in full maps

Each SpL of the full maps are extracted, and all points of a SpL are used to parametrize (19). Flow at unity pressure ratio is then calculated using (22). Since the maximum flow point of a full map SpL ($\bar{W}_{\text{max,full}}$) is a reasonable approximation of flow at unity pressure ratio, at least for lower and higher speeds, these flows were also extracted for each map. The modeled (using (22)) and approximated flows ($\bar{W}_{\text{max,full}}$) for each map, were then used to parametrize low and high speed unity pressure ratio flow models according to (13) and (14), respectively.

The resulting model fits for all 25 full maps are presented in Fig. 14. Blue circles represent the maximum measured flow of each SpL, in each map. The black triangles show the Ellipse model. The data for $\bar{N} < \bar{N}_{s,3}$ are normalized by each maps $\bar{N}_{s,3}$ and $\bar{W}_{s,3}$. This means that the models for each map collapse to a single line, which is shown in solid red. The points at $\bar{N} > \bar{N}_{s,3}$ are for each map individually normalized so that also these models collapse into a single

line. The lower plot shows the corresponding relative errors between the model and each of the two estimates. It can be seen that the simple model captures $\bar{W}_{\Pi_c=1}$, where most points from medium to high speeds have a relative model error of less than three percent. The extrapolation for lower $\bar{N}$ is worse, were both models generally underestimate the flow.

Two $\bar{W}_{\Pi_c=1}$-models hence result for each map, one for the extrapolation using (22), and one for the measured approximate flow (i.e. $\bar{W}_{\max,\text{full}}$). Each model consists of 3 parameters; the slope $c_{7,1}$ of the linear low speed model (13), and the slope $c_{7,1}$ and constant $c_{7,0}$ of the affine high speed model (14). The switching speed $\bar{N}_{s,3}$ and corresponding switching flow $\bar{W}_{s,3}$ between the low and high speed models are calculated as

$$\bar{N}_{s,3} = \frac{c_{8,0}}{c_{7,1} - c_{8,1}} \tag{27}$$

$$\bar{W}_{s,3} = c_{7,1} \cdot \bar{N}_{s,3} \tag{28}$$

The average switching flow for the full maps were 91% and 87% of maximum flow, for the maximum flow points and the Ellipse extrapolation respectively. These flows were obtained at an average switching speed of 81% and 71%, respectively. This means that the last 19% in speed, only gives a gain of 9% in flow for the measured maximum flow points. For the Ellipse extrapolation, the upper 29% in speeds only gives 13% of the relative flow. The average slope ratio for the models parametrized to the maximum measured flow points of each SpL was 2.75. For the models parametrized to the Ellipse extrapolation points, a mean of 3.44 was found. None of the calculated slope ratios were less than one. Both the average slope ratio and relative switching speed is considerably higher than those found for at least the smaller extended maps.

5.2 Extrapolation to $\Pi_c = 1$ in normal maps

The same investigation as in Section 5.1, was also done using the normal maps, and the resulting model fits are presented in Fig. 15. As in Fig. 14, blue circles represent the highest measured $\bar{W}$ of each SpL, and black triangles represent the extrapolation using (22). The resulting models are given in solid red lines. The lower plot shows the relative errors.

It can be seen that, compared to the full map extrapolation presented in Fig. 14, the scattering of the points increases. This is natural since a larger uncertainty is introduced in the extrapolation due to that the last measured points are further away from $\Pi_c = 1$. However, the simple models (13) and (14), give a good description of the data. Some outliers are present, which are caused by model parametrization errors of (19), and that the highest speedline often has its last point far from $\Pi_c = 1$. In general, however, the relative model errors are less than 5%. As for the full maps, the relative error increases for smaller speeds. This is natural as the absolute value approaches zero.

The mean relative switching $\bar{W}$ and $\bar{N}$ are for the normal maps found to be 93% and 83% respectively, for the models using the maximum measured flow. For the models resulting from (22), the mean relative switching $\bar{N}$ and $\bar{W}$ are found to be 86% and 71%, respectively. The ratios of the models' slopes are

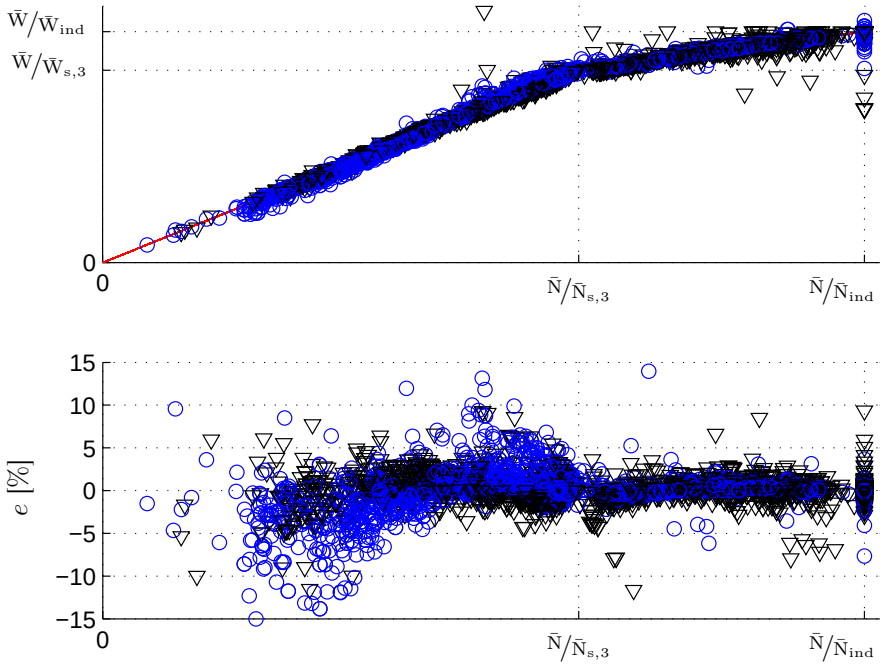

Figure 15: Validation of model (13) and (14), parametrized for $\bar{W}_{\Pi_c=1}$ estimated for each SpL using (22) (black triangles), and to the maximum $\bar{W}$ of each SpL (blue circles). For $\bar{N} < \bar{N}_{s,3}$ the data is normalized by the switching $\bar{N}$ and $\bar{W}$, respectively. All map individual model hence collapse to a single line (shown in red). A map individual ($\bar{N}_{\text{ind}}$ and $\bar{W}_{\text{ind}}$) normalization has been conducted to collapse all models to a single line (shown in red) for the higher speeds. The lower plots shows the relative errors. The 275 normal maps are used.

on average 3.03 and 4.05 respectively. As for the full map analysis, none of the slope ratios were below one.

6 Extending the Ellipse model

It is here shown how the experimental findings and models presented can be used to extend the Ellipse model from Section 4. It should be noted that the findings and models can easily be implemented in other models, and the findings should be applicable to other centrifugal compressors.

6.1 Novel choke capable model

The extended model keeps the original model formulation for flows smaller than the zero slope flow (given by (18)). The model for pressure ratio at zero flow is

given by

$$\Pi_{c0} = 1 + c_{11,1} \cdot \bar{N}^{c_{11,2}} \tag{29}$$

The novelty of the extension comes from changing the original assumption of having a constant choking pressure ratio (i.e. $\Pi_{c,\mathrm{ChL}} = 0$). The main equation (19) is changed to

$$\Pi_{c,El,nov} = \left(1 - \left(\frac{\bar{W} - \bar{W}_{\mathrm{ZS}}}{\bar{W}_{\mathrm{Ch}} - \bar{W}_{\mathrm{ZS}}}\right)^{\mathrm{CUR}}\right)^{\frac{1}{\mathrm{CUR}}} \cdot (\Pi_{c,\mathrm{ZS}} - \Pi_{c,\mathrm{Ch}}) + \Pi_{c,\mathrm{Ch}} \tag{30}$$

where the choking pressure ratio $\Pi_{c,\mathrm{Ch}}$ is modeled using (12), $\Pi_{c,\mathrm{ZS}}$ is modeled using (20) and $\bar{W}_{\mathrm{ZS}}$ is modeled using (21). To have uniquely defined speedlines (i.e. only one Π_c for each $\bar{W}$), it is then decided to avoid the backwards bending after choking in the model. This means that the choking flow must never be less than the unity pressure ratio flow. The model for unity pressure ratio flow relies on (13) for low $\bar{N}$, and on (14) for high $\bar{N}$. Since none of the slope ratios are below one, see Sections 5.1 and 5.2, the flow at unity pressure ratio can be modeled as

$$\bar{W}_{\Pi_c=1} = \min\left[\text{Eq.(13)},\ \text{Eq.(14)}\right] \tag{31}$$

The speed $\bar{N}_{s,4}$ for when (31) and (9) are equal, is calculated. The choking line flow is then given by

$$\bar{W}_{\mathrm{ChL}} = \begin{cases} \text{Eq.(9)} & \bar{N} \leq \bar{N}_{s,4} \\ \text{Eq.(31)} & \bar{N} > \bar{N}_{s,4} \end{cases} \tag{32}$$

The curvature was parametrized as a second order polynomial as

$$\mathrm{CUR} = c_{12,0} + c_{12,1} \cdot \bar{N} + c_{12,2} \cdot \bar{N}^2 \tag{33}$$

For simulation purposes it is further useful to have a model that is uniquely defined for any flow. The following is therefore proposed for corrected flows larger than the choking flow ($\bar{W} > \bar{W}_{\mathrm{Ch}}$)

$$\Pi_{c,El,nov} = \Pi_{c,\mathrm{Ch}} \cdot \left(1 - \left(\bar{W} - \bar{W}_{\mathrm{Ch}}\right)^{\frac{1}{c_{13,2}}}\right)^{c_{13,2}} \tag{34}$$

where $c_{13,2}$, is chosen large to ensure that the SpL extend from the choking line almost vertically (here $c_{13,2} = 9$ was used), and approaches $\Pi_c = 0$ as $\bar{W}$ goes to infinity.

An overview of the this novel model is presented in Fig. 16. The main difference as compared to the Ellipse model presented in Fig. 12, is the model for choking line pressure ratio.

6.2 Extended model parametrization

Given a map, the characteristic properties of the map discussed in Section 2.4 are extracted: zero slope line, choking line, and the flow at unity pressure ratio, and used to parametrize the corresponding models.

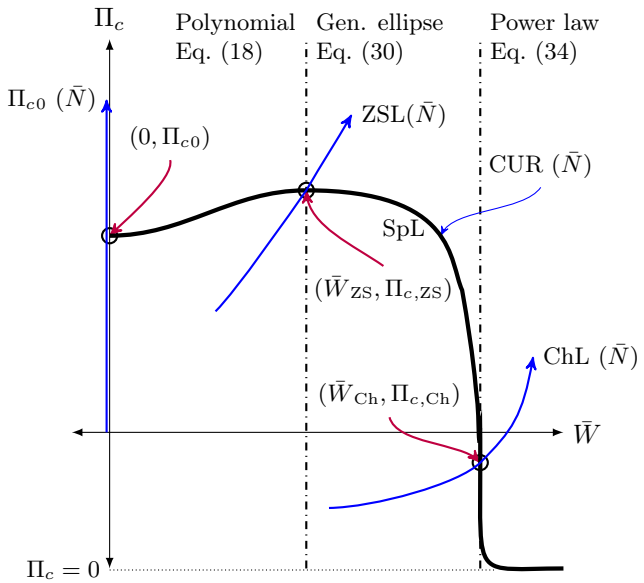

Figure 16: Overview of the novel compressor model. The main difference as compared to the Ellipse model presented in Fig. 12, is the model for choking line pressure ratio.

With these models considered "locked", nonlinear least squares are then used to estimate the optimal curvature CUR of each SpL-model. Since the flow at unity pressure ratio model, is not explicitly used in (30) for $\bar{N} < \bar{N}_{s,1}$, for these speedlines the following is used. Given a measured SpL, as many points as are measured on that particular SpL are added at the modeled unity pressure ratio flow. By varying the number of points added, this can be seen as a weighted least squares optimization. The measured and the added points are then used in the nonlinear least squares optimization of the curvature, for that SpL. This method gives a way to balance the fit to measured data, while obeying the experimental findings on flow at unity pressure ratio. The second order polynomial curvature model was then fitted to the optimal curvatures for each SpL-model. A global optimization routine could have been called, using the parametrization process just described as initial parameter estimates. This extra step was though here not taken, to keep the parametrization process simple.

A minor comment of practical importance for the optimization in the parameter tuning, is that the actual parameter estimation was conducted in a normalized form of $\bar{N}$ as $\tilde{\bar{N}} = {}^{\bar{\mathrm{N}}}/_{\max(\bar{\mathrm{N}})}$, to avoid numerical problems with largely different parameter values.

6.3 Example of extended model

The extended Ellipse model was parametrized to the largest (in flow) of the extended maps, the TD04, which was considered to be a representative example.

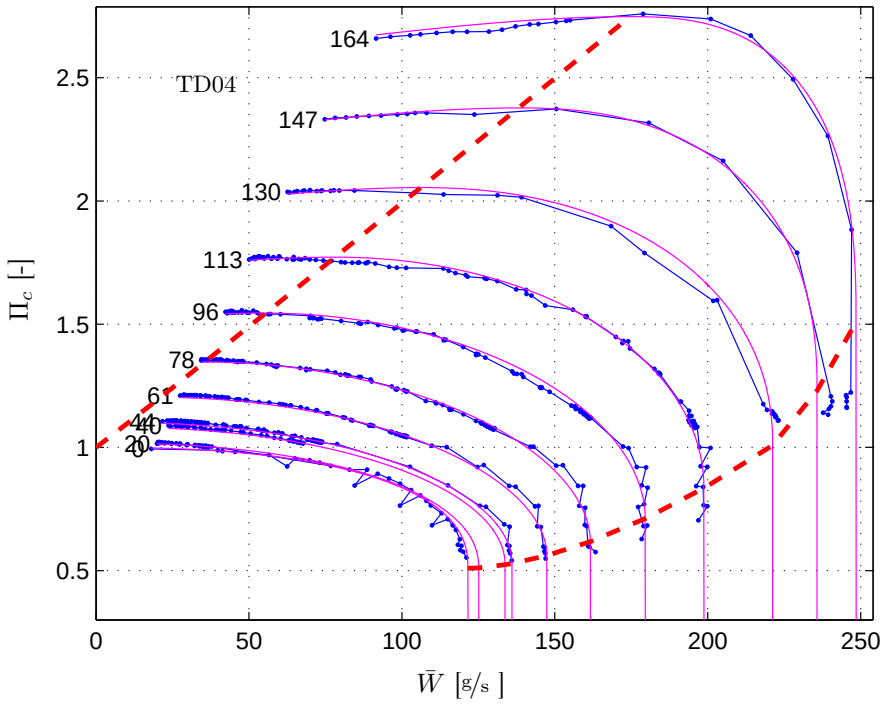

Figure 17: Example of model fit for the TD04 extended map. Blue dots represent measurement, and the solid magenta lines represent the model. Dashed lines represent the modeled zero slope line and the choking line. The numbers indicate $\bar{N}$ in krpm.

The model fit to the measurement is presented in Fig. 17. Blue dots represent measurement, and the solid magenta lines represent the model. Dashed lines represent the modeled zero slope line and the choking line.

It can be seen that the model captures the important properties for high $\bar{W}$/low Π_c-operation. The model enables an infinite slope for an increasing Π_c for increasing $\bar{N}$, and choking pressure ratios above one for higher speeds. Further, though a $\bar{W}_{\Pi_c=1}$-model is used in the parametrization process, the final model does not use an explicit formulation for this, but still gives the behavior presented in the measurement analysis. The experimental behavior presented can hence be captured by simple models. A total of seventeen parameters are used for the model.

7 Conclusions

Two methods to measure extended compressor maps with restriction operation in a gas stand are proposed, and can successfully be applied for both stand-still and rotating compressor operation. The measurement methodology is repeatable, and different compressor individuals of the same model show small

differences in measured restriction characteristics. Compressor speedlines that give a smaller corrected mass flow for a decrease in pressure ratio, are found in seventeen of the maps of the compressor map database. The maps are from compressors from different manufacturers, as well as measured in independent gas stands.

The measured standstill compressor characteristics with compressor inlet pressure at 200kPa, generally show higher corrected flows than the speedlines measured with the compressor outlet at ambient pressure and inlet pressures less than 200kPa. The compressor wheel orientation does not affect the measured standstill characteristic. The measured standstill characteristics are accurately modeled using two proposed models. Applying the general compressible flow restriction model, is not successful in describing the standstill flow.

The choking point of a speedline is defined as the point with infinite slope. The corrected choking mass flow of a compressor map is accurately described by a novel power law model, up to approximately medium corrected speeds. The proposed model is able to extrapolate stand still choking flow. The standstill choking corrected mass flow is approximately half of the maximum corrected flow of a map. A saturation in choking corrected mass flow is visible for maximum speeds.

The choking pressure ratio is accurately modeled using a power law model. The model is capable of extrapolating standstill choking pressure ratio. Standstill choking pressure ratio is approximately 0.5, and increasing with corrected speed up to approximately 1.5 at maximum speed. For all five extended maps measured, choking pressure ratios are higher than one for the highest speeds, which is further supported by twelve of the other maps in the database.

Corrected mass flow at unity pressure ratio can be accurately described by a linear model, from standstill up to medium speeds. This simple model is supported by dimensional analysis. An affine model is supported by the measured data for high speeds. The corrected mass flow at unity pressure ratio and the choking corrected mass flow converges for higher speeds. The maximum measured corrected mass flow of maps measured down to the discharge characteristics of a gas stand, approximately agrees with the unity pressure ratio flows for low and high speeds. The difference is larger for intermediate speeds.

The Ellipse compressor flow model can be used as a compressor speed line flow model, to extrapolate normal and full maps to flow at unity pressure ratio. Using the model, the switching point between the proposed linear and affine models for unity pressure ratio flow is approximately at $75 - 80\%$ of maximum flow, and correspondingly at approximately 90% of maximum speed. The extrapolation capability, of the Ellipse model, to pressure ratios well below unity is less accurate highlighting the importance of measurements if this region is to be modeled.

An extension to the Ellipse model is shown to accurately capture the experimental findings for low pressure ratio and compressor restriction operation, from standstill up to maximum speed.

Funding

This work was supported by the Vinnova Industry Excellence Center: LINK-SIC Linköping Center for Sensor Informatics and Control.

Declaration of conflicting interests

The authors declare that there is no conflict of interest.

References

[1] ASME (1997). PTC 10-1997, Performance test code on compressors and exhausters. American Society of Mechanical Engineers, New York.

[2] Borila, Y. (1988). A sequential turbocharging method for highly-rated truck diesel engines. In *SAE*, Techn. Paper 860074.

[3] Casey, M. & Fesich, T. (2009). On the efficiency of compressors with diabatic flows. In *Proc. of ASME Turbo Expo*, GT2009-59015.

[4] Casey, M. & Schlegel, M. (2010). Estimation of the performance of turbocharger compressors at extremely low pressure ratios. *Proc. of the IMechE, Part A: J. of Power and Energy*, 224(2).

[5] Chapman, K. S. & Shultz, J. (2003). *Guidelines for: Testing Large-Bore Engine Turbochargers.* Technical report, The National Gas Machinery Laboratory, Kansas State University, 245 Levee Drive.

[6] Chasse, A., Moulin, P., Albrecht, A., Fontvielle, L., Guinois, A., & Doléac, L. (2008). Double stage turbocharger control strategies development. In *SAE World Congr.*, Techn. Paper 2008-01-0988.

[7] Cormerais, M., Hetet, J., Chesse, P., & Maiboom, A. (2006). Heat transfer analysis in a turbocharger compressor: modeling and experiments. In *SAE World Congr.*, Techn. Paper 2006-01-0023 Detroit, USA.

[8] Eidenböck, T., Mayr, K., Neuhauser, W., & Staub, P. (2012). The new BMW six-cylinder diesel engine with three turbochargers part 1: Drive unit and turbocharger system. *MTZ*, 73(1), 18–24.

[9] Emmenthal, K., Hagemann, G., & Hucho, W. (1979). Turbocharging small displacement spark ignition engines for improved fuel economy. In *SAE*, Techn. Paper 790311.

[10] Eriksson, L., Lindell, T., Leufvén, O., & Thomasson, A. (2012). Scalable component-based modeling for optimizing engines with supercharging, E-boost and turbocompound concepts. *SAE I.J. of Engines*, 5(2), 579–595.

[11] Galindo, J., Climent, H., Guardiola, C., & Domenech, J. (2009). Strategies for improving the mode transition in a sequential parallel turbocharged automotive diesel engine. *I.J. of Automotive Technology*, 10(2), 141–149.

[12] Guzzella, L., Wenger, U., & Martin, R. (2000). IC-engine downsizing and pressure-wave supercharging for fuel economy. In *SAE World Congr.*, Techn. Paper 2000-01-1019.

[13] Heywood, J. B. (1988). *Internal Combustion Engine Fundamentals*. McGraw-Hill series in mechanical engineering. McGraw-Hill.

[14] Hiereth, H. & Prenninger, P. (2007). *Charging the Internal Combustion Engine*. Springer Wien NewYork.

[15] Jensen, J., Kristensen, A., Sorenson, S., Houbak, N., & Hendricks, E. (1991). Mean value modeling of a small turbocharged diesel engine. In *SAE World Congr.*, Techn. Paper 910070.

[16] Larsson, P.-I., Westin, F., Andersen, J., Vetter, J., & Zumeta, A. (2009). Efficient turbo charger testing. *MTZ*, 70(07-08), 16–21.

[17] Leufvén, O. & Eriksson, L. (2008). Time to surge concept and surge control for acceleration performance. In *Proc. of IFAC World Congr.* (pp. 2063–2068).

[18] Leufvén, O. & Eriksson, L. (2010). Engine test bench turbo mapping. In *SAE World Congr.*, Techn. Paper 2010-01-1232.

[19] Leufvén, O. & Eriksson, L. (2011). Surge and choke capable compressor model. In *Proc. of IFAC World Congr.* (pp. 10653–10658).

[20] Leufvén, O. & Eriksson, L. (2012). Investigation of compressor correction quantities for automotive applications. *I.J. of Engine Research*, 13(6), 588–606.

[21] Lewis, R. I. (1996). *Turbomachinery Performance Analysis*. Arnold.

[22] Moraal, P. & Kolmanovsky, I. (1999). Turbocharger modeling for automotive control applications. In *SAE World Congr.*, Techn. Paper 1999-01-0908.

[23] Müller, M., Sumser, S., Fledersbacher, P., Rößler, K., Fieweger, K., & Bauer, H. (2005). Using the centrifugal compressor as a cold-air turbine. In *Int. conf. on turbochargers and turbocharging* London.

[24] Nitta, J., Minato, A., & Shimazaki, N. (2011). Performance evaluation of three-stage turbocharging system for heavy-duty diesel engine. In *SAE World Congr.*, Techn. Paper 2011-01-0374.

[25] Petitjean, D., Bernardini, L., Middlemass, C., Shahed, S., & Hurley, R. (2004). Advanced gasoline engine turbocharging technology for fuel economy improvements. In *SAE World Congr.*, Techn. Paper 2004-01-0988.

[26] SAE standard (1995a). J1826 – Turbocharger Gas Stand Test Code.

[27] SAE standard (1995b). J922 – Turbocharger Nomenclature and Terminology.

[28] Shaaban, S. (2004). *Experimental Investigation and Extended Simulation of Turbocharger Non-adiabatic Performance.* PhD thesis, Leibniz Universität Hannover.

[29] Sirakov, B. & Casey, M. (2011). Evaluation of heat transfer effects on turbocharger performance. In *Proc. of ASME Turbo Expo*, GT2011-45887.

[30] Watson, N. & Janota, M. (1982). *Turbocharging the internal combustion engine.* MacMillan London.

[31] Westin, F. & Burenius, R. (2010). Measurement of interstage losses of a twostage turbocharger system in a turbocharger test rig. In *SAE World Congr.*, Techn. Paper 2010-01-1221.

[32] Willems, F. & de Jager, B. (1999). Modeling and control of compressor flow instabilities. *Control Systems, IEEE*, 19(5), 8–18.

[33] Zhang, Z., Deng, K., Wang, Z., & Zhu, X. (2008). Experimental study on the three-phase sequential turbocharging system with two unequal size turbochargers. *SAE I.J. of Fuels and Lubricants*, 1, 1181–1186.

[34] Zinner, K. (1985). *Aufladung von Verbrennungsmotoren. Grundlagen, Berechnungen, Ausführungen.* Springer Verlag.

A Extended map gas stand setup details

The gas stand and acquisition system are made by AVL. Two Atlas Copco screw-compressors feed a charge-air-to-water intercooler where the air is conditioned. The air can be delivered to both compressor and turbine, using valves. A diesel burner is used to increase turbine gas flow temperature. Both turbo oil and water supply temperature and pressure can be individually controlled. The measurement stations for $T_{0i},\ i = \{1, 2, 3\}$ were equipped with 8 sensors each. The sensors were divided into two groups of four sensors, spread out evenly circumferential around the measurement planes for redundancy and diagnostic purposes. PT100 sensors were used for the cold temperatures, and K-type thermocouples were used in the hot flows. The measurement stations for $p_j,\ j = \{1..4\}$ consisted of two measurement rings each, using relative pressure sensors. Two McCrometer Vcone differential pressure based measurement rings were used to measure different ranges of compressor mass flow. The differential pressure sensors were of model PMP4110 from GE Druck. JAQUET model T411-S5 tachometers were used to measure turbo shaft speed.

B Offline re-estimation of mass flow signal

McCrometer Vcone sensor mass flow is calculated as[1]

$$W = \frac{\pi}{4} \cdot \sqrt{2 \cdot \rho} \cdot \frac{D^2 \cdot \beta^2}{\sqrt{1 - \beta^4}} \cdot \sqrt{\Delta p} \cdot C_f(\mathrm{Re}) \cdot Y \tag{35}$$

where W is mass flow, ρ density, D pipe diameter, β beta ratio, Δp differential pressure, $C_f(\mathrm{Re})$ calibration function containing geometry information and constants, Re Reynolds number, and Y gas expansion factor. No geometry data (D or β, or the calibration function $C_f(\mathrm{Re})$ were available for the offline calculations.

The raw data from the gas stand used contains signals for both measured and calculated quantities, and the following are used in the offline re-estimation: W, Re, p, T, Δp, and Y. The ratio of specific heats was first calculated using the measured temperature and an 1D-interpolation table: $\gamma = f_{interp1}(T)$. The dynamic viscosity was then calculated using Sutherlands's formula[2] as: $\mu(T) = \mu_0 \cdot \frac{T_0 + C}{T + C} \cdot \left(\frac{T}{T_0}\right)^{3/2}$, where $\mu_0 = 18.27 \cdot 10^{-6}\,\mathrm{Pa/s}$ is reference viscosity, $C = 120\mathrm{K}$ Sutherland's constant, and $T_0 = 291.15\mathrm{K}$ reference temperature. The density was calculated as $\rho = \mathrm{P}/\mathrm{R \cdot T}$, with $R = 287\,\mathrm{J/kgK}$. The beta ratios were then estimated for both Vcones taking the mean of

$$\beta = \left(\frac{\frac{\gamma \cdot p}{\Delta p} \cdot (1 - Y) - 0.649}{0.696} \right)^{1/4} \tag{36}$$

for all map points. The pipe diameters where then estimated as the mean of

$$D = \frac{4 \cdot W}{\pi \cdot \mu \cdot \mathrm{Re}} \tag{37}$$

for all map points. Re was then re-estimated using $\mathrm{Re} = 4 \cdot \mathrm{W}/(\pi \cdot \mathrm{D} \cdot \mu(\mathrm{T}))$.

Constants values of the calibration functions $C_f(\mathrm{Re})$ were than calculated as the mean of C_f from (35), for low to medium Reynolds number for which the original calibration was believed to be more reliable. The mass flow was finally re-calculated using (35) for all points, with least squares estimated D, β and C_f.

[1] `http://www.mccrometer.com/library/pdf/24509-54.pdf`, downloaded 130317.
[2] `http://en.wikipedia.org/wiki/Viscosity`, downloaded 130317.

Linköping studies in science and technology. Dissertations.
Division of Vehicular Systems
Department of Electrical Engineering
Linköping University

No. 1 Magnus Pettersson *Driveline Modeling and Control*, 1997

No. 2 Lars Eriksson *Spark Advance Modeling and Control*, 1999

No. 3 Mattias Nyberg *Model Based Fault Diagnosis: Methods, Theory, and Automotive Engine Applications*, 1999

No. 4 Erik Frisk *Residual Generation for Fault Diagnosis*, 2001

No. 5 Per Andersson *Air Charge Estimation in Turbocharged Spark Ignition Engines*, 2005

No. 6 Mattias Krysander *Design and Analysis of Diagnosis Systems Using Structural Methods*, 2006

No. 7 Jonas Biteus *Fault Isolation in Distributed Embedded Systems*, 2007

No. 8 Ylva Nilsson *Modelling for Fuel Optimal Control of a Variable Compression Engine*, 2007

No. 9 Markus Klein *Single-Zone Cylinder Pressure Modeling and Estimation for Heat Release Analysis of SI Engines*, 2007

No. 10 Anders Fröberg *Efficient Simulation and Optimal Control for Vehicle Propulsion*, 2008

No. 11 Per Öberg *A DAE Formulation for Multi-Zone Thermodynamic Models and its Application to CVCP Engines*, 2009

No. 12 Johan Wahlström *Control of EGR and VGT for Emission Control and Pumping Work Minimization in Diesel Engines*, 2009

No. 13 Anna Pernestål *Probabilistic Fault Diagnosis with Automotive Applications*, 2009

No. 14 Erik Hellström *Look-ahead Control of Heavy Vehicles*, 2010

No. 15 Erik Höckerdal *Model Error Compensation in ODE and DAE Estimators with Automotive Engine Applications*, 2011

No. 16 Carl Svärd, *Methods for Automated Design of Fault Detection and Isolation Systems with Automotive Applications*, 2012.